NASA Conference Publication 2065
Part II

Recent Advances in Structures for Hypersonic Flight

Proceedings of
a symposium held at
Langley Research Center
Hampton, Virginia
September 6-8, 1978

NASA

NASA Conference Publication 2065
Part II

Recent Advances in Structures for Hypersonic Flight

Proceedings of
a symposium held at
Langley Research Center
Hampton, Virginia
September 6-8, 1978

NASA
National Aeronautics
and Space Administration

Scientific and Technical
Information Office

1978

PREFACE

The proceedings of the NASA Symposium - Recent Advances in Structures for Hypersonic Flight held at Langley Research Center on September 6-8, 1978, are reported in this NASA Conference Proceedings. The papers at this Symposium were presented by 24 speakers representing airframe, missile, and engine manufacturers, the U.S. Air Force, and two NASA Research Centers.

The Symposium was organized in six sessions as follows:

I. Overviews
II. Engine Structures
III. Cooled Airframe Structures
IV. Hot Structures and TPS
V. Tankage and Insulation
VI. Analysis Methods

Papers and the authors thereof are grouped by session and identified in the CONTENTS. The order of papers is the actual order of speaker appearance at the Symposium.

The papers contained in this compilation were submitted as camera-ready copy and have been edited only for clarity and format. Technical contents and views expressed are the responsibility and opinions of the individual authors. The size of the compilation necessitated publication in two parts (Parts I and II). A list of attendees, by organizational affiliation, is included at the back of Part II.

We would like to express appreciation to session chairmen and speakers whose efforts contributed to the technical excellence of the Symposium.

Certain commercial materials are identified in this paper in order to specify adequately which materials were investigated in the research effort. In no case does such identification imply recommendation or endorsement of the product by NASA, nor does it imply that the materials are necessarily the only ones or the best ones available for the purpose. In many cases equivalent materials are available and would probably produce equivalent results.

S. C. Dixon
Symposium Chairman

C. P. Shore
Symposium Coordinator

CONTENTS

Part I*

PREFACE iii

WELCOME 1
R. R. Heldenfels

SESSION I - OVERVIEWS
Chairman: A. J. Henderson

1. HYPERSONIC STRUCTURES: AN AERODYNAMICIST'S PERSPECTIVE (OR ONE MAN'S DREAM IS ANOTHER MAN'S NIGHTMARE) 5
J. D. Watts, L. R. Jackson, and J. L. Hunt

2. STRUCTURAL REQUIREMENTS FOR MILITARY HYPERSONIC SYSTEMS (Paper not available for publication)
P. Lane

3. AIRFRAME-INTEGRATED PROPULSION SYSTEM FOR HYPERSONIC CRUISE VEHICLES 39
Robert A. Jones and Paul W. Huber

4. RECENT ADVANCES IN CONVECTIVELY COOLED ENGINE AND AIRFRAME STRUCTURES FOR HYPERSONIC FLIGHT 47
H. Neale Kelly, Allan R. Wieting, Charles P. Shore, and Robert J. Nowak

SESSION II - ENGINE STRUCTURES
Chairman: H. N. Kelly

5. DESIGN AND ANALYSIS OF A SCRAMJET ENGINE 65
O. A. Buchmann

6. THERMOSTRUCTURAL ANALYSIS OF A SCRAMJET FUEL-INJECTION STRUT 119
Allan R. Wieting and Earl A. Thornton

7. ADVANCED FABRICATION TECHNIQUES FOR COOLED ENGINE STRUCTURES 145
O. A. Buchmann

8. HYDROGEN EMBRITTLEMENT AND ITS CONTROL IN HYDROGEN-FUELED ENGINE SYSTEMS 195
W. T. Chandler

*Papers 1 to 14 are presented under separate cover.

9. CARBON-CARBON COMPOSITE APPLICATION FOR INTEGRAL ROCKET RAMJET COMBUSTORS (Paper not available for publication)
H. A. Holman

SESSION III - COOLED AIRFRAME STRUCTURES
Chairman: C. P. Shore

10. DESIGN AND FABRICATION OF A SKIN STRINGER DISCRETE TUBE ACTIVELY COOLED STRUCTURAL PANEL 253
Frank M. Anthony

11. DESIGN AND ANALYSIS OF A PLATE-FIN SANDWICH ACTIVELY COOLED STRUCTURAL PANEL 319
L. M. Smith

12. FLUXLESS BRAZING AND HEAT TREATMENT OF A PLATE-FIN SANDWICH ACTIVELY COOLED PANEL 375
Charles S. Beuyukian

13. DESIGN AND FABRICATION OF A RADIATIVE ACTIVELY COOLED HONEYCOMB SANDWICH PANEL 449
Leland C. Koch

14. RADIATIVE-ACTIVELY COOLED PANEL TESTS RESULTS 493
Charles P. Shore, Robert J. Nowak, and Ellsworth L. Sharpe

Part II

SESSION IV - HOT STRUCTURES AND TPS
Chairman: H. L. Bohon

15. TESTS OF BEADED AND TUBULAR STRUCTURAL PANELS 539
John L. Shideler, Roger A. Fields, and Lawrence F. Reardon

16. STRUCTURES FOR HYPERSONIC AIRBREATHING TACTICAL MISSILES 577
William C. Caywood and Robert M. Rivello

17. STRUCTURES AND TPS FOR THE NHFRF/HYTID 601
Harvey J. Hoge

18. DESIGN AND FABRICATION OF A SUPER ALLOY THERMAL PROTECTION SYSTEM 629
A. Varisco, W. Wolter, and P. Bell

19. MULTIWALL TPS 671
L. Robert Jackson

20. DRYDEN FLIGHT RESEARCH CENTER HOT STRUCTURES RESEARCH 707
Roger A. Fields

SESSION V - TANKAGE AND INSULATION
Chairman: R. D. Witcofski

21. LIQUID HYDROGEN TANKAGE DESIGN 759
George W. Davis

22. EXTERNAL INSULATION FOR LIQUID HYDROGEN TANKS 807
Ellsworth L. Sharpe

SESSION VI - ANALYSIS METHODS
Chairman: W. C. Walton, Jr.

23. RECENT ADVANCES IN THERMOSTRUCTURAL FINITE ELEMENT ANALYSIS 851
Earl A. Thornton and Allan R. Wieting

24. RECENT ADVANCES IN THERMAL-STRUCTURAL ANALYSIS AND DESIGN 897
Howard M. Adelman and James C. Robinson

ATTENDEES 943

SESSION IV - HOT STRUCTURES AND TPS

TESTS OF BEADED AND TUBULAR STRUCTURAL PANELS

John L. Shideler
NASA Langley Research Center

Roger A. Fields and Lawrence F. Reardon
NASA Dryden Flight Research Center

15

INTRODUCTION

(Figure 1)

When hot structure is used in the design of hypersonic vehicles, special design considerations such as accommodating thermal growth have to be considered. A study conducted by Lockheed a number of years ago (reference 1) determined that the optimum design for a hot wing structure consists of ribs and spars with corrugated webs covered by spanwise stiffened beaded panels. In these panels, chordwise thermal growth results in an increased bead depth. Thus, panel thermal stresses in the chordwise direction become of small concern. Corrugated heat shields protect the load carrying structure from excessive temperature and provide a smoother aerodynamic surface. The leading edge is segmented to reduce thermal stress, and insulation is used between the exposed surface and the primary structure where the heat shield alone isn't enough to protect the primary structure. The structure is René 41, except for the heat shields near the wing leading edge which are TD-Ni-20Cr.

The two most efficient panel concepts identified by this study were the beaded panel, shown in the figure, and a tubular panel. Since no data base for these panels existed, studies to determine their structural performance began at Dryden and Langley Research Centers.

OPTIMUM DESIGN HOT WING STRUCTURE

NASA CR-1568

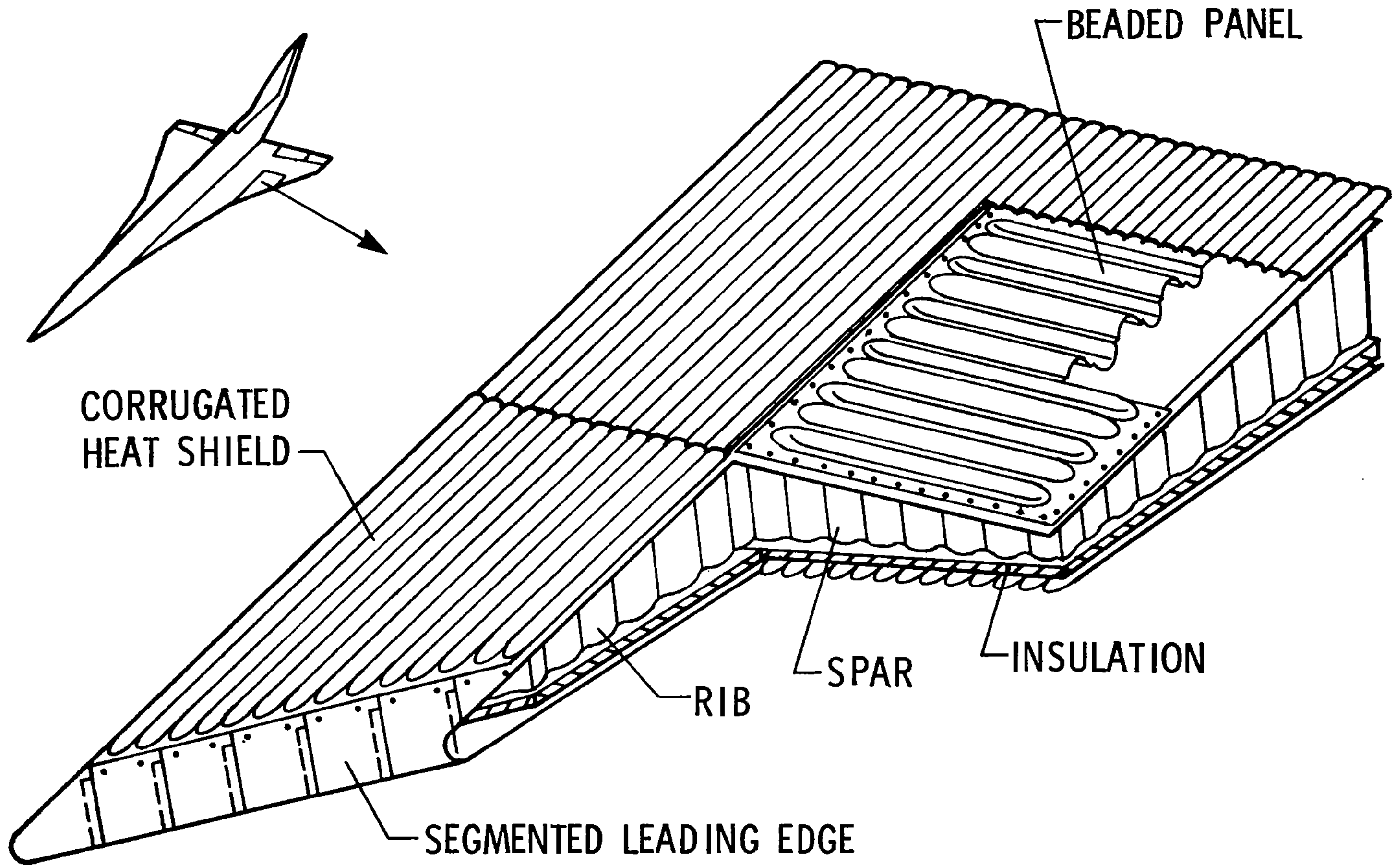

Figure 1

MASS COMPARISON OF ALUMINUM BEADED AND TUBULAR PANELS

(Figure 2)

The calculated mass of several 1 m by 1 m (40 inch by 40 inch) aluminum panels are shown as a function of compressive end load, N_x. The curves are based on buckling and are for configurations optimized under combined compression, shear equal to 1/3 of the compression load, and bending due to a 6.9 kN/m^2 (1 psi) lateral pressure. The curve for a z-stiffened skin is shown for comparison with conventional concepts.

The potential mass savings shown for the beaded and tubular panels led to the starting of a contractual program in 1971 to develop the design technology required to reliably predict the structural performance of panels constructed from curved elements (reference 2). If this potential mass efficiency was to be realized, all failure modes needed to be identified and properly accounted for in panel design. Several types of test models were fabricated and tested. The types of models are shown on the next figure.

MASS COMPARISON OF ALUMINUM BEADED AND TUBULAR PANELS

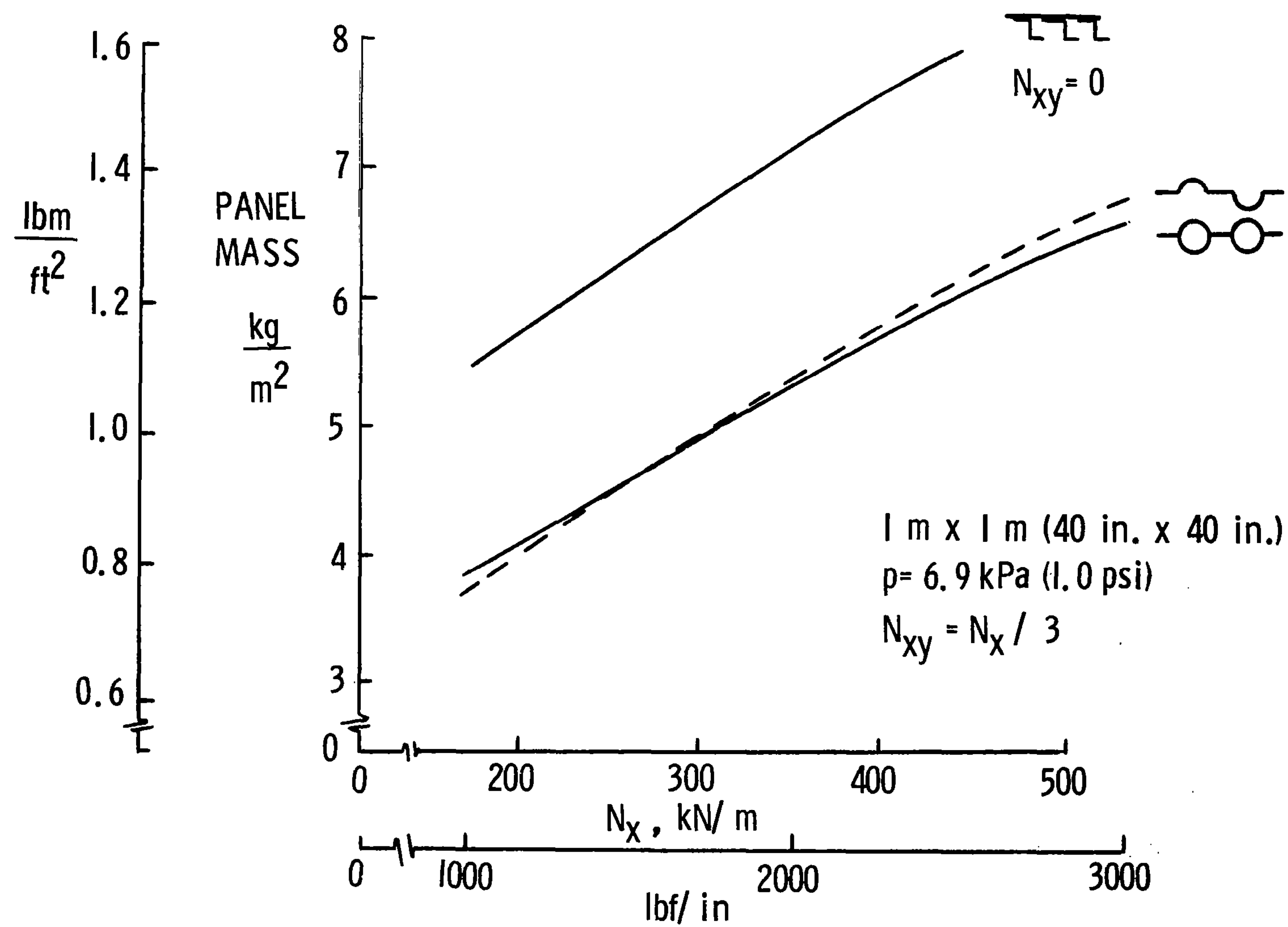

Figure 2

TEST MODELS

(Figure 3)

Three basic types of test models (end closure, local buckling, and 1 m by 1 m (40 inch by 40 inch) panels) were tested under combined compression, bending and shear. The test panels were fabricated from 7075-T6 aluminum to reduce fabrication costs inasmuch as the initial design technology development was independent of material characteristics. The end closure and local buckling specimens were imbedded in a potting material to stabilize the ends and to facilitate attachment to a loading fixture. End closures were tested to verify the capability to carry specified design loads, but no attempt was made to optimize the end closure designs. Local buckling specimens were tested to identify local buckling failure loads, and analytical methods were modified, where necessary, to achieve better agreement with test results. The large optimized panels were then designed and tested to determine buckling characteristics for comparison with theory. The method for testing these large panels is shown on the next figure.

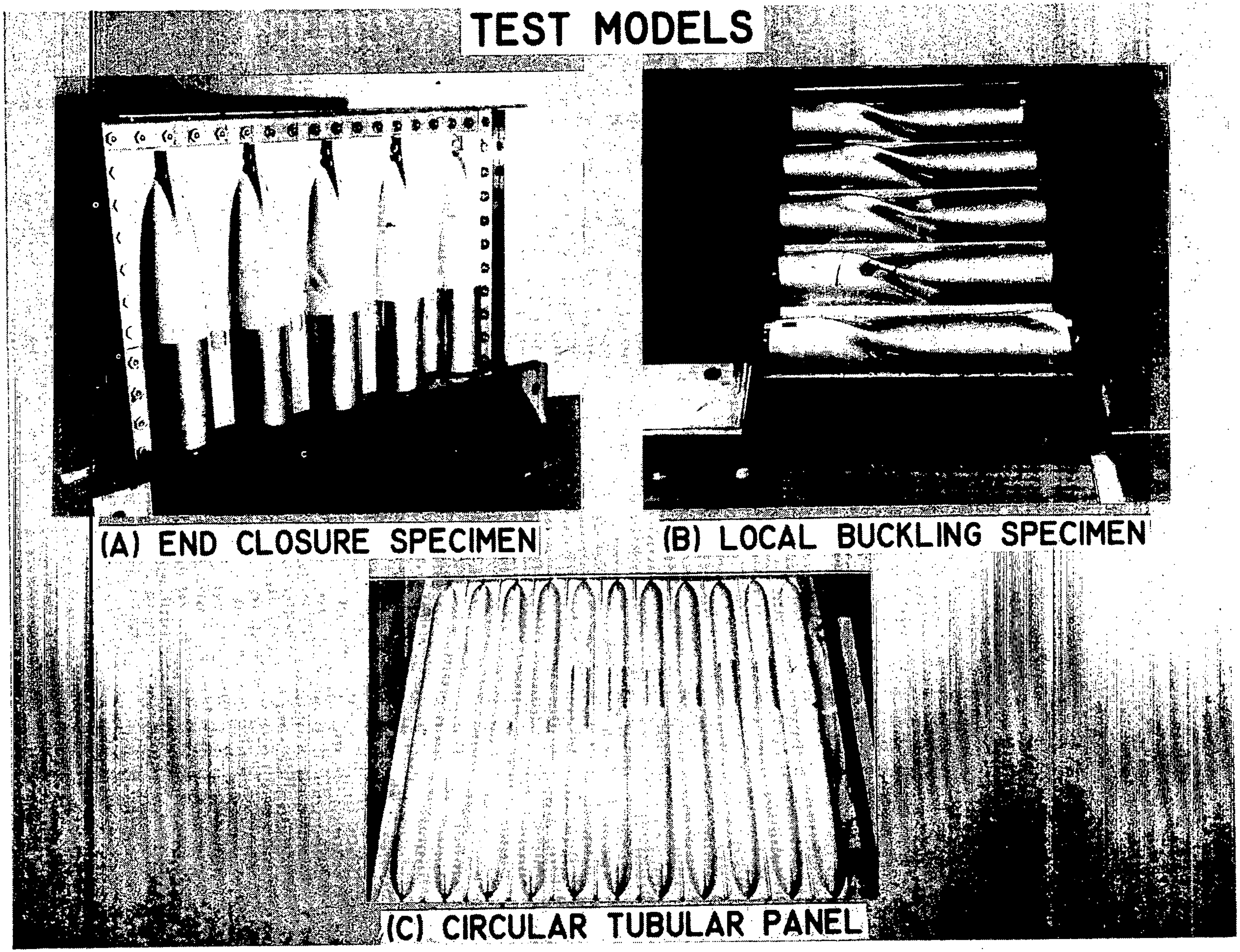
TEST MODELS
(A) END CLOSURE SPECIMEN
(B) LOCAL BUCKLING SPECIMEN
(C) CIRCULAR TUBULAR PANEL

Figure 3

TEST TECHNIQUE

(Figure 4)

The test fixture on the left was used to apply combined compression, shear and bending to the large panels. Compression was applied by the actuators on each side of the panel, shear was applied by the horizontal actuator to the left of the test panel, and bending was applied by an air bag behind the panel. The test panel is in the center, and buffer panels were used to distribute the load into the test panel. A stiff truss system with pivoting attachments behind the panels was used to prevent general instability of the three-panel system. Edge members prevented local buckling along the panel sides.

The figure on the right illustrates the test load sequence; R_C, R_B, and R_S are ratios of the applied load to the failure load in pure compression, bending and shear respectively. The curve is the theoretical interaction boundary for combined compression, bending and shear, and the point shows a typical panel design condition. Ten load conditions were selected, and the arrows show part of the load sequence for two load conditions. Load was increased to 60% of the theoretical interaction boundary, and strain measurements were made which were used to predict panel buckling loads using a nondestructive test method called the "force-stiffness method." (See reference 3.) The panel was tested in a second load condition, and again, a force-stiffness prediction was made. Force-stiffness predictions were made at 60%, 80%, and 90%. As the applied load is increased, better force-stiffness predictions are obtained. Most of the test data were obtained between the 80 to 90% load conditions.

Results are shown for the tubular panel on the next figure.

TEST TECHNIQUE

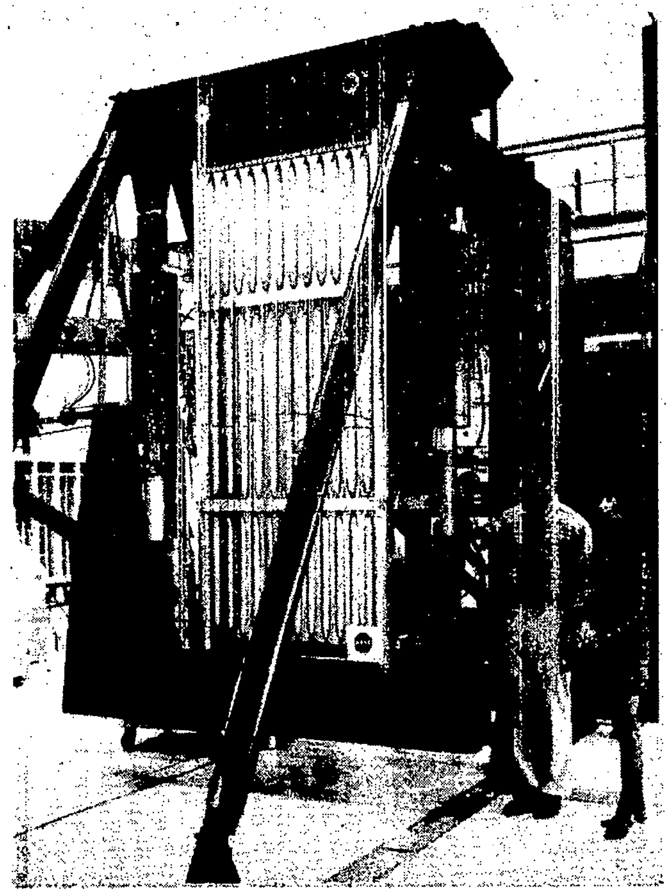

(a) TEST FIXTURE

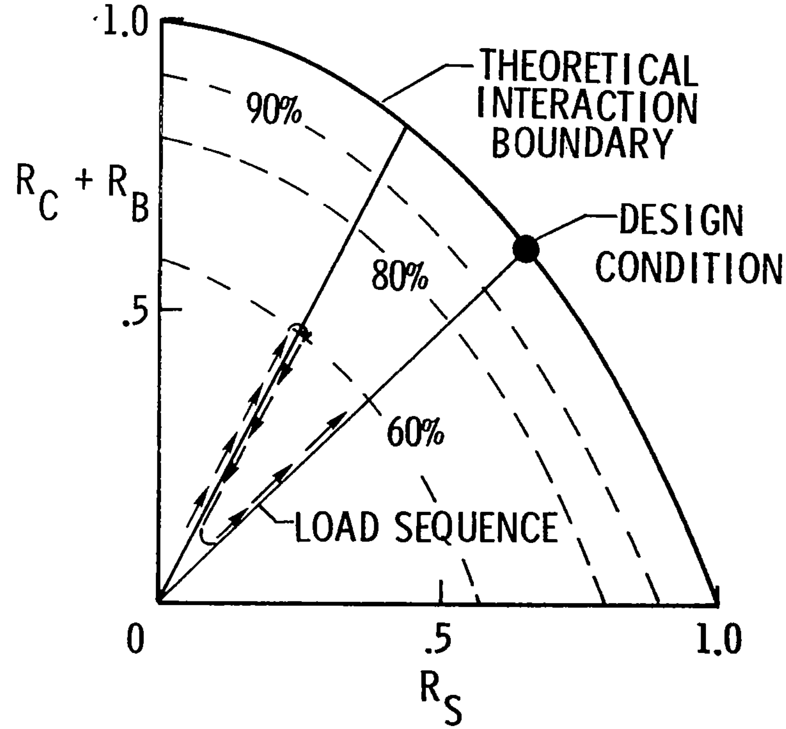

(b) TEST LOAD SEQUENCE

Figure 4

CIRCULAR TUBULAR RESULTS COMPARED TO MODIFIED THEORY

(Figure 5)

The three sets of curves show the theoretical interaction between compression, shear and bending for three levels of lateral pressures of 0, 6.9 kN/m^2 (1 psi), and 13.8 kN/m^2 (2 psi). The solid lines identify bead crippling, the local mode of failure, and the dashed lines identify general panel instability which was determined by assuming the panel to be a simply supported wide column. The open circles indicate the force-stiffness predictions for bead-crippling failure and the open squares indicate force-stiffness predictions for panel instability. The solid symbols show actual panel failure points which were used to verify the force-stiffness predictions. The test data are shown for 10 loading conditions, and were obtained from three essentially identical panels.

General instability failures were detected only in pure compression where theory indicates that local and general instability occur at the same load. The slightly unconservative data points, shown for pure compression, are believed to result from a deficient end closure which was only marginally satisfactory in pure compression. The agreement is consistent, and it is believed that the theory used to predict the behavior of the circular tubular panel is acceptable for design purposes. These data are reported in reference 4.

In addition to these relatively closely controlled tests, tests of beaded and tubular panels are being conducted in a realistic built-up structure. The next several figures show the structure which we call the Hypersonic Wing Test Structure.

CIRCULAR TUBULAR RESULTS COMPARED TO MODIFIED THEORY

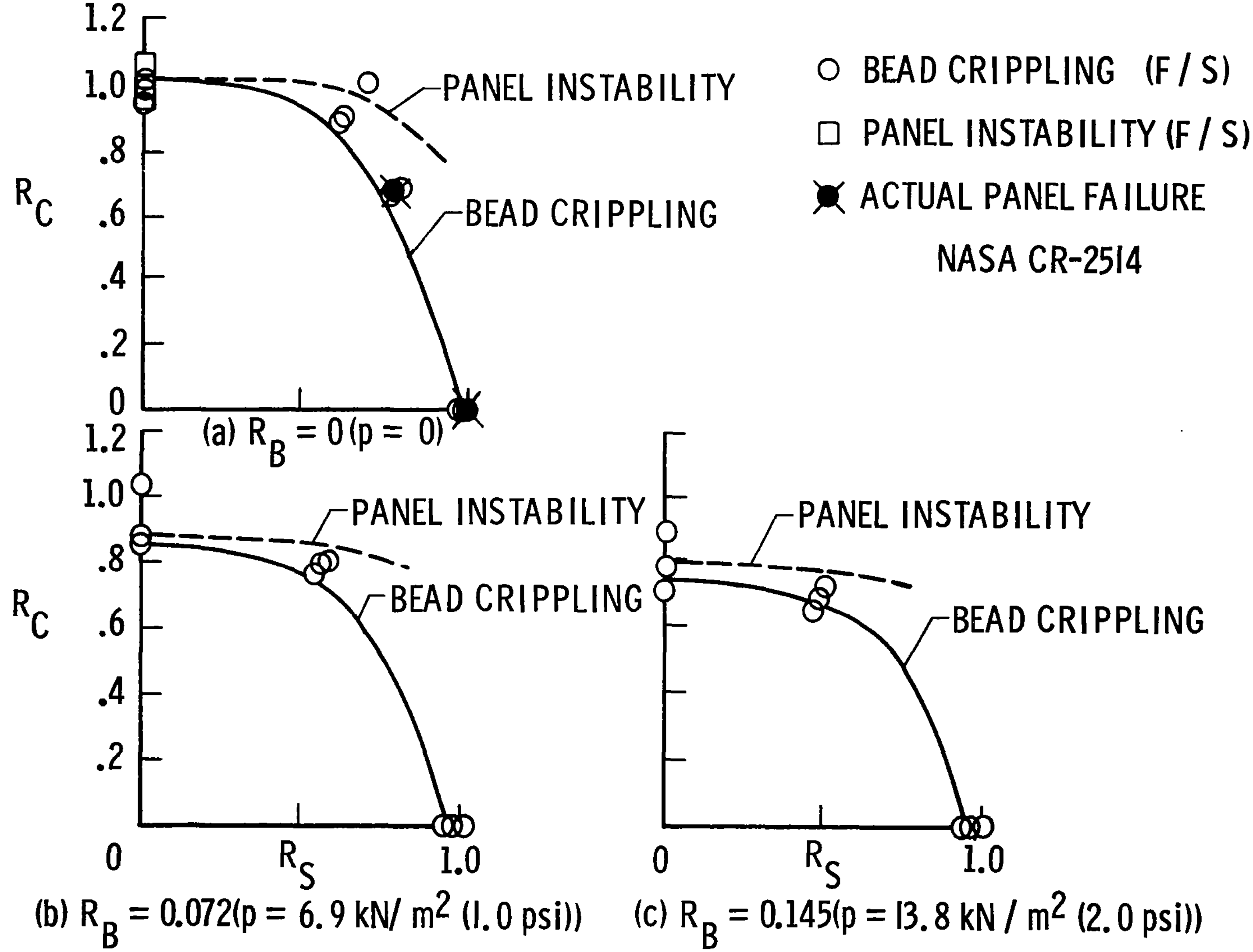

Figure 5

HYPERSONIC WING TEST STRUCTURE

(Figure 6)

Based on the structural concepts defined in the hypersonic cruise vehicle study (reference 1), a Mach 8, hot structure, hypersonic research airplane about one-third the size of the cruise vehicle was studied. The condition that designed the wing was a 2.5g pullup at Mach 8. A 7.9 m^2 (85 $ft.^2$) section of the wing of this research airplane was designed and fabricated (reference 5) and is being used at Dryden Research Center to evaluate the hot structure concept.

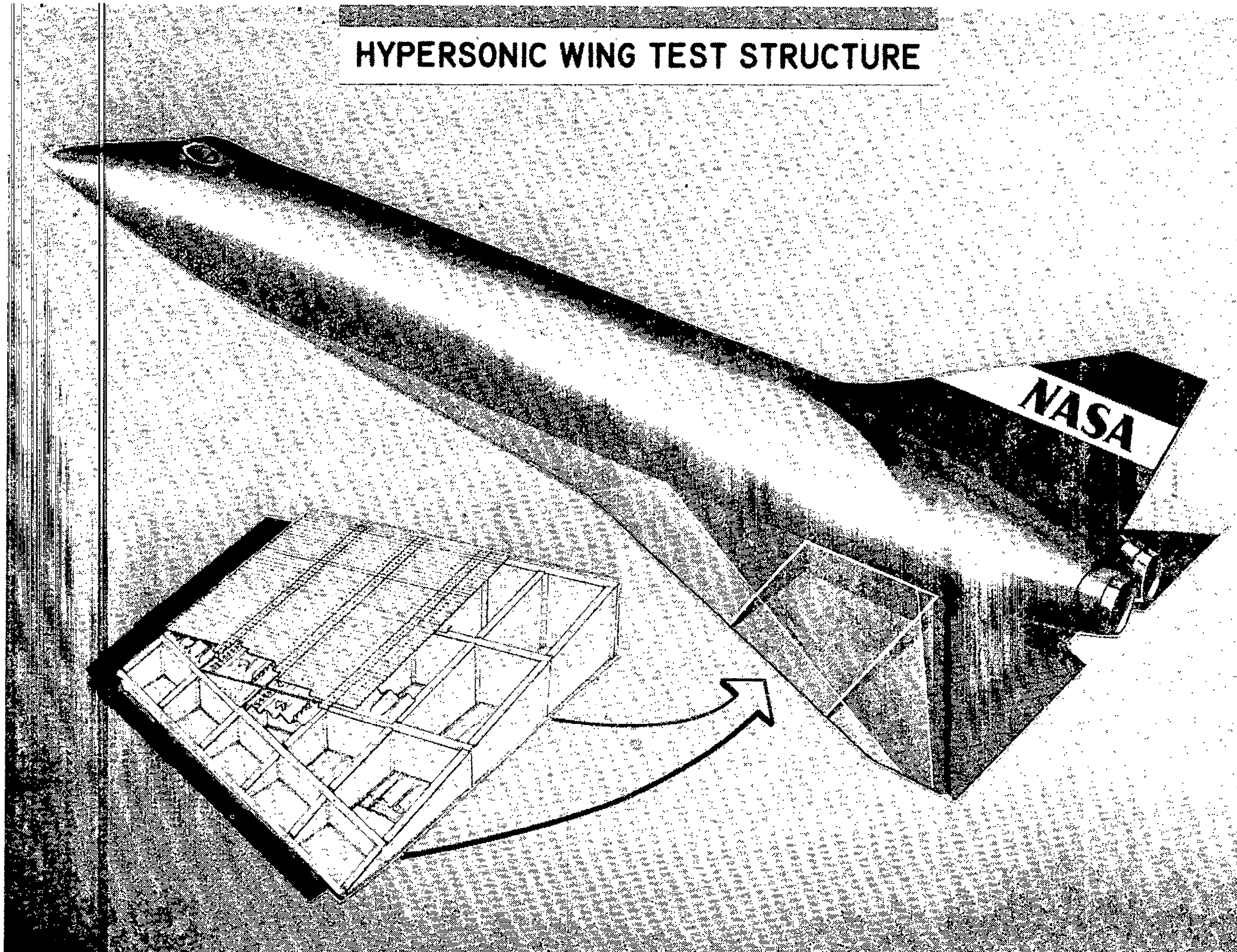

Figure 6

HYPERSONIC WING TEST STRUCTURE

(Figure 7)

This figure shows the Hypersonic Wing Test Structure (HWTS) with the heat shields removed. The windward side of the wing is the top surface because the wing is mounted upside down to facilitate loading and heating of the HWTS. The structure has 6 spars and 5 cover panels along the root chord. These cover panels are the single-sheet beaded concept, and the brackets on the cover panels are used to support the heat shields. The forward part of the windward surface is covered with 96 kg/m^3 (6 lbm/ft^3) Dyna-Flex insulation to keep the structural temperature below a limiting value of 1061 K (1450°F) in the area of highest heating. In addition to limiting the temperature to a value acceptable for the material, the insulation also served to reduce in-plane thermal gradients and thereby reduce thermal stress .

HYPERSONIC WING TEST STRUCTURE

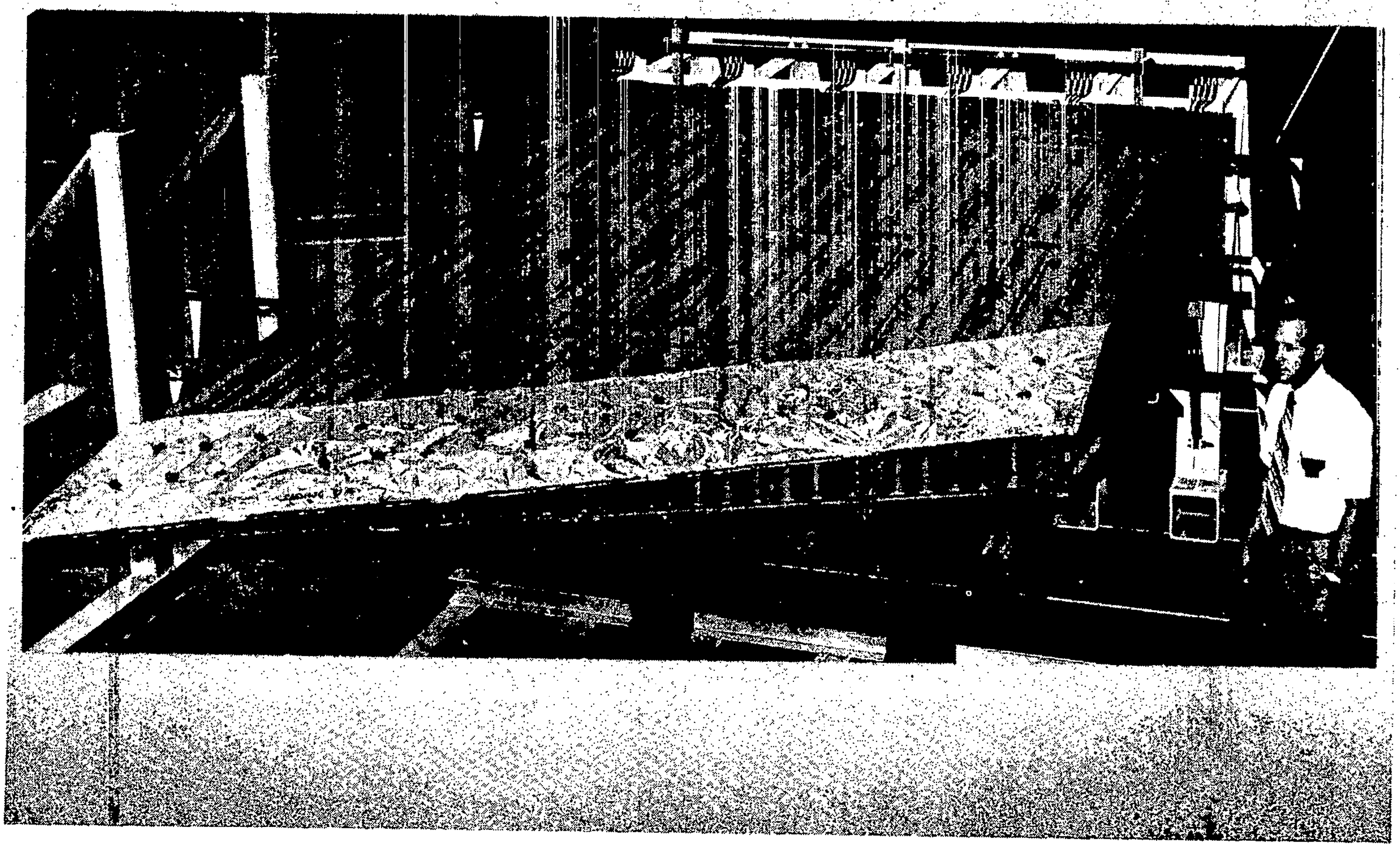

Figure 7

DFRC HYPERSONIC WING TEST STRUCTURE

(Figure 8)

This figure shows some of the detail of the fabrication. The structure is made of beaded cover panels, corrugated ribs and spars, and is fabricated from René 41. While multiple-pass forming of the panels is required and burn-through welding is used for the web-to-cap attachment, the fabrication methods are considered to be state-of-the-art.

DFRC HYPERSONIC WING TEST STRUCTURE

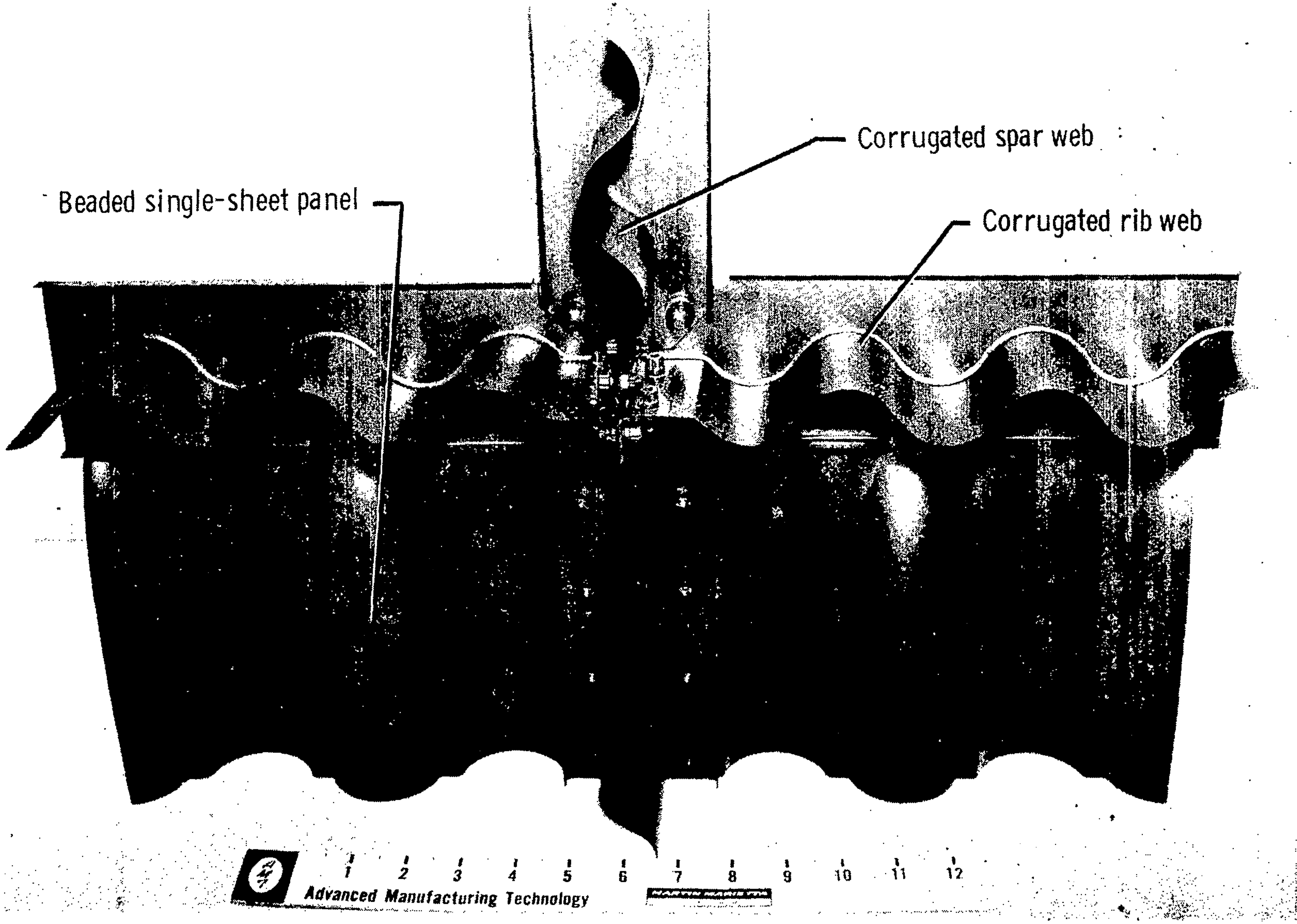

Figure 8

HYPERSONIC WING TEST STRUCTURE WITH HEAT SHIELDS

(Figure 9)

This view of the HWTS shows the heat shields attached. The heat shields are also made from Rene 41 except for those along the leading edge which are TD Ni-20Cr. The structure is cantilevered from a support structure which is rigidly attached to the floor. The loading rods hanging beneath the structure are used to apply wing bending loads.

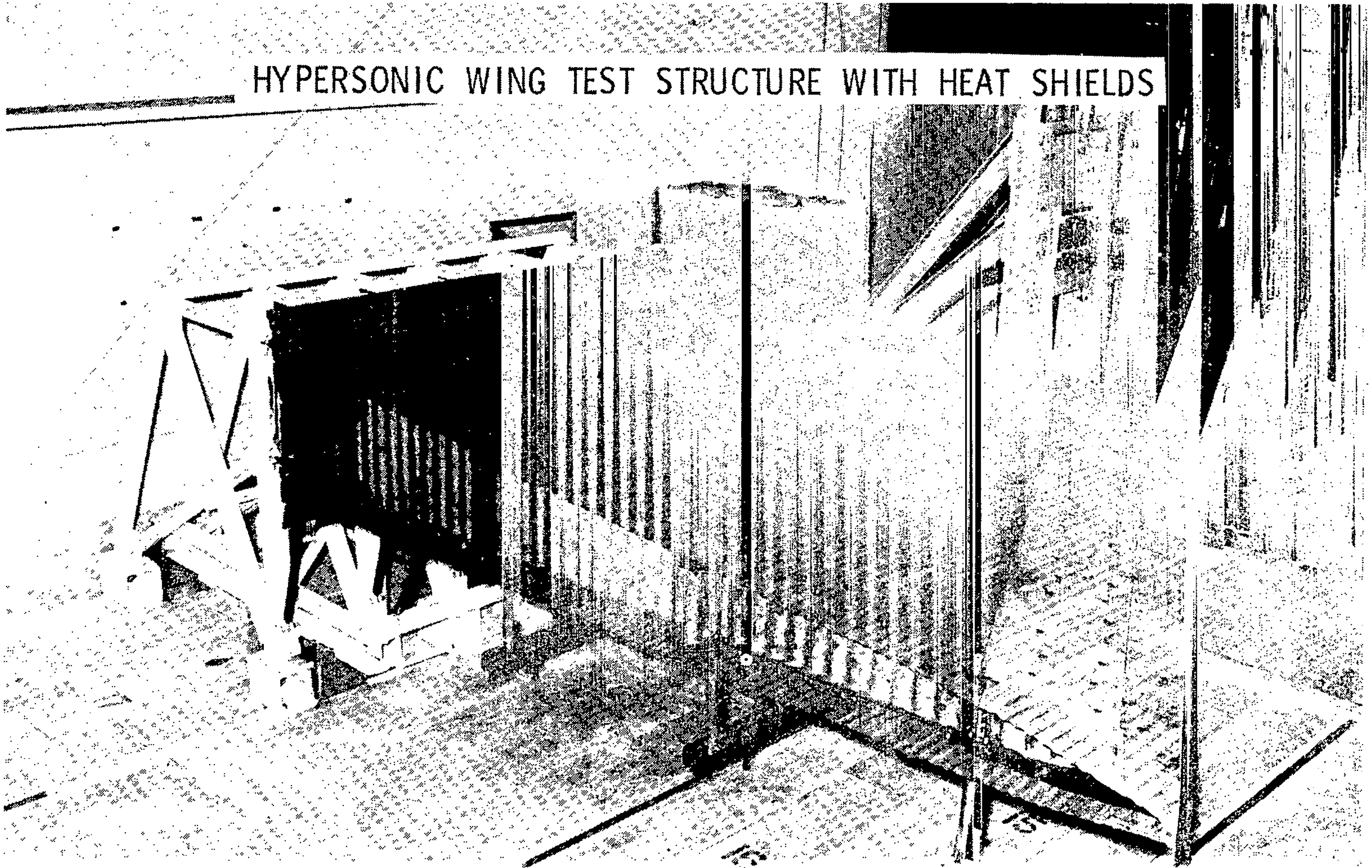

HYPERSONIC WING TEST STRUCTURE WITH HEAT SHIELDS

HWTS--APPLIED MECHANICAL LOADS

(Figure 10)

This figure shows how some of the mechanical loads were applied. The whiffle tree arrangement was used to apply vertical loads, and other actuators, which can't be seen in this view, were used to apply horizontal loads at the wing edges. A pressure load was applied to the five root-chord cover panels by using Inconel foil air bags inside the wing.

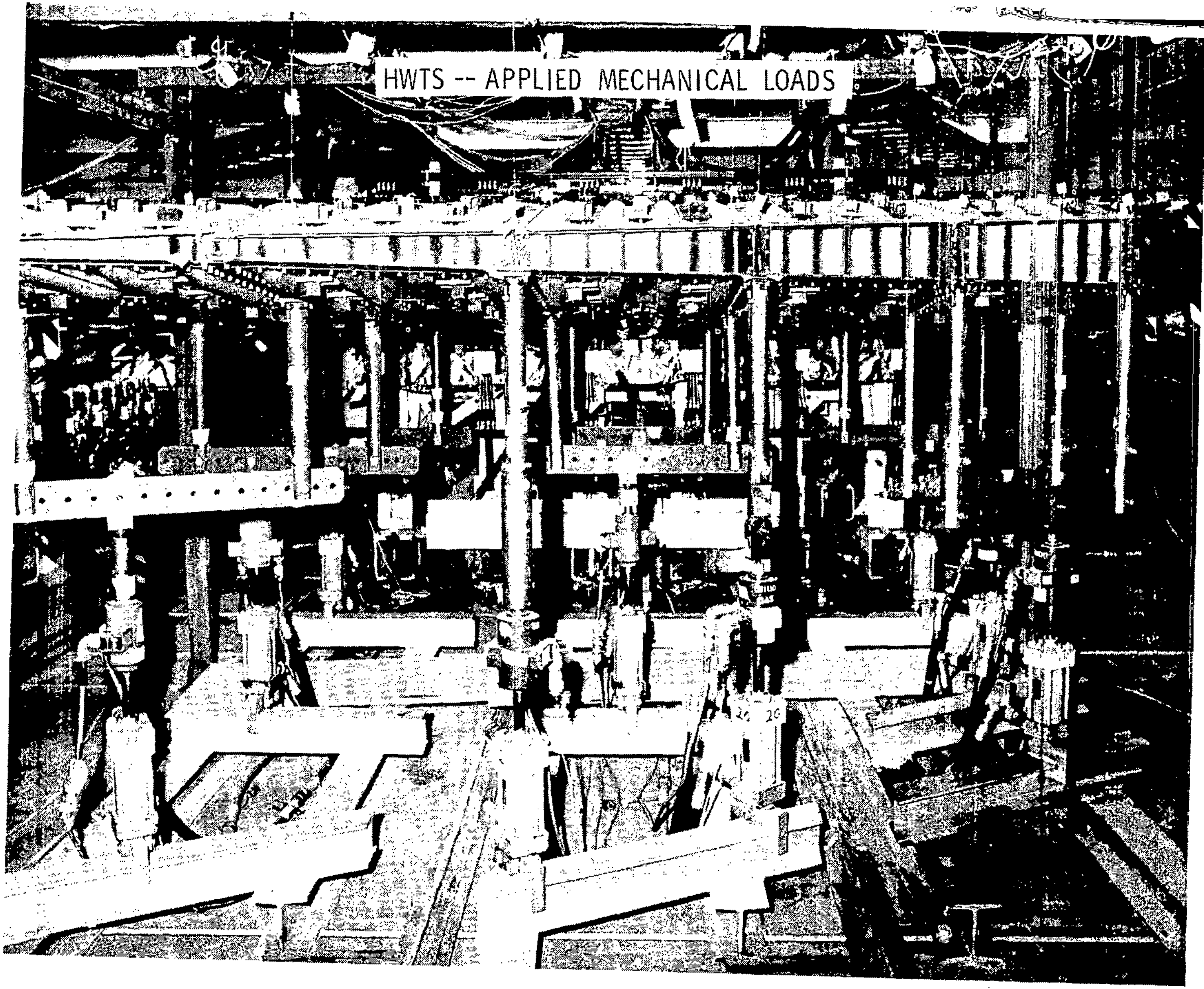

Figure 10

HWTS--APPLIED THERMAL LOADS

(Figure 11)

This figure shows how the thermal loads were applied. Banks of quartz lamps supported by water cooled reflectors were mounted so that they could be rolled underneath and over the structure. Loading rods from the structure project through holes in the lower array of lamps. During heating tests, quartz cloth curtains that are rolled up in this view prevent convective air currents from interfering with the tests.

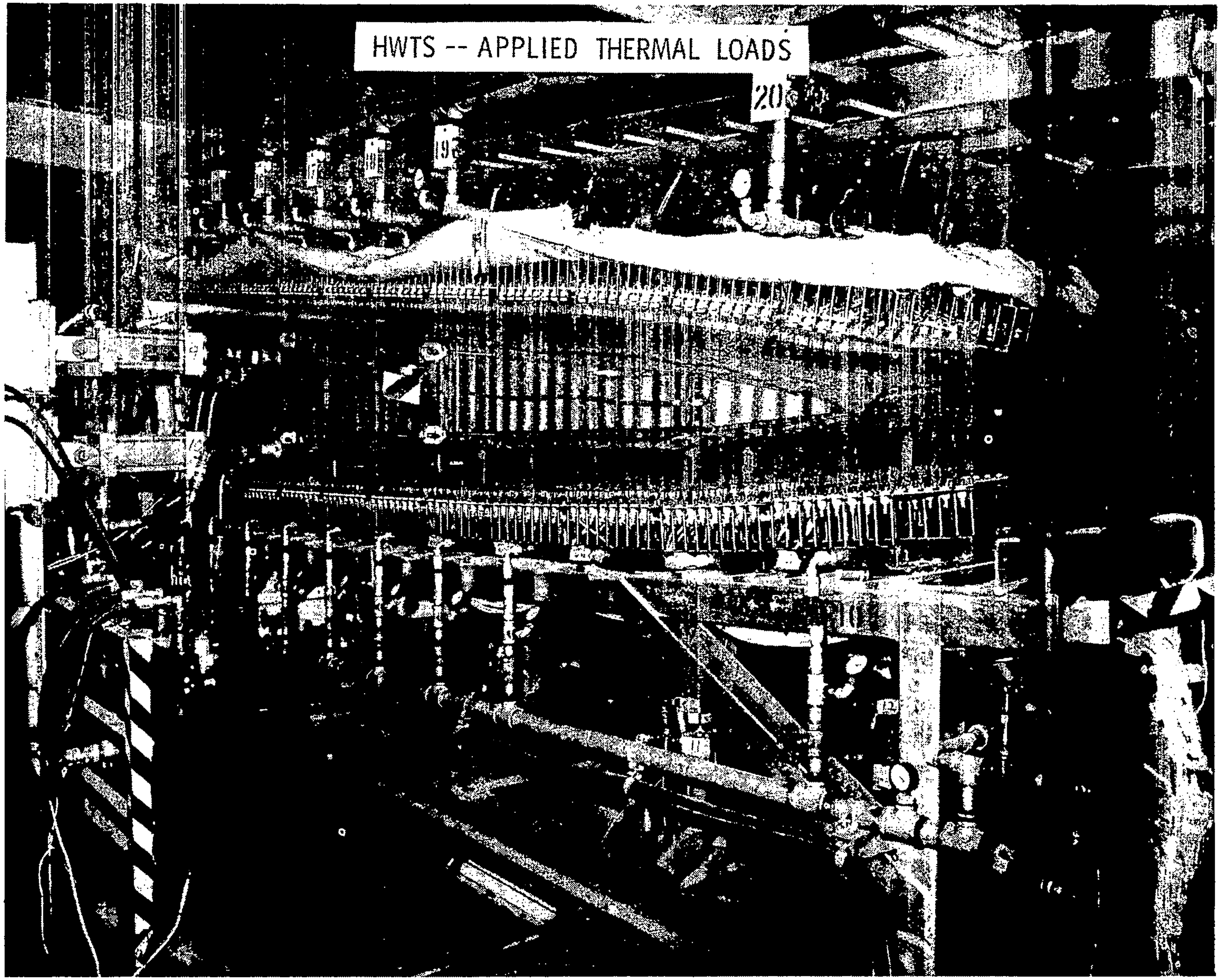

Figure 11

HWTS--THERMAL TEST

(Figure 12)

This figure shows the structure being heated to a realistic temperature distribution for Mach 8 flight. The structural temperatures reach 1061 K (1450°F) on the windward surface and 1005 K (1350°F) on the leeward surface. The heat shield temperatures are about 222 K (400°F) hotter than the structure. In this test, the thermal loads are being applied alone, although in subsequent tests, mechanical and thermal loads were applied simultaneously. These are very complex tests for a research program, and the facilities at Dryden Research Center (references 6 and 7) lend themselves very well to these types of tests.

Finite element models are being used to obtain analytical data for comparison with test data. The models are shown on the next figure.

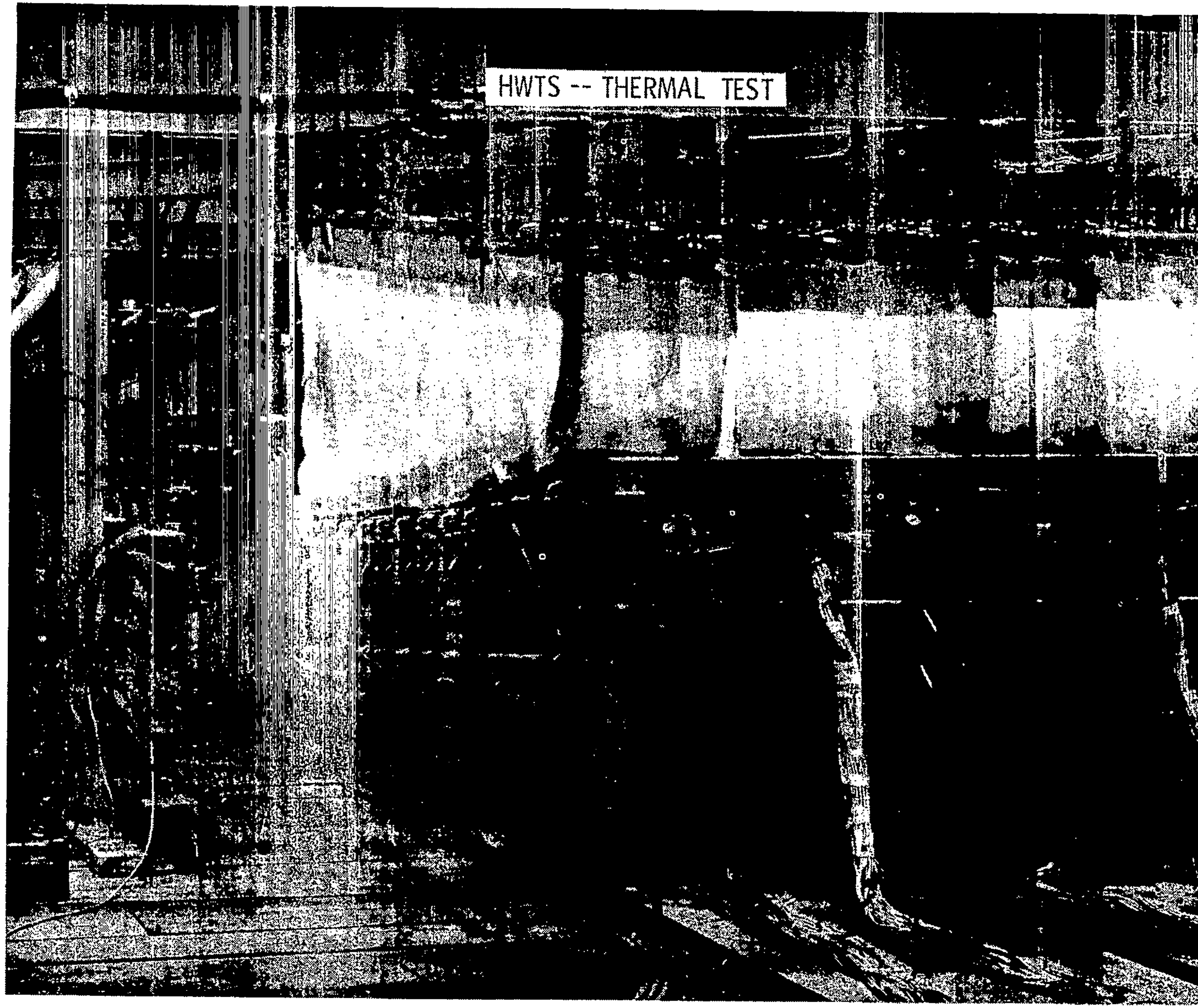

Figure 12

FINITE ELEMENT MODELS

(Figure 13)

Finite element analyses have been used to study the structural behavior of the research airplane, wing test structure, and wing cover panels. The finite element analysis of the research airplane was used to obtain internal loads in the wing during various flight conditions, including the 2.5g pullup design condition. These internal loads were then used as applied loads for the model of the Hypersonic Wing Test Structure (HWTS). In the test structure model, a single element represented a wing cover panel. Consequently, in order to study the wing panels in more detail, wing panel finite element models were constructed for the beaded and tubular panels, and internal loads from the test structure were used as applied loads to the wing panel models.

Comparison of analytically predicted wing panel stresses with measured stresses at room temperature are shown in the next figure.

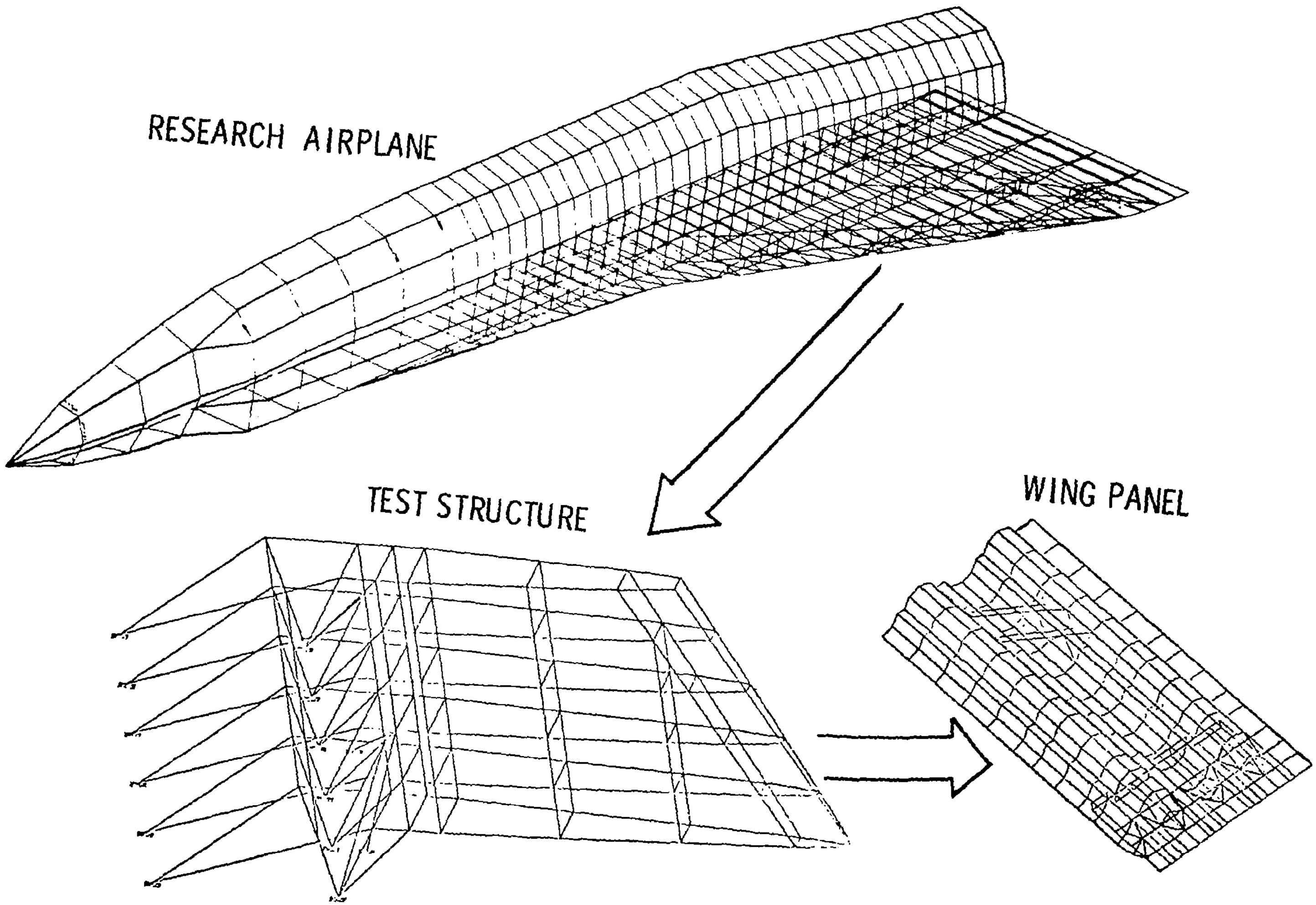

Figure 13

SPANWISE STRESS FOR BEADED PANELS IN HWTS AT ROOM TEMPERATURE (PRELIMINARY)

(Figure 14)

The upper part of the figure shows a cross section of the 5 root-chord panels in the HWTS. The open symbols identify measured stress, and the solid symbols identify stresses predicted by the finite element analysis. The circles show stresses on the flats and the squares show stresses on the beads. The lines connect the stresses measured on an adjacent up-bead, flat, and down-bead at the center of each panel.

The applied mechanical loads represent a $2\frac{1}{2}$g maneuver, which includes a pressure load of 5.2 kPa (3/4 psi) on each panel. The test data show a general level of compression of about 82.7 MPa (12 ksi), and the lines indicate the general level of bending that's occurring at the center of the panels. Comparison of the test data with the calculated data indicates that the trends are in good agreement, but the calculated stresses are about 34.5 MPa (5 ksi) greater than the measured stresses. Also, the calculated stresses at the flats are not centered between the stresses at adjacent beads, as they are for the measured stresses. An error in the method for applying loads to the finite element models has been detected, and agreement between test data and theory may improve when this error is corrected.

The next slide shows typical measured data for the same panels but at elevated temperatures.

SPANWISE STRESS FOR BEADED PANELS IN HWTS AT ROOM TEMPERATURE (PRELIMINARY)

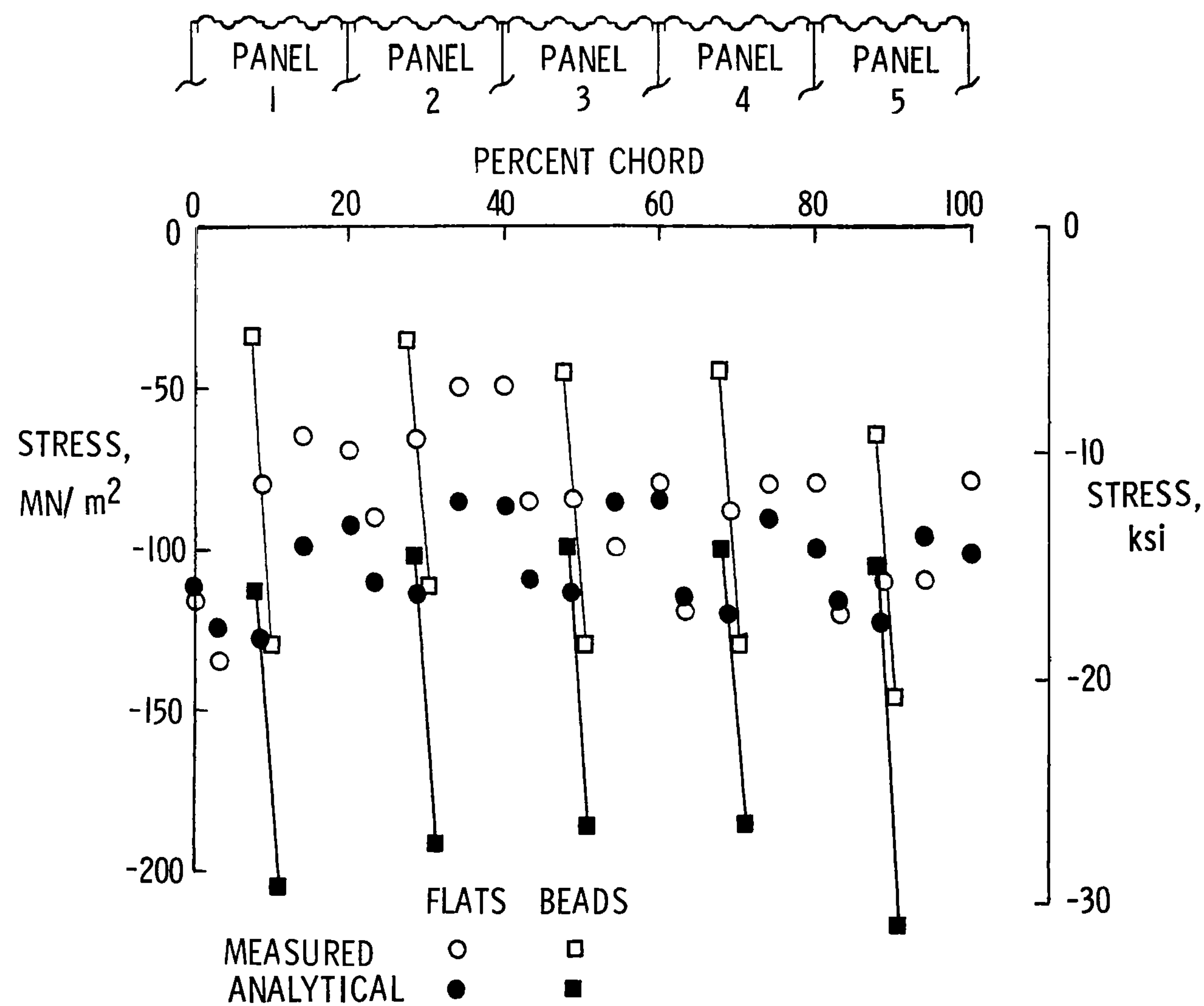

Figure 14

MEASURED SPANWISE BENDING STRESS FOR BEADED PANELS AT ELEVATED TEMPERATURE (PRELIMINARY)

(Figure 15)

The squares repeat the room temperature data from the previous slide, the diamonds are for a temperature of 561 K (550°F) where the whole wing structure is soaked at a uniform 561 K (550°F), and the triangles are for a temperature of 1006 K (1350°F) where the structure has been exposed to a Mach 8 heating history and has thermal gradients representative of actual flight. The strain gages which were located on the flats were not designed to withstand elevated temperatures, so data were obtained only for strain gages which were located on the beads. Also, only four strain gages, located on panels 2 and 4, were capable of withstanding 1006 K (1350°F). These are a type of capacitance strain gage, and they are relatively expensive. The mechanical loads are again those for the 2.5g maneuver.

At many points, the data at 651 K (550°F) are nearly the same as the room temperature data which is as would be expected. If the wing structure were at a uniform temperature, no thermal stress would exist except those due to effects from boundary conditions. The 1006 K (1350°F) test data differ quite a bit from the other data, which is also expected because thermal stress should exist since there are thermal gradients for this load condition. Calculated data for comparison are not yet available.

After testing of the beaded panels was completed, the five compression panels along the root-chord were replaced with tubular panels which were designed based on the previously discussed data base for tubular panels (reference 4). The design and fabrication of these five René 41 panels is reported in reference 8. The next figure shows test results for the tubular panels in the HWTS at room temperature and for the same applied loads associated with the 2.5g maneuver.

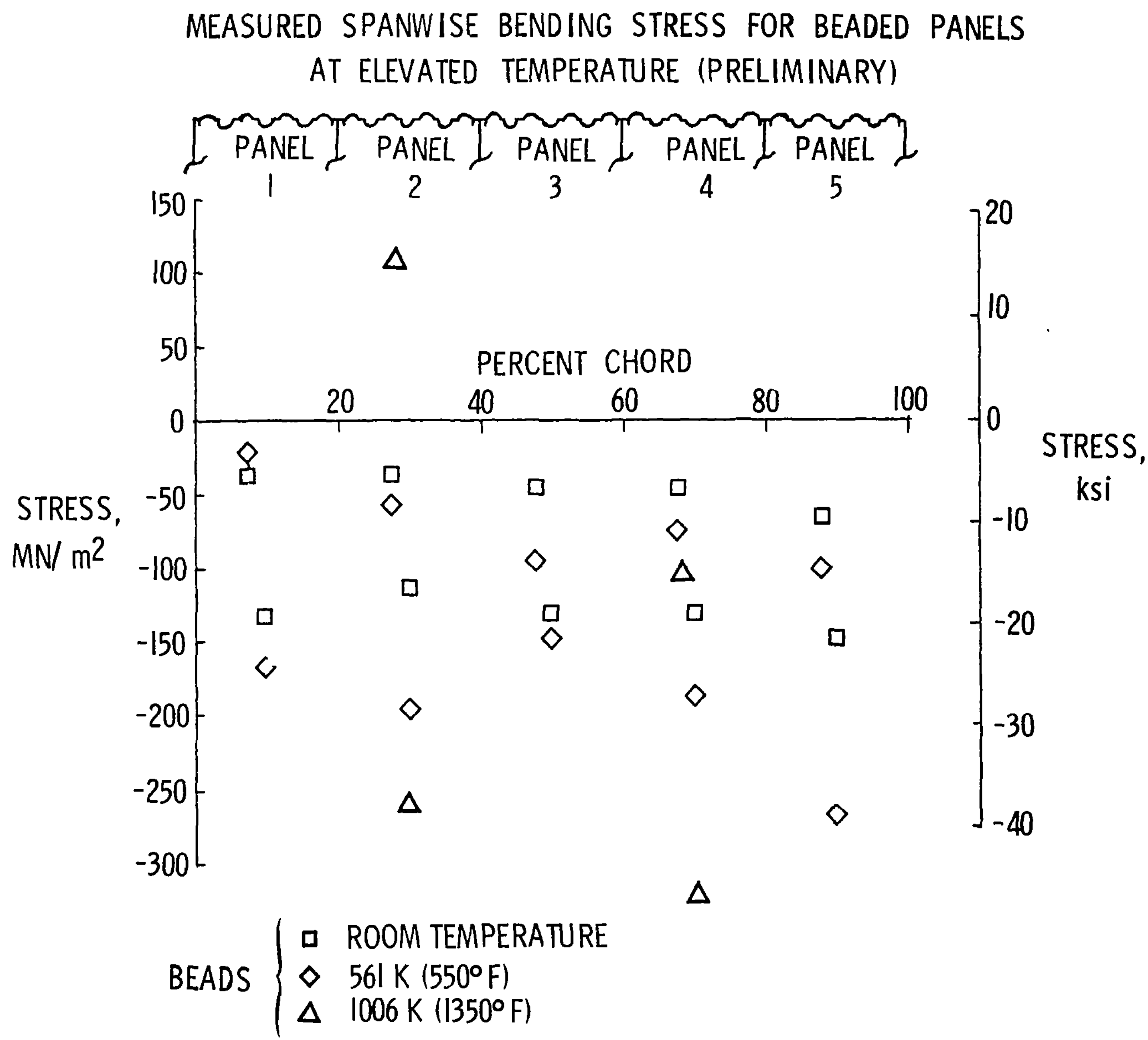
MEASURED SPANWISE BENDING STRESS FOR BEADED PANELS
AT ELEVATED TEMPERATURE (PRELIMINARY)
PANEL 1
PANEL 2
PANEL 3
PANEL 4
PANEL 5
PERCENT CHORD
20
40
60
80
100
150
100
50
0
-50
-100
-150
-200
-250
-300
STRESS, MN/ m2
20
10
0
-10
-20
-30
-40
STRESS, ksi
BEADS
ROOM TEMPERATURE
561 K (550° F)
1006 K (1350° F)

Figure 15

MEASURED SPANWISE STRESS FOR TUBULAR PANELS IN HWTS AT ROOM TEMPERATURE (PRELIMINARY)

(Figure 16)

Each panel has four tubes which are oval in cross-section rather than circular because minimum gage constrained the design. The tubular panels have the same equivalent thickness as the single-sheet beaded panels which they replaced. The circular symbols show stresses on the flats between the tubes. The average stress here is less than what it was for the beaded panels which implies that the tubes are carrying more load than the beads did.

The squares show stresses on the outer surface of the tubes, and the squares with tick marks show stresses on the inner surface or opposite side of the tubes. The lines connect stresses on opposite sides of the tubes for the two center tubes of each panel indicating bending stresses due to the lateral pressure. The bending stresses in the tubes next to the spars are not known because strain gages are located on only one side of the tube; but the difference in stress levels indicate that the spars are preventing these tubes from bending. Again, analytical data to compare with these test data are not yet available.

However, the force-stiffness method is being used to predict buckling for the tubular panels. This is illustrated on the next figure.

MEASURED SPANWISE STRESS FOR TUBULAR PANELS IN HWTS AT ROOM TEMPERATURE (PRELIMINARY)

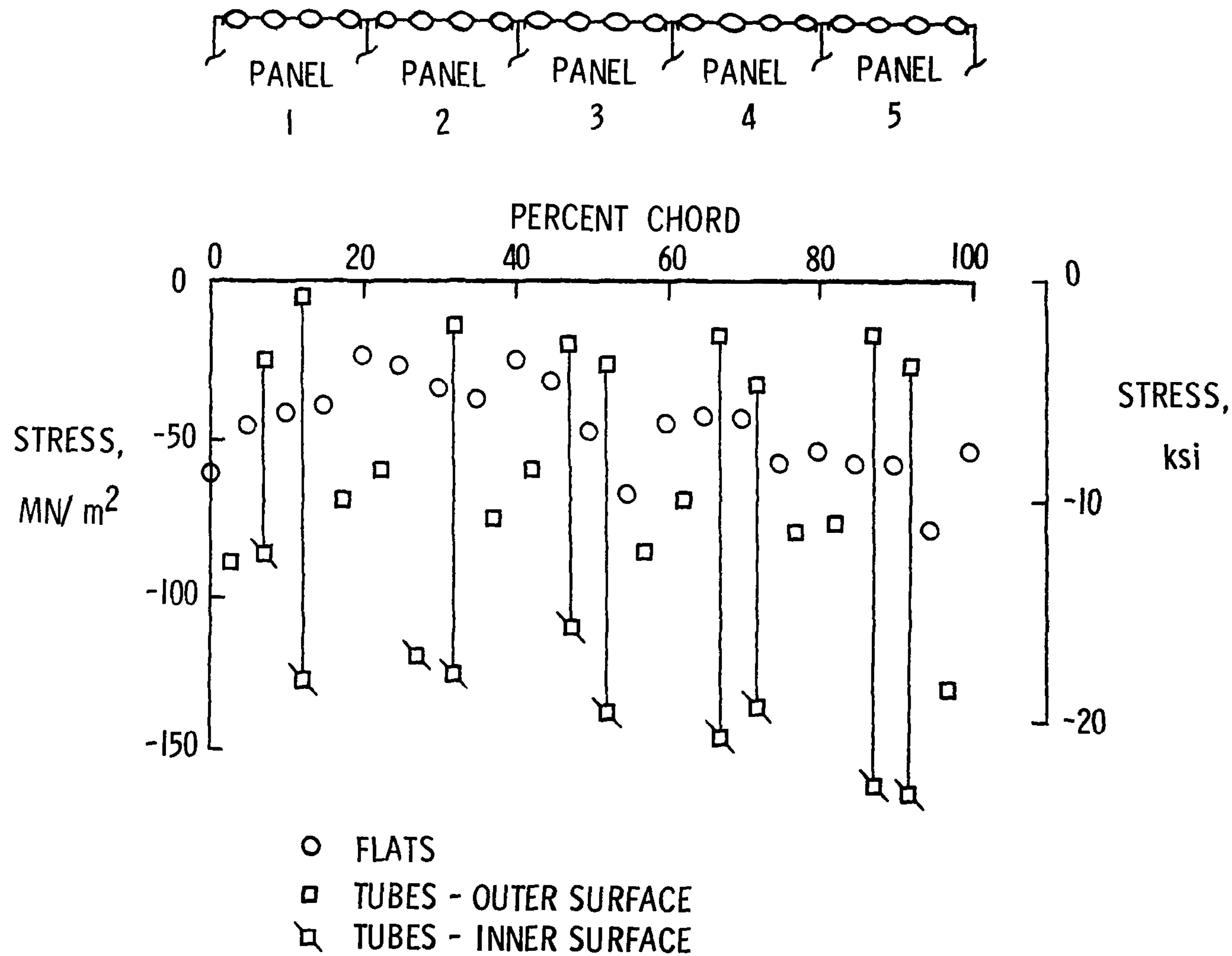

Figure 16

COMPRESSION-SHEAR INTERACTION FOR RENE 41 TUBULAR PANELS IN HWTS

(Figure 17)

This figure shows the room temperature compression-shear interaction for the tubular panels which are nominally 109 cm. (43 in.) long and 49 cm. (20 in.) wide. The curve shows the analytically predicted buckling curve for compression and shear for a lateral pressure of 5.2 kPa (0.75 psi). The solid circles indicate the maximum combined loads which were applied to the panels, and the open circles are preliminary force-stiffness estimates of panel buckling. These data, except for the single data point near pure shear, indicate that the tubular panels will carry more load than that predicted by the analytical methods given in reference 8. Higher applied loads would give more accurate force-stiffness predictions, but load levels are currently limited to those shown in the figure to minimize the risk of failing other components of the HWTS.

The room temperature tests for the tubular panels have been completed. Elevated temperature tests on the HWTS with the tubular panels along the root-chord are ready to begin.

COMPRESSION - SHEAR INTERACTION
FOR RENE 41 TUBULAR PANELS IN HWTS

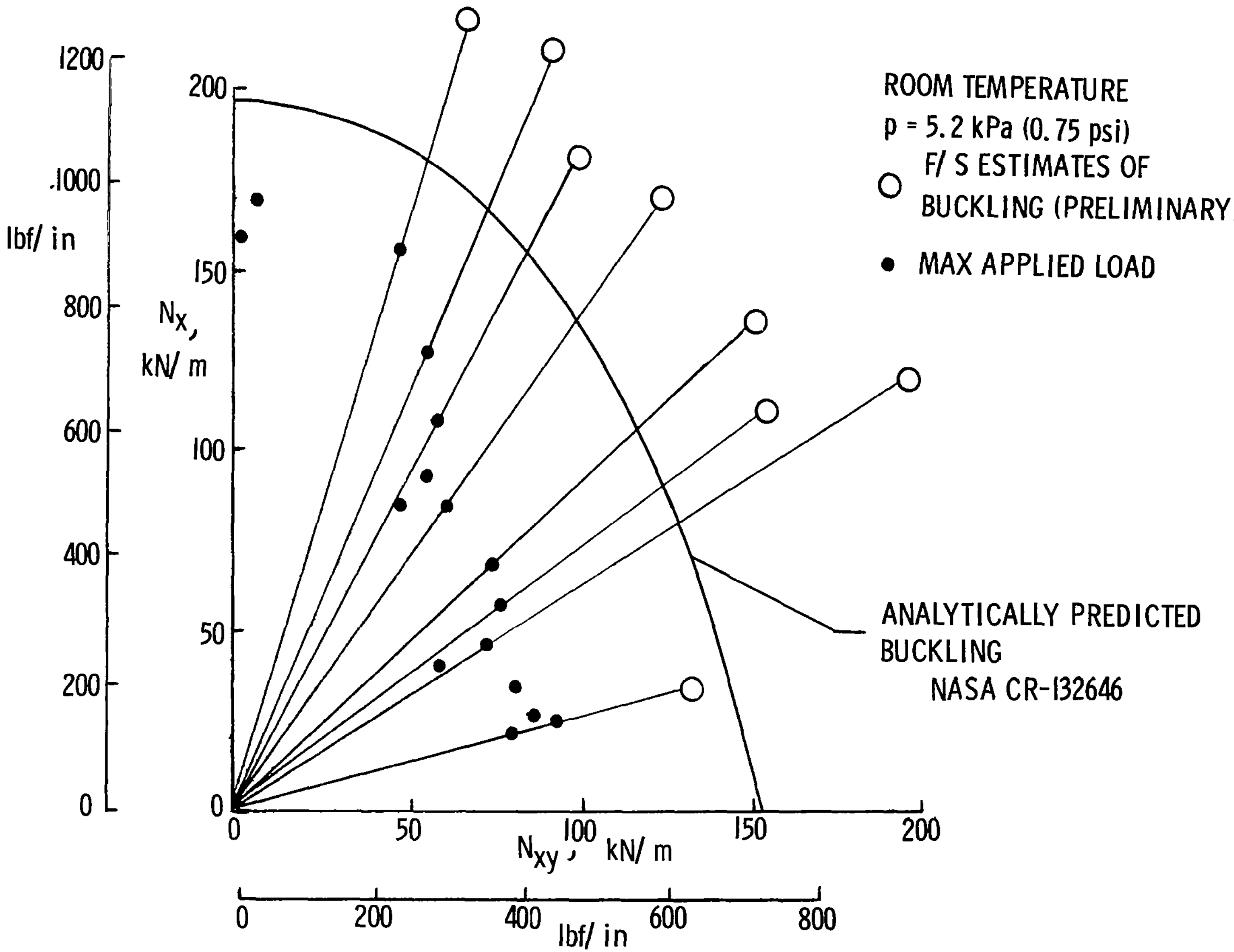

Figure 17

SUMMARY

(Figure 18)

In summary, two efficient concepts built from curved elements have been identified, and a data base for tubular panels has been developed. The tubular panel failure modes are understood and the data base for these panels indicate that their performance can be predicted. The concepts are currently being tested in a realistic built-up structure; 157 room temperature tests and 67 hot tests have been made with no structural failures, although all of these tests were not at the design load of the structure. Our future work is to complete the tests at Dryden, to complete our analyses of beaded and tubular panels, and to compare results with test data to establish an understanding of the behavior of beaded and tubular wing cover panels.

ACCOMPLISHMENTS

- EFFICIENT CONCEPTS IDENTIFIED
- DATA BASE FOR TUBULAR PANELS HAS BEEN DEVELOPED
- TUBULAR PANEL FAILURE MODES ARE UNDERSTOOD AND PERFORMANCE CAN BE PREDICTED

STATUS

- TESTING PANELS IN REALISTIC BUILT-UP STRUCTURE
- 157 RT AND 67 HOT TESTS WITH NO STRUCTURAL FAILURES

FUTURE

- COMPLETE TESTS AT DRYDEN
- ANALYZE AND COMPARE WITH TEST DATA

Figure 18

REFERENCES

1. Plank, P.P.; Sakata, I.F.; Davis, G.W.; and Richie, C.C: Hypersonic Cruise Vehicle Wing Structure Evaluation. NASA CR-1568, May 1970.

2. Musgrove, M.D.; and Greene, B.E.: Advanced Beaded and Tubular Structural Panels, Summary Document. NASA CR-2514, 1975.

3. Jones, R.E.; and Greene; B.E.: The Force/Stiffness Technique for Nondestructive Buckling Testing. AIAA Paper No. 74-351, Presented at AIAA/ASME/SAE 15th Structures, Structural Dynamics and Materials Conference, Los Vegas, Nevada, April 17-19, 1974.

4. Greene, B.E.: Substantiation Data for Advanced Beaded and Tubular Panels, Volume 1, Design and Analysis. NASA CR-132460, 1975.

5. Plank, P.P.; and Penning, F.A.: Hypersonic Wing Test Structure Design, Analysis and Fabrication. NASA CR-127490, August 1973

6. Sefic, Walter J.; and Anderson, Karl F.: NASA High Temperature Loads Calibration Laboratory. NASA TM X-1868, September 1969.

7. Fields, Roger A.: Dryden Flight Research Center Hot Structures Research. Recent Advances in Structures for Hypersonic Flight, NASA CP-2065, 1978. (Paper no. 20 of this compilation.)

8. Greene, Bruce E.; and Northrup, Russell F.: Design and Fabrication of René 41 Advanced Structural Panels. NASA CR-132646.

STRUCTURES FOR HYPERSONIC AIRBREATHING TACTICAL MISSILES

William C. Caywood and Robert M. Rivello
Applied Physics Laboratory/Johns Hopkins University

INTRODUCTION

Studies have shown the tactical advantages of hypersonic speed coupled with long range in missiles designed for the U.S. Navy's fleet defense when: the speed of the attacking weapon is high, its release range is large, and ships in addition to the launching vessel must be defended. When threats that are anticipated to be technically feasible in the 1980's are considered the requirement for long range hypersonic defensive missiles becomes apparent. Studies also indicate the weight and volumetric advantages that a supersonic combustion ramjet (scramjet) missile holds over a rocket-powered missile when both operate at hypersonic speeds over long ranges.

The design of hypersonic tactical missiles, whether scramjet or rocket powered, poses many severe structural problems whose solutions are beyond the current state-of-the-art. The temperatures of leading edges and scramjet engine components exceed the maximum temperatures in aircraft jet engines by more than 1000°F. Heating conditions in the scramjet engine approach those in the throat section of rocket motors, but are more damaging because the flow is oxidizing rather than reducing. The scramjet also requires sharp leading edges and a stable geometry to maintain its propulsive performance advantages. As a result of these considerations, many of the problems of the scramjet tactical missile are unique and technologies that are being developed for aircraft, rocket-powered missiles, and reentry vehicles are frequently not applicable to their solution.

In this report, highlights of the exploratory development work on hypersonic tactical missile structures conducted at the Applied Physics Laboratory of The Johns Hopkins University (APL/JHU) are reviewed. The baseline missile study configuration is described and analytical and experimental work relating to some of the critical structural components is discussed. The report concludes with a listing of candidate materials for some of the critical structural components.

The exploratory development work on hypersonic tactical missile structures has been supported by the Materials and Mechanics Division of the Naval Sea Systems Command (NAVSEA-035).

SUPERSONIC COMBUSTION RAMJET MISSILE (SCRAM)

(Figure 1)

Research on structures for hypersonic missiles can provide misleading results if it is not based upon realistic vehicle configurations and design conditions. For this reason, the work that is reported upon has made use of the results from the Supersonic Combustion RAmjet Missile (SCRAM) program at APL/JHU. SCRAM is a surface-to-air missile for wide area fleet defense and operates at speeds up to Mach 5 at sea level and Mach 8 at high altitudes. Initial thrust is obtained from a solid propellant booster that separates from the missile at the completion of the boost phase.

Some of the features of the SCRAM configuration include a radome, interferometer antennas, a "crown-inlet" with sharp swept leading edges, four separate inlet ducts and combustion chambers, and a single exhaust nozzle. Combustion takes place supersonically in the combustion chambers.

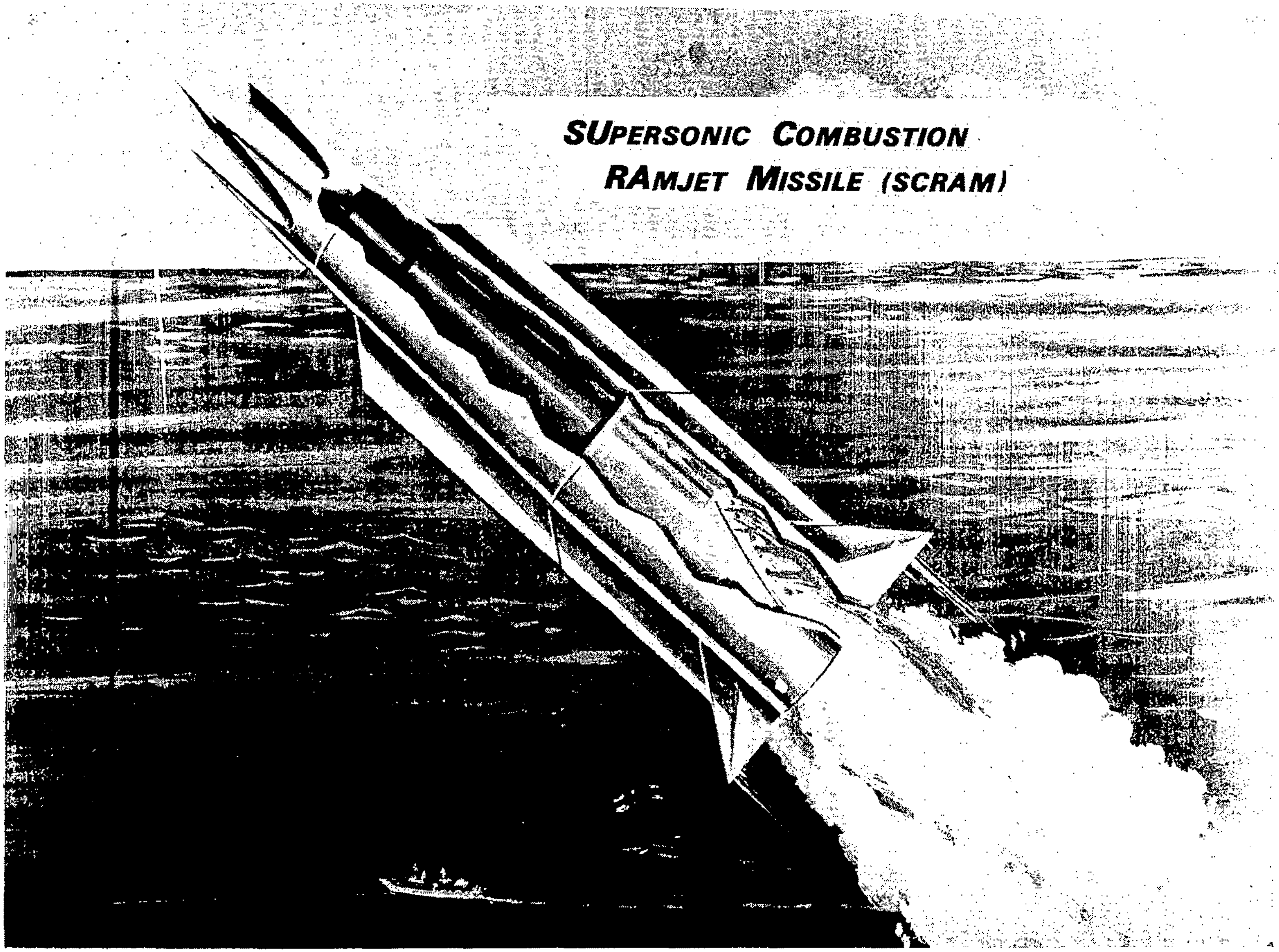

Figure 1

HYPERSONIC TACTICAL MISSILE (HYTAM) BASELINE CONFIGURATION

(Figure 2)

To avoid the day-to-day perturbations that occur in the configuration and performance estimates of SCRAM and (when it is desirable from a structures research viewpoint) to provide independence from the SCRAM propulsion program, idealizations have been made in the trajectories, performance requirement, weights, etc. To this end a new acronym, HYTAM, has been coined for the HYpersonic TActical Missile concept that has been used in the Hypersonic Structures research program

The HYTAM baseline configuration is shown in Figure 2. Like SCRAM, it is an airbreathing surface-to-air tactical missile capable of hypersonic speeds at both sea level and high altitudes. It is intended to be launched from a box-type launcher. The missile has an overall length of 4.01 m (158 in.) and a base diameter of 0.66 m (26 in.). The total length of the missile and booster is 6.30 m (248 in.). Other features of the missile are:

RF (radio frequency) and interferometer guidance systems

Four (4) separate engine thru ducts and combustors with common inlet and nozzle sections

Main fuel tank located within the centerbody and auxiliary tanks located between the thru ducts

Aerodynamic control surfaces foldable to fit within a rectangular launching box (not shown in Fig. 2)

Outer structure of missile is primary load bearing structure for both shear and bending moments

HYPERSONIC TACTICAL MISSILE BASELINE CONFIGURATION

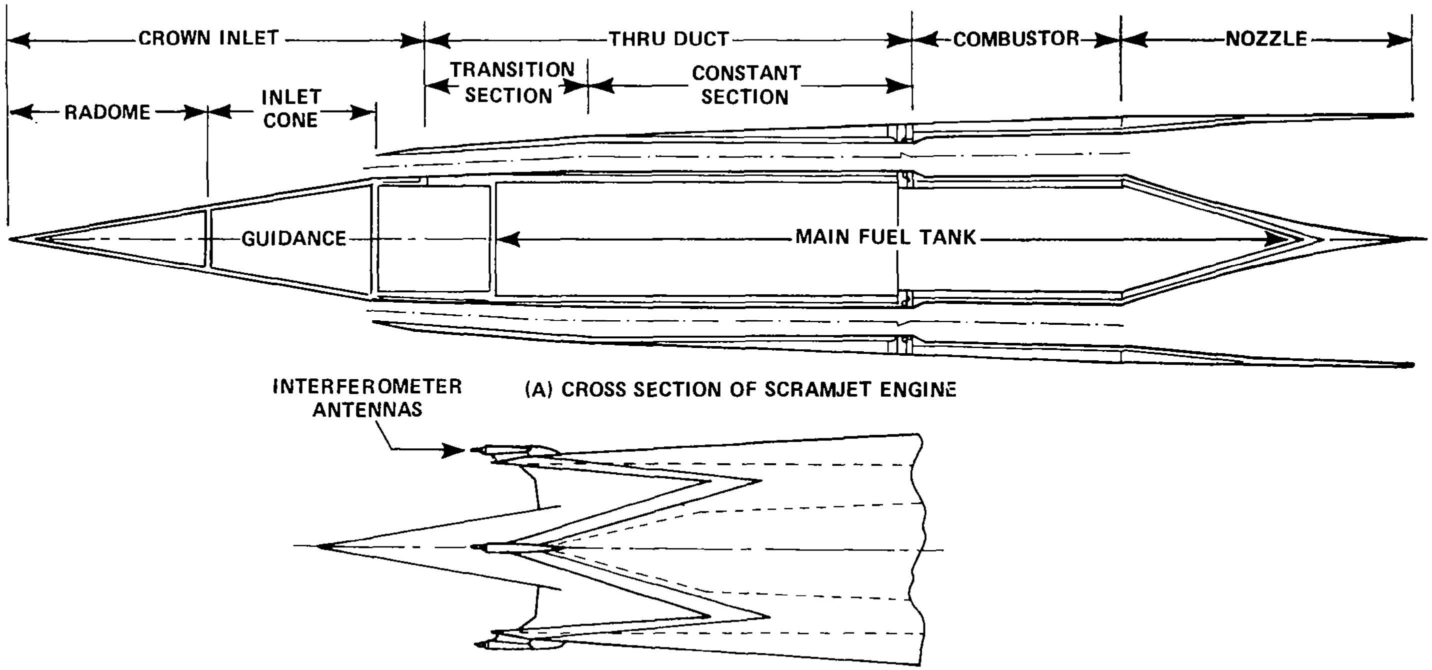

(A) CROSS SECTION OF SCRAMJET ENGINE

(B) CROWN INLET ROTATED 45°

Figure 2

HYTAM DESIGN CRITERIA

(Figure 3)

One of the initial tasks undertaken was a definition of the criteria for use in the structural design of the HYTAM configuration. Some of the requirements are given in Figure 3.

HYTAM is launched from a vertical box launcher with inside dimensions of 1.04 m x 0.91 m x 6.35 m (41" x 36" x 250"). The aerodynamic control surfaces must fold to fit within this box. The launch weight is 2585 kg (5700 lb) and the missile weight after booster separation is 1088 kg (2400 lb). Cruise speeds up to Mach 8 at high altitudes are attained. Ranges up to 740 km (400 n. mi.) are achieved

Some of the dimensional constraints are also indicated in Figure 3. The radii on the tips, crotches and swept leading edges of the inlet shall be kept to a minimum consistent with design and structural requirements. For preliminary studies radii less than 0.125 cm (0.050 in.) need not be considered. Material loss within the engine ducts and combustor due to ablation, shear and erosion shall be such that the cross sectional area does not increase by more than 10%.

The radome is restricted to a conical shape having a 0.166 rad (9.5°) half angle, a maximum nose radius of 0.254 cm (0.1 in.) and an outside base diameter of 17.8 cm (7 in.). To facilitate flight through rain at the hypersonic speeds, a metal nosetip will be required. Since boresight error slope change must be kept to about 0.01%, the allowable erosion of the radome wall will be near zero. The dielectric constant should be in the range of 3 to 9 but more important is the change with temperature. This change should be small (a maximum change of about 10% for a 1650 K (3000°R) change in temperature). Also, the loss tangent of the radome material should be less than 0.01 and its change with temperature should be small.

For the interferometer antennas the tolerances on the angular and radial displacements during flight are relatively generous. A 1% change in spacing between diametrically opposite antennas is acceptable and a 0.035 rad (2°) angular rotation from their initial orientation is permissible. The ablation of the antenna nosetip is restricted to about 0.254 cm (0.1 in.).

HYTAM DESIGN CRITERIA

SIZE CONSTRAINTS

STOWAGE WITHIN BOX LAUNCHER	1.04m X 0.91m X 6.35m (41" X 36" X 250")

WEIGHT

MISSILE & BOOSTER	2585 kg (5700 LB)
MISSILE (FULLY FUELED)	1088 kg (2400 LB)

SPEED

SEA LEVEL	UP TO M5
24-30 km (80-100 KFT)	UP TO M8

RANGE

HIGH ALTITUDE CRUISE	UP TO 740 km (400 n.mi.)

DIMENSIONAL CONSTRAINTS

LEADING EDGE RADII	0.125 cm (.050")
ENGINE DUCTS & COMBUSTOR	10% AREA CHANGE

Figure 3

FLIGHT LIMITATIONS OF RANDOME MATERIALS

(Figure 4)

As part of the APL/JHU Structures research and exploratory development effort, a computer code has been developed to calculate the flight limitations of radome materials. This code calculates the boresight error slope, thermal stress, and mechanical stress limits of missile radomes for any prescribed flight trajectory. In Figure 4 are presented the performance limits for some of the more common radome materials. The flight limitations are imposed by either thermal stress or boresight error considerations which are based on aerodynamic heating. No consideration has been given to damage due to rain or dust environments. A proposal has been made to NAVSEA to expand our computer program to include this mode of radome failure design.

For the HYTAM, slip cast fused silica appears to be the most promising radome material; however, during the coming year we plan to investigate the limits of several silicon nitride materials.

FLIGHT LIMITATIONS OF RADOME MATERIALS

(BASED ON AERODYNAMIC HEATING EFFECTS)

MATERIAL	MACH NO. AT LOW ALTITUDE
REINFORCED EPOXY	2
ALUMINA	3 – 3.5
REINFORCED POLYIMIDE	3.5
PYROCERAM 9606	4.5 – 5.5
SLIP CAST FUSED SILICA	6 – 7

Figure 4

CRITICAL TEMPERATURE REGIONS OF SCRAMJET INLET

(Figure 5)

At the tips and crotches of a scramjet inlet the driving temperature due to aerodynamic heating will be the stagnation temperature. These regions are indicated in Figure 5. At Mach 8 at altitude, the stagnation temperature will be about 2500 K (4500°R). Depending upon the structural material and the inlet geometry, the material in the stagnation regions will reach temperatures 220-335 K (400-600°R) below stagnation. The swept leading edges will be another 110-220 K (200-400°R) lower. Temperatures along the body of the missile will be between 1/2 to 2/3 the stagnation temperature. For HYTAM, temperatures of the air inlet tips and crotches may reach the 2085-2250 K (3750-4050°R) range. Small leading edge radii preclude the use of ablative coatings for thermal protection and from the standpoints of reliability and cost, a passive hot structure in these stagnation regions is preferable to an active cooling system.

CRITICAL TEMPERATURE REGIONS OF SCRAMJET INLET

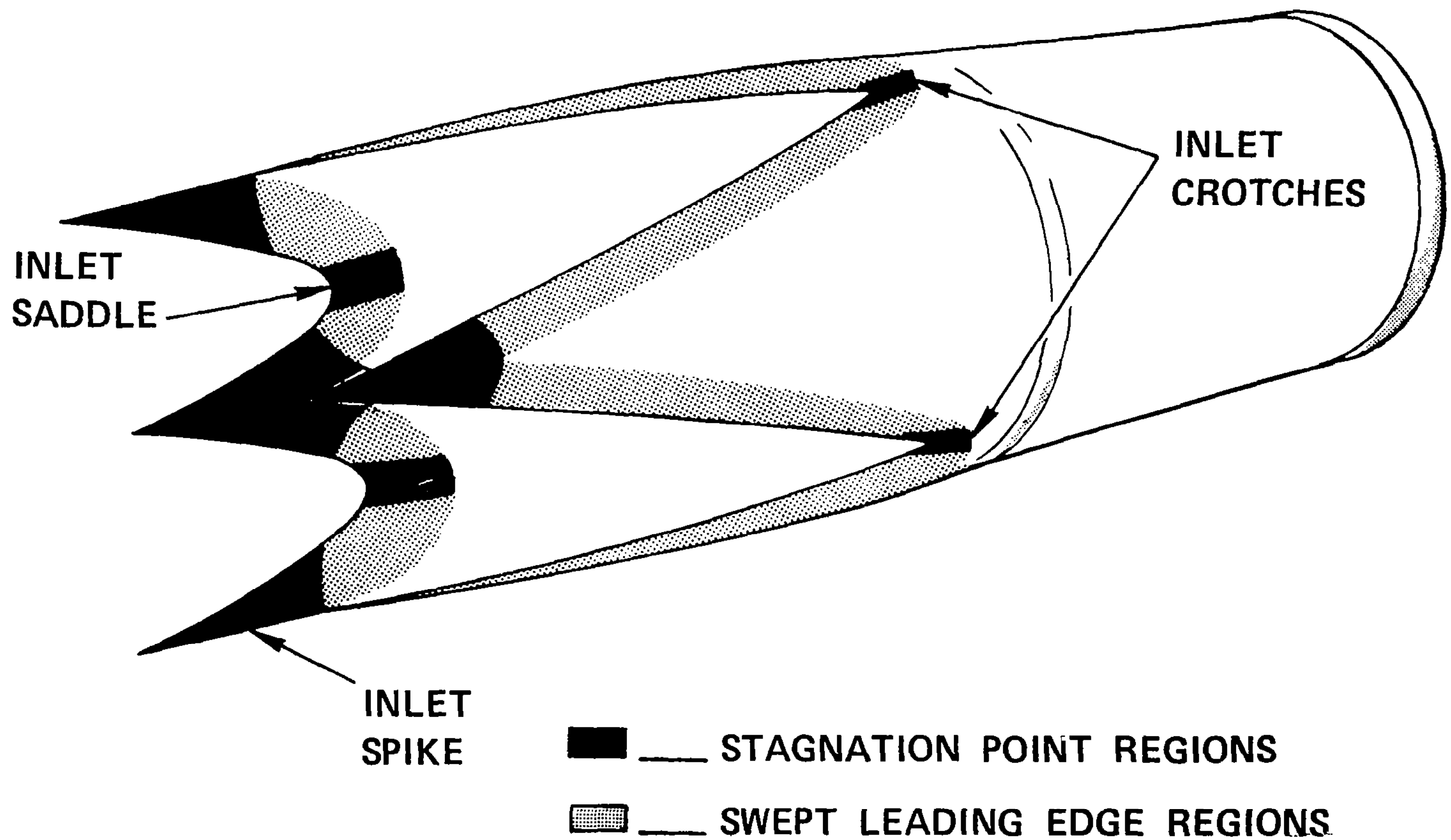

Figure 5

LEADING EDGE TEST RESULTS

(Figure 6)

Accommodating the high temperatures of the HYTAM inlet in a hot structure requires an advance in the state-of-the-art in refractory materials and coatings which must possess oxidation and erosion resistance in addition to mechanical strength and thermal shock resistance. An experimental program to test candidate materials for hypersonic leading edges was conducted by APL from 1965 to 1972. A two phase process consisting of material characterization tests followed by freejet testing was used to examine promising materials. Materials that gave satisfactory results in creep and oxidation tests in static air were tested in the APL Propulsion Research Laboratory (PRL) arc jet capable of simulating flight conditions of Mach 7.5 at 11.6 km (38,000 ft). Materials tested included carbides, diborides, silicones, graphites, and the refractory metals tungsten, tantalum, and columbium. Tests were made on both coated and uncoated specimens and covered wedge angles from 0.26 to 1.57 rad (15 to 90°) and leading edge radii R_o from 0 to 0.15 cm (0 to 0.06 in).

A summary of the test results is given in Figure 6. Of the materials tested, specimens of tantalum alloy T222 with a hafnia coating survived the arc-jet test without damage. However, facility limitations restricted the test duration to about 11 s. When protected against moisture absorption, the HD-0092 boron nitride specimens also withstood the arc-jet test without damage. The tantalum T222 with a hafnia coating is considered the most promising candidate material for leading edge applications.

LEADING EDGE TEST RESULTS

EXPOSURE SIMULATES STAGNATION-POINT HEATING
FOR M 7.7 AT 11.6 km (38 KFT)

MATERIAL	WEDGE RAD (DEG)	R_o cm (IN)	TIME (SEC)	REMARKS cm/s (IN/S)
JTA GRAPHITE	0.52 (30)	0.13 (0.05)	7.5	MELTING, FLOWING, 0.11 (0.042)
TUNGSTEN-IMPREG 10% Ag	0.26 (15)	0.03 (0.01)	7.8	MELTING, FLOWING 0.11 (0.044)
GE TUNGSTEN-30% Si	0.52 (30)	0.03 (0.01)	9.0	SOFTENING, EXCESSIVE WARPING
ATJ GRAPHITE	0.52 (30)	0.13 (0.05)	–	RAPID ABLATION, 0.12 (0.048)
HD-0092 BORON NITRIDE	1.57 (90)	0.13 (0.05	10.0	NO DAMAGE
Ta-T222/HfO_2 COATING	0.26 (15)	0.08 (0.03)	11.2	NO DAMAGE
Ta-T222/Hf 20% Ta COATING	0.26 (15)	0.08 (0.03)	–	COATING ERODED THROUGH IN 2s, EROSION AT 0.64 (0.250)

Figure 6

HYTAM FRONT END AND DUCT CROSS SECTION

(Figure 7)

The forward segment of the engine thru duct is a transition piece that changes from a non-circular to a circular cross section over a length of 45.7 cm (18 in.). Because of this unusual non-circular shape (Fig. 7) and the high internal pressures and temperatures that this component is subjected to, it was chosen as one of the critical structural design areas requiring study. A design investigation involving thermal and stress analyses has been made to identify materials that are suitable for the thru duct. These candidate materials were then screened to determine which alloys should result in the lightest weight or lowest volume structure.

The thermal and stress analyses were performed for both the sea-level short-time and the high-altitude long-range-cruise trajectories. The terminal phase of the long-range trajectory consists of a dive to a lower altitude and Mach number followed by a powered intercept "run-in". The pressure and temperature histories of the two trajectories are very different and should bracket the environmental conditions experienced by the HYTAM thru duct. While the Mach number and temperature during the long-range trajectory are greater than for the sea-level trajectory, the high altitudes result in low duct pressures. During dive and intercept, moderately high duct pressures and temperatures occur simultaneously. It is not possible to say which of these trajectories is critical in the design without analyzing both cases.

HYTAM FRONT END & DUCT CROSS SECTION AT STATION 46

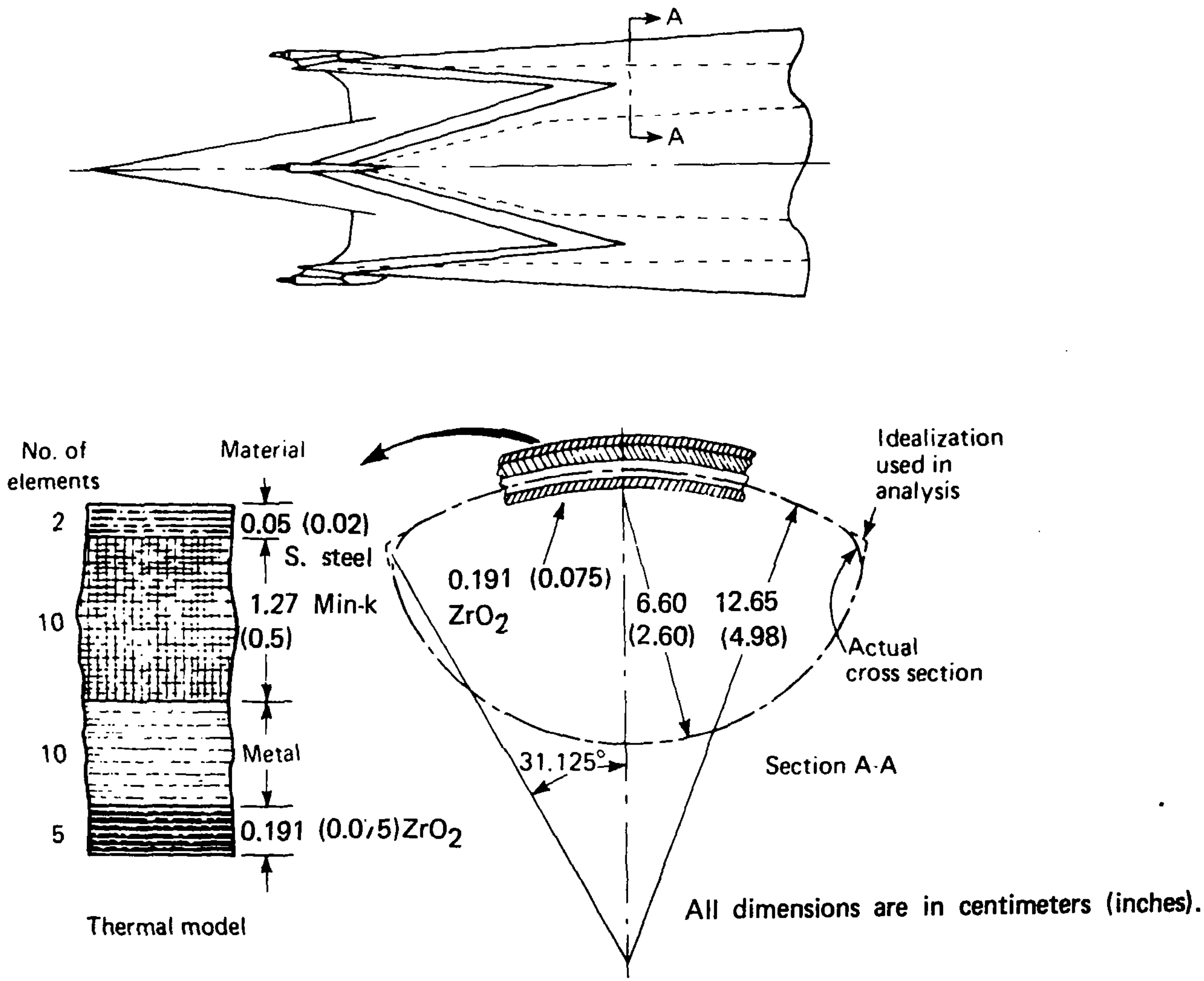

Figure 7

MATERIAL SELECTION STUDY DESIGN CURVES FOR 0.051 m (0.2 in.) F-85 COLUMBIUM

(Figure 8)

After considering alternatives it was decided that the most informative way to present the data is that shown by the typical curves of Figure 8. The curves are for 0.51 cm (0.2 in.) thick F-85 columbium alloy insulated by a 0.191 cm (0.075 in.) layer of ZrO_2. Two types of curves are shown in this figure. The hatched curve is a plot of the allowable ultimate tensile strength of the material as a function of temperature. The second type of curve is a plot of the history of the actual design ultimate stress due to both internal pressure and thermal gradients against the average wall temperature, $\overline{T}$, through the thickness of the wall. In these curves, time is a parameter that increases along the curve. Curves are plotted for both the sea-level and high-altitude cruise trajectories.

In a plot of the form of Figure 8, the design has adequate strength if all points on the actual-design-stress curves for both trajectories remain below the hatched allowable-strength curve of the material. For the 0.51 cm (0.2 in.) thick F-85 columbium alloy insulated with ZrO_2, the design is satisfactory for the sea-level condition but is overstressed at the end of the dive and during intercept in the long-range-cruise trajectory. In other cases of thicknesses and materials the sea-level rather than the long-range-cruise trajectory can be critical.

The results of the study showed that uninsulated materials provided both the lightest weight and thinnest wall structures. Uninsulated F-85 columbium results in the lightest weight. Two materials investigated, uninsulated Tantalum T-222 and uninsulated arc cast and extruded tungsten alloy W-HfC, were found to result in the smallest wall thickness; however, the lightest weight material, uninsulated F-85 columbium, is only 0.10 cm (0.04 in.) thicker.

DESIGN CURVE FOR ZrO_2
INSULATED 0.05 cm (0.2 in.) THICK
F-85 COLUMBIUM

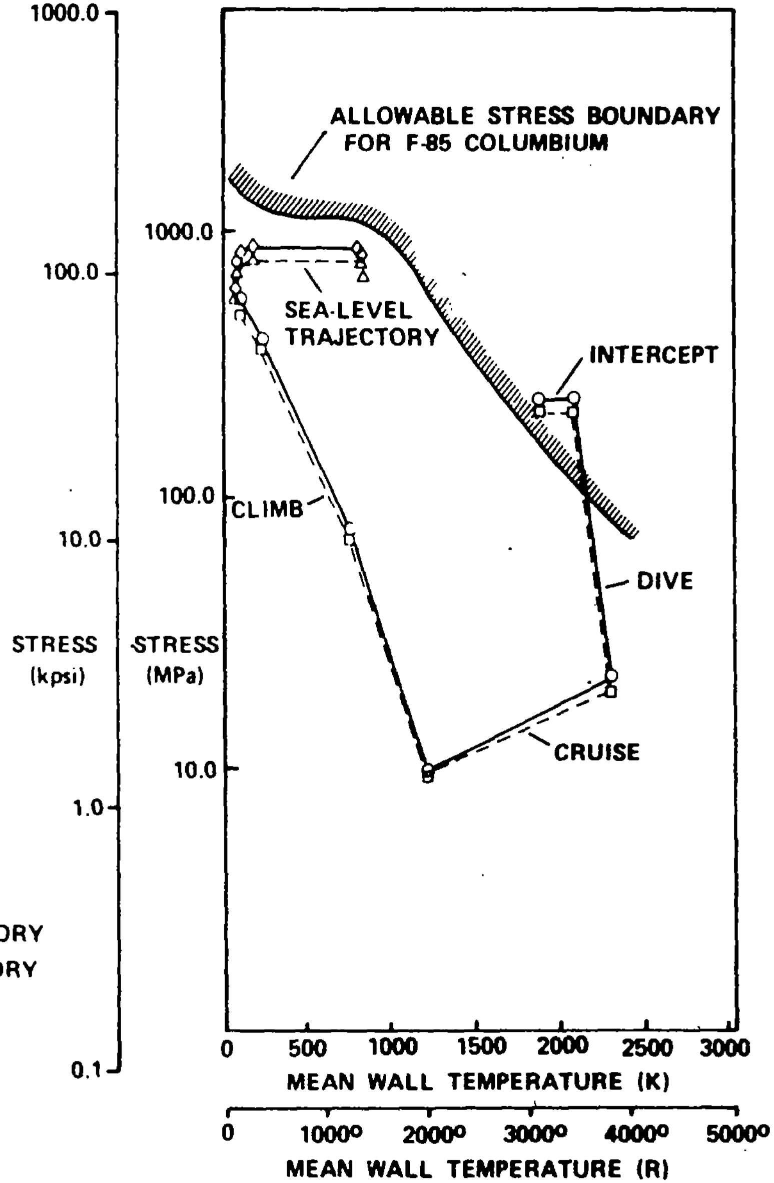

○ ___ DUCT INNER SURFACE, CRUISE TRAJECTORY
□ ___ DUCT OUTER SURFACE, CRUISE TRAJECTORY
◇ ___ DUCT INNER SURFACE, SEA-LEVEL TRAJECTORY
△ ___ DUCT OUTER SURFACE, SEA-LEVEL TRAJECTORY
——— ___ TENSION
- - - ___ COMPRESSION

Figure 8

REENTRY NOSE TIP AND HYTAM COMBUSTOR ENVIRONMENT COMPARISON

(Figure 9)

The HYTAM combustor presents one of the most critical design problems. The combustor is subjected to total temperatures greater than 2220 K (4000°R) and static pressures of about 6.9 MPa (1000 psi) during sea level trajectories and temperatures as high as 3160 K (5700°R) at low static pressures during the long-range-cruise trajectories. In terms of pressure and temperature this environment is similar to that of a rocket motor, the major difference being the HYTAM environment is oxidizing whereas the rocket motor environment is reducing.

The HYTAM combustor environment has been compared with the environment associated with reentry vehicles in hopes that materials developed for reentry vehicle nose tips could be used in the HYTAM combustor. This comparison is presented in Figure 9. The static pressure, enthalpy, gas velocity, and cold wall heat flux environments given for the reentry nose tip are conditions to which representative nose tip materials have been tested. The measured minimum ablation rate for the best of these materials was about 0.38 cm/s (0.15 in/s). The sea level HYTAM combustor environment is seen to be quite similar to that of the nose tip. However, to maintain satisfactory engine performance, the cross sectional area change of the combustor ducts should be held to less than 10%. This implies that the combustor material must not ablate by more than about 0.0076 cm/s (0.003 in/s). This rate is considerably less than that measured on nose tip materials. Therefore, materials acceptable for reentry nose tip applications are not suitable for the HYTAM combustor.

REENTRY NOSE TIP & HYTAM COMBUSTOR ENVIRONMENT COMPARISON

CONDITION	REENTRY NOSE TIP	HYTAM COMBUSTOR
STATIC PRESSURE – atm	100	90
GAS TO WALL ENTHALPY DIFFERENCE – MJ/kg (Btu/lb)	4.7 (2000)	4.9 (2100)
GAS VELOCITY – m/s (FT/S)	SUBSONIC	915 (3000)
COLD WALL HEAT FLUX – MW/m^2 ($Btu/FT^2{\cdot}S$)	34.0 (3000)	44.3 (3900)
MINIMUM ABLATION – cm/s (IN/S)	0.38 (0.15) (MEASURED)	0.008 (0.003) (DESIRED)

Figure 9

PG/SiC-COATED ATJ GRAPHITE COMBUSTOR TEST SECTION

(Figure 10)

Tests on materials, which date back to 1968, indicate that a codeposited coating of silicon carbide and pyrolytic graphite (PG/SiC) will hold the HYTAM combustor ablation rate to acceptable limits. The optimum amount of SiC was found to be about 30% by weight and the substrate used in all test specimens has been ATJ graphite. These tests have been conducted in various environments with gas flow from arc heaters, potassium perchlorate solid propellants, gel motors, and in a connected pipe SCRAM combustor test rig.

In 1974, a small diameter PG/SiC coated ATJ graphite specimen was tested in a subsonic flow produced by a potassium perchlorate solid propellant. The nominal chamber conditions were a total pressure = 20.7 MPa (3000 psia) and a total temperature = 2890 K (5200°R). The resulting static pressure in the test section was 16.1 MPa (2330 psi). The coating experienced an ablation rate as low as 0.008 cm/s (0.003 in/s) for 30% SiC content. In 1978 the PG/SiC coated specimen shown in Figure 10 was tested in the closed pipe SCRAM propulsion test rig at the APL Propulsion Research Laboratory (PRL). By placing the test section immediately downstream of the fuel injectors, the specimen was subjected to the maximum static pressure and heat transfer. Some regions of the specimen were exposed to a total temperature of about 3050 K (5500°R) and static pressure of about 3.45 MPa (500 psia) for 25 sec. The results of the test indicated an average ablation rate of 0.0025 cm/s (0.001 in/s) at the most critical section of the specimen.

While the tests on codeposited PG/SiC coating on an ATJ substrate have produced encouraging results, the combination is not optimum. The strength of ATJ is low relative to woven carbon/carbon (C/C) materials and as a result the ATJ is inefficient with regard to weight and volume. Unfortunately, while C/C materials have high strength they do not have the excellent oxidation resistance of PG/SiC. Furthermore, the coefficients of expansion of PG/SiC and C/C are not compatible so that the PG/SiC cannot be used as a coating for the C/C. Pyrolytic graphite is compatible with C/C, however, and it may be possible to start by depositing pure PG and increasing the percent of SiC in the deposition until it reaches 30% at the inner surface of the combustor.

Another approach being pursued is the incorporation of metallic additives into three-dimensional C/C materials.

PG/SiC-COATED ATJ GRAPHITE COMBUSTOR TEST SECTION

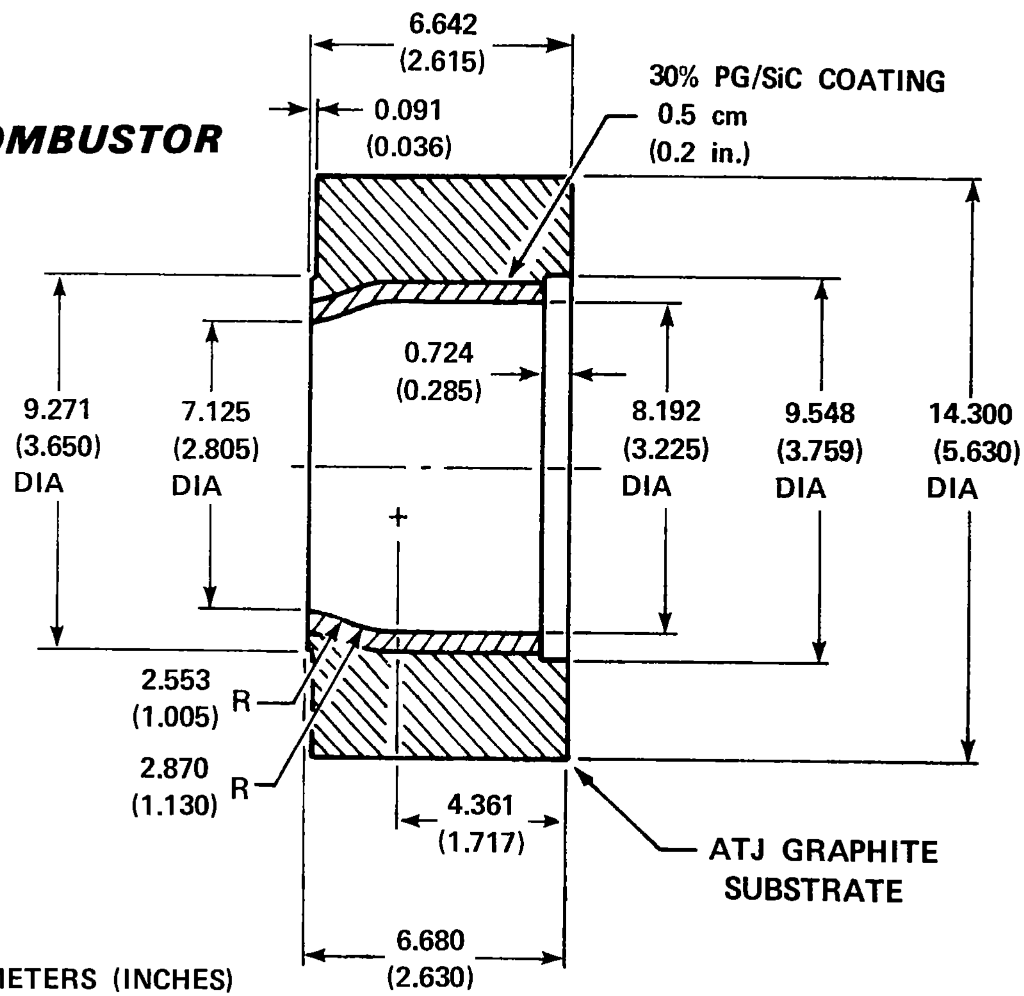

DIMENSIONS ARE IN CENTIMETERS (INCHES)

Figure 10

CONCLUDING REMARKS

SUMMARY OF CANDIDATE MATERIALS

(Figure 11)

In conclusion, it should be stated that much remains to be done in developing materials and design concepts that are representative of flight-weight missile structures. The tests that have been run are too few to provide a sufficient data base for design purposes and in some cases have not fully simulated the critical design environments. Problems of reducing analytical results and component test data to flight-weight hardware remain to be considered. The studies to date, however, are encouraging and do indicate that materials are available or can be developed to satisfy the scramjet requirements. In Figure 11 some of the more promising materials for the critical components are indicated. This information can be summarized as follows:

Radome	Slip cast fused silica is the current candidate, but others are being investigated. One shortcoming of slip cast fused silica is its susceptability to rain damage.
Inlet Leading Edges	A refractory metal with a good oxidation protective coating will be required. Tantalum T222 with a Hafnia coating looks promising.
Inlet Ducts	An uninsulated refractory alloy will be required. Columbium F-85 was the best of those considered for the non-circular ducts.
External Body	The external body temperatures are sufficiently low to permit the use of super alloys. The choice of alloy will depend upon the specific application.
Combustor and Nozzle	The pyrolytic graphite/silicon carbide (PG/SiC) coating is very attractive for use in the combustor and nozzle areas. The application of this coating to a high strength substrate still needs development. An attractive substrate is 3D carbon/carbon, but problems associated with thermal expansion mismatch need resolution. An alternate solution is the impregnation of oxidation suppressants into carbon/carbon.

SUMMARY OF CANDIDATE MATERIALS

RADOME

SLIP CAST FUSED SILICA

INLET LEADING EDGES

TANTALUM T222 WITH HfO_2 COATING

INLET DUCTS

UNINSULATED REFRACTORY; e.g.,
F-85 COLUMBIUM

EXTERNAL BODY

SUPER ALLOYS

COMBUSTOR & NOZZLE

PG/SiC COATED 3D C/C

Figure 11

STRUCTURES AND TPS FOR THE NHFRF/HYTID

Harvey J. Hoge

Rockwell International, Los Angeles Division, California

INTRODUCTION

(Figure 1)

The Air Force was engaged in the development of the Hypersonic Technology Integration Demonstrator (HYTID), formerly known as NHFRF, to accelerate the development and demonstration of technology for future military systems designed to operate within the atmosphere at speeds between Mach 4 and 8.

The primary objective of HYTID was to conduct experimental research in the hypersonic test environment available within its flight capability envelope. Sufficient design flexibility was built into HYTID so that it could accommodate the aerodynamic drag, thermal interference heating, and flight control perturbations brought about by the installation and operation of all candidate experiments. Those experiments that have a major vehicle design impact are associated with the airbreathing propulsion tests. As the specific impulse of airbreathing propulsion systems is an order of magnitude higher than rockets, their ultimate use in hypersonic vehicles is an attractive goal. To provide the test-bed capability to assure the development of these high-performance propulsion systems, HYTID was configured to the requirements of these systems. The most promising of these concepts today are the scramjets. However, they cause a major configuration impact, as the forebody of the fuselage must be configured to provide the inlet precompression properties required, while the afterbody must conform to the engine exhaust expansion requirements.

Recent hypersonic research airplane studies (References 1 through 7) have investigated a few selected structural concepts with alternate propulsion options. The objective of this study was to determine the most cost-effective construction method of all the leading candidates, to determine the most promising rocket engine combinations, and to develop a total system that provides a broad experimental research capability.

HYPERSONIC TECHNOLOGY INTEGRATION DEMONSTRATOR (HYTID)

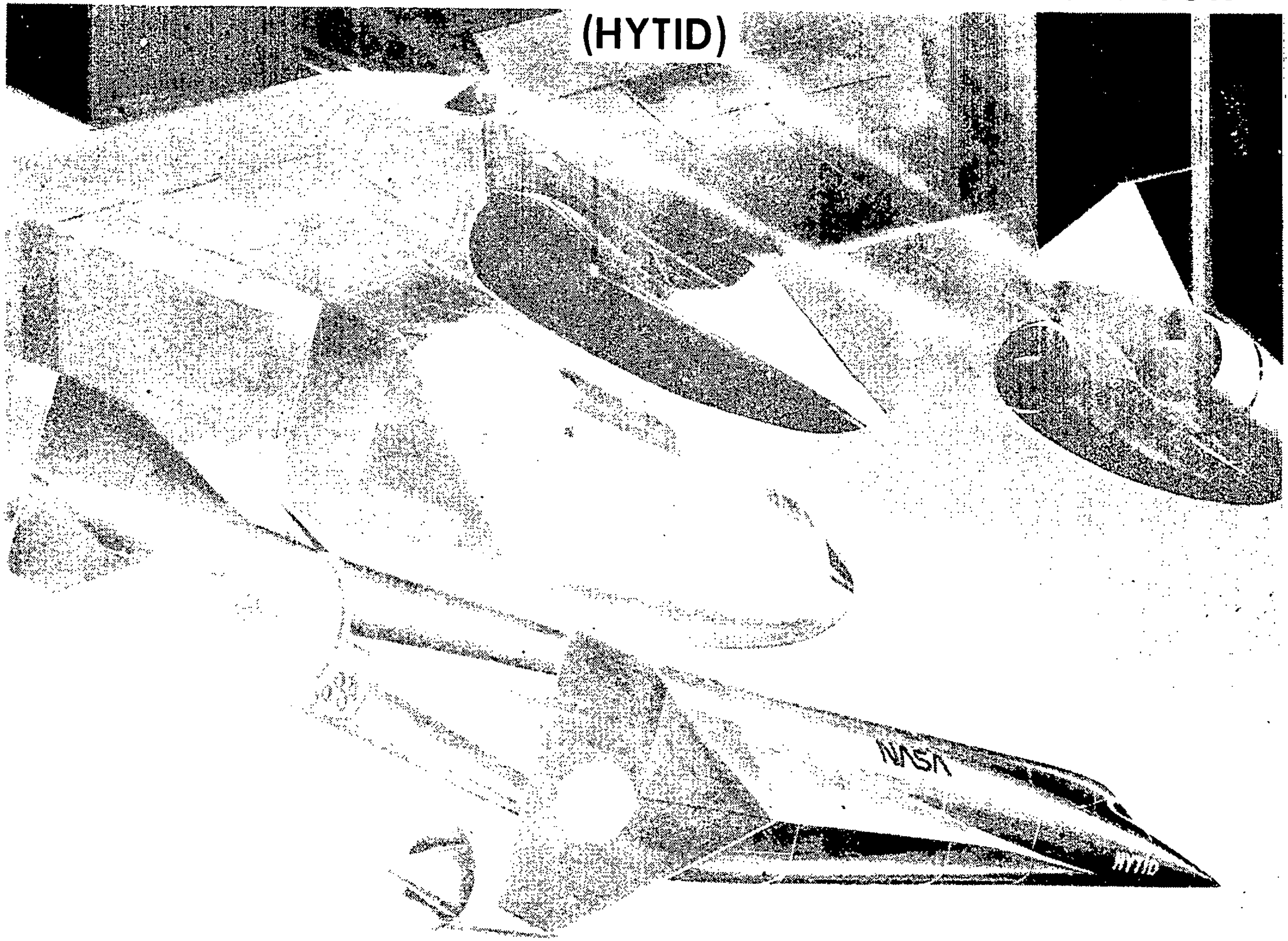

Figure 1

INITIAL DESIGN CONSTRAINTS & REQUIREMENTS

(Figure 2)

This table presents the minimum requirements which were formulated to insure that the vehicle when finally built would satisfy the basic goals of the program. These goals are:

1. Develop a flight research vehicle capable of advancing and demonstrating technology in the Mach 4 to 8 region

    - Airbreathing Propulsion - Flight verification of advanced airbreathing propulsion systems, their performance inlets, and their integration with the airframe

    - Structures - Flight demonstration of reliable, reusable, and lightweight critical structural components

    - Aerodynamics - Flight verification of existing hypersonic aerodynamic and aerothermodynamic prediction techniques

    - Systems - Evaluation of the influence of hypersonic flight on a variety of operational and mission oriented systems and subsystems

2. Develop a flight research vehicle which is also flexible to allow for additional capability in terms of experimental test conditions and performance

3. Minimize program and annual expenditure

INITIAL DESIGN CONSTRAINTS & REQUIREMENTS

- M6 CRUISE 40 SECONDS
- MAXIMUM DYNAMIC PRESSURE = 47.9 $\frac{kN}{m^2}$ (1000 PSF)
- INTEGRATED SCRAMJET PROVISIONS
- B-52G UNDERWING CARRY / AIR LAUNCH
- 45,350 kg (100,000 LB) MAXIMUM LAUNCH WEIGHT
- MANNED VEHICLE
- 3.05 m (10 FT) LONG DEDICATED PAYLOAD BAY
- STATE-OF-ART/EXISTING EQUIPMENT
- EXISTING BOOST ENGINE (LR-105 OR YLR-99)
- EXISTING ROCKET CRUISE ENGINE (LR-101 OR XLR-11)
- LAND ON CONVENTIONAL RUNWAY

Figure 2

HYTID FLIGHT ENVELOPE

(Figure 3)

This figure encompasses the HYTID design mission profiles. The mission definitions used for performance calculations consist of two cruise mission profiles and one maximum Mach mission. The rocket cruise and scramjet cruise profiles are equivalent with the exception of the source of cruise thrust and level of external drag. The profile consists of launch from the carrier vehicle, followed by propulsion system ignition and a short acceleration to climb speed. An optimum climb (minimum time) to cruise conditions precedes boost propulsion shutdown and cruise propulsion ignition. A constant Mach number constant altitude cruise is conducted using either rocket power or scramjet power for the two different missions, and an unpowered descent to landing concludes the mission. The maximum Mach mission is similar except that no payload or external propulsion is carried, and all fuel is used in the boost engine to provide a higher Mach and altitude condition than attainable for the cruise mission. Additional speed is gained through deletion of the experiment package carried on the rocket cruise mission.

HYTID FLIGHT ENVELOPE

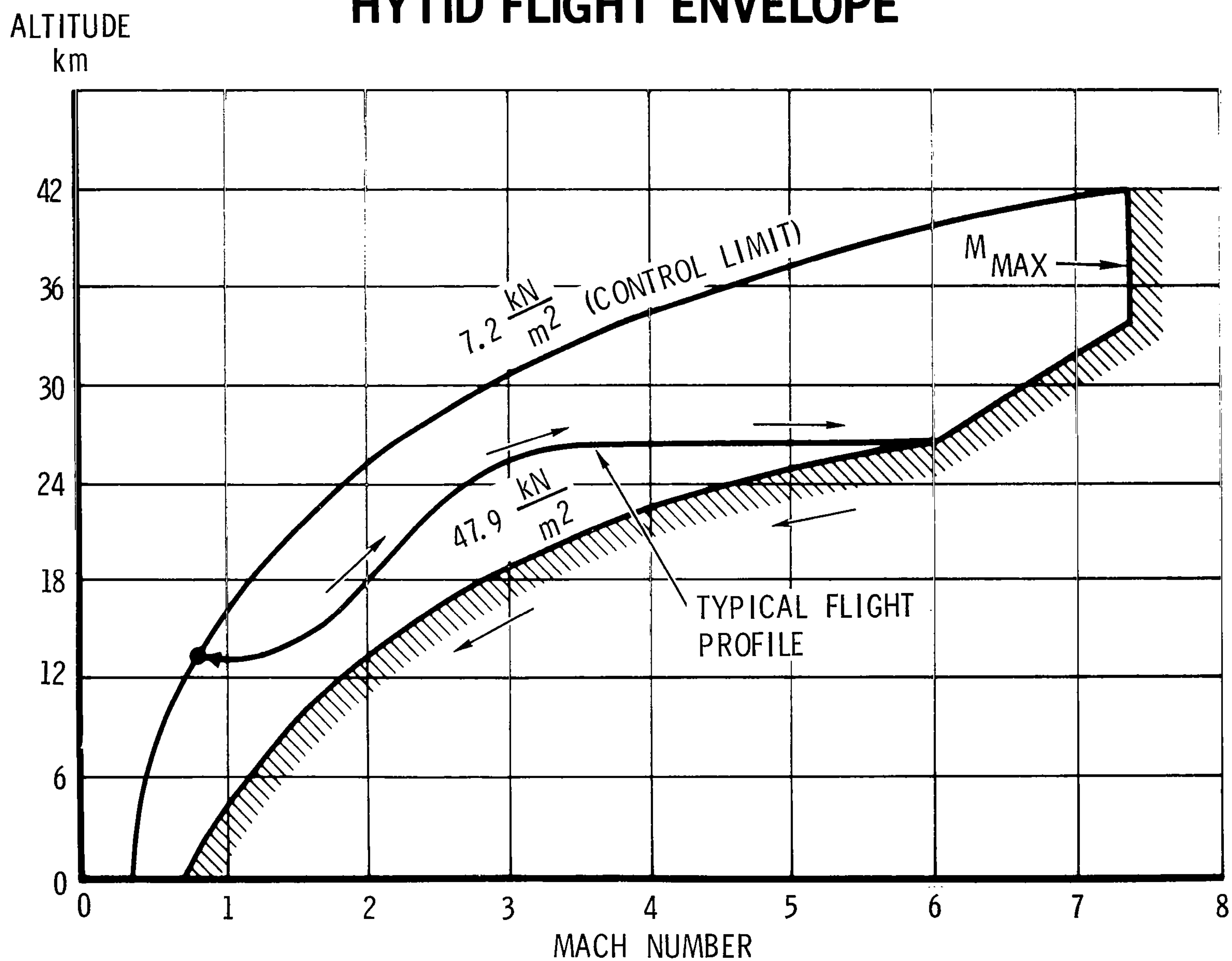

Figure 3

TRADE STUDY VEHICLE DEFINITIONS

(Figure 4)

The trade study, conducted during the initial effort, considered a total of 24 vehicle concepts. Variables that were incorporated include:

1. Integral and nonintegral propellant tanks

2. Six alternate material/construction methods

3. Two alternate rocket boost engines (each with compatible cruise engines)

4. Seven parametric sensitivities (q, n_z, cruise time, payload size, etc)

For each of the 24 concepts, estimates were made that included:

1. Launch and empty weight

2. Procurement cost of 1 and 2 vehicles

3. Evaluation of research capability

Cost was the major criterion in making the final selection. The YLR-99 rocket engine was selected for the boost engine from a safety and low initial cost standpoint. With uprating of the engine at a later date, the procurement cost could be minimized without jeopardizing the ultimate capability of attaining 40 seconds of Mach 6 cruise. Other features that were selected included the integral propellant tanks, superplastic forming/diffusion bonding (SPF/DB) truss core sandwich for TPS, and wing and tail skins.

TRADE STUDY VEHICLE DEFINITIONS
24 ALTERNATE CONCEPTS

Seq. No.	Concept	Structure	Dynamic pres. (kN/m^2)	Mach No.	Cruise propulsion	Test time (sec)	Load factor, n_z	Payload (kg wt / drag)	Bay length (L/D)
1	1	Al/Ti truss core	47.9	6	Rocket	40	3	1,587 / 567	2.0
2	3	Ti TC/nonint. tanks							
3	6	Al/Ti truss core							
4	8	Al/Ti truss core							
5	1	Al/Ti skin-stringer							
6	1	Al/Inconel 718							
7	1	Al/Lockalloy							
8	3	Lockalloy/nonint. tanks							
9	1	Al/insulative TPS							
10	1	Al/metallic TPS							
11	1	Al/Ti truss core	24.0						
12	1		71.9						
13	1		47.9	4.5					
14	1			5.0					
15	1			6.0		20			
16	1					80			
17	1				SCRAMJET	20			
18	1				Rocket	40	4		
19	1						5		
20	1						3	907 / 272	
21	1							2,268 / 907	
22	1							1,587 / 567	1.5
23	1								3.0
24	1	+ Stability Aug.							2.0

Figure 4

SELECTED VEHICLE CHARACTERISTICS

(Figure 5)

Results of the trade studies of 24 separate vehicles served as the basis for selecting a basepoint configuration. Sizing computations were performed to derive the desired vehicle size and volumetric requirements. Several preliminary weight and balance iterations were then performed to optimize the arrangement and size of the lifting and control surfaces, fuselage, landing gears, propellant tanks, and subsystems. Detailed mass distributions were defined for the concept which evolved from this configuration development process to implement external loads, flutter, and structural analyses. Propellant and ancillary expendable fluid usage sequences were defined for trajectory analysis of the rocket cruise, maximum Mach, and scramjet cruise missions.

The initial 10 basic vehicle requirements were adhered to accept where it would be possible to reduce costs, such as the elimination of the B-52G as a launch vehicle. By continuing to use the B-52B-008 as a launch vehicle, the high cost of modifying a B-52G could be eliminated. However, this restriction imposes a 25,850 kg limit for a launch weight, and made the HYTID design somewhat more difficult. Even with these restrictions, a concept definition has been developed, and was further analyzed and studied during the conceptual design phase of the study. The concept is similar to the NASA-generated L16 configuration, but with wing tip installed vertical tails to provide directional stability throughout the entire Mach range. A four-scramjet module with depth H_c = .56 m can be installed at the lower aft extremity of the fuselage.

SELECTED VEHICLE CHARACTERISTICS

- INITIAL BOOST ROCKET ENGINE: YLR-99
- GROWTH BOOST ROCKET ENGINE: YLR-99 (MAXIMUM UPRATING)
- CRUISE ROCKET ENGINE: (2) XLR-11 (CRUISE ONLY)
- BOUST PROPELLANT TANK SIZING: MAX LAUNCH WEIGHT = 25,850 kg (57,000 LB) WITH YLR-99 (MAXIMUM UPRATING)
- LAUNCH VEHICLE B-52B-008
- THERMAL / STRUCTURE DESIGN: M6, $q = 47.9 \frac{kN}{m^2}$ (1000 PSF) 40 SEC CRUISE (ROCKET CRUISE MISSION)
- MAXIMUM STRUCTURAL LOAD FACTOR: 4G
- PAYLOAD WEIGHT: 1587 kg (3500 LB)
- PAYLOAD M6 DRAG: 567 kg (1250 LB)
- SCRAMJET PROVISIONS: 2 TO 4 SCRAMJET MODULES, H_C = .56 m (22 IN) 3.68 m^3 (130 FT^3) LH_2 IN P/L BAY
- INTEGRAL ALUMINUM PROPELLANT TANKS
- SPF / DB TITANIUM TRUSS CORE SANDWICH: TPS, WING AND TAIL SKINS

Figure 5

GENERAL ARRANGEMENT

(Figure 6)

This figure presents the general geometric features of the HYTID.

The configuration development was initiated with the Langley-derived X24C-L16 wing-body arrangement. This vehicle was an outgrowth of the X24C-10C/X24C-12I lifting body configuration, and evolved from design efforts directed at increasing the vehicle slenderness in order to decrease the airbreathing propulsion system size required for hypersonic cruise and to improve the low-speed landing, lift-drag ratio.

To incorporate integral fuel tankage efficiently, aerodynamic studies were made to minimize the maximum cross-sectional area of the fuselage and to increase the fore- and afterbody slenderness. In order to provide the required propellant volume, the fuselage length was increased 16 percent, which further decreased the body closure angles. An 11-percent reduction in maximum area was realized, and corresponds to about 60 percent of the original lifting body. Further reduction in base area was sought by more tightly wrapping the boost and cruise rocket nozzles and eliminating the wing blunt trailing edge. A 25-percent decrease was realized, and corresponds to about one-fourth the base area of the lifting body.

Wing-mounted tip fins were incorporated early in the configuration evolution to provide directional stability at high angle of attack where test results indicate a centerline vertical tail become ineffective. Directional control was incorporated into these surfaces to design around the transonic centerline vertical rudder control reversal found experimentally.

GENERAL ARRANGEMENT

ENGINES
- YLR-99 BOOST
- (2) XLR-11 CRUISE
- PROVISIONS FOR FOUR .56 M (22 IN.) SCRAMJETS

WING

AREA	65.27 M^2 (702.59 FT^2)
AR	0.831
LE SWEEP	72°
SPAN	7.366 M (290 IN)

CENTER VERTICAL TAIL (FIXED)

AREA	5.48 M^2 (59 FT^2)
AR	0.963
LE SWEEP	50°

WING TIP VERTICAL

-UPPER

AREA	2.05 M^2 (22.1 FT^2)
AR	0.514
LE SWEEP	63.3°

-LOWER

AREA	2.59 M^2 (27.9 FT^2)
AR	0.672
LE SWEEP	62.8°

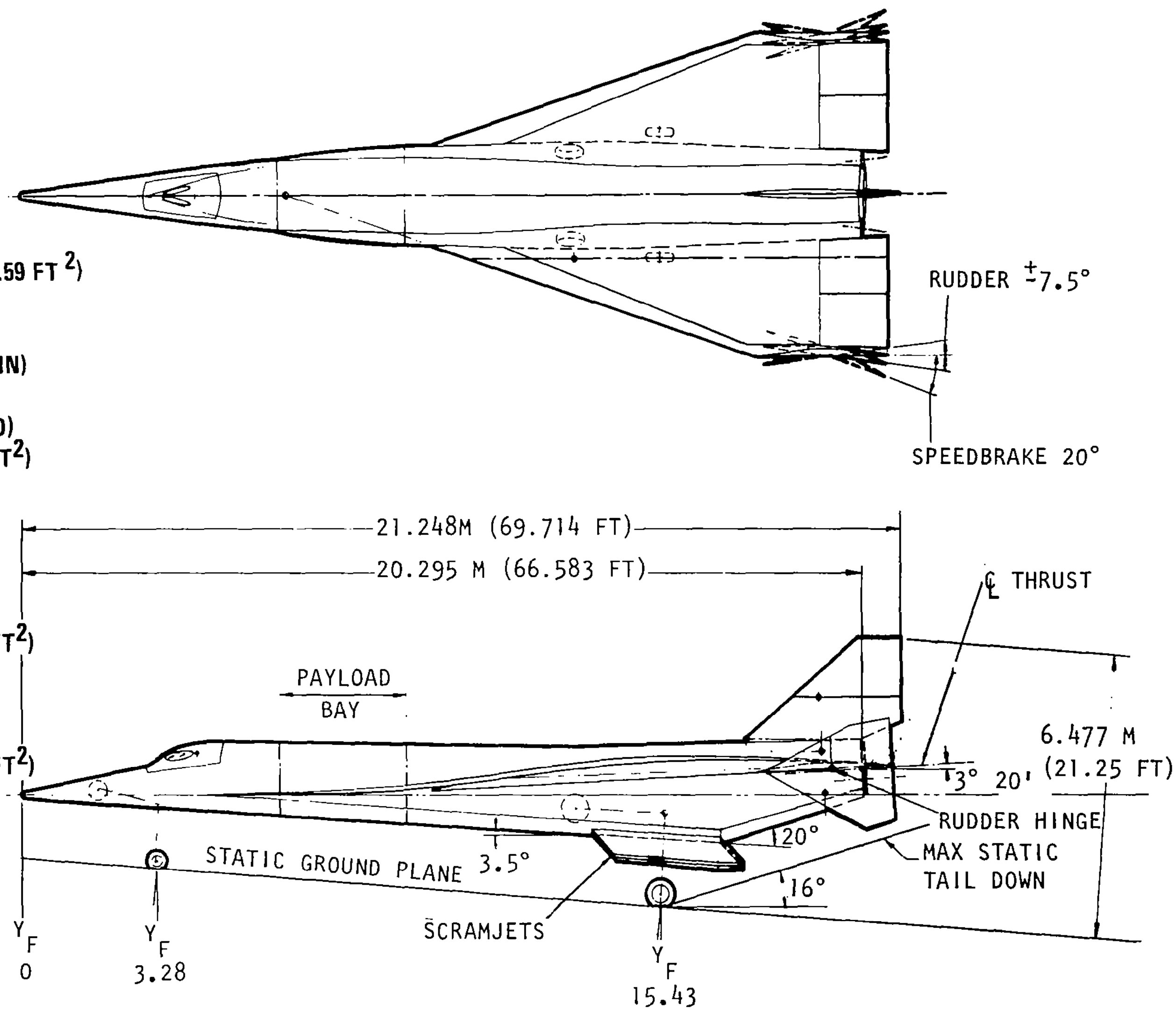

Figure 6

CANDIDATE METALLIC MATERIALS

(Figure 7)

Design criteria established for the HYTID indicate that the facility be capable of 100 flights at Mach 6 for a duration of up to 40 seconds. Hence, the cumulative time at maximum temperature for this structure could be 4,000 seconds (1.11 hours). Thermodynamic analyses indicate that a range of temperatures, depending on type of structure and material employed, will be experienced on the airframe due to aerodynamic heating. Leading edge temperatures in the 922° to 1,033° K temperature range are expected. In addition, temperatures up to 1,260° K will be encountered in the aft fuselage ramp area due to exhaust plume heating.

Selection of materials and processing methods for HYTID was made with the view of applying advanced materials and fabrication techniques to the extent necessary to maximize structural efficiency, balanced against the need for maintaining risk at acceptable levels. Low risk in the application of materials and processes implies the maintenance of high vehicle reliability and the reduction of restrictions which might otherwise limit available flight research time. In order to maintain low risk, the materials and processing methods selected for the program were based on the criterion that they be at or near state-of-the-art status; i.e., the material/process has gone through laboratory development, reduction to manufacturing practice, and application to flight hardware.

Aluminum alloys will be a major structural material for the HYTID. The 2000 series aluminum alloys will be used where temperatures up to 450° K are encountered. Welded components, such as tankage, will use artificially aged 2219. Where service temperatures permit, advantage will be taken of the higher strength 7075 alloy. For the majority of these applications, the stress corrosion-resistant overaged tempers will be selected, T73, or T76, depending on the particular design and usage.

Two titanium alloys, 6Al-4V and 6Al-2Sn-4Zr-2Mo, were selected for the heat sink and radiative thermal protection system structure on the HYTID. Ti-6Al-2Sn-4Zr-2Mo retains both strength and creep resistance at temperatures up to 811° K; whereas, a significant decrease in these properties occurs in Ti-6Al-4V at temperarures above 700° K. In general, Ti-6Al-2Sn-4Zr-2Mo extends the temperature capability of titanium alloys by 111° K to 139° K and is therefore a primary material for the HYTID.

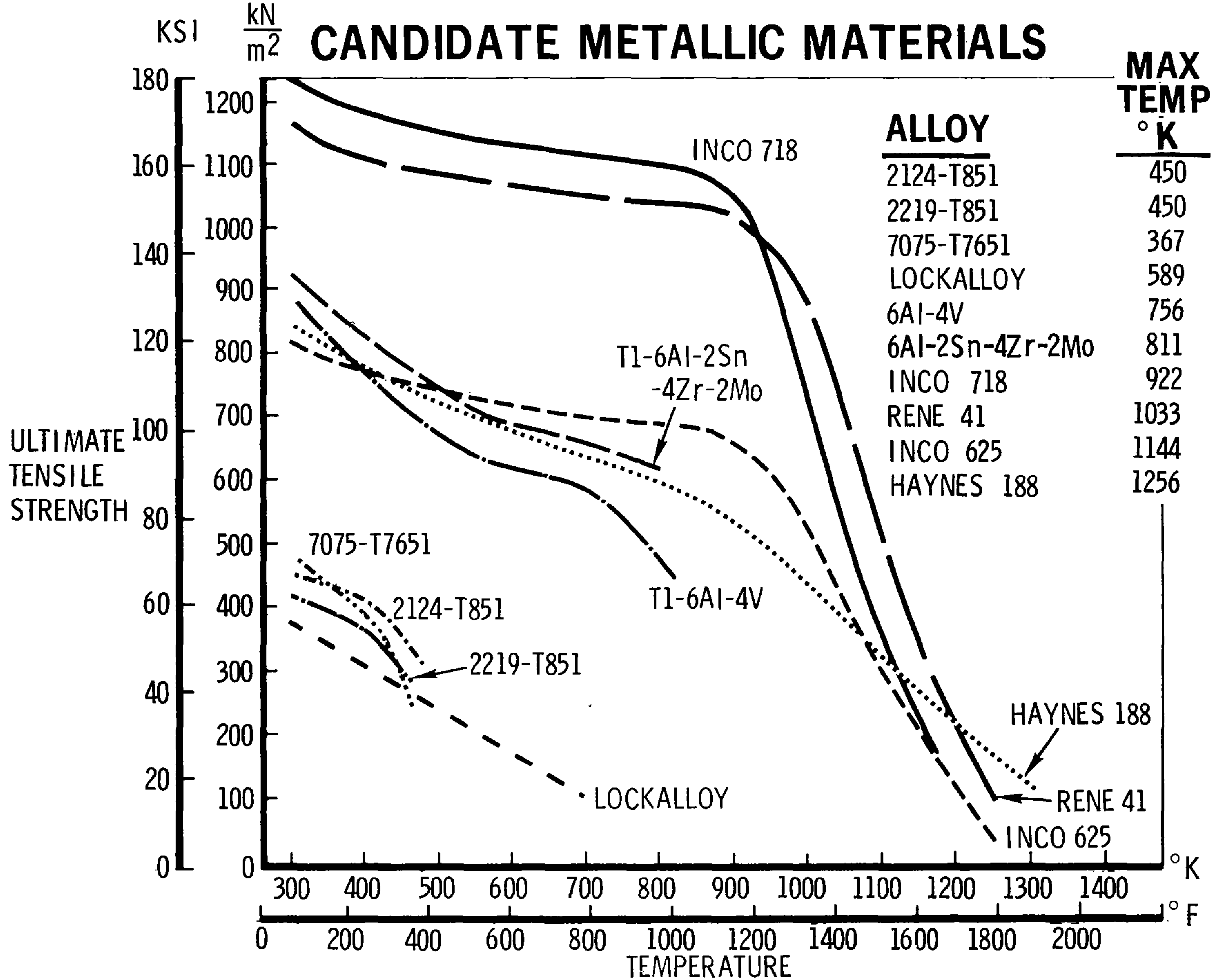
CANDIDATE METALLIC MATERIALS
KSI
kN/m2
ULTIMATE TENSILE STRENGTH
180
160
140
120
100
80
60
40
20
0
1200
1100
1000
900
800
700
600
500
400
300
200
100
0
TEMPERATURE
°K
300
400
500
600
700
800
900
1000
1100
1200
1300
1400
°F
0
200
400
600
800
1000
1200
1400
1600
1800
2000
INCO 718
T1-6Al-2Sn -4Zr-2Mo
T1-6Al-4V
7075-T7651
2124-T851
2219-T851
LOCKALLOY
HAYNES 188
RENE 41
INCO 625
ALLOY
2124-T851
2219-T851
7075-T7651
LOCKALLOY
6Al-4V
6Al-2Sn-4Zr-2Mo
INCO 718
RENE 41
INCO 625
HAYNES 188
MAX TEMP °K
450
450
367
589
756
811
922
1033
1144
1256

Figure 7

SPF/DB TITANIUM TRUSS CORE PANEL THERMAL IMPULSE TEST

(Figure 8)

The basic titanium design of the HYTID employs titanium truss core sandwich for fuselage thermal protection and for forward fuselage and wing primary skin structure. While several methods exist for producing titanium sandwich (resistance welding, brazing, roll diffusion bonding, organic bonding, etc), the method selected for the HYTID program is superplastic forming/concurrent diffusion bonding (SPF/DB). The SPF/DB expanded sandwich process again exhibits weight and cost savings over other methods of sandwich fabrication.

The performance of SPF/DB titanium truss core sandwich in a simulated hypersonic environment has been demonstrated by a radiant heating test. A Ti-6Al-4V truss core sandwich panel was subjected to quartz lamp heating on one side while simply supported at the panel corners in one test, and with additional supports at midedge locations in another. The panel was instrumented on both hot and cold sides to measure temperature gradients and thermal stresses developed, as well as in-plane expansion and normal bowing deflections. Results show that hot-side skin temperatures of 579°, 700°, and 811° K were attained in 100 seconds, corresponding to the temperatures that occur during a 40-second, Mach 6, $q = 47.9 \frac{kN}{m^2}$ flight at several representative locations on the vehicle. Incident heating rates are also shown. The results indicate that even with a $\Delta T = 443°$ K through the panel thickness, no structural damage occurred. Panel deflections were less than predicted, deformation was entirely elastic, and thermal stresses measured were within structural allowables for temperatures attained. Several additional SPF/DB Ti-6-4 truss core samples were subjected to extremely short-time thermal impulses, resulting in hot-side temperatures in excess of 1,370° K for the B-1 program. Except for loss of paint and slight surface contamination on the exposed side of the outer skin, no structural damage occurred. The panels were .15 x .15 x .0127m with .0025m core and .005m face sheets. Two coats of polyurethane paint over one coat of epoxy primer were applied to the outer skin surface as a topcoat treatment.

SPF/DB TITANIUM TRUSS CORE PANEL THERMAL IMPULSE TEST

• PANEL TEST SPF/DB Ti-6Al-4V

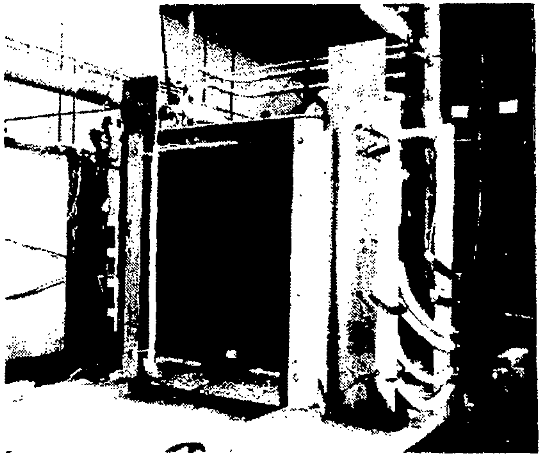

PANEL CONFIGURATION

• SIZE: .71 x .71 x .013 m
• CROSS SECTION:

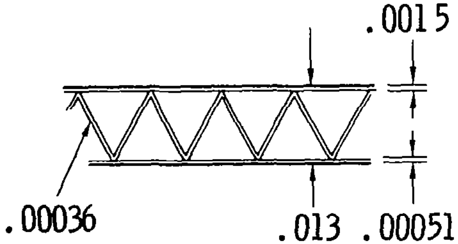

OBJECTIVE

• DEMONSTRATE STRUCTURAL INTEGRITY

• MEASURE
- TEMPERATURE GRADIENTS
- THERMAL STRESS
- IN-PLANE EXPANSION
- NORMAL BOWING DEFLECTIONS

RESULTS

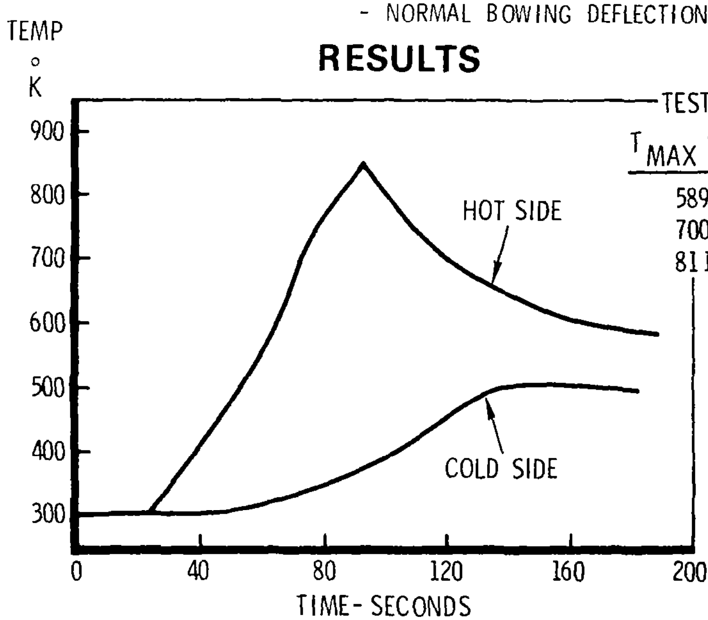

TESTS CONDUCTED

T_{MAX} (°K)	(kW/m^2)
589	69.2
700	78.3
811	80.5

• NO STRUCTURAL DAMAGE
• PANEL BOWING DEFLECTIONS LESS THAN PREDICTED; NO PERMANENT DEFORMATION
• MEASURED THERMAL STRESSES WITHIN STRUCTURAL ALLOWABLES FOR TEMPERATURES ATTAINED

Figure 8

PRIMARY FUSELAGE STRUCTURE

(Figure 9)

The HYTID structural concept uses the heat-sink philosophy and is tailored to produce a maximum surface temperature of 922° K on those areas subjected to stagnation temperatures (these areas to be fabricated from Inconel), 811° K on the titanium truss core skins, and 450° K on the exposed upper center-line aluminum structure.

The primary centerbody fuselage structure consists of 2219 aluminum monocoque construction that forms the integral tankage for both the NH_3 and the LOX propellants. Both tanks are mechanically fastened to a short intertank structure also made of aluminum. Enclosed within this intertank structure is the high-pressure helium supply contained with a torroidal titanium tank. In the lower quadrant of the same area, provisions have been made to stow the wheels of the main gear. An insulated pan is installed above the wheels to protect the tires from the extreme cold of the LOX, while the doors have an insulated layer to protect the tires from the hot structure. For the exposed portions of both tanks, the skin thickness is tailored to produce a maximum surface temperature of 450° K. The starting temperature is 233° K for the NH_3 tank and 89° K for the LOX tank. The temperature extremes from ambient first produce a .013-m shortening and then a .019-m growth that require the mechanization of a slip joint to accommodate these changes in length, yet permit torsional and shear loads to be transmitted. The lower portion of the aluminum tank is protected from the higher heating with a secondary structure that consists of SPF/DB titanium truss core sandwich skins mounted on SPF/DB titanium frames that are attached with clevis-type pins to accommodate the differential thermal growth.

Wherever practical, mechanical fasteners will be eliminated and either TIG or plasma arc welding will be employed as the principal method of assembly, resulting in a considerable cost and weight savings. Welding is compatible with the use of titanium SPF/DB components, as they are used in the "as-formed" or annealed condition.

PRIMARY FUSELAGE STRUCTURE

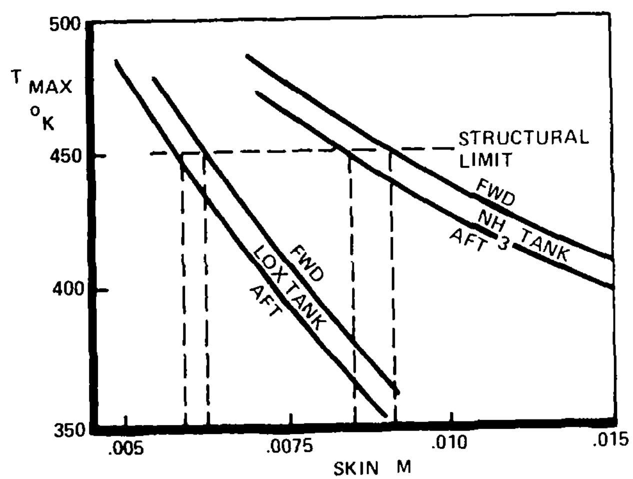

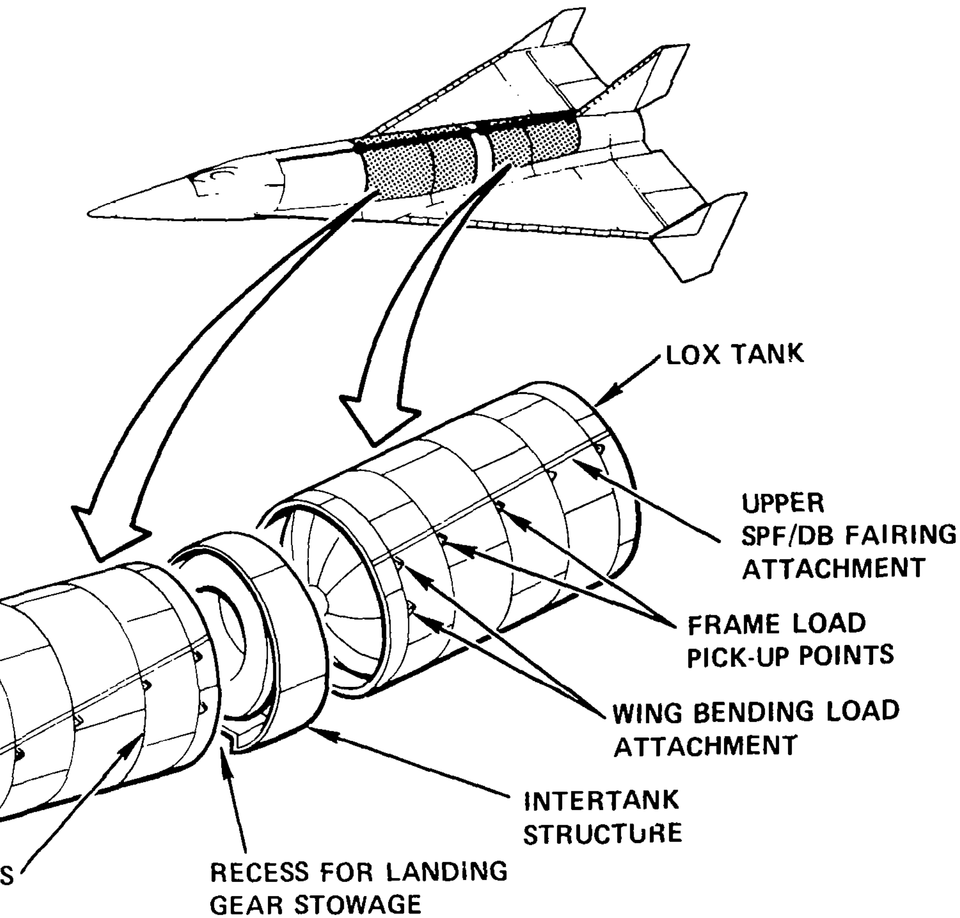

- ALUMINUM SEMI-MONOCOQUE CONSTRUCTION
- INTERNAL RING FRAMES FOR STIFFNESS & LOAD DISTRIBUTION
- TANKS PARTITIONED TO CONTROL C.G. TRAVEL

Figure 9

SECONDARY FUSELAGE STRUCTURE

(Figure 10)

This figure shows typical sections in the centerbody of the fuselage. A typical frame is shown where the wing attaches to an internal tank ring frame by means of two external lugs. The lower portion of the frame attaches to the wing at the top and to similar ring frame lugs at the lower part of the frame. The clevis pin mounting and frame bowing permit thermal expansion and contraction to take place, as required. The main gear trunnion loads are split between two frames. The loads from each external frame are transferred to the inner ring frame by means of axial load struts. This concept has also been used on the Space Shuttle and provides a unique method to transfer loads and still permit thermal expansion to take place.

SECONDARY FUSELAGE STRUCTURE

PRIMARY INTERFACE

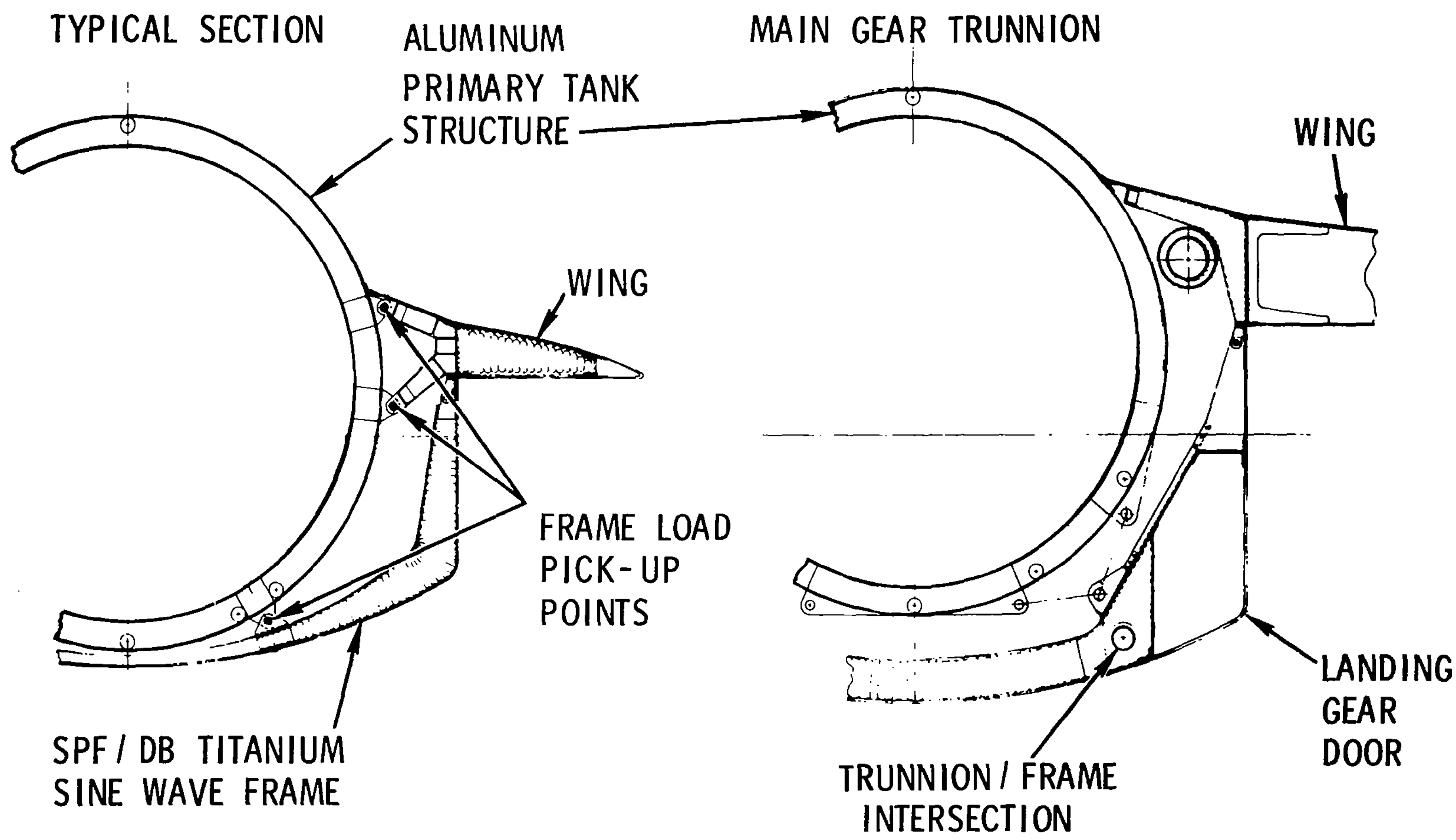

• SPF / DB TITANIUM TRUSS CORE SANDWICH FOR TPS & SKINS

Figure 10

WING STRUCTURE

(Figure 11)

The wing is a multispar design employing a root rib and a tip rib. The leading edge is removable back to the front spar and employs a segmented sintered Inconel extreme leading edge to provide the heat sink required for the stagnation temperatures. With the exception of the sintered Inconel leading edge, all skin panels will be SPF/DB titanium truss core. The multiple spars will be SPF/DB titanium and will employ a sine wave web to minimize thermal stresses. Intercostal-type ribs are employed in the area of the elevon actuators, and the skin panels are removable to accommodate installation and servicing of the actuators. All other skin panels will be TIG or plasma arc welded to the spar caps.

Wing panel attachment to the fuselage is accomplished through the use of SPF/DB cantilever fittings. Two main spars in the area of the elevon actuators are hard mounted to the afterbody carry-through structure. The remaining four cantilever fittings are designed to accommodate the thermal growth differential between the attach structure and the wing, with the ability to transfer both shear and moment.

The principal structural design criteria are the thermal stresses to which the aircraft will be subjected. This results in extremely low stress levels from the applied aerodynamic loads. To minimize differential thermal stresses, the ΔT across the skin panels has been limited to 332° K, although in preliminary testing of a truss core panel fabricated from Ti-6-4 it was subjected to a surface temperature of 867° K, with the resulting ΔT being 500° K. No permanent damage was observed as a result of these extremes.

WING STRUCTURE

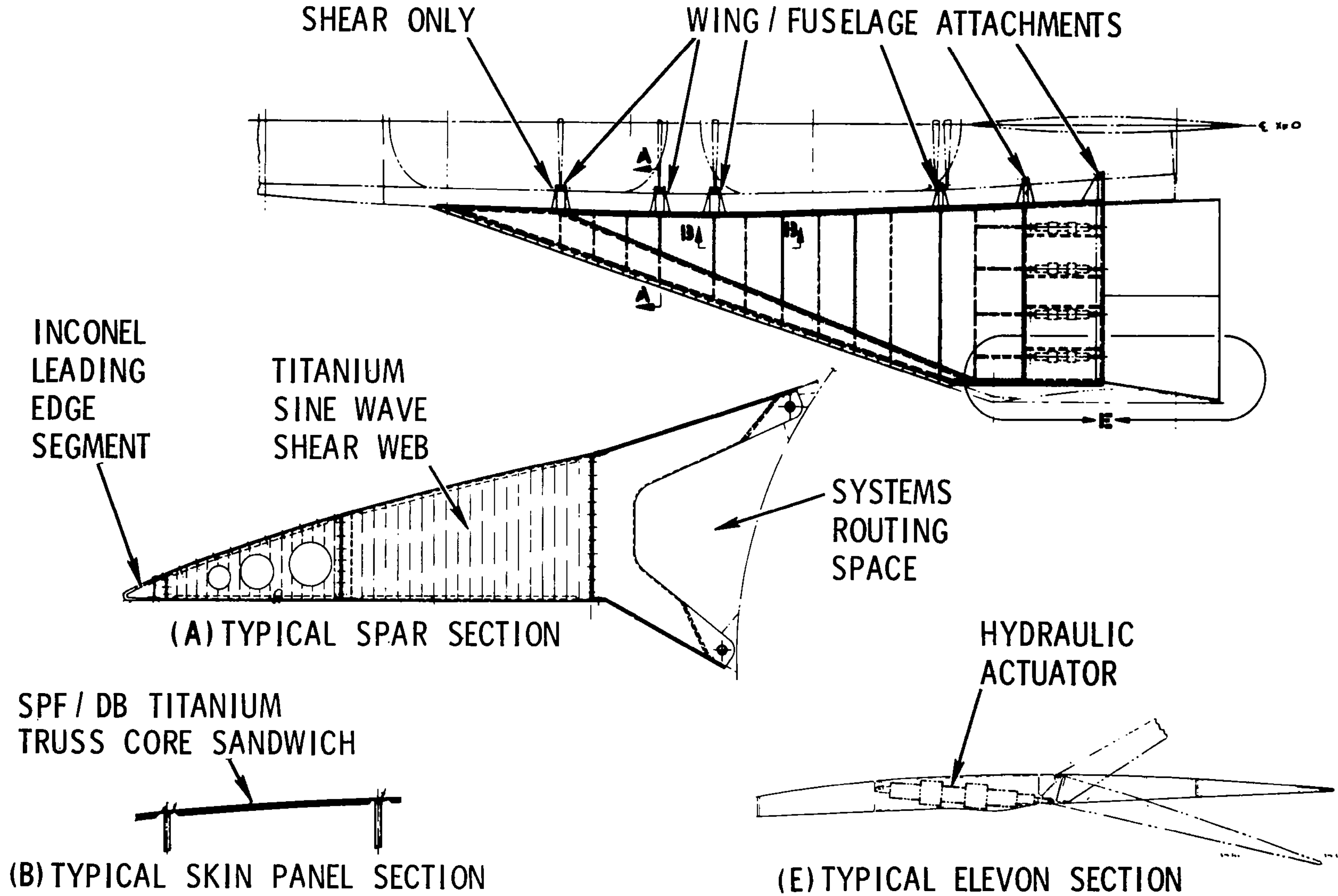

Figure 11

GROWTH POTENTIAL/FLEXIBILITY

(Figure 12)

The selected structural approach for constructing HYTID should permit an excellent growth potential capability and a broad experimental flexibility. Because of the selected method of construction, HYTID can easily be modified to incorporate nose- and wingtip-mounted reaction jets that will permit very-high-altitude ballistic trajectories to be flown. The large base area and internal space provided in the aft engine compartment will enable alternate engines or uprated versions of the YLR-99 to be easily incorporated without affecting the external lines of the vehicle. External tanks can be provided to improve the boost performance so that a Mach 8 mission can be achieved with the capability of maintaining 20 seconds of cruise duration. The external skin surfaces can be protected from this hotter thermal mission with various choices of externally added insulative TPS such as the Martin 220M, ESA-3560, or ESA-5500. Since most of the external skin of HYTID is aluminum plate or SPF/DB titanium truss core sandwich, it will make an ideal mounting surface for any of the proposed insulative TPS materials considered. The payload bay, wing panels, and vertical tails are of modular construction and can be readily replaced with alternate concepts to validate new approaches under actual flight environmental conditions.

GROWTH POTENTIAL/FLEXIBILITY

MACH 8.0, $q = 47.9 \frac{kN}{m^2}$ 20 SEC CRUISE

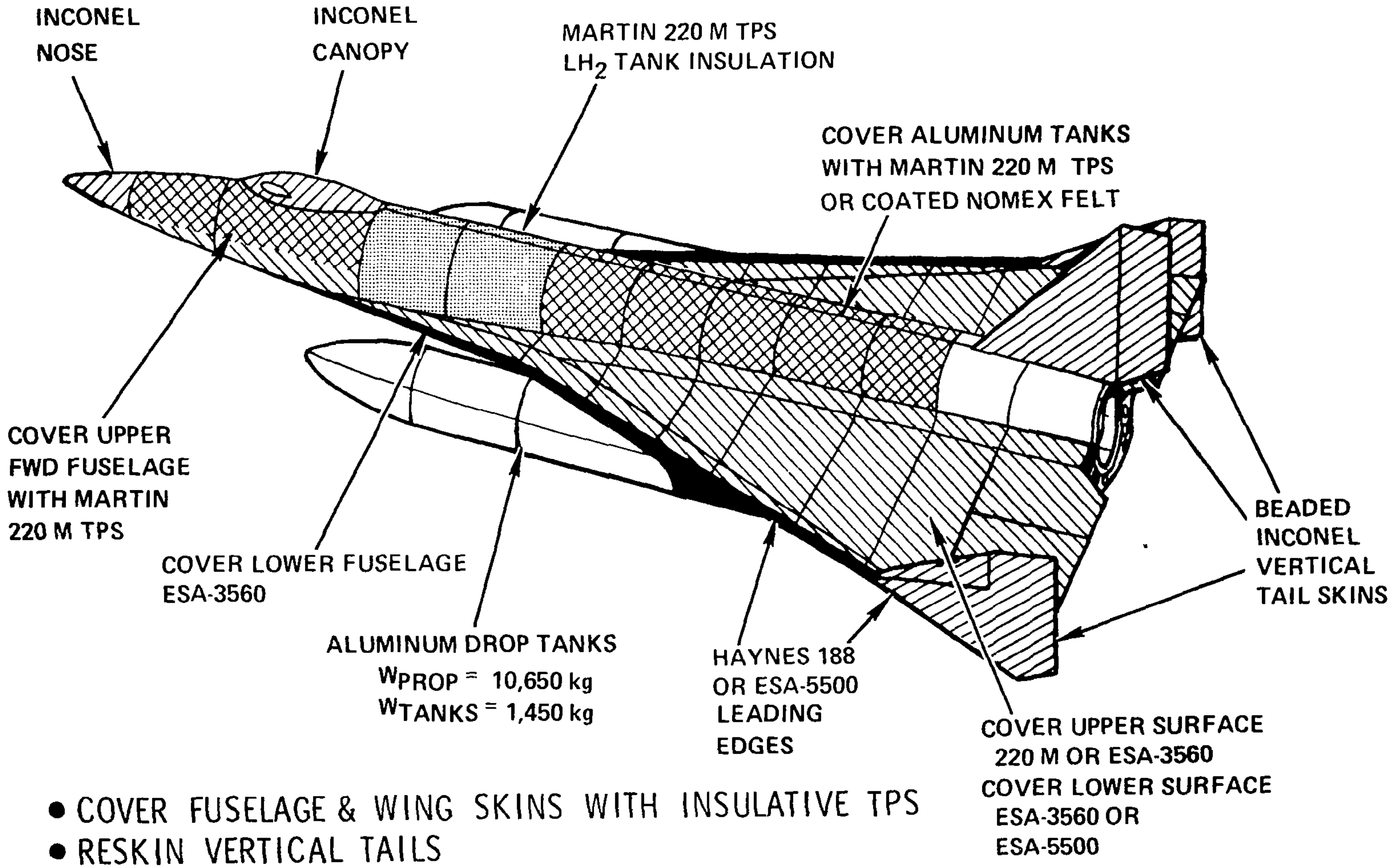

- COVER FUSELAGE & WING SKINS WITH INSULATIVE TPS
- RESKIN VERTICAL TAILS
- ADD ALUMINUM DROP TANKS

Figure 12

CONCLUDING REMARKS

The goal of HYTID is to provide a cost-effective hypersonic vehicle constructed of near-state-of-the-art systems and structure with sufficient margins to assure no vehicle flight development problems, and to permit concentration of flight operations on hypersonic research with a broad series of experiments carried in a dedicated payload bay or on the exposed surface of the lower aft fuselage.

REFERENCES

1. Kirkham, F. S., Jones, R. A., Buck, M. L., and Zima, R. P., "Joint USAF/NASA Hypersonic Research Aircraft Study," AIAA Paper, 1975

2. Hearth, D. P. and Preyss, Col. A. E., "Hypersonic Technology - Approach to an Expanded Program," Astronautics and Aeronautics, December 1976

3. Williams, E. T. and Coakley, R. C., "Costing Methodology for High Speed Research Airplanes Including Parametric Cost Trend Evaluations," NASA CR-132658, January 1975

4. Combs, H. G., et al, "Configuration Development Study of the X-24C Hypersonic Research Airplane - Phase I," NASA CR-145032, September 1976

5. Combs, H. G., et al, "Configuration Development Study of the X-24C Hypersonic Research Airplane - Phase III," NASA CR-145103, January 1977

6. Combs, H. G., et al, "Configuration Development Study of the X-24C Hypersonic Research Airplane - Phase II," NASA CR-145074, January 1977

7. Weidner, J. P., Small, W. J., and Penland, J. A., "Scramjet Integration on Hypersonic Research Airplane Concepts," Journal of Aircraft, May 1977

DESIGN AND FABRICATION OF A SUPER ALLOY THERMAL PROTECTION SYSTEM

A. Varisco, W. Wolter, and P. Bell
Grumman Aerospace Corp.

INTRODUCTION

A program was undertaken to develop a lightweight, efficient, metallic thermal protection system (TPS) applicable to future shuttle-type reentry vehicles, advanced space transports, and hypersonic cruise vehicles. Technical requirements and criteria were derived generally from the space shuttle.

Grumman's corrugation-stiffened TPS design was used as the baseline starting point. The system was updated and modified to incorporate the latest technology developments and design criteria emphasizing minimum weight for the overall system.

One basic design concept was developed during the program, and this concept was optimized for operation at two different temperatures using two different materials: René 41, a nickel-base alloy for use to 1144 K (1600°F), and Haynes 188, a cobalt-base alloy for use to 1255 K (1800°F). Significant weight reductions were achieved over the baseline system.

Two extensively instrumented, full-scale test panels were fabricated, one from each material. Each panel represented one and one-half bays and included an expansion joint. Both test articles were delivered to NASA/Langley for evaluation of cyclic life characteristics in the Langley Thermal Protection System Test Facility, which is capable of test conditions representative of entry flight.

The results of this program are reported in "Design and Fabrication of Metallic Thermal Protection Systems for Aerospace Vehicles," NASA CR 145313.

18

TYPICAL TPS WEIGHT
(Figure 1)

Baseline metallic TPS weight for corrugation-stiffened beaded skin design using low density fiber insulation is shown in the graph. These weights include all panel hardware and the insulation system. The design trajectory is for a high cross range shuttle orbiter vehicle. The insulation is sized to prevent a 0.5-cm (0.2-inch) thick aluminum substructure from exceeding 450 K (350° F) including soak back after landing. The temperature at the start of entry was assumed to be 311 K (100° F).

Also shown is the nominal weight for a reusable surface insulation (RSI) TPS of the type used on the present shuttle orbiter.

The objective of this program was to optimize the design of the metallic TPS in the range of 811 K (1000°F) to 1255 K (1800°F). A typical area of application is the lower flat surfaces of a shuttle orbiter as shown in the figure.

STATE-OF THE ART TPS UNIT WEIGHT vs MAX ENTRY TEMPERATURE

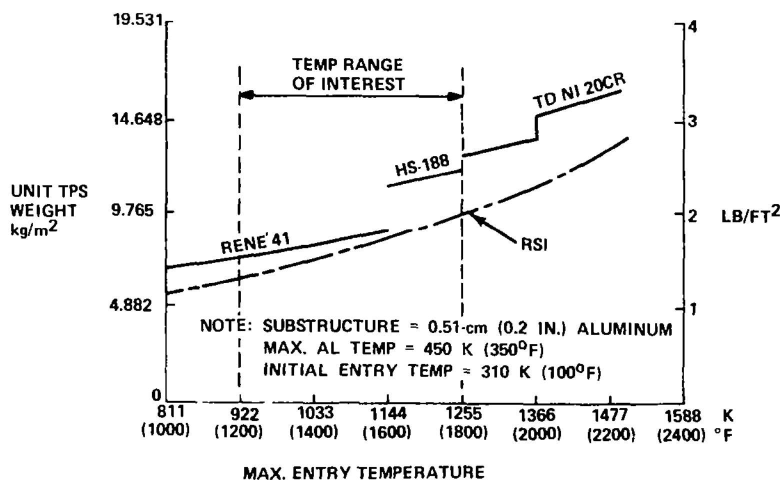

TYPICAL AREA OF APPLICATION FOR METALLIC TPS

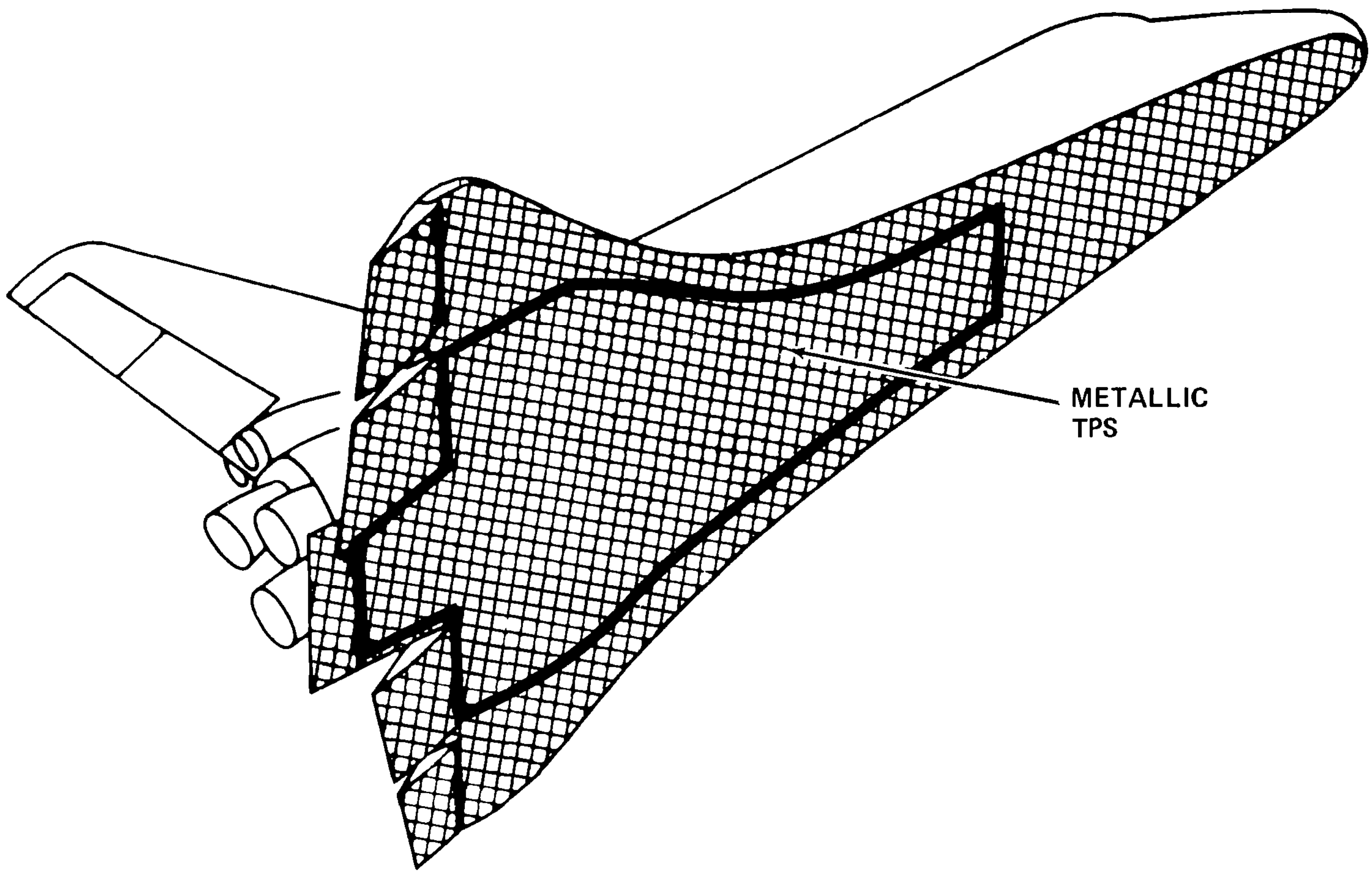

Figure 1.- Concluded

DESIGN CRITERIA AND GOALS
(Figure 2)

In addition to the loading and thermal criteria listed in the accompanying table, the test specimen was designed to meet the following goals:

- Reuse capability of 100 missions
- Minimum leakage at expansion joints
- Simple removal of panels
- Surface emittance of 0.80 or higher
- Moisture absorption - In contrast to the current orbiter design, no special requirements were included in this design to control TPS moisture absorption. The most significant concern in relation to water absorption for fibrous insulation is the associated increase in mass. It was assumed that during ground storage, prelaunch, and ferrying the vehicle will be protected from exposure to direct water impingement and high humidity conditions by ground support equipment. Immediately after entry and up to one hour after landing, the insulation will not absorb moisture because the residual heat stored in it during entry is sufficient to dry the insulation. This built-in protection would be effective in situations short of heavy rainstorms. If the vehicle is inadvertently exposed to rain or high-humidity condensing cycles, a drying cycle will be required before vehicle launch.
- Surface contour - The allowable panel surface normal permanent deflection between supports was $y = 0.254 + 0.01L$, where y is maximum deflection in cm and L is panel span. This requirement will limit the total amount of creep deformation over 100 mission cycles.
- Surface roughness - To avoid uncontrolled ingestion of high-energy boundary-layer air in the panel expansion joints, all such potential gaps were aft facing in relation to the general flow direction. Also, the height of surface steps, beads, and protruding fasteners will be such that local interference-heating effects will not be excessive.

LOWER SURFACE (MID-FUSELAGE) DESIGN CONDITIONS

CONDITION		
CONTINUOUS SURFACE PRESS. AT T_{MAX} (ENTRY)	862-2490 Pa	18-52 PSF
MAX MANEUVER SURFACE PRESS. AT T_{MAX} (ENTRY)	8618 Pa	180 PSF
MAX TEMP LEVEL DURING ENTRY – HAYNES	1255 K	1800°F
MAX TEMP LEVEL DURING ENTRY – RENÉ	1144 K	1600°F
MAX DYNAMIC PRESS. – ENTRY	11 490 Pa	240 PSF
MAX DYNAMIC PRESS. – BOOST	33 516 Pa	700 PSF
MAX SURFACE PRESS. DIFFERENTIAL – BOOST	+13 885 Pa	+290 PSF
	-20 588 Pa	-430 PSF
MAX SURFACE PRESS. DIFFERENTIAL – POSTENTRY (SUBSONIC FLIGHT)	+16 758 Pa -12 448 Pa	+350 PSF -260 PSF
ACOUSTIC ENVIRONMENT		
LIFTOFF		
• OVERALL SOUND PRESS. LEVEL	161 db	
• CRITICAL 1/3-OCTAVE BAND LEVEL	150 db	
MAX $q\alpha$ (ASCENT)		
• OVERALL SOUND PRESS. LEVEL	158 db	
• CRITICAL 1/3-OCTAVE BAND LEVEL	146 db	
ALLOWABLE PERMANENT DEFLECTION BETWEEN PANEL SUPPORTS	δ = 0.254 + .01L = CM (δ = 0.1 + .01L = INCHES)	
FACTORS OF SAFETY		
MECHANICAL LOADS	1.0 LIMIT 1.15 YIELD 1.4 ULTIMATE	
THERMAL EFFECTS	1.0 CREEP DEFLECTION 1.0 LIMIT 1.4 ULTIMATE	
MAX PRIMARY STRUCTURE TEMP RISE ($T_{MAX} - T_{INITIAL}$ = 350°F – 120 = 230°F)	230°F 128°C	
FLUTTER	AFFDL-TR-67-140	

Figure 2

THERMAL CONDITIONS
(Figure 3)

The primary thermal requirement for the TPS is entry heating from orbit, with a 100-mission reusability goal. The space shuttle orbiter entry trajectory was used as a design requirement for this program. The specific area of concern for the test specimen is the 1144-1255 K (1600 to 1800°F) temperature range. The surface-temperature history is shown in the accompanying figure.

The thermal condition which determines the insulating requirement for the TPS is that in which the maximum TPS/primary structure temperature exists at the beginning of entry. The space shuttle mission, which is a launch into orbit and return to the launch site within a single revolution, creates this condition. The temperature on the lower surface structure at the start of entry for this mission is 322 K (120°F).

The insulation was sized to limit the temperature of the primary structure to a maximum of 450 K (350°F) during entry and subsequent postlanding soak-out. The primary structure had the equivalent thermal heat-sink capacity of a 0.51-cm (0.2-in.) thick aluminum plate with an adiabatic back face.

Another thermal condition of significance is that which produces the maximum temperature gradients in the TPS/structure. Studies have shown that this condition is one in which the minimum TPS/structure temperature exists at the start of entry. The minimum starting temperature assumed is 202.6 K (-95° F).

DIFFERENTIAL PRESSURE LOADING

Two levels of static pressure loadings were considered in the design of the TPS. The first is maximum maneuver-load conditions, which are intermittent and of short duration. The static strength of the panel must be sufficient to withstand these loads. The maximum maneuver load factor is 2.5g during entry and subsonic flight. However, there is insufficient aerodynamic force to produce 2.5g maneuver until about 1200 sec after the start of entry, which is near the end of maximum heating. The maximum maneuver line on the graph represents the maximum transient pressure differential on the lower surface.

The second type of static pressure loading considered is the continuous-loading level at high temperature, which was used to determine the amount of creep that occurs in the panel. This is the equilibrium flight pressure loading line shown on the graph.

SURFACE TEMPERATURE AND PRESSURE PROFILE

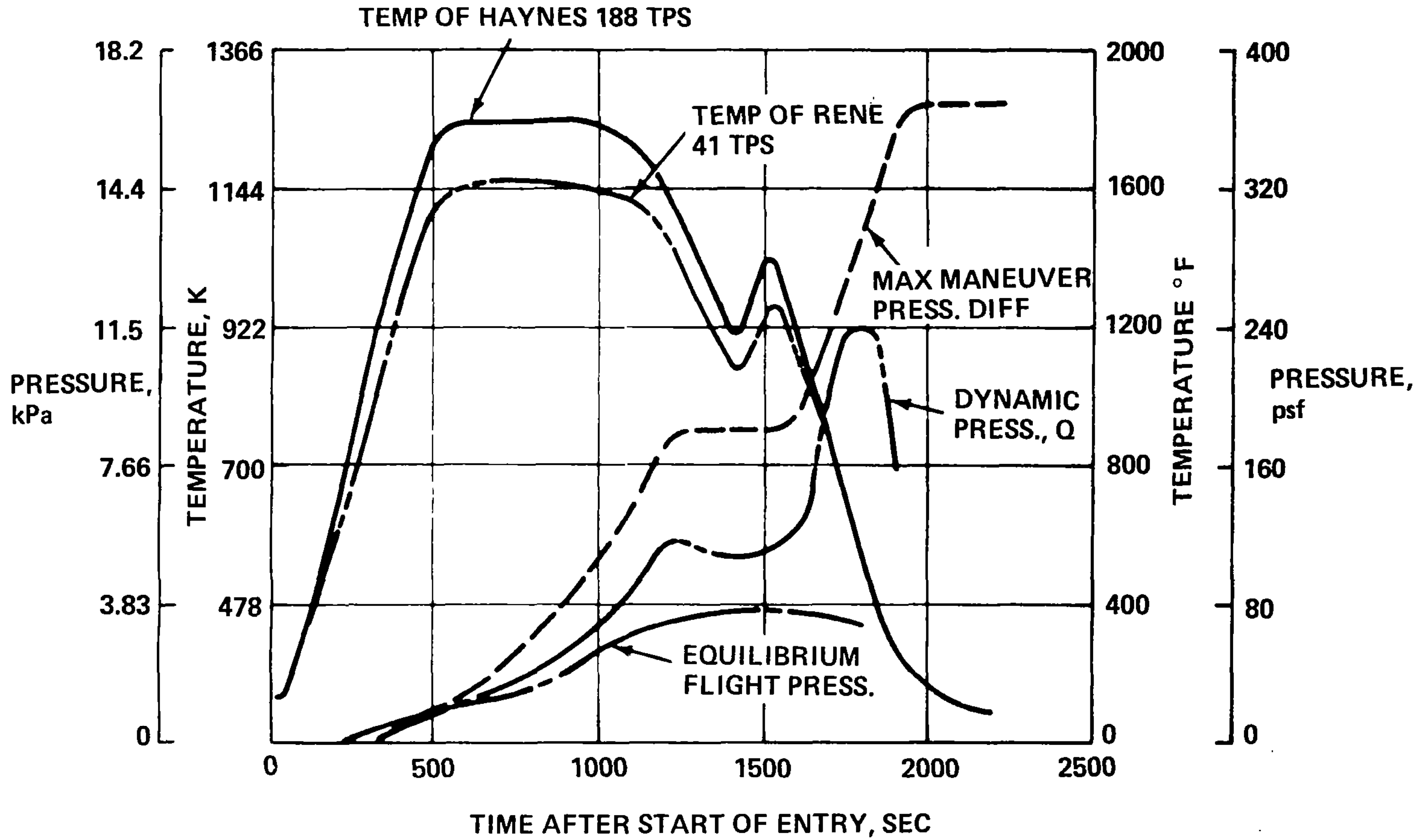

Figure 3

DESIGN CONCEPT
(Figure 4)

The TPS considered in this program is a shingled, radiative system. Heat-rejection rate, therefore, depends on the fourth power of the surface temperature, and becomes large if high temperatures can be tolerated. Thus, the intensity of heating which can be accommodated is limited by the temperature capability of the panel material.

An existing Grumman-developed TPS, using Haynes 25, designed for operation at 1255 K (1800°F) was selected as a baseline design in the program. The concept, shown in the accompanying figure, consists of a corrugation-stiffened beaded skin, insulation, and beaded support ribs. The corrugations are welded to the beaded skin to form an efficient panel with high longitudinal bending stiffness. Applied surface-pressure loading is transferred by beam action to the rib supports. The supports are located on 51-cm (20.0-in.) centers, with an expansion joint every 102 cm (40.0 in.) to permit longitudinal growth of the panel. Although the panel is considered to be 102 cm (40.0 in.) long, it is fixed at the center support so that a 51-cm (20.0-in.) span expands in each direction. The center support rib includes a drag support to react longitudinal (drag) loads. The panel lateral expansion is absorbed by flexing of the beads in the skin. The corrugations have little effective stiffness in the lateral direction.

The advantage of this concept is that the panels are not size-limited in the lateral direction, and an expansion joint is required only in the longitudinal direction. The design also eliminates forward-facing steps and incorporates a simple splice of adjacent panels, thus facilitating panel removal and inspection.

TPS DESIGN CONCEPT

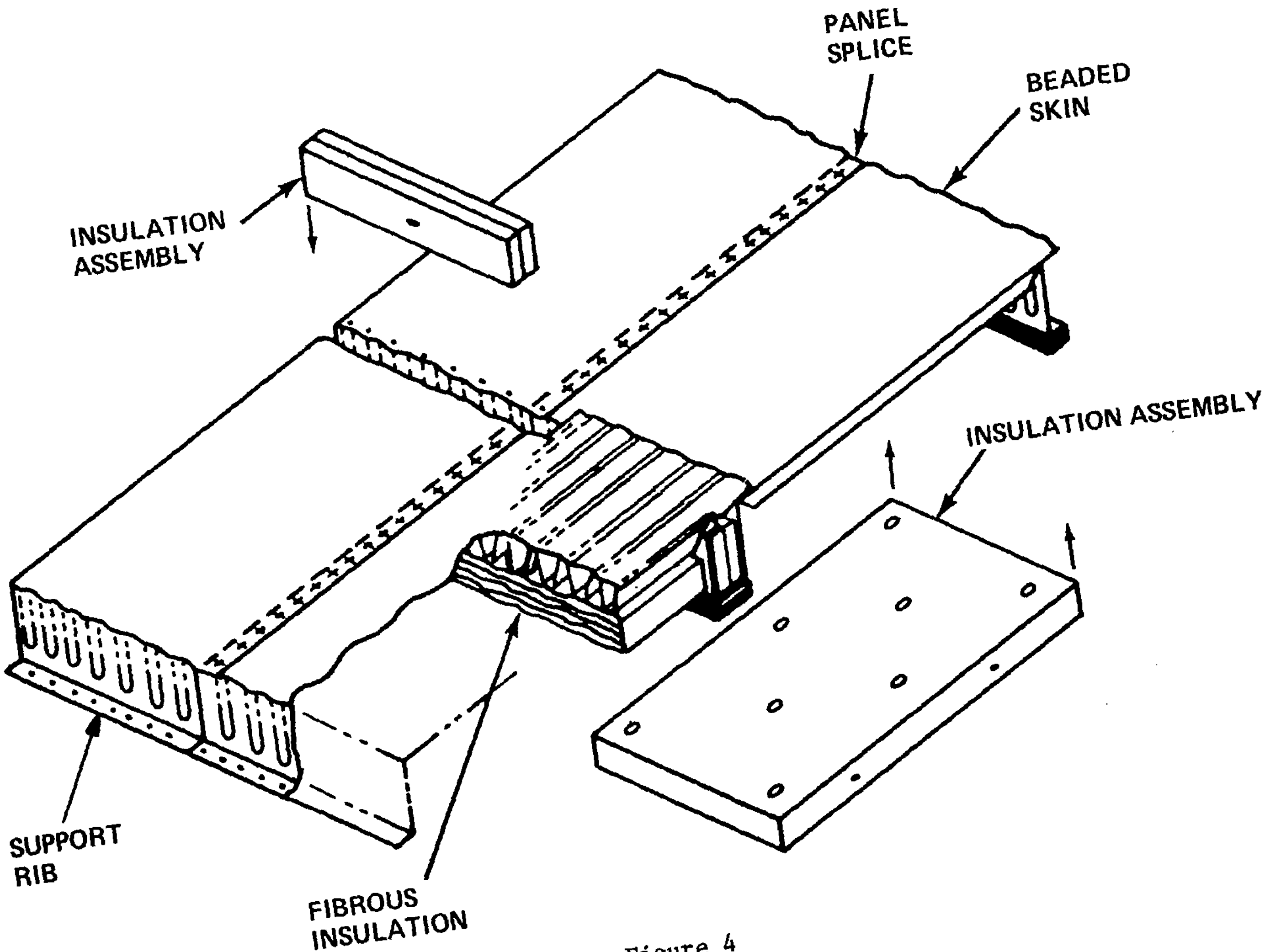

Figure 4

CANDIDATE MATERIALS
(Figure 5)

Grumman has performed studies to determine which of the commercially available high-temperature metal alloys appear most attractive for use in the surface panel and support structure. Consideration was given to the availability, fabricability, oxidation resistance, thermal stability at peak temperature, and availability of sufficient mechanical properties data at temperature. The candidate alloys were Ti-6Al-2Sn-4Zn-2Mo, duplex annealed; Rene' 41 solution heat treated and aged at 1172 K (1650°F); Haynes 25 or 188, solution heat treated at 1422 K (2100°F); Inconel 718, heat treated to 1228 K (1750°F); TD Ni-20Cr; and Cb 752 coated with R512C. A conceptual panel design was used as the focal point of a design analysis to determine comparative weights of metal panels utilizing the candidate alloys over a temperature range from 589 K (600°F) to 1588 K (2400°F). The pressure load during entry at the maximum temperature was varied as a parameter.

The results of this comparison are shown in the accompanying figure where the temperature and loading regime of each least weight panel are shown. The following material application temperature ranges have been chosen:

- Rene' 41 — 811 to 1144 K (1000 to 1600°F)
- HS 25 or 188 — 1144 to 1255 K (1600 to 1800°F)
- TD Ni Cr — 1255 to 1477 K (1800 to 2200°F)

Inconel 718 was eliminated because the ranges of applicability and weight advantage were too small.

RFGIMES OF MATERIAL CHOICE FOR LIGHTEST METALLIC HEAT SHIELDS

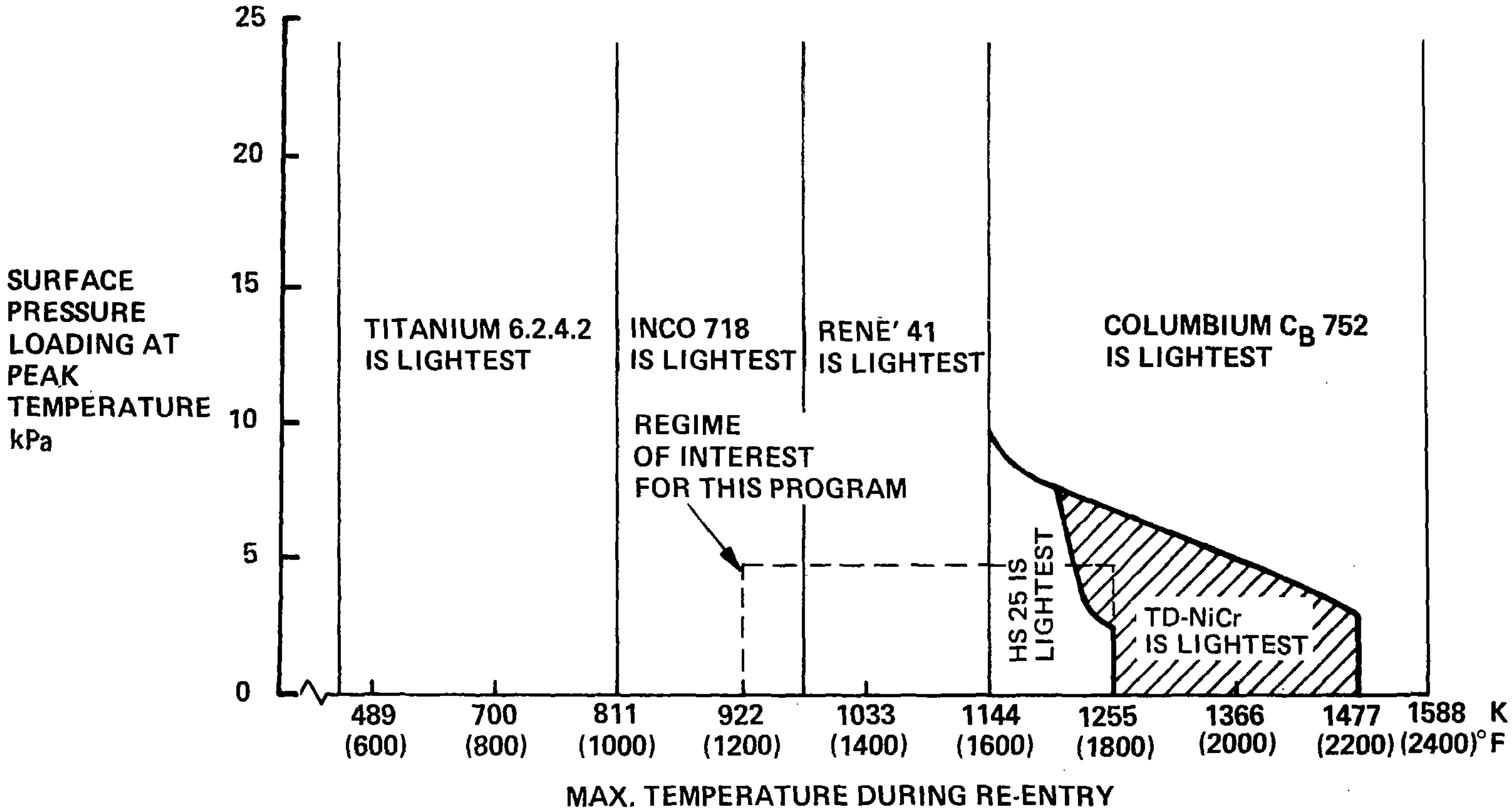

Figure 5

MATERIAL PROPERTIES
(Figure 6)

HAYNES 188

Haynes 188 alloy is a cobalt-base alloy possessing excellent high-temperature strength and oxidation resistance to 1367 K (2000°F). Its excellent oxidation resistance results from minute additions of lanthanum to the alloy system. The lanthanum modifies the protective oxide scale in such a manner that the oxide becomes extremely tenacious and impervious to diffusion when exposed to temperatures through 1367 K (2000°F). All properties which follow for Haynes 188 are for the solution-heat-treated condition - heating to 1450 K (2150°F) followed by either a rapid air-cool or water quench.

RENE′ 41

Rene′41 is a vacuum-melted, nickel-base alloy possessing exceptionally high strength in the temperature range of 920-1255 K (1200-1800°F). It is a precipitation-hardening alloy, and its strength is developed by various solutioning and aging heat treatments. All properties which follow for Rene′41 are for forging at 1450 K (2150°F), age hardening at 1172 K (1650°F) for 4 hr, and air cooling.

MECHANICAL PROPERTIES

HAYNES 188

PROPERTY	ALLOWABLE STRESS AT TEMPERATURE			
	294 K	70° F	1255 K	1800° F
F_{tu}*	896 MPa	130 ksi	145 MPa	21 ksi
F_{ty}*	379 MPa	55 ksi	76 MPa	11 ksi
F_{cy}*	379 MPa	55 ksi	76 MPa	11 ksi
E*	234 GPa	34 000 ksi	94.4 GPa	13 700 ksi

RENE' 41

PROPERTY	ALLOWABLE STRESS AT TEMPERATURE			
	249 K	70° F	1144 K	1600° F
F_{tu}*	1158 MPA	168 ksi	603 MPa	87.4 ksi
F_{ty}*	876 MPa	127 ksi	524 MPa	76.0 ksi
F_{cy}*	931 MPa	135 ksi	400 MPa	58.0 ksi
E*	218 GPa	31 600 ksi	122 GPa	17 700 ksi

*F_{tu}, ultimate tensile strength; F_{ty}, 0.2- percent tensile yield stress;

F_{cy}, 0.2- percent compression yield strength; E, Young's modulus

Figure 6

DESIGN ALLOWANCE FOR OXIDATION LOSS
(Figure 7)

ALLOWANCE REQUIRED FOR EMITTANCE TREATMENT

The emittance requirements were to be fulfilled by a preoxidation treatment during final stages of component fabrication. An oxide film thickness of 0.00025 cm (.0001 in.) was sufficient to achieve the required value.

ALLOWANCE REQUIRED FOR OXIDATION LOSSES

Oxidation under entry conditions is dependent on peak temperature, number of exposure cycles, atmospheric pressure at peak temperature, and airflow rate. Two experimental oxidation studies have been conducted on HS-188 under conditions that simulate space shuttle entry conditions.

The first of these activities, at NASA Lewis, involved the cyclic self-resistance heating of sheet specimens in a reduced-pressure air environment. The thermal cycle involved heating to 1477 K (2200°F), holding for 30 min, and then cooling to room temperature. The specimens underwent 100 thermal cycles. The test atmosphere, air, was maintained at a pressure of 1333 Pa (10 torr). The test specimens underwent a metal thickness loss of 0.00089 cm (0.00035 in.) per side.

The second effort in this area, at NASA Lewis and NASA Ames, utilized an arc-jet to simulate space shuttle entry conditions. Sheet specimens were inserted into a Mach 6 test stream for 30 min and then allowed to cool. The test temperature was 1378 K (2020°F), surface pressure was 1013 Pa (7.6 torr). After 50 30-min cycles, the test specimens had lost 0.0019 cm (0.00075 in.) of thickness per side.

An oxidation loss of 0.0010 cm (0.0004 in.) was used for the external surfaces of the TPS panel.

OXIDATION RESISTANCE IN DRY AIR, 100-HR TEST

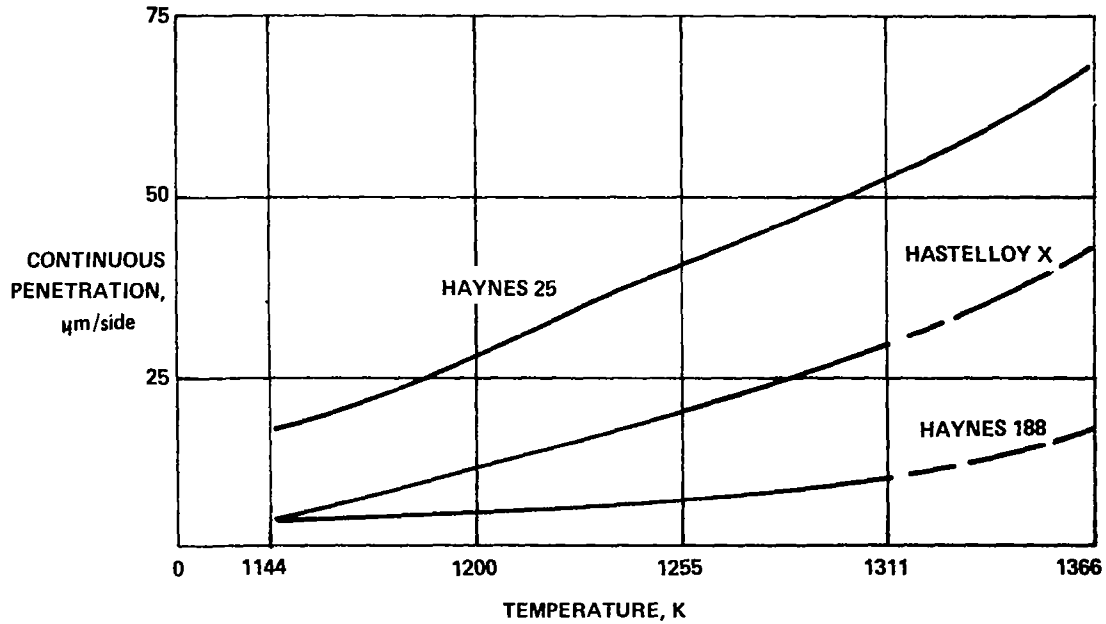

TOTAL ALLOWANCE REQUIRED FOR EMITTANCE & OXIDATION

• EXTERNAL AIR-PASSAGE SURFACE (BEADED SKIN)		
- EMITTANCE ALLOWANCE (0.00025 cm/SIDE):	0.00051 cm	0.0002 in.
- OXIDATION ALLOWANCE (0.0010 cm, EXTERIOR):	0.00100	0.0004
- TOTAL ALLOWANCE:	0.00151 cm	0.0006 in.
• INTERNAL SURFACES (CORRUGATION)		
- EMITTANCE ALLOWANCE (0.00025 cm/SIDE):	0.00051 cm	0.0002 in.

Figure 7

SURFACE PANEL CROSS SECTION SELECTION
(Figure 8)

Several surface panel configurations were considered, including trapezoidal and semicircular corrugation-stiffened skin, double-faced corrugation, integrally stiffened plate, and honeycomb sandwich. Double-faced corrugations and honeycomb sandwich designs were eliminated due to thermal stresses induced by the temperature gradient from outer to inner face sheets. Integrally stiffened plate designs were eliminated because this approach is not mass-competitive. Another disadvantage of those designs which have flat skins is the requirement for expansion joints at four edges. The semicircular corrugation was eliminated because it is not as mass-efficient as the trapezoid. Examination of the baseline design indicated that the corrugation sidewalls were operating at low stress levels. This resulted from the use of one material thickness for the entire corrugation.

To minimize corrugation mass, two approaches were considered: first, the use of one thickness as before but with the addition of lighting holes; and second, the use of chem-milling. A weight estimate showed the holes would not significantly reduce mass. Moreover, punching holes in thin-gage material and the subsequent deburring would be very costly. Chem-milling, however, permitted the maximum elimination of unnecessary material. Moreover, since the skin/corrugations are sized to meet the maximum bending moment at the span center, additional weight could be saved by profiling the chem-mill at the span edges. Additionally, with the use of chem-milling, the thickness of each element of the cross section could be permitted to vary for maximum efficiency. It was decided, therefore, to chem-mill the test specimen.

SURFACE PANEL CROSS SECTION SELECTION

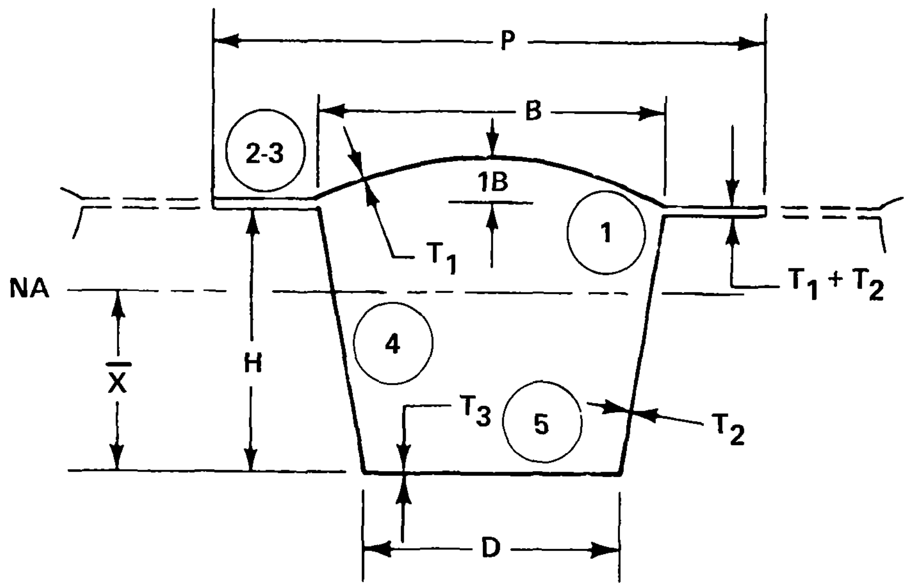

Figure 8

PANEL OPTIMIZATION CONSIDERATIONS
(Figure 9)

It is generally accepted that for a nonredundant structure such as these panels, the least-mass design is obtained when the applied stress in each element is equal to the allowable stress for as many of the design conditions as possible. For example, element 1 of the section definition shown should be buckling-critical under maximum pressure, creep-critical under maximum temperature, flutter-critical under the design dynamic pressure, and yield-critical under conditions of lateral thermal expansion. It is, however, usually not possible to satisfy all conditions.

Additionally, design constraints, such as minimum-gage considerations, may constrain the optimum design even further. The accompanying figure illustrates such a situation. It also shows that if the thickness and flat-width design constraints were neglected, the least-mass section occurs when the neutral axis is at the midheight of the section. In this case, both the upper and lower fibers would be creep-critical, as well as buckling-critical, for the appropriate conditions. Addition of the design constraints, however, increases the mass by a significant amount. For example, by modifying the neutral-axis location to 55% of the total section height (central curve), the section is less efficient from a strength standpoint than the previous design, but when the design constraints are considered, the acceptable section is lighter than its companion in the first case.

PANEL OPTIMIZATION CONSIDERATIONS

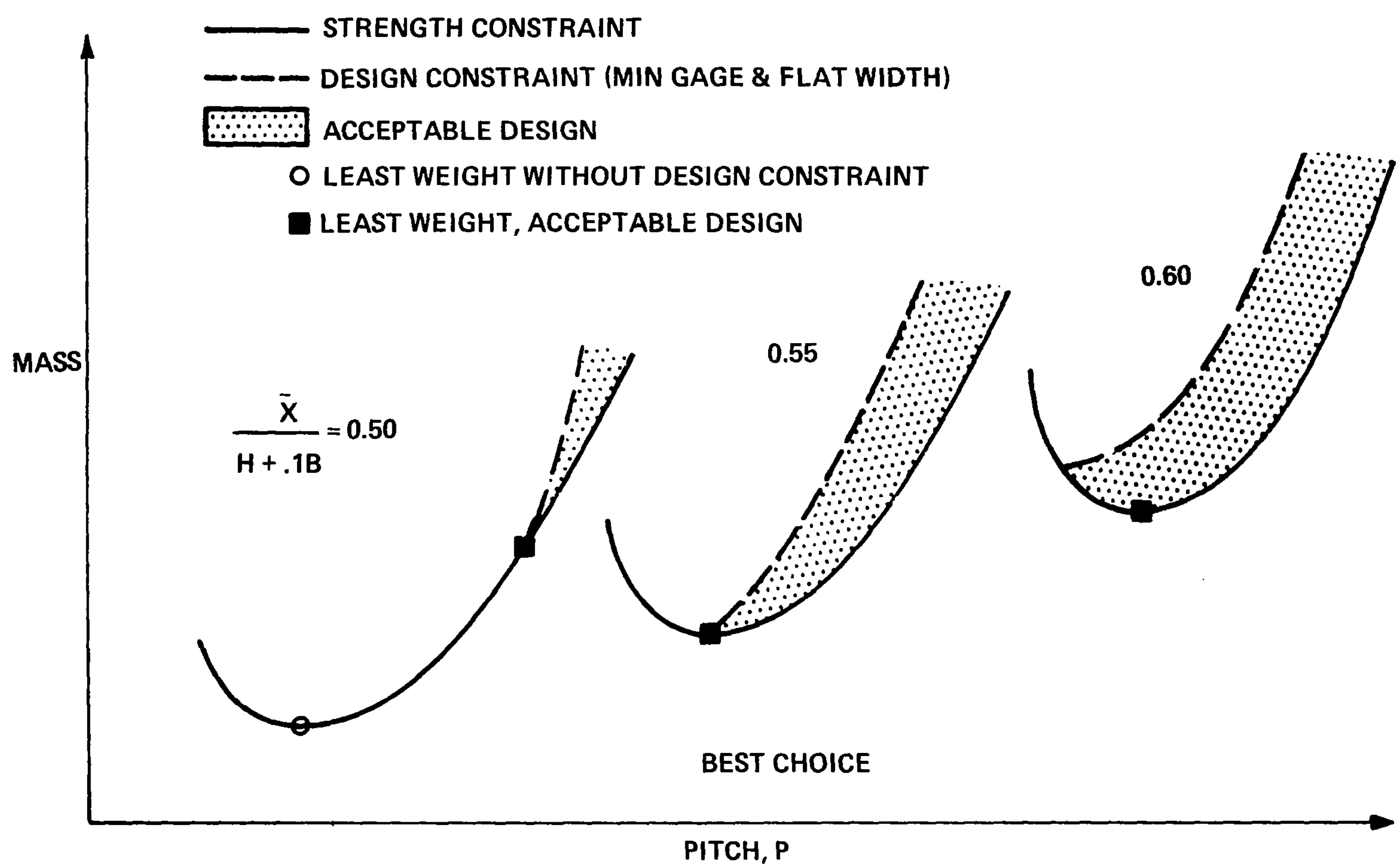

SCHEMATIC OF LEAST MASS DESIGNS VS PITCH FOR THREE NEUTRAL AXIS LOCATIONS

Figure 9

COMPROMISE HAYNES/RENÉ OPTIMUM SECTION
(Figure 10)

One objective of the program was to address the problem of "interface" between metallic TPS optimized and fabricated from different metals. It was decided, therefore, that a compromise section geometry would be selected for the skin panel so that the Haynes and René systems could be used as adjacent panels. Moreover, the use of one skin geometry could significantly lower fabrication and tooling costs for a flight vehicle.

Since only the skin of each system interfaces at the expansion joint, the corrugation of each configuration can still be optimized independently. The pitch of the Haynes section is somewhat above the optimum René 41 pitch of 2.39 cm (0.94 in.). From a cost and mass standpoint, it is desirable to increase section pitch to reduce the number of clips and attaching rivets on the rib support. To identify a compromise pitch, a simplified study was conducted; it included the effects of pitch on panel mass, and accounted for upper and lower clip mass for both the center and end support ribs. Items not included in the study because their mass remains relatively constant with respect to pitch include support rib webs, drag brackets, miscellaneous fasteners, and insulation.

The results of the study are shown in the figure. It can be seen that the Haynes 188 total mass (panel plus clips) is minimized at a pitch of 3.91 cm (1.54 in.). The minimum-mass René 41 panel occurs at a pitch of 2.39 cm (0.94 in.). The middle curve shows a mass-pitch curve for a 50% Haynes 188/50% René 41 panel mix. The minimum composite mass occurs at a pitch of 3.58 cm (1.41 in.). The dashed line connects the three calculated points and is an estimated relationship between optimum pitch and surface panel mass. Based on these curves, the greater density of Haynes 188, and the desire to space an even number of corrugations across a 61-cm (24-in.) span, it was decided to use a common pitch of 3.81 cm (1.50 in.) for Haynes 188 and René 41.

MASS STUDY RESULTS

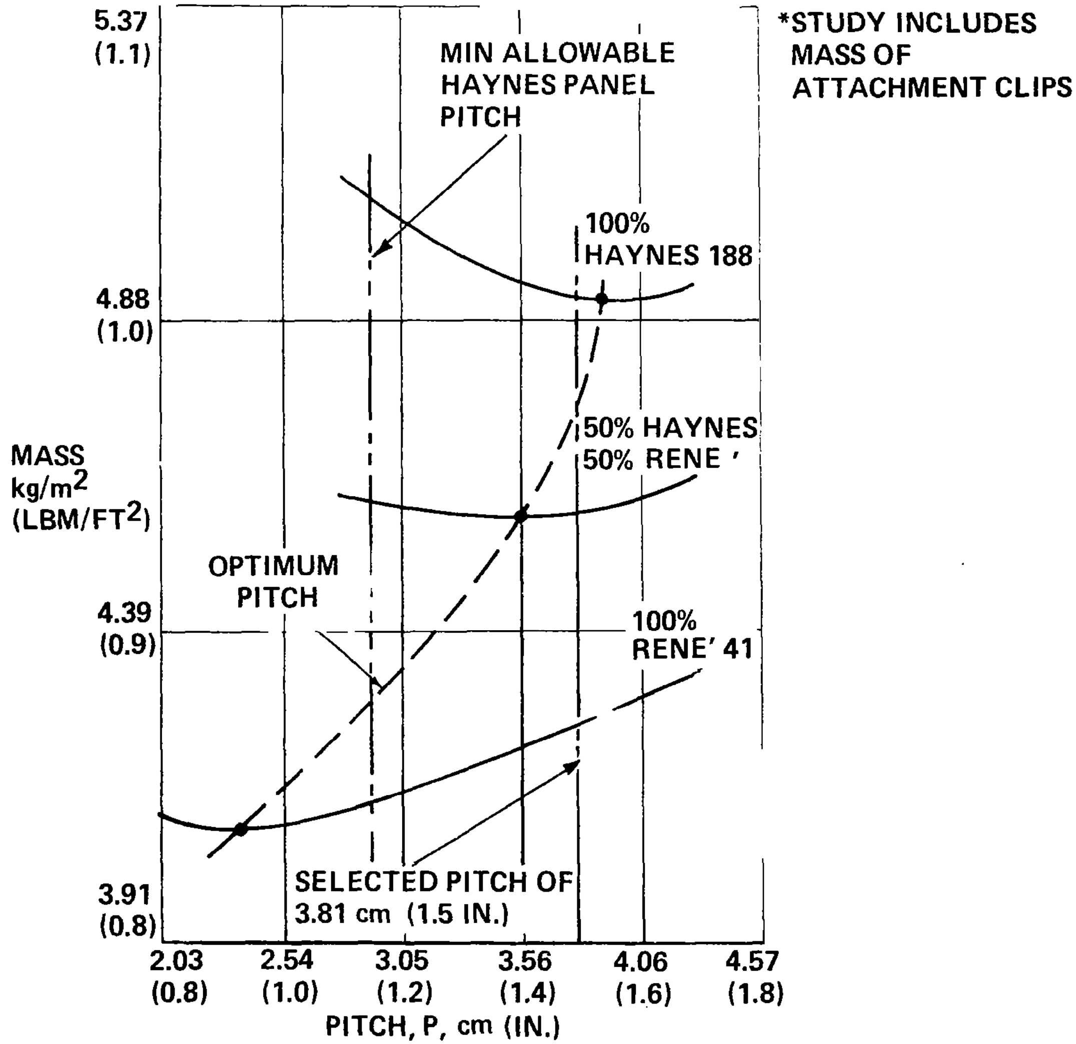

Figure 10

SELECTION OF OPTIMUM PRODUCTION SECTIONS
(Figure 11)

OPTIMUM HAYNES 188 SECTION

The results of the optimization program for the minimum-mass section are illustrated in the figure. A panel with a pitch of 3.81 cm (1.50 in.) was selected for the final design. Dimensions of the selected section, which define the midspan cross section, are also shown. This section produced a surface panel with a mass of 4.27 kg/m^2 (0.875 lbm/ft^2). This section, however, was modified to accommodate surface emittance treatment and material oxidation losses during the 100-mission life. Additionally, the corrugation lower cap pad was sculptured to minimize mass and provide uniformity of stress. The modified section, which was the section that was fabricated, is shown. The mass of this section, including doublers, attachment rivets, and mass reduction resulting from sculpturing, is 4.536 kg/m^2 (0.929 lbm/ft^2). This new design indicated a 22% reduction in mass from the baseline panel.

OPTIMUM RENÉ 41 SECTION

The principal differences between René 41 and Haynes 188 are that René 41 has superior mechanical properties at room temperature and suffers less degradation in mechanical properties at elevated temperature because its service temperature is lower - 1144 K (1600°F) vs 1255 K (1800°F). Although the moduli of elasticity are similar, the creep strength of René 41 at service temperature is typically 69 MPa (10,000 psi) vs 27.6 MPa (4000 psi) for Haynes 188. The increased creep strength produced two effects on the optimum René 41 section relative to the Haynes section: the overall section height (and associated dimensions) decreased, and the width-to-thickness ratio for the various elements decreased. The latter effect resulted from satisfying buckling criteria.

SELECTION OF OPTIMUM PRODUCTION SECTIONS

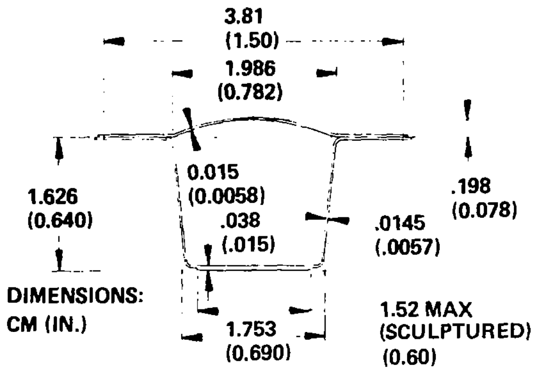

(a) Haynes 188 production section.

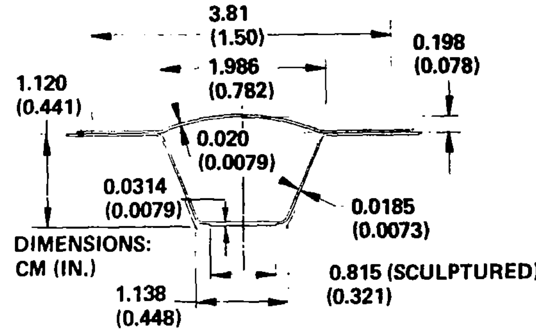

(b) René 41 production section.

FULLY ASSEMBLED HAYNES 188 SURFACE PANEL

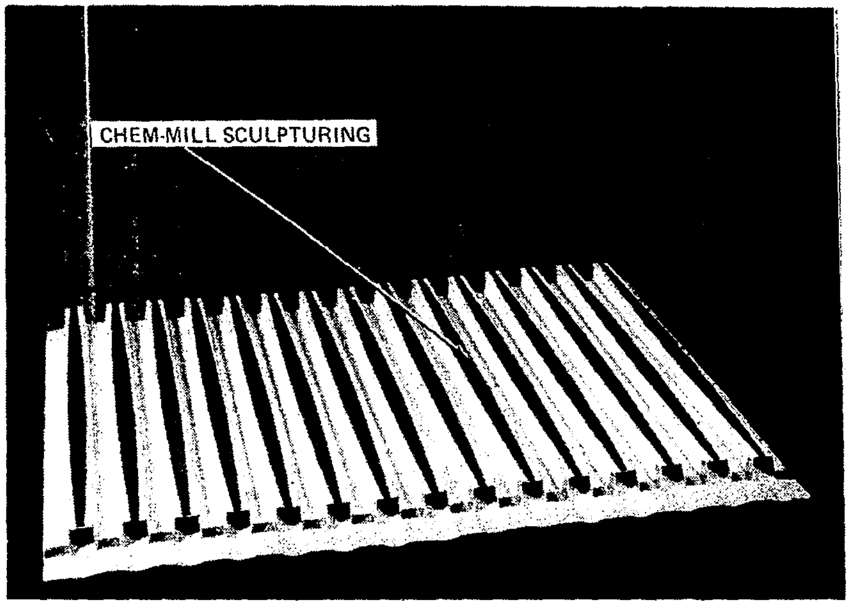

Figure 11

SKIN BEAD FLUTTER AND THERMAL CONSTRAINTS
(Figure 12)

SKIN BEAD FLUTTER

Previous experience with similar designs indicated that flutter requirements could determine the skin thickness. The minimum required face-sheet thickness to prevent local flutter of the skin bead was determined using the analysis procedure given in AFFDL-TR-67-140. The procedure is summarized as shown.

LATERAL THERMAL EXPANSION

The lateral thermal expansion is constrained by the adjacent panel, which prohibits lateral growth, and the support ribs, which prevent normal displacements. Thermal strains are absorbed by the face sheet beads in bending. The value B/10 is sufficiently large to avoid thermal buckling of the circular arc.

The maximum fiber stress was limited to yield (0.2% permanent deformation) at peak temperature, resulting in an allowable total strain, ϵ_T, and commensurate allowable elastic stress F_{allow}. (The factor of safety was taken as 1.0.) The allowable skin thickness lies between the solid line and the appropriate dashed line.

HAYNES 188 FLUTTER AND THERMAL CONSTRAINTS

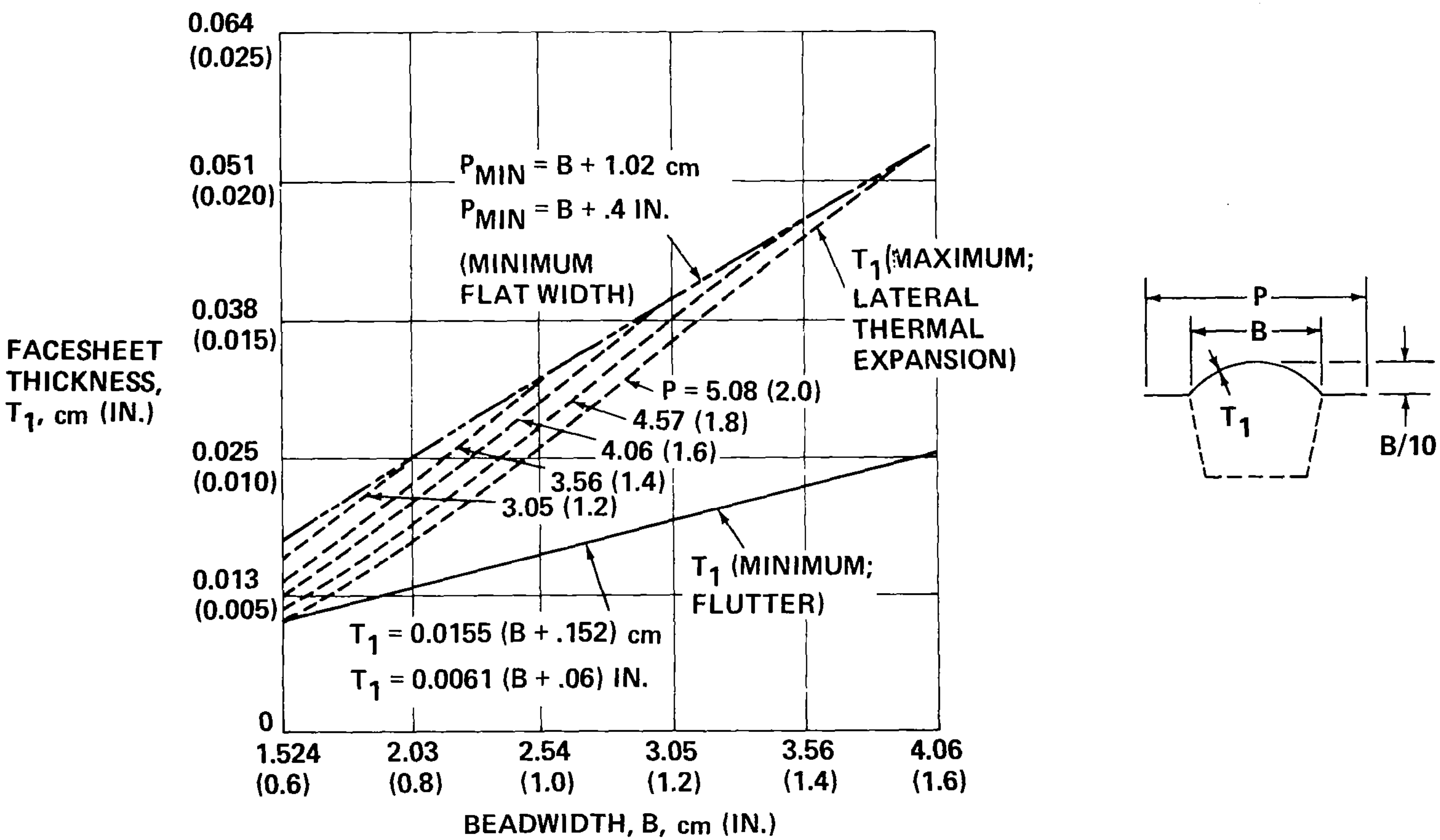

Figure 12

THERMAL STRESSES IN SURFACE PANEL
(Figure 13)

SELECTION OF CRITICAL CONDITIONS

An analysis was performed to determine at which times during the trajectories the maximum thermal stresses occur. Only thermal stresses resulting from gradients within the surface panel were considered. The thermal stress analysis assumed that the panel was free to expand in the direction parallel to the corrugations. The panel was also free to bow up between end supports without incurring any significant bending moments at the end supports. Thermal stresses, therefore, are produced only when the temperature gradient through the depth of the panel cross section is nonlinear. The thermal stresses produced are in a direction parallel to the corrugations. Therefore, they are coincident with the bending stresses produced by surface pressure on the panel. Significant gradients exist only during the following time intervals:

- Boost phase 90 through 160 sec
- Entry phase 60 through 170 sec
- Postentry phase 1700 through 2100 sec

DETERMINATION OF ELEMENT STRESSES

The thermal-stress model consisted of a simple finite-element representation of the panel cross section, as shown in the insert. The appropriate coefficient of expansion, Young's modulus, areas, and temperatures were inputted to a transient-temperature structural analysis computer program which determined the stress level in each element.

Examination of the results indicates a fluctuation of stress as the transient temperature gradients change with time. From each figure, times which produced the largest thermal stress and which would combine with the stresses due to aerodynamic pressure loadings were selected. At maximum temperature, the thermal gradients in the panel are very small because almost constant heating conditions exist, and the strong radiant heat interchange between panel elements reduces temperature differences to small values. The margin of safety was 0.14 for the worst combination of aerodynamic and thermal stresses.

BOOST

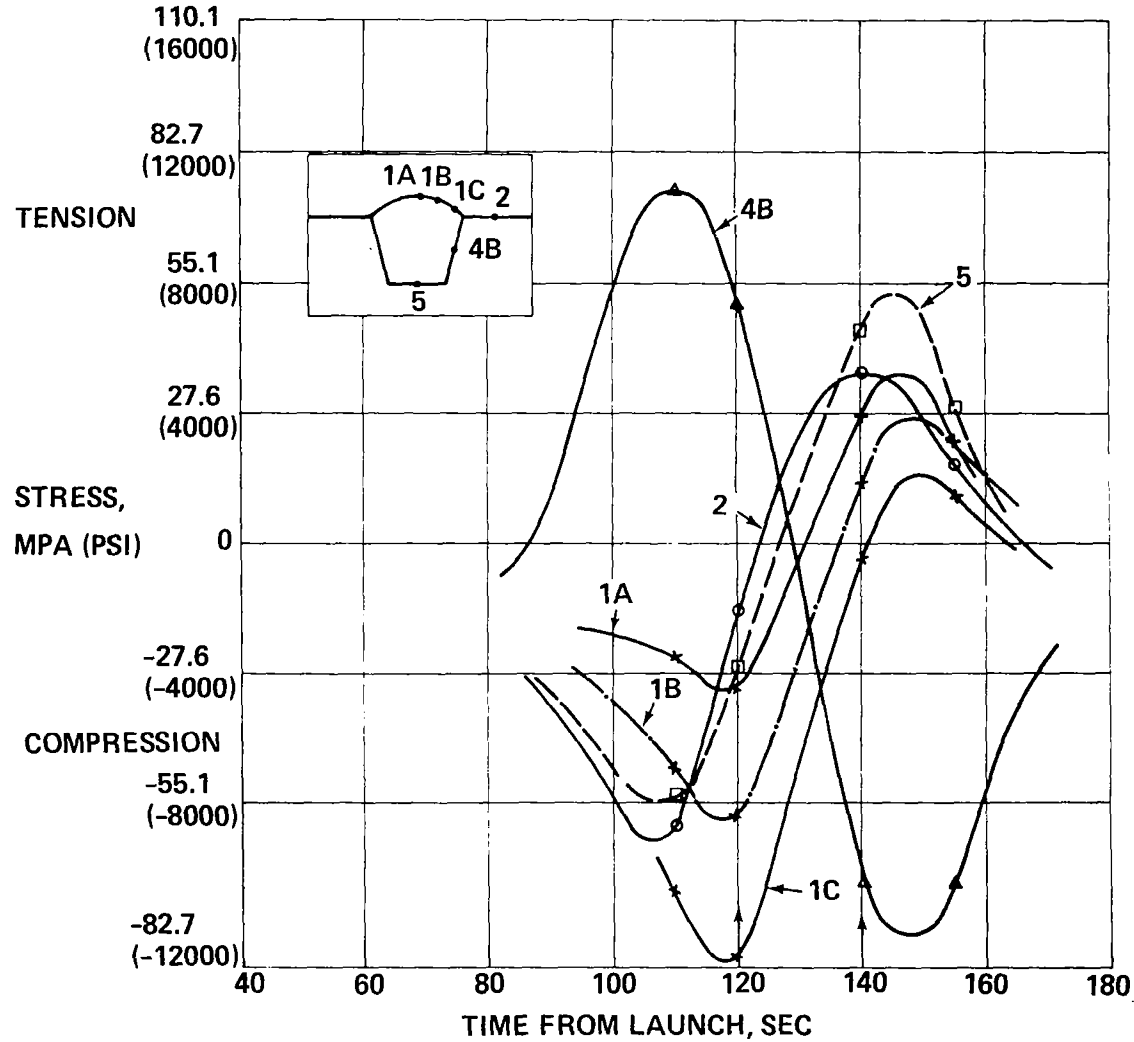

Figure 13

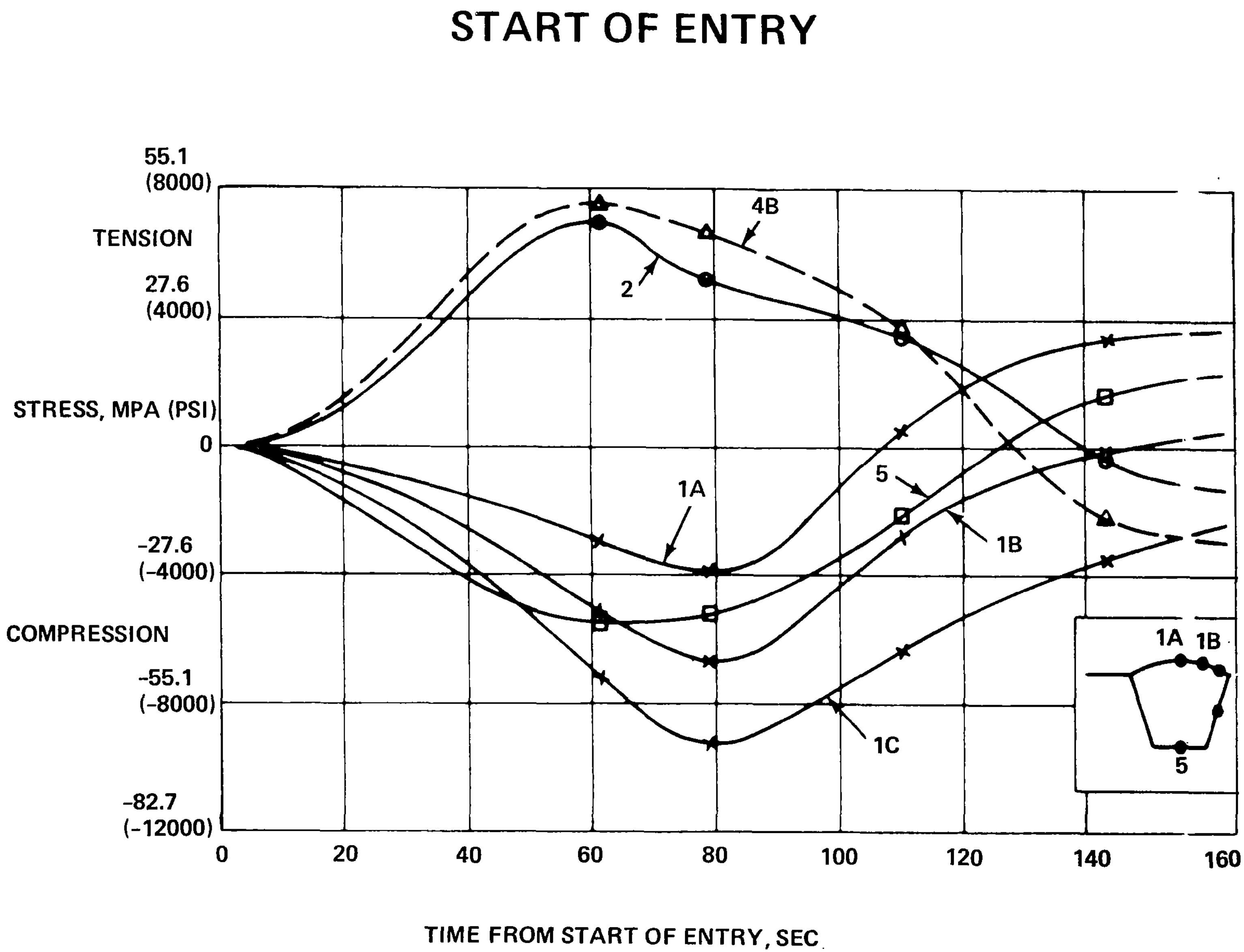

Figure 13.- Continued

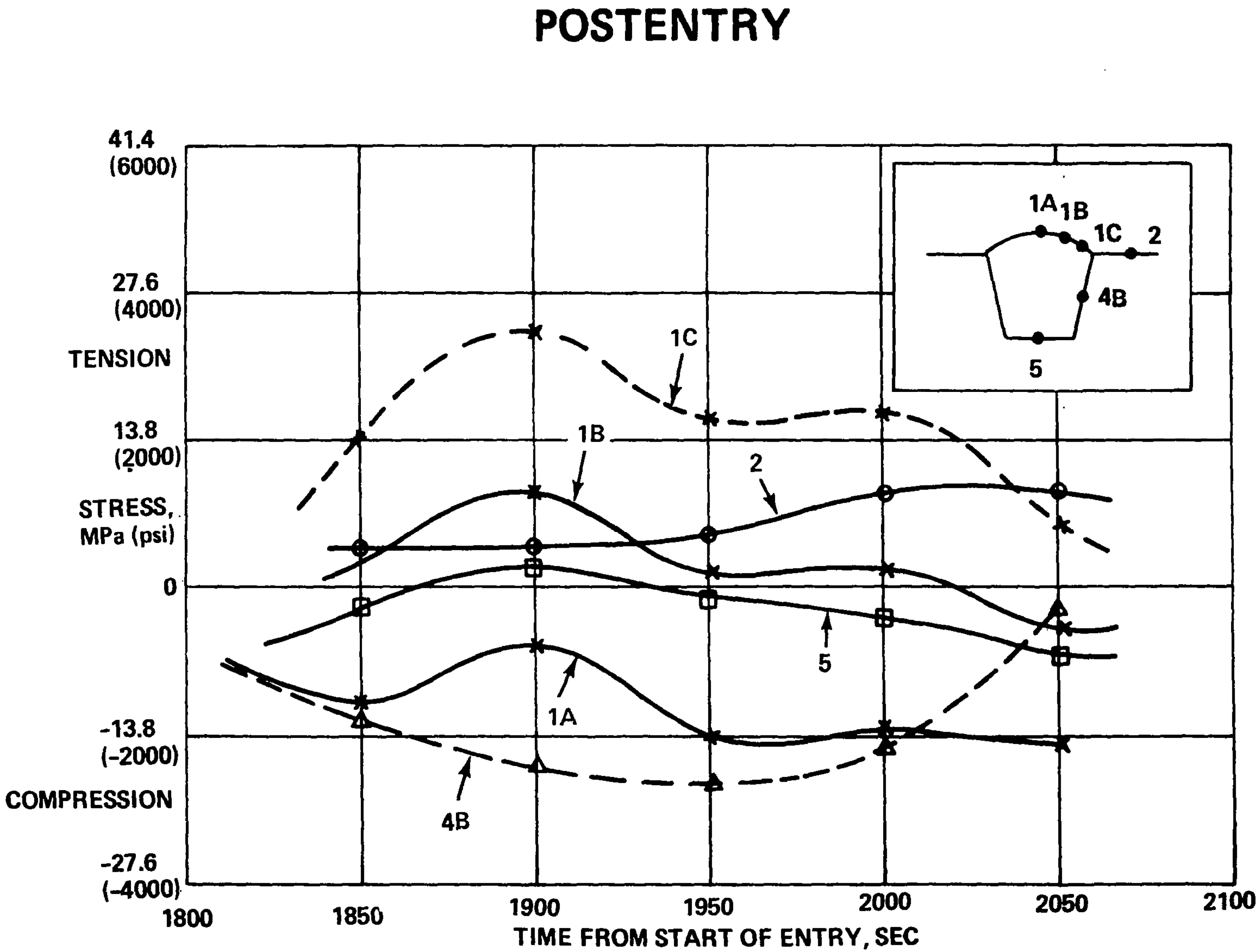

Figure 13.- Concluded

SUPPORT RIB DESIGN
(Figure 14)

The support rib must transfer aerodynamic pressure and panel inertial loads to the vehicle primary structure while causing a minimum heat short. Two types of supports are used: a flexible one at the expansion joint, and a fixed type where two adjacent panels butt.

Several support rib concepts were considered. To simplify mass comparisons between these designs, the following parameters were fixed: standoff height, 9.22 cm (3.63 in.); web thickness, 0.25 cm (0.010 in.); and upper and lower clip thickness, 0.111 cm (0.044 in.). Full web and truss concepts were also considered.

The selected configuration is something between a full web and a truss. The lower arches have adequate radii so that flange cracking is eliminated. The beads serve to eliminate thermal stresses and provide vertical stiffness. Heat shorting is reduced from that of the baseline design since lower attachments occur at a 7.62-cm (3.0-in.) pitch instead of 3.81 cm (1.50 in.). To further minimize heat shorting, 0.32-cm (0.125-in.) thick insulating washers, fabricated from a glass-reinforced silicone laminate, insulate the lower clip from the aluminum primary structure.

With a mass of 0.657 kg/m^2 (0.135 lbm/ft^2), this design provides a 25% weight reduction from the baseline design.

MODIFIED WEB CONCEPT

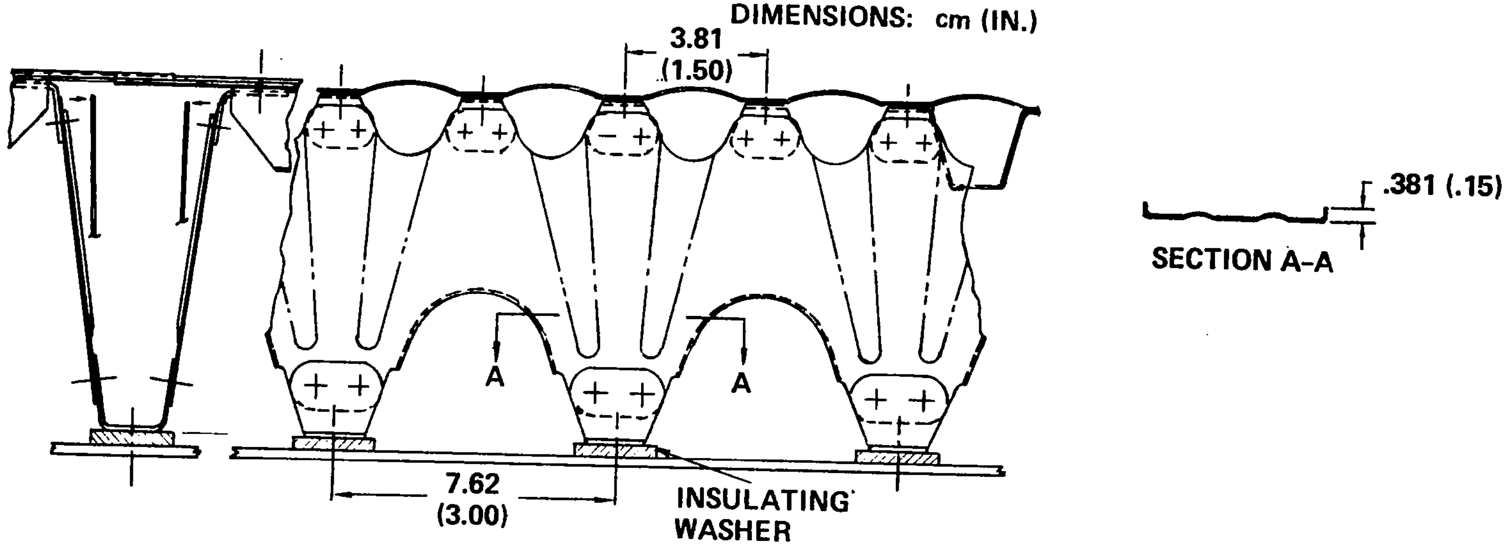

END FLEXING RIB

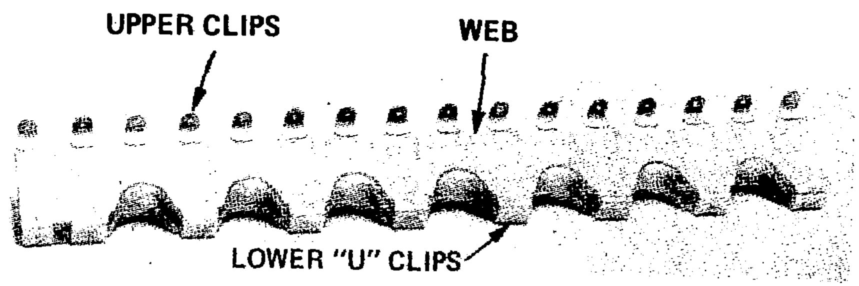

Figure 14

DRAG SUPPORT DESIGN
(Figure 15)

Because the support-rib standoffs cannot react loads parallel to the skin corrugations (in the longitudinal or drag direction), a drag support is employed at 30.48-cm (12-in.) intervals laterally along the center support to react these loads. The drag support consists of two bent-up channels riveted to each side of the center support rib which stabilizes the channels. The channels pick up the surface-panel screws in their normal location. The drag load is transferred to the primary structure by four screws at the bottom of the channels. Insulating washers are used under the lower clip to minimize heat shorting.

CENTER SUPPORT (FIXED) RIB

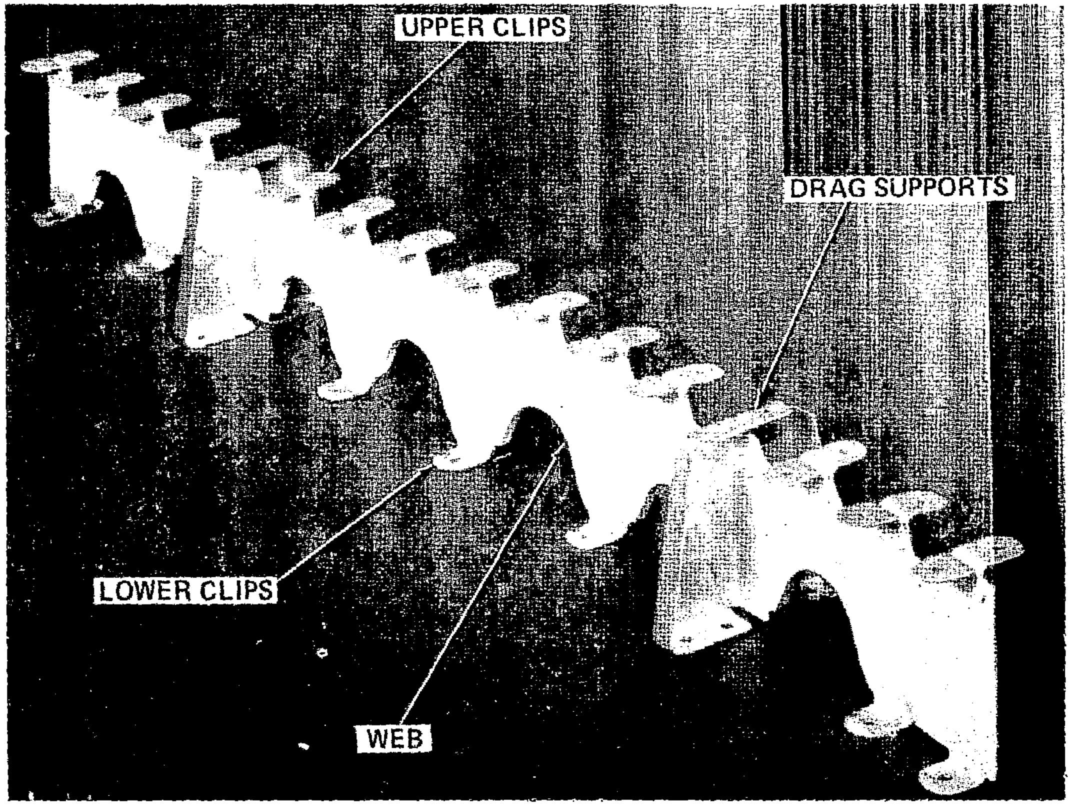

Figure 15

THERMAL INSULATION SYSTEM DESIGN & ANALYSIS
(Figure 16)

The insulation system provides the main barrier to radiative heat transfer from the hot surface panel to the vehicle primary structure. The objective of the program was to obtain the lowest-mass system which would withstand the thermal, cold-soak, and vibration environments.

Only commercially available nonexotic materials were considered. The insulation for the baseline system used for comparison in this study is a homogeneous blanket of 56-kg/m^3 (3.5-lbm/ft^3) Microquartz enclosed in a bag of resistance-welded Inconel foil. The purpose of the bag was to protect the blanket from excessive moisture absorption and damage during handling. However, since the foil bags must be vented, their effectiveness seems questionable. The bags are costly to fabricate and add 1.56kg/m^3 (0.32 lbm/ft^3) to the total TPS mass. For these reasons, protective foil bags were not included in this insulation system design. Further modifications to the baseline system which were considered are:

- The use of lower-density high-temperature insulation: 17.6kg/m^3 (1.1-lbm/ft^3) Astroquartz
- A composite of low-density insulation (TG 15000) and Microquartz
- The use of metal foil radiation barriers in fibrous insulation

INSULATION SYSTEM COMPARISONS

The initial comparison of the efficiencies of the insulation candidates was made by comparing the density-conductivity (ρk) product. The ρk product for Microquartz and Astroquartz with 0.006 cm (0.00025 in.) metal foils inserted as radiation barriers was examined. The results reveal that the emissivity of the foils must be kept low (≈ 0.05) to effect a significant reduction in ρk, and are advantageous only above 644 K (700°F). The oxidizing environment to which the TPS insulation would be exposed results in nickel foil having an unacceptable emissitivity of 0.5 or higher. Aluminum foil has a maximum temperature capability of only 700 K (768°F). Platinum foils appear effective, but are considered too exotic and expensive.

COMPOSITE SYSTEM SELECTED

Comparison shows that the composite system of Microquartz and TG15000 is the lightest. The mass of the system is 0.29 kg/m^2 (0.06 lbm/ft^2) less than the baseline system which represents a 10% mass reduction. This system was, therefore, selected for use on the test specimens.

RENE' 41 PANEL INSULATION SYSTEM DIMENSIONS

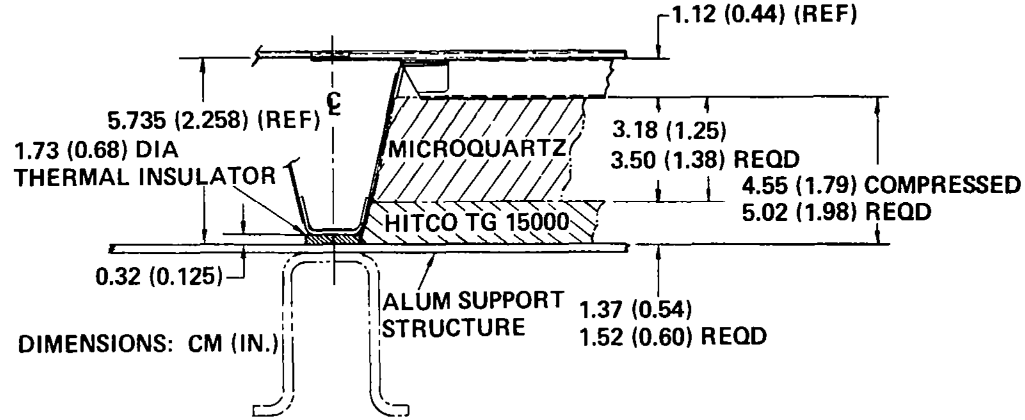

(a)

HAYNES 188 PANEL INSULATION SYSTEM DIMENSIONS

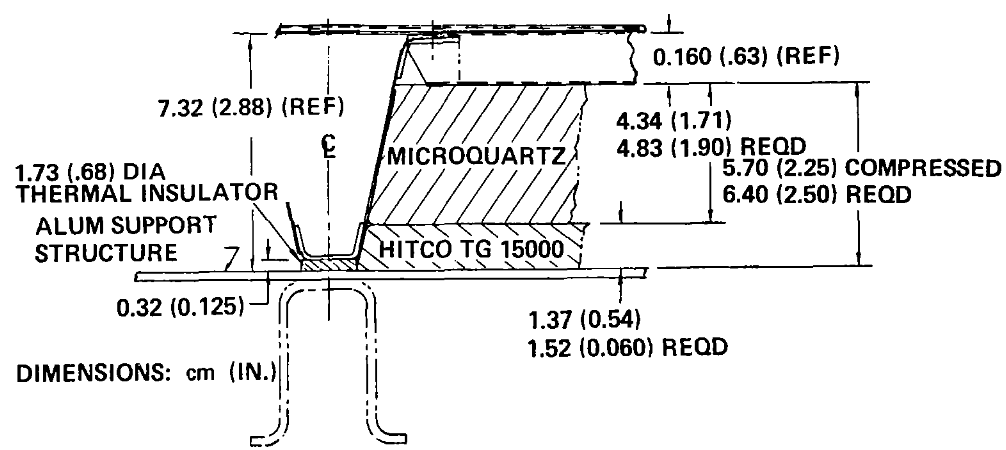

(b)

Figure 16

CONCEPT MASS BREAKDOWN
(Figure 17)

The unit mass breakdown of the original baseline design and the new Haynes 188 design is given in the figure. The first column gives the estimated mass of the original system. The second column gives the unit mass breakdown of the new design based on nominal material thicknesses. The reductions in mass of the new design are 25% for the surface panel, 50% for the support structure, and 40% for the insulation. This results in an overall 35.4% reduction in mass from the baseline design. The most significant reductions appear for the skin, where the thickness decreased from 0.025 cm (0.010 in.) to 0.0145 cm (0.0057 in.); the support structure, where mass reductions were achieved by reducing the number of lower clips and attaching hardware; and in the insulation system, where reductions were obtained by eliminating foil bagging and support hardware, and the use of low-density TG 15000 insulation.

MASS (ESTIMATED NOMINAL WEIGHTS) COMPARISON OF ORIGINAL BASE LINE AND NEW DESIGN

COMPONENT	ORIGINAL BASELINE HAYNES 25 kg/m²	ORIGINAL BASELINE HAYNES 25 LBM/FT²	NEW DESIGN HAYNES 188 kg/m²	NEW DESIGN HAYNES 188 LBM/FT²
SURFACE PANEL				
SKIN	2.554	0.523	1.3994	0.2866
CORRUGATION	3.242	0.664	2.8749	0.5888
DOUBLERS	–	–	0.1460	0.0299
ATTACH RIVETS	0.264	0.054 [a]	0.1172	0.0240
SUBTOTAL	6.060	1.241	4.5375	.9293
% CHANGE	–		-25.1	
SUPPORTS				
WEBS	0.439	0.090	0.2632	0.0539
UPPER CLIPS	0.537	0.110	0.5195	0.1064
LOWER CLIPS	0.801	0.164	0.2671	0.0547
DRAG BRACKET	0.151	0.031	0.0771	0.0158
ATTACH HARDWARE	0.635	0.130	0.1475	0.0302
SUBTOTAL	2.563	.525	1.2744	0.2610
% CHANGE	–		-50.3	
INSULATION				
MICROQUARTZ	3.223	0.660	2.7055	0.5541 [c]
	1.709	0.350 [b]	0.2441	0.0500
SUBTOTAL	4.932	1.010	2.9496	0.6041
% CHANGE			-40.2	
TOTAL	13.555	2.776	8.7615	1.7944
% CHANGE	–		-35.4	

[a] 8-32 SCREWS AND NUTS USED
[b] INCONEL BAGGING AND SUPPORTS
[c] TG 15000 INSULATION

Figure 17

TEST SPECIMEN INSTRUMENTATION
(Figure 18)

The test specimen instrumentation configuration is shown in the figure. Fifty-three thermocouples (T/C) were installed in the locations indicated to monitor test specimen temperatures. The eight T/Cs, which monitored heat-sink temperatures, were fabricated using chromel/alumel fiberglass-insulated 30-gage wire, and attached with a high-temperature adhesive. All other T/Cs are the ceramo type, spotwelded to the test panel. The Haynes 188 and René 41 test articles were instrumented identically.

PANEL DEFLECTION MEASUREMENTS

Skin-panel deflections were measured at the center of the 51-cm (20.0-in.) test panel. Measurements were made by a cable-type linear-displacement transducer capable of operation in a 477 K (400°F) environment, with a resolution of 0.003 cm (0.001 in.).

INSULATION SYSTEM TEMPERATURES

To evaluate temperature gradients through the insulation thickness, four T/Cs were placed 1.27 cm (0.5 in.) apart on a support plate. Two such arrangements were employed. One is located at the panel center, and one near the flexing rib.

EXPANSION JOINT LEAKAGE

To evaluate expansion joint leakage, three T/Cs were placed in line under the skin, in the expansion joint area. If leakage were to occur, it was expected that the center T/C would record a higher temperature. This arrangement was employed at three locations in the expansion joint area.

SURFACE PANEL INSTRUMENTATION - LOWER SURFACE

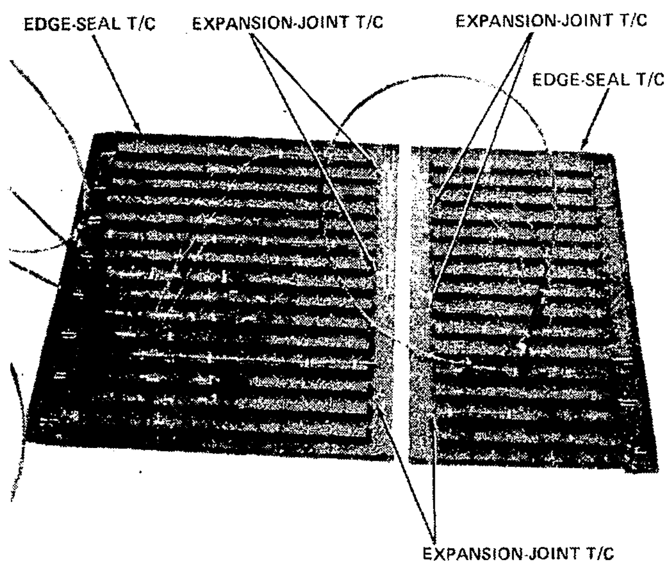

(a)

SUPPORT STRUCTURE HEAT - SINK INSTRUMENTATION - TOP

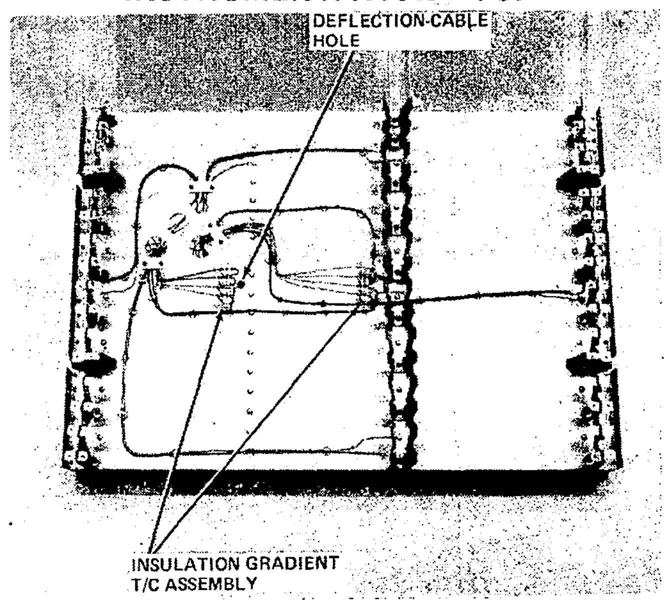

(b)

Figure 18

SUMMARY
(Figure 19)

A lightweight metallic TPS was designed, and two test articles were fabricated, one from Haynes 188 and one from René 41. A baseline TPS concept, selected at the beginning of the program, consisted of a Haynes 25 corrugation-stiffened beaded skin surface panel, a specially designed support system, and an insulation system. By optimizing the structure for the design loads and by chem-milling to remove material not needed, the mass of the baseline surface panel was reduced 25%, and the mass of the support structure was reduced 50%. The insulation system mass was reduced 40% by using two types of insulation, each suited to its temperature range, and by eliminating a foil bag which encapsulated the baseline insulation system. These reductions resulted in an overall 35% reduction in mass of the Haynes 188 panel from the baseline Haynes 25 design. Similar reductions were achieved with the René 41 system.

The overall program led to the following conclusions:

- René 41 and Haynes 188 heat shields appear to be viable approaches for a thermal protection system for vehicles sustaining temperatures up to 1255 K (1800°F)

- A René 41 TPS with a mass of 7.08 kg/m^2 (1.45 lbm/ft^2) and a Haynes 188 TPS with a mass of 8.7615 kg/m^2 (1.794 lbm/ft^2) can be fabricated using state-ot-the-art production techniques

- Two thermal protection systems, optimized for different materials and operating temperatures, can be used as adjacent compatible systems, with only a small decrease in mass efficiency resulting from the compromise

In view of these results, it is concluded that the basic technology for flat metallic TPS is available.

SUMMARY

- RENE' 41 AND HAYNES 188 HEAT SHIELDS APPEAR TO BE VIABLE APPROACHES FOR A THERMAL PROTECTION SYSTEM FOR VEHICLES SUSTAINING TEMPERATURES UP TO 1255 K (1800° F)

- A RENE' 41 TPS WITH A MASS OF 7.08 KG/M^2 (1.45 LBM/FT^2) AND A HAYNES 188 TPS WITH A MASS OF 8.7615 KG/M^2 (1.794 LBM/FT^2) CAN BE FABRICATED USING STATE-OF-THE-ART PRODUCTION

- TWO THERMAL PROTECTION SYSTEMS, OPTIMIZED FOR DIFFERENT MATERIALS AND OPERATING TEMPERATURES, CAN BE USED AS ADJACENT COMPATIBLE SYSTEMS, WITH ONLY A SMALL DECREASE IN MASS EFFICIENCY RESULTING FROM THE COMPROMISE.

Figure 19

MULTIWALL TPS

L. Robert Jackson

NASA Langley Research Center

INTRODUCTION

(Figure 1)

In design of thermal protection systems (TPS) for aerospace vehicles, an effective means of transmitting aerodynamic loads (shear and in some cases pressure difference) through the TPS is essential. That is, the load transfer method must have low weight, result in low thermal stresses, and not transfer excessive heat to the underlying structure.

Two approaches have been developed to satisfy these load-bearing and thermal isolation functions at low thermal stresses. One approach (figure 1(a)) is to use metal heat shields supported by slender metal stand-off supports that penetrate a nonload-bearing insulation (ref. 1). The flexible stand-offs bend as the shields expand on heating, thus imposing little restraint or thermal stress. This approach requires many small pieces forming a complex installation. The other approach (fig. 1(b)) is to use a load-bearing insulation attached to the primary structure. Since most load-bearing insulations have a high modulus of elasticity, they are usually segmented with small gaps for low thermal stress. One load-bearing insulation developed to date includes sintered quartz-fiber tiles (reusable surface insulation of the space shuttle, ref. 2). Generally, the nonmetallic insulations are simple to attach to the structure, but they have a common potential disadvantage. That is, they are weak materials, consequently, surface frayings, erosion, cracking or breakage rates may be high and may increase refurbishment requirements.

A need exists for an efficient thermal protection system that has the toughness of the metal shield systems and the simplicity of the load-bearing insulation systems.

THERMAL PROTECTION SYSTEMS

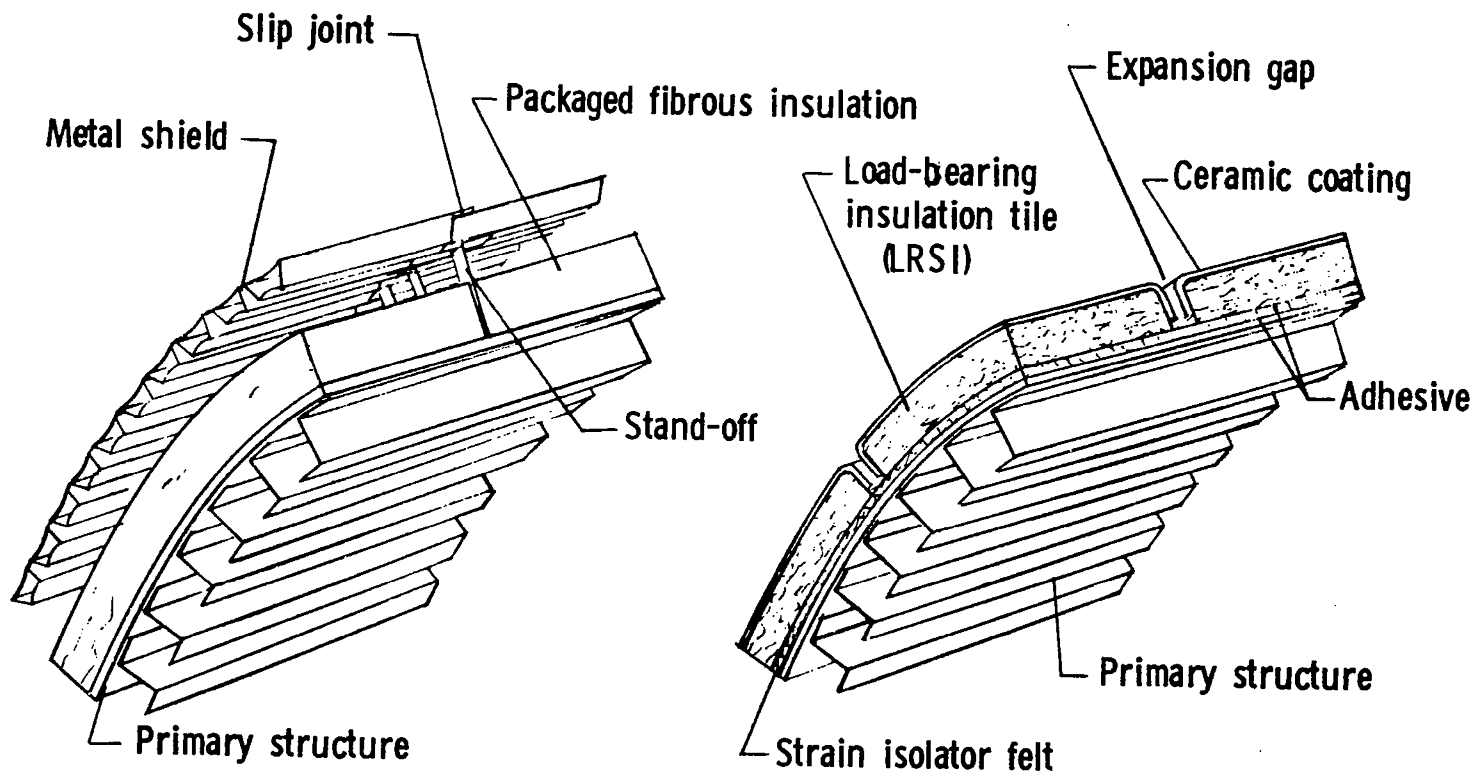

(a) METALLIC TPS

(b) NONMETALLIC TPS

Figure 1

MULTIWALL THERMAL PROTECTION SYSTEM

(Figure 2)

This paper describes a lightweight metallic-load-bearing insulation, fabricated as panels that are installed as tiles. Each panel consists of multiple layers of dimpled and plain foils joined at dimple crests to form a strong load-bearing insulation. Thermal stresses are minimized by using simple support that is also slip jointed. With scarfed edge closures, flow seals, and mechanical attachments, the panel installation is designated multiwall TPS and shown in figure 2.

Initial development of multiwall TPS consisted of analyses and tests of structural and thermal characteristics reported in reference 3. Additional development of a conical multiwall structure, representative of hydrogen-fueled hypersonic aircraft construction, is reported in reference 4. In this effort the multiwall TPS was a continuous shell welded to the integral tank, also of multiwall construction. Current effort is focused on separate multiwall TPS tiles mechanically attached to the vehicle structure. The current approach facilitates installation of preassembled panels and removal for inspection of the structure or repair of the TPS.

In addition to a description of multiwall TPS, the theory (which shows how a metallic insulation can be an efficient insulation) is discussed, analyses of multiwall TPS performance for specific applications such as the space shuttle and an advanced space transport are reported, and planned wind tunnel tests are described followed by some concluding remarks.

MULTIWALL THERMAL PROTECTION SYSTEM

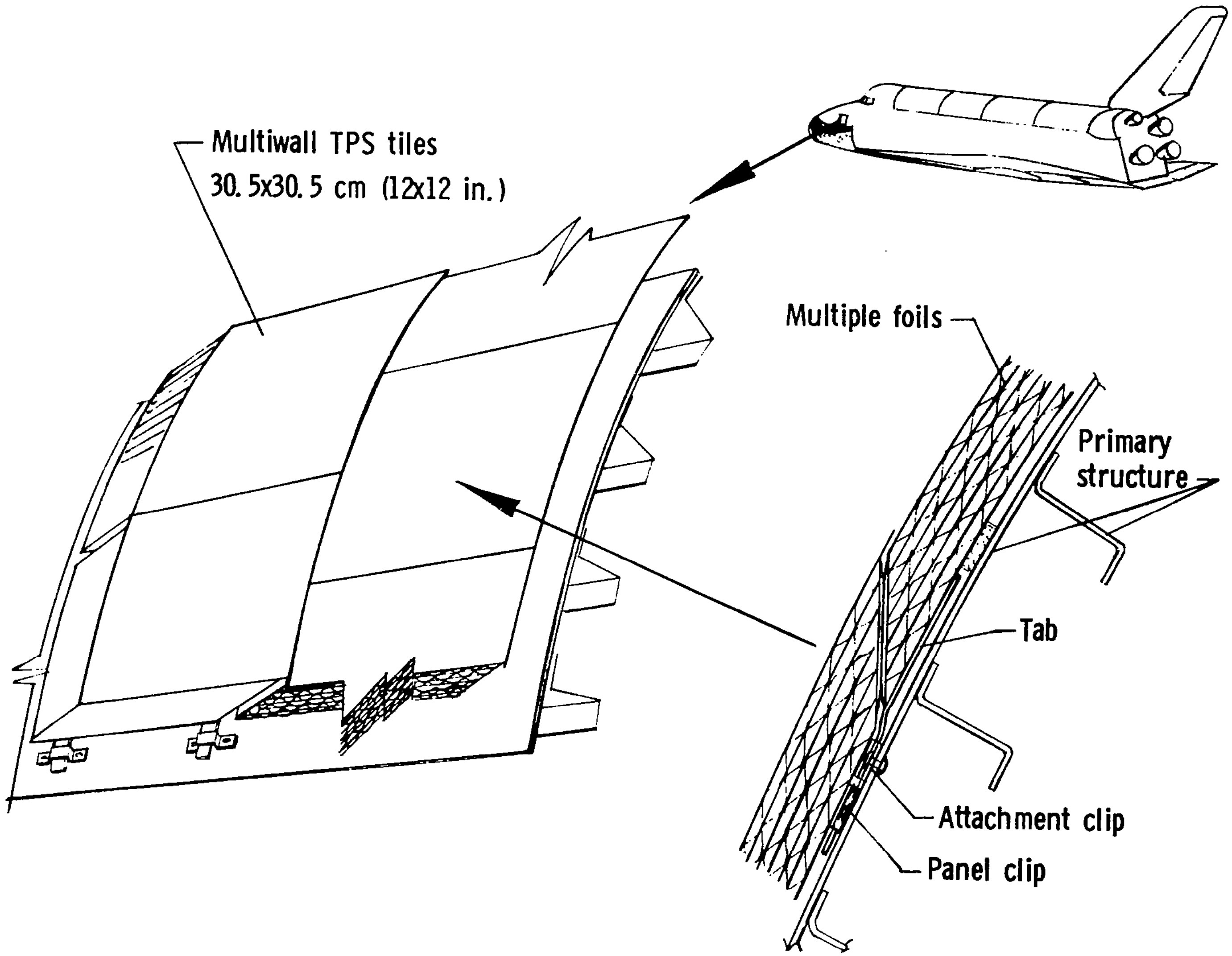

Figure 2

CONDUCTIVITY OF MULTIWALL TPS

(Figure 3)

Insulating properties of multiwall TPS panels are best described with the aid of the equations given in figure 3, which were derived for reference 3 to approximate the thermal conductivity.

Metallic Conduction.- The through-metal mode of heat transfer is partly governed by the conductivity of the metal selected. For instance, titanium alloys have much lower conductivities than aluminum alloys. A second factor is the percentage of through metal which is governed by the thickness of the dimple sheets, dimple contact size, and contact number per unit area of panel surface. Typically, through-metal conduction area is less than 0.2 percent. A final factor is the relatively long conduction path length.

Gaseous Conduction.- The gaseous conduction mode is governed principally by the conductivity of the gas in the voids of the multiwall panel.

Radiation Conduction.- The third mode of heat transfer through multiwall TPS is radiation. Radiation conductivity is governed primarily by the number of radiation barriers in a given thickness. This fact has been exploited in the super insulations (ref. 5), which consist of up to 29 foils per cm (75 foils per inch) of thickness. Evacuated superinsulations have the lowest known conductivities. Also, the emittance of each side of the foils is important since the lower the emittances, the lower the radiation transfer. The radiation component is very important at high temperatures.

CONDUCTIVITY OF MULTIWALL TPS

$$k = k_{metal} + k_{gas} + k_{radiation}$$

$$k_{metal} = k_m A_m \left(\frac{L}{P}\right)$$

$$k_{gas} = k_{air}$$

$$k_{radiation} \propto \frac{\varepsilon T^3}{\left(\frac{n}{L}\right)}$$

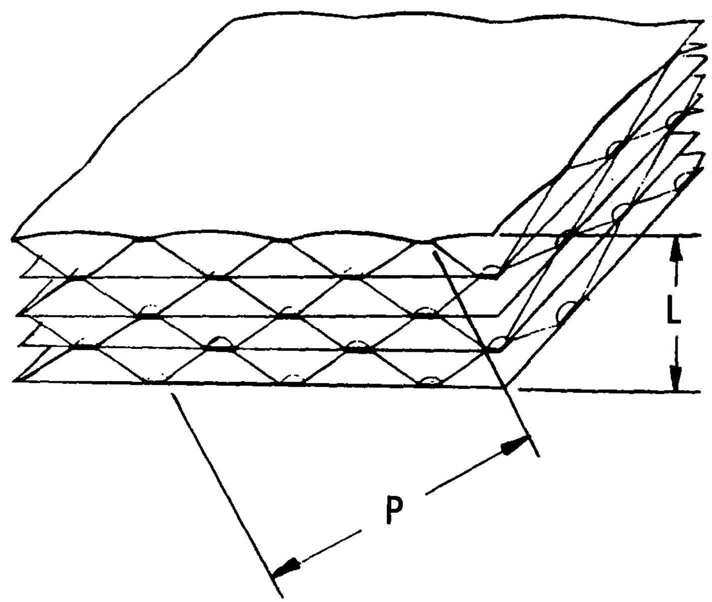

Figure 3

MULTIWALL CONDUCTIVITY AND COMPONENT MODES

(Figure 4)

Figure 4 shows the apparent conductivity calculated for titanium alloy multiwall TPS and the contribution of each of the heat transfer modes. A surprising result is the metallic conduction mode offers the least heat transfer through the panel for the selected dimple pitch and foil thickness.

Gaseous conduction is greater than all other modes at temperatures below 811 K (1000°F). Furthermore, if the cell size within the multiwall TPS is too large, free convection will occur, greatly increasing the heat transfer. However, a feature of multiwall TPS is that the cell size may be reduced to avoid free convection.

A further consideration related to gas conduction is the use of evacuated multiwall TPS panels. By evacuating to a pressure of 0.001 mm Hg the gas conduction is eliminated. At the low temperature range, evacuation has a significant effect on apparent thermal conductivity.

Figure 4 shows the effect of temperature on radiation transfer, which increases by the cube of the absolute temperature. However, the number of foils has a strong effect on radiation, since doubling the number of foils halves the radiation transfer through multiwall insulation.

MULTIWALL CONDUCTIVITY AND COMPONENT MODES

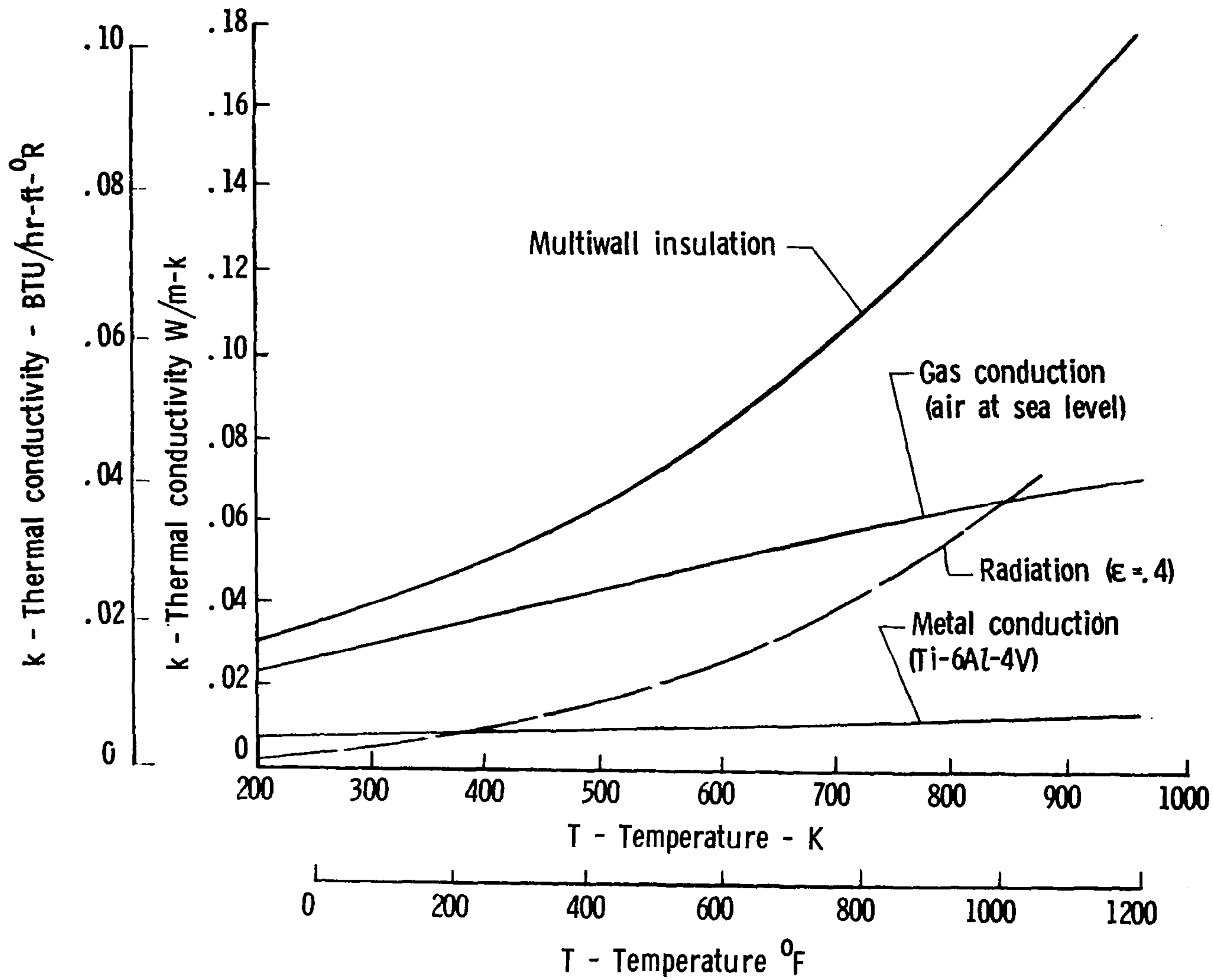

Figure 4

MULTIWALL THEORY VS. EXPERIMENT

(Figure 5)

The theory has shown metallic insulation to be thermally and structurally efficient. Experiments have been performed to verify both thermal and structural theories; and, with the exception of some of the structural tests, results were reported in reference 3. Although not exhaustive, the tests did include conductivity determination, resistance to sonic fatigue, thermal cycling, panel buckling, specimen crippling and core crushing. Briefly, these tests and results are discussed in the following sections:

Conductivity.- Apparent thermal conductivity was determined experimentally for two panels, each of welded stainless steel with oxidized surfaces and air in the voids at sea-level pressure. Results are shown in figure 5. It is seen that the theory predicts the apparent thermal conductivity through the test range of average temperatures of from 505K (450°F) to about 1256 K (1800°F).

Sonic Fatigue.- A multiwall sandwich panel ((1.27 x 50.8 x 50.8 cm) (0.5 x 20 x 20 in.)) of stainless steel foil with welded edge closures was tested under random noise of 162 dB for 90 minutes. The panel successfully sustained the sonic environment.

Thermal Cycling.- Thermal cycling, consisting of heating the hot face from 450 K (350°F) to 1242 K (1775°F) in two minutes followed by cooling for two minutes to 450 K (350°F), was performed on a multiwall panel. The panel ((2.54 x 30.5 x 30.5 cm) (1.0 x 12 x 12 in.)) was unrestrained and of welded stainless steel foil. After 25 cycles, the hot face sheet, which had the greatest thermal load, remained attached to the core.

MULTIWALL THEORY VS. EXPERIMENT

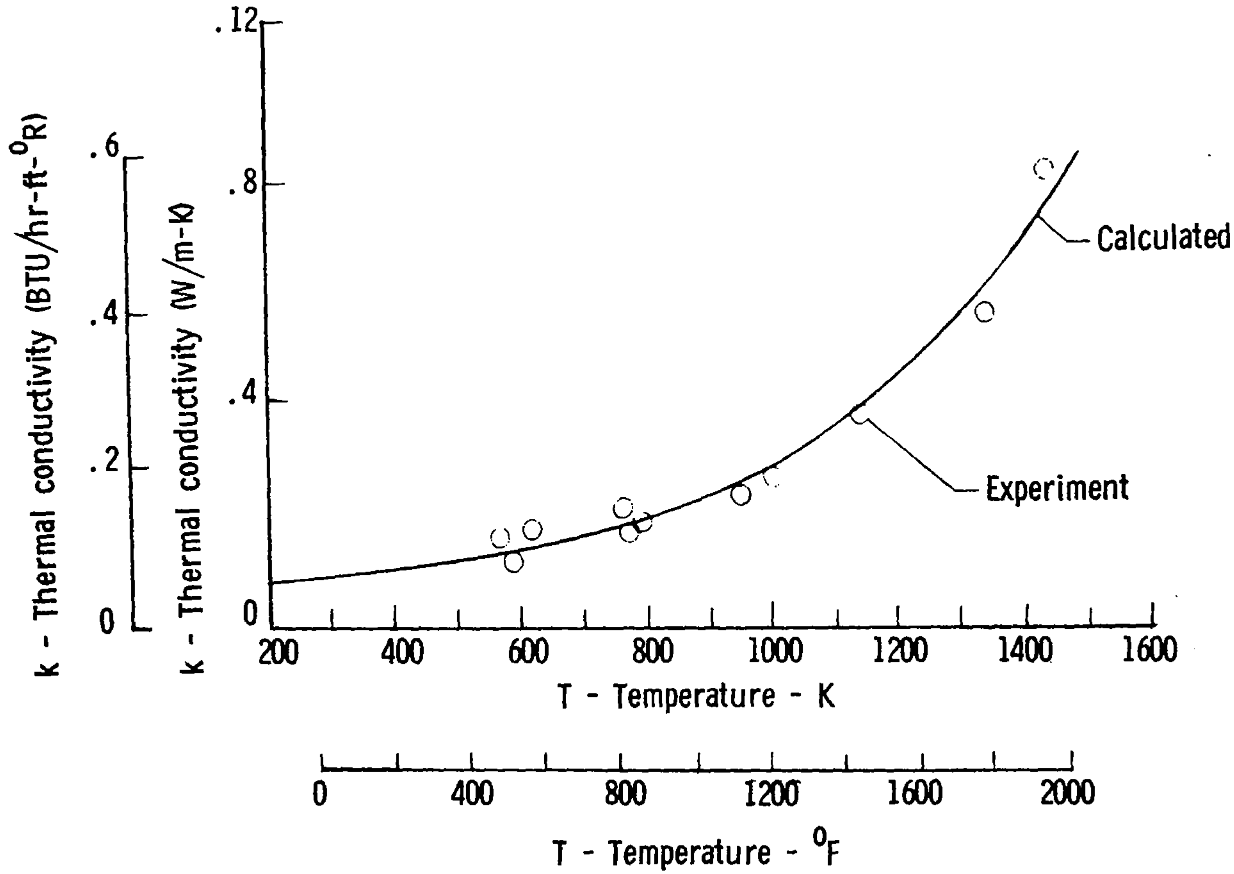

Figure 5

MULTIWALL TPS AS AN ALTERNATIVE TO LRSI

(Figure 6)

An efficient load-bearing insulation was baselined for the space shuttle orbiter. This material is sintered quartz-fiber tiles, known as LRSI on upper surfaces of the shuttle and HRSI on lower surfaces. The primary difference between them is the surface coating for control of emittance and absorptance. Figure 6 shows the location of LRSI tiles on the orbiter. LRSI is exposed to a peak temperature ranging from 589 (600) to 922 K (1200°F). The HRSI is used from 922 K (1200°F) to about 1589 K (2400°F), and reinforced carbon-carbon is used for higher temperature areas such as leading edges. The LRSI, as indicated, is used for upper surfaces, which have relatively low heat loads. Consequently the tiles are thin and hence somewhat fragile. Multiwall TPS is being studied in the NASA base R&T program to determine if it is a viable alternative to LRSI.

Three body point locations, shown in figure 6, have been analyzed. The first two points are near the nose and the last point is near the midchord of the wing root. The trajectory used to calculate heating rates at all body points is shown in figure 7. The first body point experiences the highest heating rate and surface temperature, therefore results for only this point are given in this brief paper.

MULTIWALL TPS AS AN ALTERNATIVE FOR LRSI

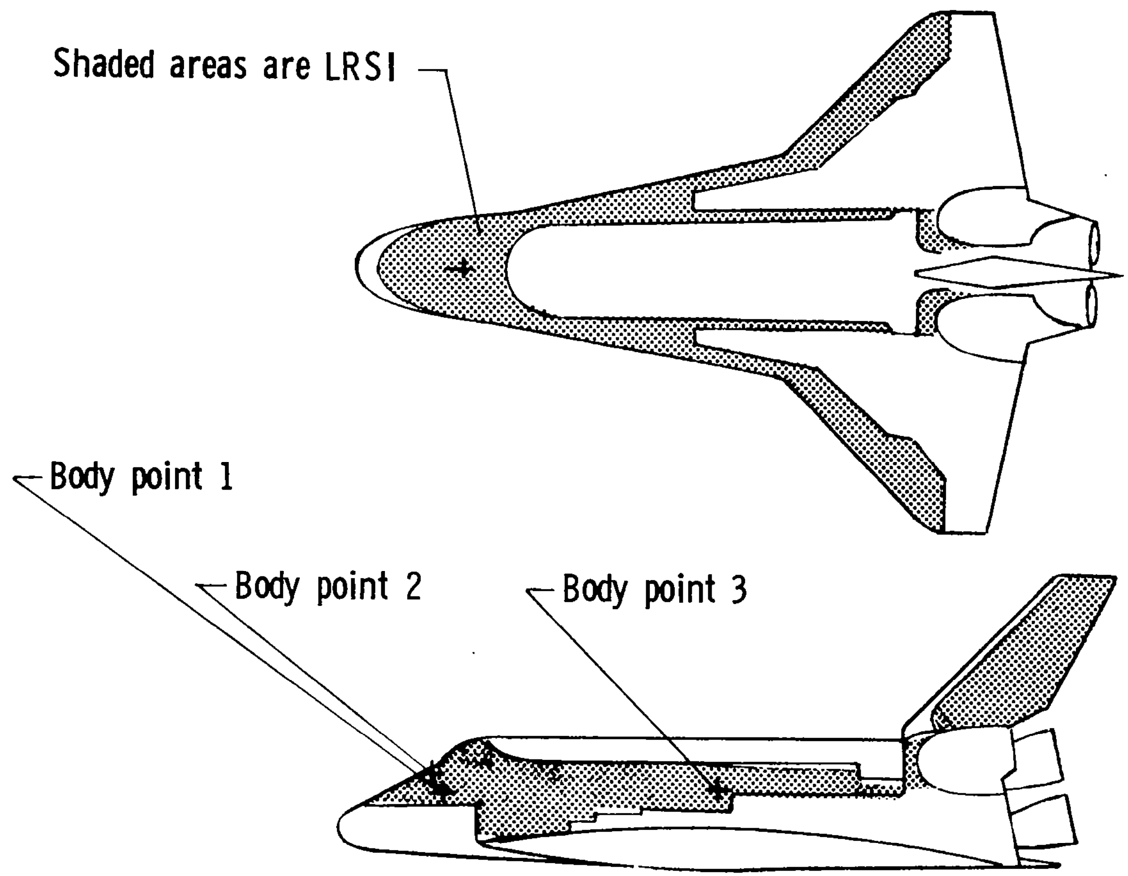

Figure 6

SHUTTLE TPS DESIGN TRAJECTORY

(Figure 7)

This figure shows the space shuttle trajectory used for design of the TPS. Critical parameters are altitude, velocity, and angle of attack. Each is shown as a function of time. Entry time is about half an hour.

SHUTTLE TPS DESIGN TRAJECTORY

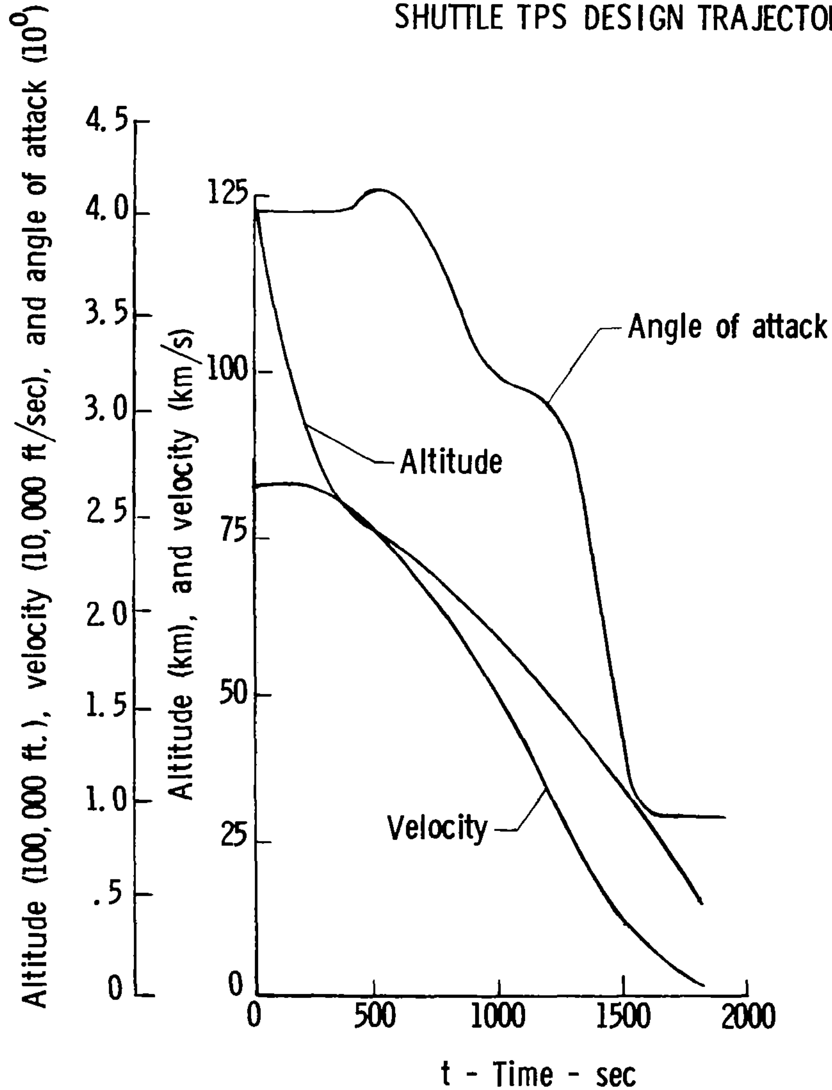

Figure 7

TEMPERATURE HISTORY OF SHUTTLE

(Figure 8)

Figure 8 shows temperature histories for the aerodynamic surface and the aluminum structure at the first body point. At this location, the peak temperature of the aerodynamic surface is 903 K (1166°F). Therefore, a bimetal multiwall TPS is used. The inner layers are titanium alloy and the outer layers are nickel alloy. Two emittance values were selected for analysis. An emittance of 0.2 represents the initial condition with polished foils and an emittance of 0.4 represents the condition after cyclic exposure. A further consideration is that voids between all layers are vented in the initial study of multiwall TPS. As seen in the figure, the structure temperature is less than the 450 K (350°F) allowable temperature. The thickness is equal to that of the LRSI system, and the thickness is about 70 percent greater than that required to satisfy LRSI thermal requirements. The increased thickness is necessary to fair from areas of higher heat load to areas of lower heat load. The availability of this increased thickness is principally responsible for vented multiwall satisfying the structural temperature limit. To reduce weight, evacuated titanium layers were analyzed. The resulting reduction in conductivity enables use of fewer and deeper layers to maintain the structural temperature limit. Figure 8 also shows the structure temperature history for evacuated titanium multiwall TPS. A dimple depth of about twice that of vented multiwall is used to reduce the density to 80.1 kg/m^3 (5 lbm/ft^3), which is half that of vented multiwall TPS.

TEMPERATURE HISTORY OF SHUTTLE
(BODY POINT 1)

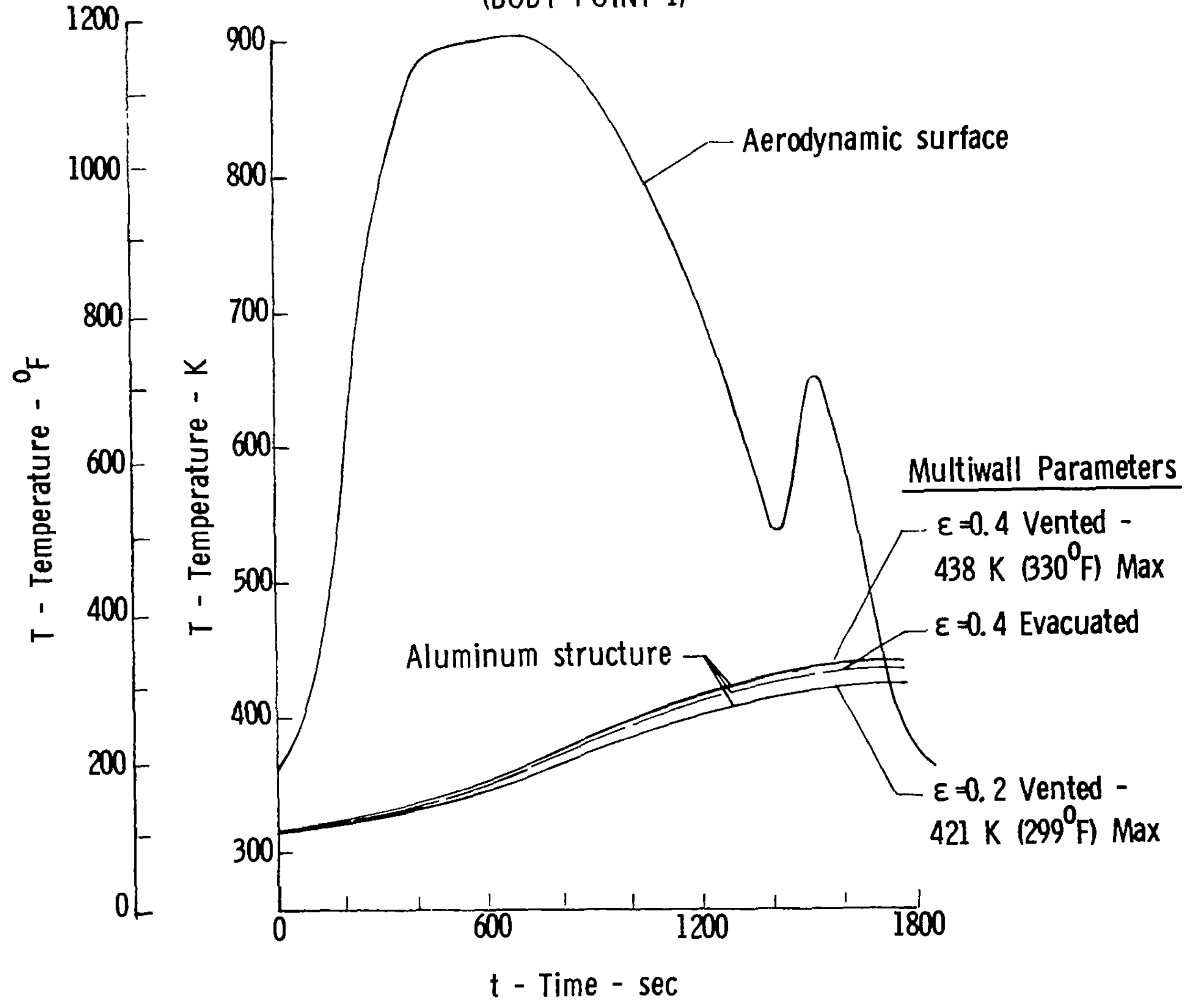

Figure 8

TEMPERATURE DISTRIBUTION THROUGH MULTIWALL TPS

(Figure 9)

The temperature distribution through the multiwall TPS at the time of peak heating is shown in figure 9. As indicated, the temperature distribution is nearly linear; consequently, the thermal stresses are small, which may be approximated by:

$$\sigma = E\alpha\Delta T$$

where the temperature difference is the difference between the actual temperature distribution and the linear distribution shown in figure 9. The maximum thermal stress is 68.95 MN/m^2 (10,000 psi) compression. Tensile thermal stress is very low - about 27.6 MN/m^2 (4,000 psi), thus fatigue and crack propagation are not likely modes of failure. This is true for other times during the trajectory, since the rate of change of heating rate is low throughout the 30 minute entry time. With simple support of the TPS panels, a center deflection of 0.254 cm (0.10 in.) occurs for 30.5 cm (12 in.) square panels. This deflection is elastic and is removed as the panel is cooled. In early studies of the space shuttle which considered metal shields, a permanent shield deflection of 1.27 cm (0.5 in.) in a 50.8 cm (20 in.) span was permitted before replacement of the shield. Therefore, the thermal bowing of multiwall TPS panels is within acceptable surface roughness for entry vehicles.

Two foil thicknesses are indicated in the figure. The original thicknesses are those used in previous multiwall development. The thinner gages were selected for current development to reduce the weight of multiwall TPS, as seen in the next figure.

TEMPERATURE DISTRIBUTION THROUGH MULTIWALL TPS

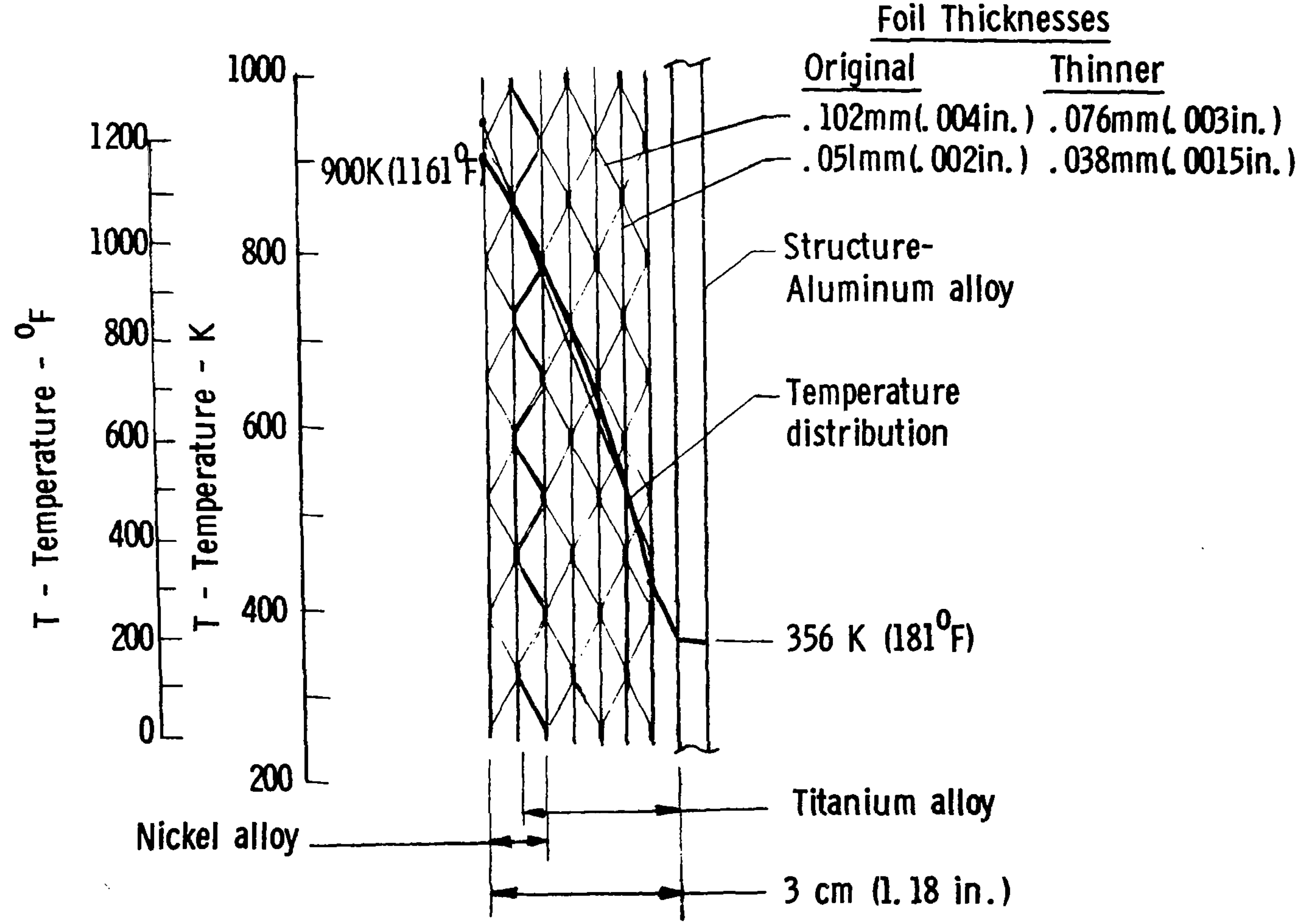

Figure 9

MASS COMPARISON OF MULTIWALL TPS AND LRSI-FIRST BODY POINT

(Figure 10)

This figure lists unit masses for multiwall TPS and LRSI for the first body point shown in figure 6. Vented multiwall TPS made of super alloy and titanium alloy has a mass of 6.78 kg/m^2 (1.39 lbm/ft^2); whereas, LRSI has a mass of 5.12 kg/m^2 (1.05 lbm/ft^2) at this location.

As indicated, multiwall TPS may be made as light as LRSI by either using thinner foils than fabricated in past developments or evacuating the titanium portion of the panels. Reducing foil thickness by about 25 percent appears to be the simpler way to reduce multiwall TPS mass. However, life and strength tests are needed to determine the least thickness of foils for a particular application.

Should developments lead to reliable evacuated panels, then the thinner foils with evacuation could save mass.

MASS COMPARISON OF MULTIWALL TPS AND LRSI

(FIRST BODY POINT)

PARAMETER	MULTIWALL TPS, kg/m^2 (lbm/ft^2)	LRSI, kg/m^2 (lbm/ft^2)	MASS DIFFERENCE, kg/m^2 (lbm/ft^2)
VENTED BIMETAL	6.78 (1.39)	5.12 (1.05)	+ 1.66 (0.34)
VENTED BIMETAL WITH THINNER FOILS	5.12 (1.05)	5.12 (1.05)	0.0 (0.0)
EVACUATED	5.12 (1.05)	5.12 (1.05)	0.0 (0.0)
EVACUATED AND WITH THINNER FOILS	4.29 (0.88)	5.12 (1.05)	- 0.83 (0.17)

Figure 10

ADVANCED SPACE TRANSPORT CONCEPT

(Figure 11)

In future space transportation systems multiwall TPS may find more extensive use than for the space shuttle. The next few figures describe the application of multiwall TPS to an advanced space transport concept.

Advanced space transportation systems may offer versatility through horizontal takeoff and economy through full reuse of all components. One concept employing near-art turbojet-powered boosters is shown in figure 11. To further assist in reusability, future transports may have a lower wing loading than the space shuttle. Consequently, the surface temperatures would be lower, allowing greater use of metallic TPS.

Since every pound saved in the thermal protection system is a pound of payload to orbit, it is essential to have a low mass TPS. However, current development of multiwall is focused on non-evacuated or vented multiwall TPS, thus performance analyses for the future space transport are for vented multiwall using the thinner gages.

ADVANCED SPACE TRANSPORT CONCEPT

(SPACEJET)

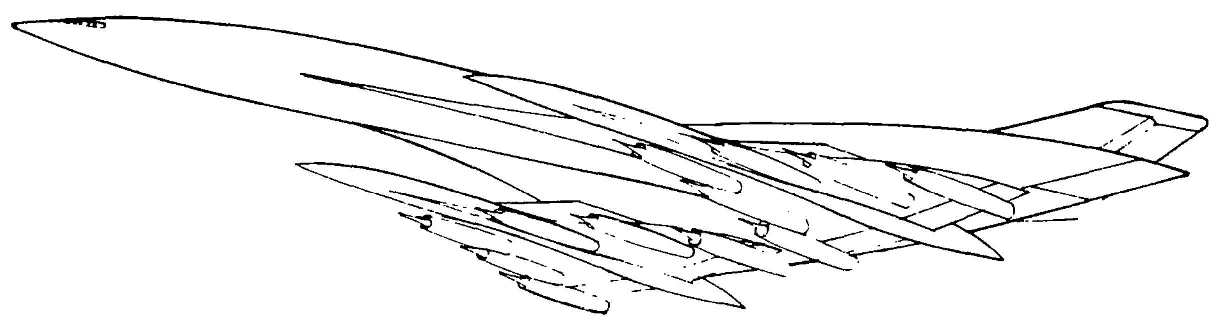

Figure 11

ENTRY TRAJECTORY FOR SPACEJET

(Figure 12)

Since the entry wing loading for the orbiter of figure 11 is about the same as the Boeing orbiter of reference 6, a trajectory similar to that of reference 6, given in figure 12, was used to calculate entry heating rates. Thermal analyses of multiwall TPS have been performed for the advanced space transport shown in figure 11. Of significance to the entry heating is the long duration of entry flight. The time is over one hour, more than twice that of the space shuttle. Increased entry time indicates increased heat load, which combined with onboard LH_2 tanks complicates the TPS. Presently available cryogenic insulations that have long life are polyurethane foams. These foams are limited to about 353 K (175°F), which is difficult to meet without a severe TPS mass penalty. The use of multiwall TPS to protect the foam is proposed for the advanced space transport.

ENTRY TRAJECTORY FOR SPACEJET

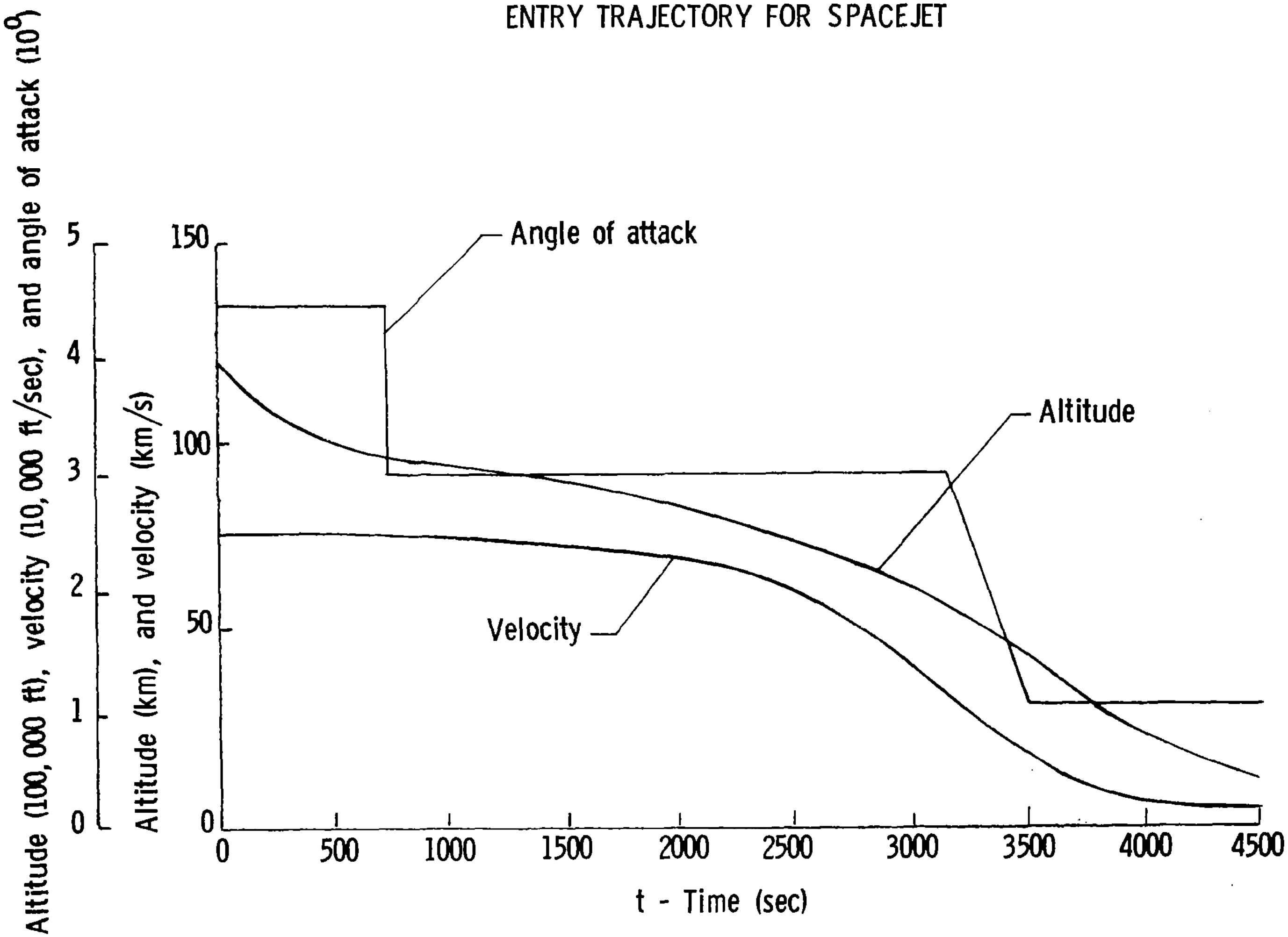

Figure 12

SPACEJET LH_2 TANK WALL

(Figure 13)

Since the location selected for analysis is the liquid hydrogen tank wall, a layer of closed-cell foam is applied to the outer surface of the aluminum integral tank. The sealed foam prevents cryopumping of air behind the multiwall TPS panels. Figure 13 shows the wall construction. An integrally zee-stiffened skin with ring stabilization serves as the integral tank-structure. Bonded to the outside of the tank skin is the closed-cell foam, covered by a Mylar-Aluminum-Mylar vapor barrier. The multiwall TPS panels protect the foam from the aerodynamic heating. Foam-filled multiwall pads are bonded to the tank wall. A clip is mounted on each multiwall pad for attaching the TPS panels. Nomex tape under panel edges prevents flow of air between the panels and the foam. The TPS thickness shown in this figure results in the temperatures shown in the next figure.

SPACEJET - LH_2 TANK WALL

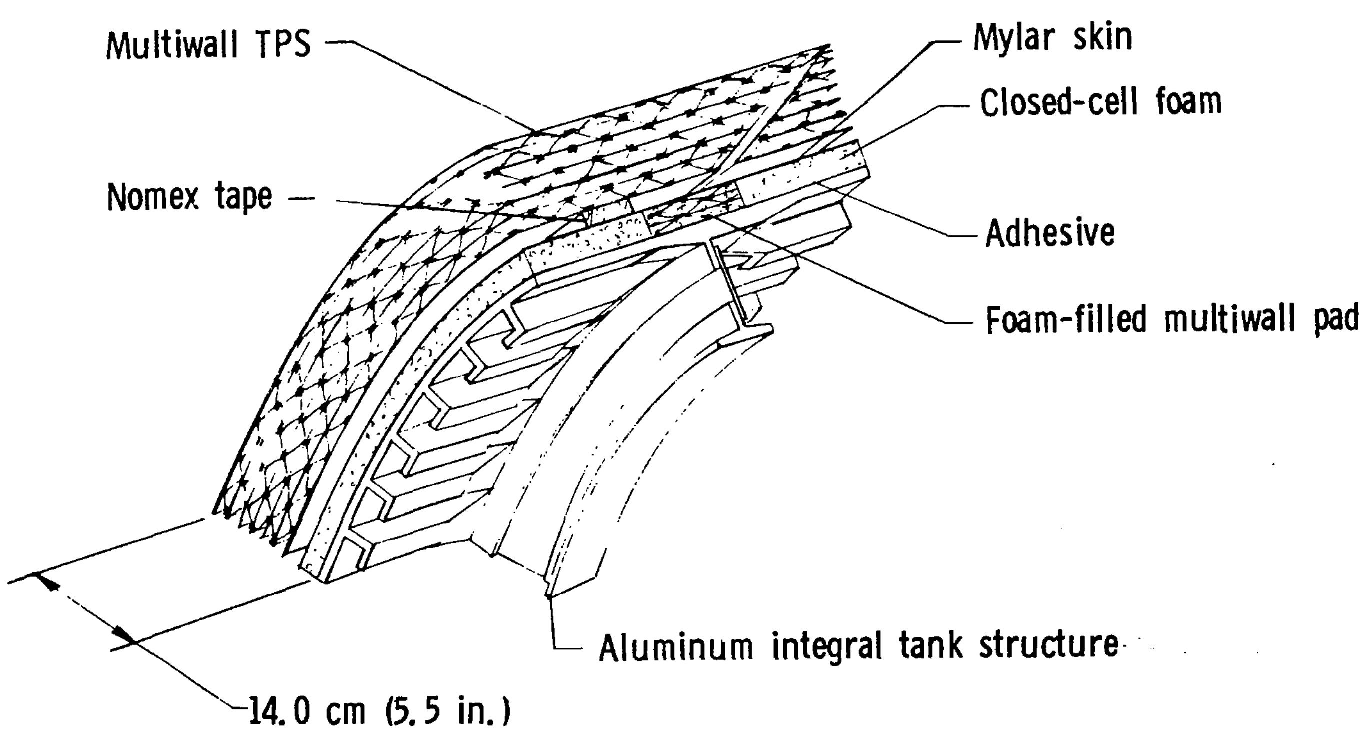

Figure 13

TEMPERATURE HISTORY FOR SPACEJET

(Figure 14)

Temperature history during entry for the lower surface of the Spacejet is shown in figure 14. As indicated, the hot face of the foam is near the 353 K (175°F) allowable temperature for an initial tank wall temperature of 144 K (-200°F). Also, the aerodynamic surface temperature is only 930 K (1215°F), much lower than the lower surface of the shuttle. This lower temperature is attributable to the lower wing loading of the Spacejet. At a weight of 17.1 kg/m^2 (3.5 lbm/ft^2) for integral tank structure, and at a total TPS weight of 19.5 kg/m^2 (4.0 lbm/ft^2), the wall weight is 36.6 kg/m^2 (7.5 lbm/ft^2). This mass is about 4.88 kg/m^2 (1.0 lbm/ft^2) greater than the shuttle which has no onboard LH_2 tanks. Thus, the combination of high cycle-life foams (ref. 7) and multiwall TPS enable use of a rather conventional aluminum structure for future space transports. However, a mass reduction of about 4.88 kg/m^2 (1.0 lbm/ft^2) could result through the development of a closed-cell foam that has long life at a reuse temperature of 478 K (400°F).

TEMPERATURE HISTORY FOR SPACEJET

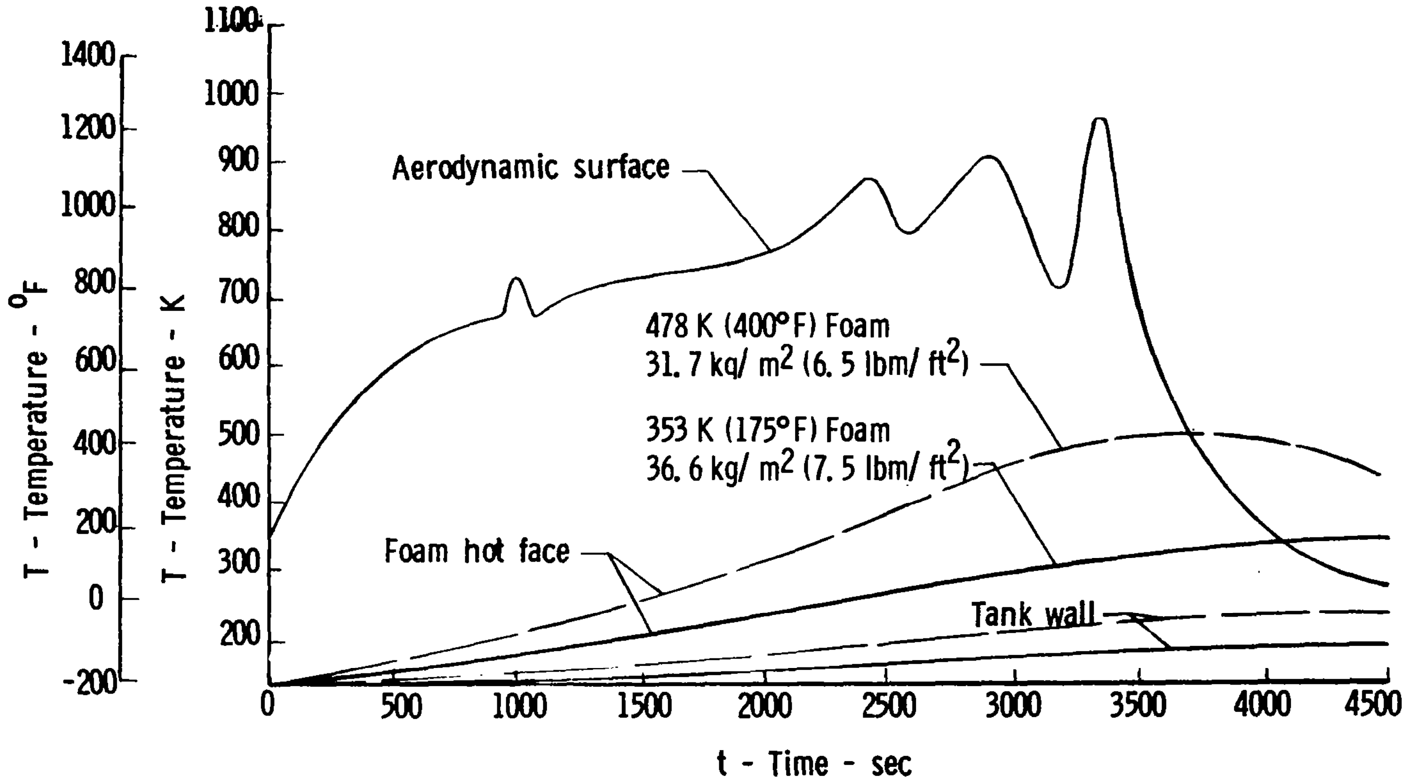

Figure 14

PLANNED MULTIWALL TPS TESTS

(Figure 15)

Although basic development has been performed on multiwall TPS, newer fabrication processes and foil thicknesses warrant further effort. Tests for strength of multiwall TPS panels are required, and true-temperature wind tunnel tests for determination of joint sealing effectiveness are essential. Moreover, flight demonstration on the space shuttle would increase confidence in multiwall TPS for future applications.

Figure 15 lists planned tests for multiwall TPS. Presently a contractual effort is underway for fabrication and tests of multiwall TPS tiles. These tests include material characterization and basic thermo-structural data determination of multiwall TPS.

The Johnson Space Center plans to perform radiant heating tests with a centerline joint between two panels. Moreover, their testing will include rain impingement for water retention.

Langley Research Center tests include sonic and thermal fatigue and cyclic exposure life determination. An array of multiwall TPS panels will be tested in the Langley 8-foot HTST for joint effectiveness prior to a flight experiment proposed for the shuttle. The next figure describes the 8-foot HTST test.

PLANNED MULTIWALL TPS TESTS

CONTRACTOR

- Strength of diffusion bonds
- Strength of thin-gage multiwall tiles
- Emittance of polished and unpolished foils
- Creep rate to 811 K (1000° F) of titanium alloy
- Thermal conductivity vs. temperature of multiwall TPS

JOHNSON SPACE CENTER

- Radiant heating of panels with a joint
- Rain impingement (water retention)

LANGLEY RESEARCH CENTER

- Sonic environment
- Cyclic heating (thermal fatigue and oxidation life)
- Mach 7 tunnel tests of a multiwall TPS tile array
- OEX flight experiment on the shuttle

Figure 15

MULTIWALL TPS PANEL ARRAY FOR MACH 7 TUNNEL TEST

(Figure 16)

The proposed Mach 7 tunnel test of an array of multiwall TPS panels is described in figure 16. The multiwall TPS panels will be mounted in a panel holder used for testing in the 8-Foot High Temperature Structures Tunnel at the Langley Research Center. Figure 16 shows the panel array in the holder. Nine 30.5 x 30.5 cm (12 x 12 in.) panels about 2.0 cm (0.8 in.) thick and made of the thinner foils are mounted in a cavity flush with the aerodynamic surface. The panels are mechanically attached to a simulated shuttle structure of aluminum. Panel edges are skewed to the stream and staggered. The panel holder will have an angle of attack sufficient to heat the TPS panels to 811 K (1000°F). Before and after aerothermal testing in the stream, the panels will be heated by a bank of quartz lamps in the pit of the tunnel. With controlled radiant heating, the entire temperature history of an entry vehicle may be simulated. Moreover, the time in the stream is deemed sufficient to test the flow seals to determine the effectiveness of the TPS panel joints in a simulated flight environment.

MULTIWALL TPS PANEL ARRAY FOR MACH 7 TUNNEL TESTS

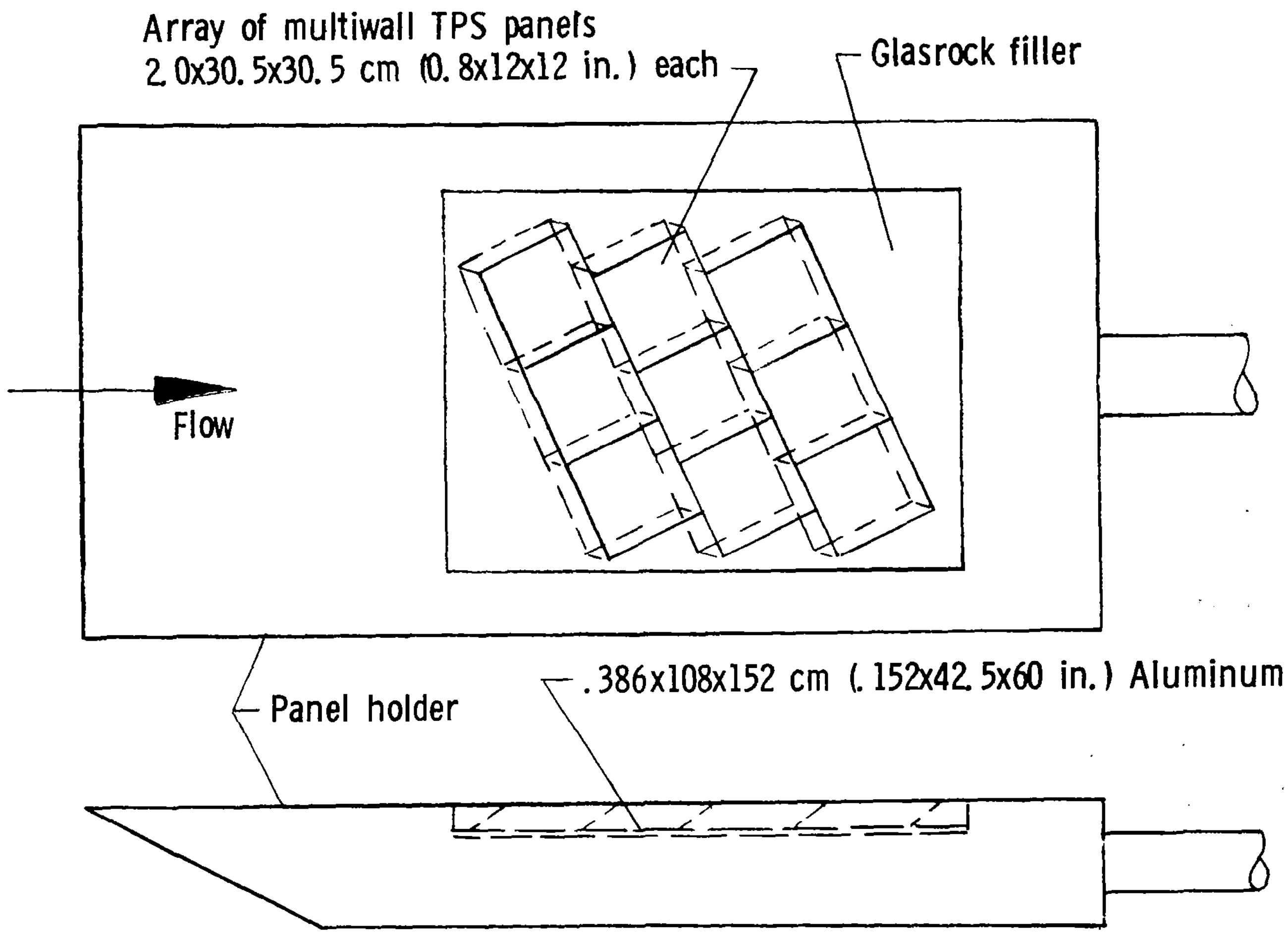

Figure 16

CONCLUDING REMARKS

The status of a metallic thermal protection system using load-bearing multiwall insulation is given. This review indicates that the tough efficient TPS provided by multiwall insulation is suited to future aerospace vehicles.

A study of multiwall TPS as an alternative to LRSI for the space shuttle indicated that vented multiwall, with foil thicknesses limited to those used in multiwall fabricated to date, is somewhat heavier than LRSI and with reduced foil thicknesses multiwall TPS may equal the weight of LRSI.

Metallic conduction through multiwall TPS transfers less heat than gas conduction or radiation. Radiation heat transfer is greatest at high temperatures; however, the number of layers selected can significantly reduce radiation. At low-to-intermediate temperatures, gas conduction transfers the most heat through multiwall TPS. Gas conduction may be eliminated by evacuation of panels. Oxidation rates will require a trade of foil thickness against life.

Multiwall TPS offers the ductile properties of tough metallic TPS and the simplicity of non-metallic TPS. However, one critically needed development is successful testing of an array of TPS panels in a hypervelocity environment.

SYMBOLS

A_m	fractional area of metallic conduction
E	modulus of elasticity
k	thermal conductivity
k_m	thermal conductivity of the metal
L	thickness of multiwall insulation
n	total number of foils
P	conduction path length
T	temperature
ΔT	temperature difference
t	time
α	coefficient of thermal expansion
ε	emittance
σ	stress

REFERENCES

1. Bohon, H. L.; Shideler, J. L.; and Rummler, D. R.: Radiative Metallic Thermal Protection Systems - A Status Report. Paper No. 77-391, AIAA/ASME 18th Structures, Structural Dynamics and Materials Conference, March 1977.

2. Strouhal, George; and Tillian, Donald J.: Testing the Shuttle Heat-Protection Armor. Astronautics and Aeronautics, Vol. 14, No. 1, January 1976.

3. Jackson, L. Robert; Davis, John G., Jr.; and Wichorek, Gregory R.: Structural Concepts for Hydrogen-Fueled Hypersonic Airplanes. NASA TN D-3162, February 1966.

4. Hirsch, Richard A.: Development of Techniques and Fabrication of a Structural Model for Research on Structures for Hypersonic Aircraft. NASA CR-66211, Martin-Marietta Corporation, 1966.

5. Ziendorf, L. R.; and Mies, G. E.: Investigation of Lightweight Self Evacuating Prefabricated Multi-layer Insulation System for Cryogenic Space Propulsion Stages. NASA CR-72017, Union Carbide, Linde Division, 1966.

6. Bangsund, Edward L., et.al: Technology Requirements for Advanced Earth-Orbital Transportation Systems. NASA CR-2879, The Boeing Company, 1977.

7. Sharpe, Ellsworth L., and Helenbrook, Robert G.: Durability of Foam Insulation for LH_2 Fuel Tanks of Future Subsonic Transports. Presented at the International Cryogenic Materials Conference, Nonmetallic Materials and Composites at Low Temperatures, Munich, West Germany, July 10-11, 1978.

DRYDEN FLIGHT RESEARCH CENTER

HOT STRUCTURES RESEARCH

ROGER A. FIELDS

NASA DRYDEN FLIGHT RESEARCH CENTER

DRYDEN FLIGHT RESEARCH CENTER HOT STRUCTURES RESEARCH OBJECTIVES

(FIGURE 1)

DRYDEN'S CURRENT HYPERSONIC VEHICLE HOT STRUCTURES RESEARCH PROGRAM DATES BACK TO 1969. OUR ORIGINAL OBJECTIVE WAS TO ESTABLISH A RESEARCH PROGRAM TO STUDY FLIGHT LOADS MEASUREMENT ON STATE-OF-THE-ART HOT STRUCTURAL CONCEPTS. THE NATURAL FALLOUTS OF SUCH A PROGRAM ARE:

1. TO DEVELOP AND UTILIZE THE LATEST ADVANCEMENTS IN HIGH TEMPERATURE STRAIN GAGE TECHNOLOGY
2. TO GAIN EXPERIENCE IN DESIGNING AND FABRICATING REALISTIC FLIGHT HARDWARE FOR LABORATORY TESTING
3. TO EVALUATE LIGHTWEIGHT HOT STRUCTURE CONCEPTS
4. TO PROVIDE EXPERIMENTAL DATA FOR EVALUATION OF STRUCTURAL ANALYSIS AND DESIGN METHODS
5. TO ADVANCE TESTING TECHNIQUES AND CAPABILITIES.

OUR PROGRAM EFFORT HAS BEEN ONE OF BOTH EXPERIMENTAL AND THEORETICAL WORK; THE PRIMARY EMPHASIS, HOWEVER, HAS BEEN ON THE EXPERIMENTAL PORTION BECAUSE OF THE UNIQUE CAPABILITIES THAT EXIST AT DRYDEN. AN OVERVIEW OF DRYDEN'S HOT STRUCTURES PROGRAM AND A SUMMARY OF THE STRUCTURAL TEST CAPABILITIES WILL BE PRESENTED.

DRYDEN FLIGHT RESEARCH CENTER HOT STRUCTURES RESEARCH OBJECTIVES

- <u>FLIGHT LOADS MEASUREMENT RESEARCH</u>
- UTILIZE HIGH TEMPERATURE STRAIN GAGE TECHNOLOGY
- DESIGN AND FABRICATION OF REALISTIC FLIGHT HARDWARE
- EVALUATE LIGHTWEIGHT STRUCTURE CONCEPTS
- EVALUATE STRUCTURAL ANALYSIS AND DESIGN METHODS
- ADVANCE TEST TECHNIQUES AND CAPABILITIES

Figure 1

DFRC FLIGHT LOADS RESEARCH FACILITY
(FIGURE 2)

THE FLIGHT LOADS RESEARCH FACILITY WAS CONSTRUCTED IN 1966 TO FULFILL A REQUIREMENT OF MEASURING FLIGHT LOADS ON AIRCRAFT AT SUPERSONIC AND HYPERSONIC SPEEDS. THE PROBLEMS INVOLVED IN MEASURING LOADS WITH STRAIN GAGES IN THE RESULTING ELEVATED TEMPERATURE ENVIRONMENTS REQUIRED THE CAPABILITY TO HEAT AND LOAD AIRCRAFT UNDER SIMULATED FLIGHT CONDITIONS. THE FACILITY DOES HAVE THE CAPABILITY OF TESTING BOTH STRUCTURAL COMPONENTS AND COMPLETE VEHICLES UNDER THE COMBINED EFFECTS OF LOADS AND TEMPERATURES, AND CALIBRATING AND EVALUATING FLIGHT LOADS INSTRUMENTATION UNDER CONDITIONS EXPECTED IN FLIGHT.

DFRC FLIGHT LOADS RESEARCH FACILITY

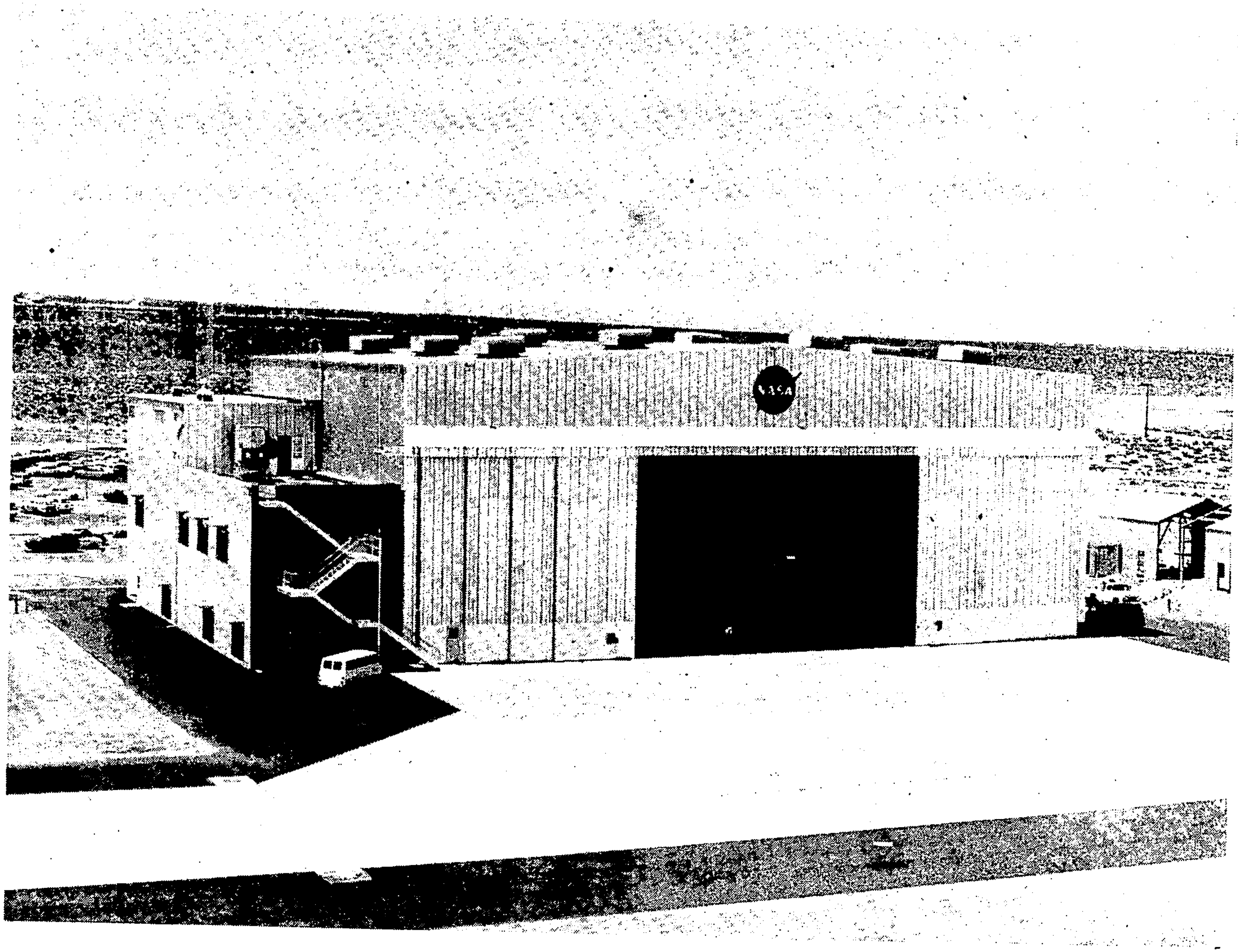

Figure 2

DFRC FLIGHT LOADS RESEARCH FACILITY CAPABILITIES

(FIGURE 3)

THE CAPABILITIES OF THE FACILITY ARE SUMMARIZED HERE. THE ELECTROHYDRAULIC LOADING SYSTEM CONSISTS OF 24 CHANNELS OF CLOSED-LOOP CONTROL. NUMEROUS FAIL-SAFE PROVISIONS ARE INCORPORATED INTO THE LOADING SYSTEM TO INSURE THE SAFETY OF FLIGHT VEHICLES. STRUCTURAL HEATING TESTS USING INFRARED QUARTZ LAMPS CAN BE CONDUCTED WITH EITHER OF TWO HEATING CONTROL SYSTEMS. THE FIRST IS AN ANALOG SYSTEM WITH A CAPABILITY OF PROVIDING 24 CHANNELS OF HEATING CONTROL. EACH CHANNEL HAS A POWER CAPABILITY OF 100 KILOWATTS. THE SECOND HEATING SYSTEM IS A DIGITAL ONE UTILIZING THE FACILITY'S DATA ACQUISITION AND CONTROL SYSTEM. THIS HEATING SYSTEM HAS THE CAPABILITY OF CONTROLLING UP TO 512 INDEPENDENT CONTROL ZONE AREAS WITH A TOTAL OF 20 MEGAWATTS OF ELECTRICAL POWER FOR A SINGLE TEST. THE DATA ACQUISITION SYSTEM HAS 12 SITES, EACH OF WHICH CAN ACCOMMODATE UP TO 100 TRANSDUCERS. THE TOTAL SYSTEM CAN, THEREFORE, HANDLE 1200 CHANNELS OF DATA. TRANSDUCER DATA CAN BE RECORDED IN RANGES FROM ± 5 mV TO ± 4 V. THE TRANSDUCER SIGNAL FROM THE SITES IS RELAYED TO THE CENTRAL CONTROL SYSTEM AND A HIGH-SPEED DIGITAL COMPUTER. THE COMPUTER FORMATS THE INCOMING DIGITAL DATA FOR RECORDING ON ONE OF TWO MAGNETIC TAPE UNITS. THERE ARE 92 POSSIBLE CHANNELS OF DATA THAT MAY BE DISPLAYED (EITHER REAL-TIME OR POST-TEST) BY THE SYSTEM ON STRIPCHARTS, A CRT, XY-PLOTTERS, A LINE PRINTER, AND ON A COMMUNICATION TERMINAL TV SCREEN. WHEN CONDUCTING HEATING TESTS, THE NORMAL CRT DISPLAY MAY BE REPLACED BY A DISPLAY OF THE DIFFERENCE BETWEEN THE MEASURED AND PROGRAMMED TEMPERATURES AT ALL CONTROL LOCATIONS. THIS ENABLES THE TEST CONDUCTOR TO ASSESS THE STATUS OF A LARGE SCALE HEATING TEST WITH ONE GLANCE.

DFRC FLIGHT LOADS RESEARCH FACILITY CAPABILITIES

LOADING

24 CHANNEL CLOSED-LOOP CONTROL ELECTROHYDRAULIC SYSTEM

HEATING

24 CHANNEL ANALOG SYSTEM / 100 KILOWATTS PER CHANNEL

512 CHANNEL DIGITAL SYSTEM / 20 MEGAWATTS TOTAL

DATA ACQUISITION

12 DATA ACQUISITION SITES / 100 CHANNELS EACH MEASUREMENT RANGES FROM $\pm$ 5 mV TO $\pm$ 4 V

DATA RECORDING / 2 MAGNETIC TAPE UNITS

DATA DISPLAY

92 CHANNELS OF DISPLAYED DATA

DISPLAY DEVICES / STRIPCHARTS, CRT, XY-PLOTTERS, LINE PRINTER, COMMUNICATION TERMINAL

Figure 3

DRYDEN FLIGHT RESEARCH CENTER HOT STRUCTURES PROGRAM

(FIGURE 4)

DRYDEN'S HOT STRUCTURES PROGRAM FOR HYPERSONIC VEHICLES WAS A FALLOUT OF A LANGLEY CONTRACT TO LOCKHEED. PROMISING HOT STRUCTURE WING CONCEPTS WERE IDENTIFIED IN THAT WORK. AS A RESULT, DRYDEN AWARDED A CONTRACT TO NORTH AMERICAN ROCKWELL TO CONSTRUCT A SINGLE-CELL BOX UTILIZING THE BEADED SKIN CONCEPT FOR EXPERIMENTAL TESTING AT DRYDEN. DURING THE COURSE OF THIS TEST PROGRAM, ANOTHER CONTRACT WAS LET TO MARTIN MARIETTA TO DESIGN AND CONSTRUCT A REALISTIC PORTION OF THE WING ON A MACH 8 RESEARCH VEHICLE. THIS TEST ARTICLE WAS ALSO TO INCORPORATE THE BEADED PANEL CONCEPT AND WOULD UNDERGO AN EXTENSIVE HEATING AND LOADING TEST PROGRAM AT DRYDEN. AT THE CONCLUSION OF SUCCESSFUL TESTS OF THE BEADED PANEL CONCEPT, THE MOST CRITICALLY LOADED BEADED PANELS WERE REPLACED ON THE WING STRUCTURE WITH ADVANCED TUBULAR PANELS THAT HAD BEEN DESIGNED AND CONSTRUCTED BY THE BOEING COMPANY UNDER A CONTRACT FROM LANGLEY.

THE OTHER IMPORTANT INGREDIENT TO OUR PROGRAM WAS THE DEVELOPMENT OF A HIGH TEMPERATURE CAPACITIVE STRAIN GAGE SYSTEM. THIS SYSTEM PROVIDED MEASUREMENTS OF STRAIN AT TEMPERATURES UP TO 1089 K (1500 °F). THE SYSTEM WAS DEVELOPED UNDER A NASA CONTRACT TO THE BOEING CO.

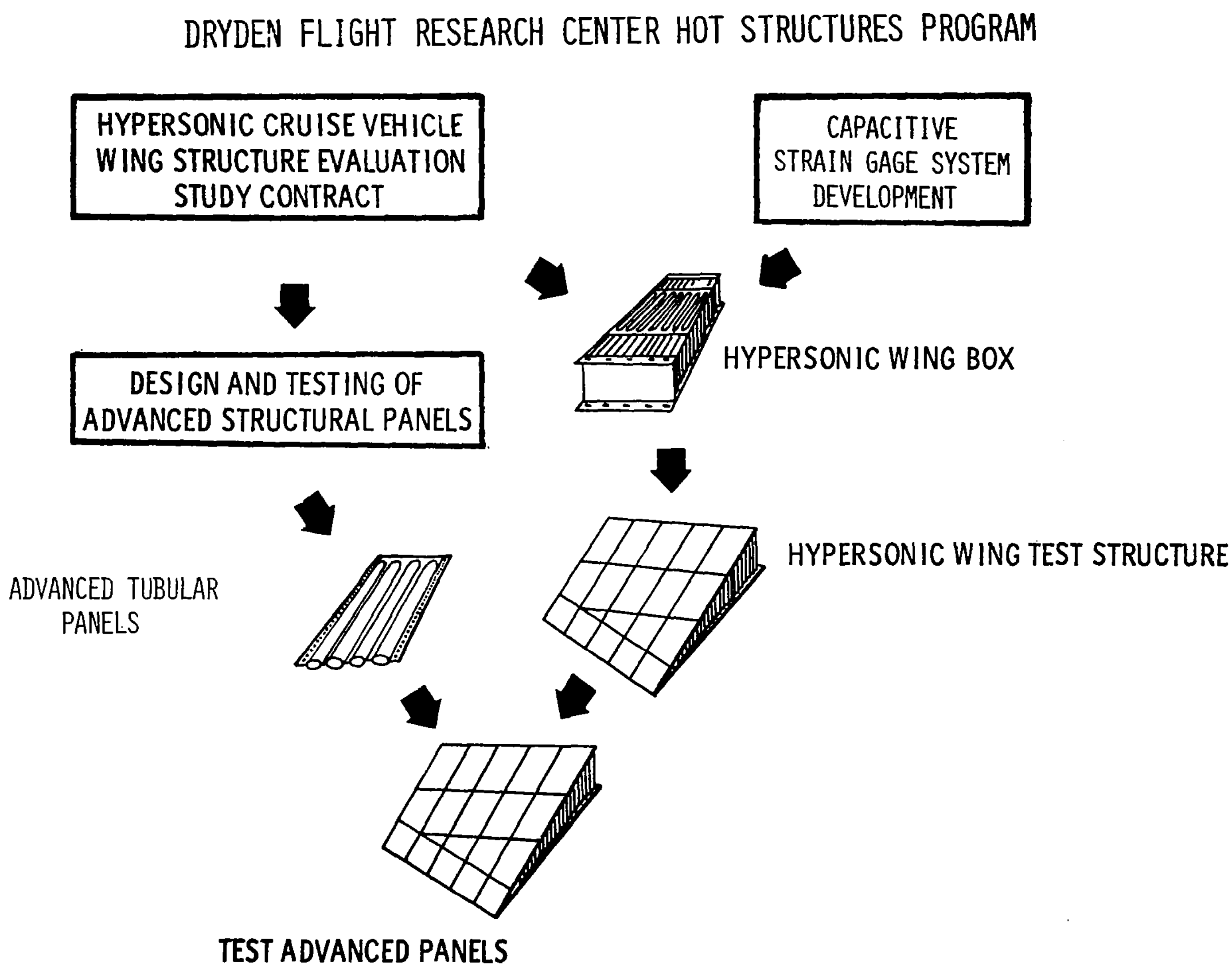
DRYDEN FLIGHT RESEARCH CENTER HOT STRUCTURES PROGRAM
HYPERSONIC CRUISE VEHICLE WING STRUCTURE EVALUATION STUDY CONTRACT
CAPACITIVE STRAIN GAGE SYSTEM DEVELOPMENT
HYPERSONIC WING BOX
DESIGN AND TESTING OF ADVANCED STRUCTURAL PANELS
HYPERSONIC WING TEST STRUCTURE
ADVANCED TUBULAR PANELS
TEST ADVANCED PANELS

Figure 4

DESIGN DATA FOR DELTA WING X-15 AND HYPERSONIC WING BOX
(FIGURE 5)

THE DESIGN OF THE WING BOX OF THE ROCKWELL CONTRACT WAS BASED ON AVAILABLE DESIGN DATA FOR THE PROPOSED DELTA-WING X-15 AIRPLANE. THE CRITICAL DESIGN PARAMETERS FOR THE WING BOX, BASED ON A THERMO-STRUCTURAL MISSION, WERE A PEAK VELOCITY OF 2320 M/SEC (7600 FT/SEC) AT AN ALTITUDE OF 25,300 M (83,000 FT), A DYNAMIC PRESSURE OF 105 kN/m^2 (2200 LB/FT^2), AND A NORMAL LOAD FACTOR OF 3 G'S. AN AREA OF THE WING ROOT NEAR THE AFT PORTION OF THE WING WAS IDENTIFIED AS THE MOST CRITICALLY LOADED. THE DESIGN OF THE WING BOX WAS, THEREFORE, BASED ON THE LOADS AND TEMPERATURES FOR THAT LOCATION.

DESIGN DATA FOR DELTA WING X-15 AND HYPERSONIC WING BOX

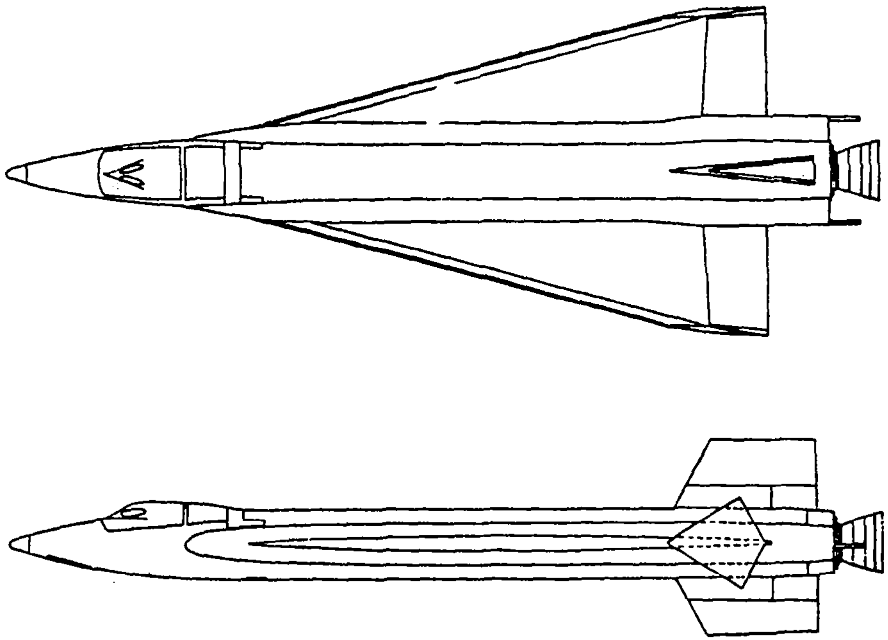

LAUNCH WEIGHT = 247 KN (55,500 LB)

LANDING WEIGHT = 79 KN (17,800 LB)

MAX VELOCITY = 2,460 M/SEC (8,060 FT/SEC)

WING DESIGN

VELOCITY = 2,320 M/SEC (7,600 FT/SEC)

ALTITUDE = 25,300 M (83,000 FT)

DYNAMIC PRESSURE = 105 KN/M^2 (2,200 LB/FT^2)

NORMAL ACCELERATION = 3 G

Figure 5

HYPERSONIC WING-BOX HARDWARE
(FIGURE 6)

THE HARDWARE DELIVERED TO DRYDEN CONSISTED OF THIS SINGLE-CELL BOX EMPLOYING THE BEADED PANEL CONCEPT AND CORRUGATED SPARS AND WEBS. THIS STRUCTURE WAS FABRICATED WITH RENÉ 41. THREE ADDITIONAL BEADED PANELS OF STAINLESS STEEL WERE ALSO PROVIDED UNDER THE CONTRACT FOR INDEPENDENT LOADING TESTS AT ROOM TEMPERATURE.

HYPERSONIC WING-BOX HARDWARE

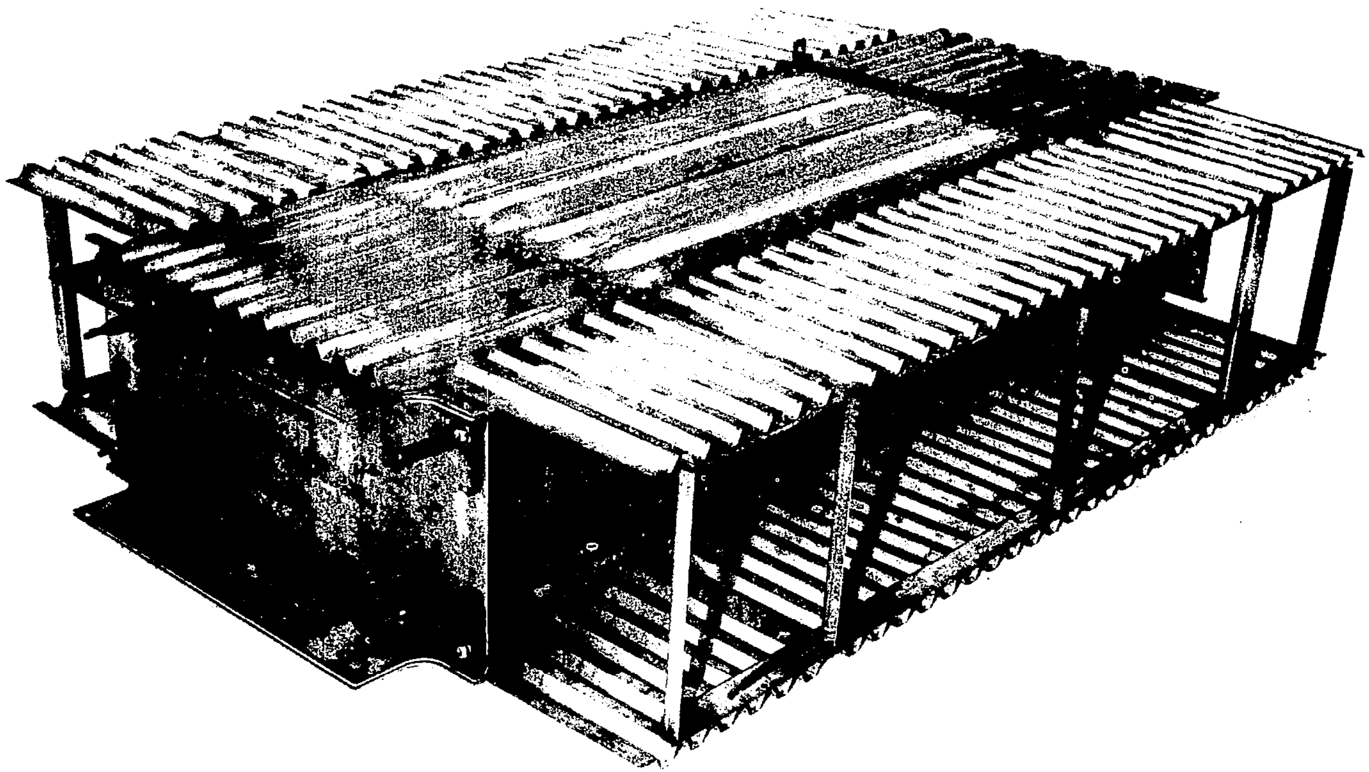

Figure 6

ROOM TEMPERATURE BEADED PANEL TEST RESULTS
(FIGURE 7)

THE RESULTS OF INPLANE SHEAR, COMPRESSION, AND NORMAL PRESSURE LOAD TESTS ON THE BEADED PANELS ARE SHOWN HERE. IN EACH CASE, THE FAILURE LOADS EXCEEDED THE DESIGN ULTIMATE LOADS.

ROOM TEMPERATURE BEADED PANEL TEST RESULTS

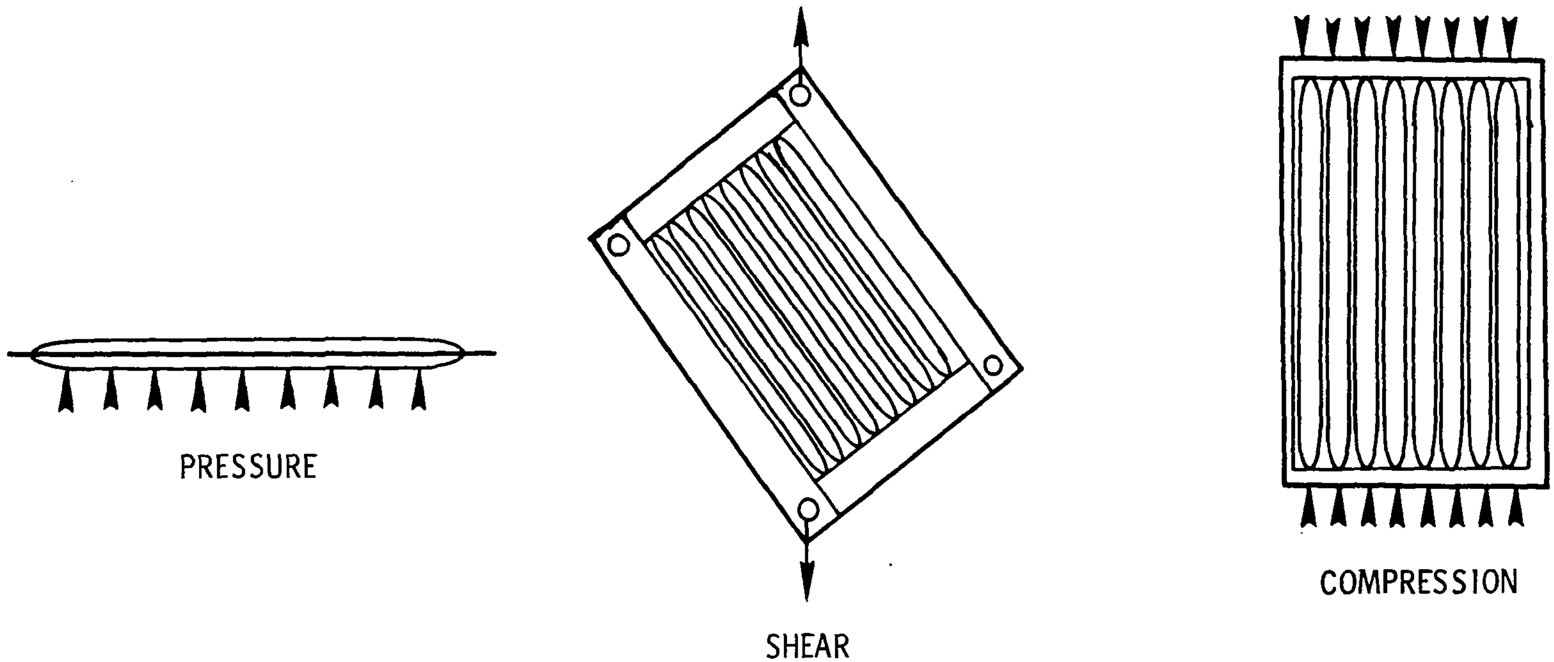

PANEL	DESIGN ULTIMATE	FAILURE LOAD/MODE
PRESSURE	6.5 N/CM^2 (9.4 PSI)	9.7 N/CM^2 (14.1 PSI)/LOCAL
SHEAR	700 N/CM (400 LB/IN.)	960 N/CM (550 LB/IN.)
COMPRESSION	1930 N/CM (1100 LB/IN.)	2360 N/CM (1350 LB/IN.)/DIAGONAL

Figure 7

SIGNIFICANT HYPERSONIC BOX TEST RESULTS
(FIGURE 8)

A TOTAL OF 36 TESTS WERE CONDUCTED ON THE BOX STRUCTURE. THIRTEEN OF THOSE TESTS WERE CARRIED OUT TO INDICATED FAILURES USING A REAL TIME FORCE STIFFNESS TECHNIQUE. THE BEADED TEST PANEL OF THE BOX FAILED DURING A TEST TO 560 K (550^{0} F) AT A LOAD APPROXIMATELY 20 PERCENT ABOVE THE DESIGN ULTIMATE LOAD FOR THE PANEL AT THAT TEMPERATURE. CAPACITANCE STRAIN GAGES THAT HAD BEEN INSTALLED ON THE TEST PANEL WERE UTILIZED IN TESTS TO 922 K (1200^{0} F). IN GENERAL, THE GAGES OPERATED SATISFACTORILY, BUT SOME PROBLEMS WITH THE STRAIN GAGE WIRING WERE IDENTIFIED

SIGNIFICANT HYPERSONIC BOX TEST RESULTS

- A TOTAL OF 36 TESTS WERE CONDUCTED ON THE BOX
- 13 OF THE TESTS WERE CARRIED OUT TO INDICATED FAILURES USING A REAL TIME FORCE-STIFFNESS TECHNIQUE
- PANEL FAILURE EXCEEDED DESIGN ULTIMATE
- HIGH TEMPERATURE CAPACITANCE STRAIN GAGES USED AT 922 K (1200 $^{\circ}$F)

Figure 8

TEST SETUP FOR HWTS
(FIGURE 9)

THE NEXT STRUCTURE TO BE TESTED IN OUR PROGRAM WAS THE HYPERSONIC WING TEST STRUCTURE. THE WING WAS DESIGNED FOR CRUISE AT MACH 8 WITH A NORMAL ACCELERATION OF 2.5 G'S AND A DYNAMIC PRESSURE OF 83.8 kN/m^2 (1750 LB/FT^2). THE TEST SETUP WAS DESIGNED SO THAT TWO LARGE INFRARED HEATERS COULD BE ROLLED IN PLACE OR REMOVED EASILY FROM THE WING STRUCTURE. THE HEATING SYSTEM USES 89 INDEPENDENTLY CONTROLLED TEMPERATURE ZONES TO PROVIDE THE REQUIRED MACH 8 TEMPERATURE PROFILES WITH MAXIMUM HEAT SHIELD TEMPERATURES OF 1310 K (1900 ^{o}F). HORIZONTAL AND VERTICAL LOADING OF THE STRUCTURE IS ACCOMPLISHED THROUGH THE USE OF 20 HYDRAULIC JACKS. THE UNISTRUT FRAMEWORK, SHOWN ABOVE THE WING, WAS USED TO SUPPORT DISPLACEMENT TRANSDUCERS DURING ROOM TEMPERATURE TESTS. THE WING WAS INSTRUMENTED FOR THE PURPOSES OF STUDYING FLIGHT LOADS MEASUREMENT, FOR STRAIN, DEFLECTION AND TEMPERATURE MEASUREMENTS TO COMPARE WITH ANALYSIS AND DESIGN DATA, AND FOR TEST MONITORING AND CONTROL. THE TOTAL NUMBER OF DATA CHANNELS WAS 824. THE TESTING PROGRAM INCLUDED LOAD CALIBRATIONS AT ROOM TEMPERATURE, AND DESIGN ULTIMATE LOADS AT ROOM TEMPERATURE AND MACH 8 PROFILE TEMPERATURE. TESTING OF THE WING STRUCTURE HAS BEEN SUCCESSFULLY COMPLETED WITH THE BEADED PANEL CONCEPT. THE MOST CRITICALLY LOADED PANELS ALONG THE WING ROOT HAVE BEEN REPLACED WITH ADVANCED TUBULAR PANELS AND TESTING IS CURRENTLY IN PROGRESS.

TEST SETUP FOR HWTS

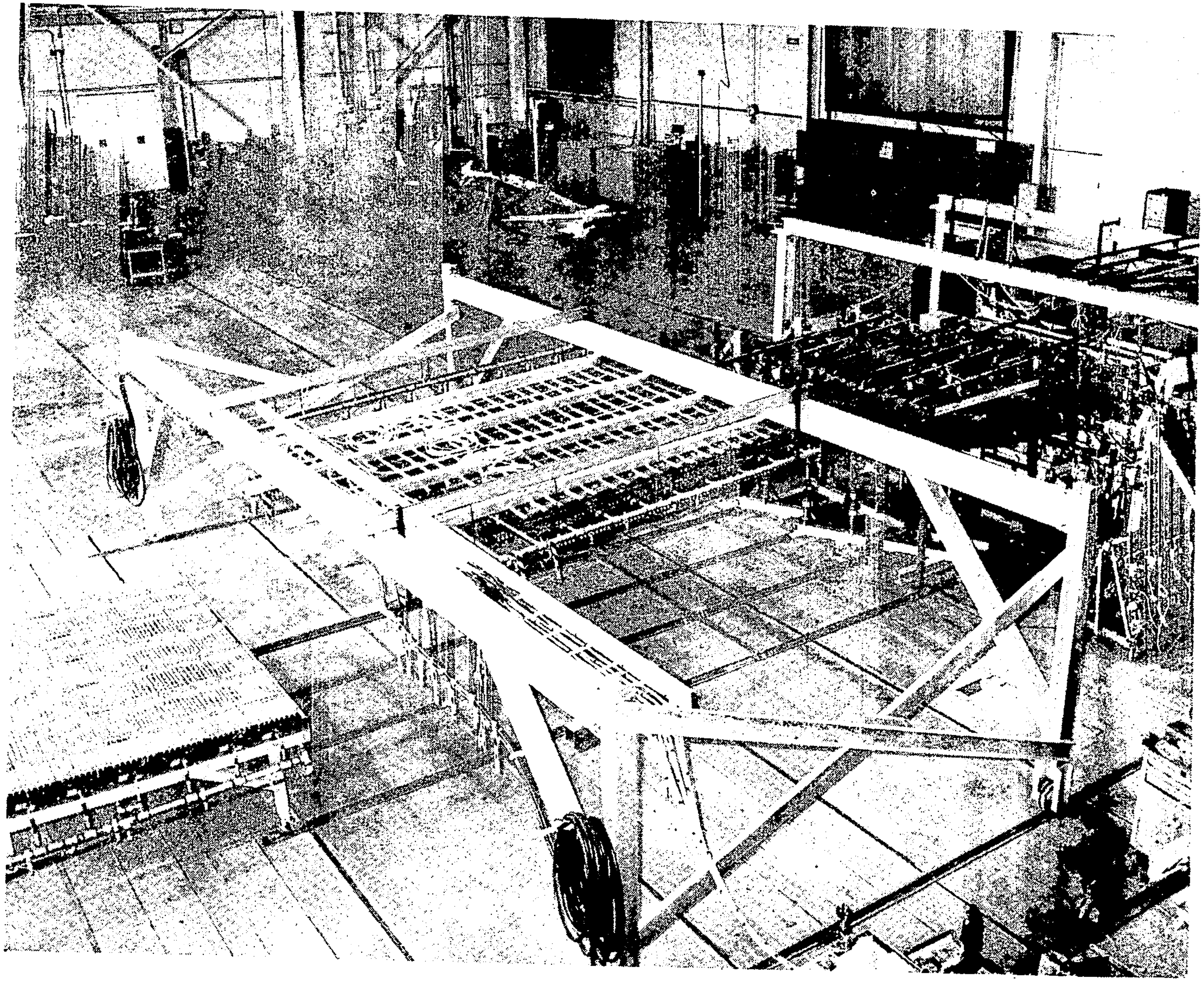

Figure 9

BEADED PANEL COMPRESSION TEST
(FIGURE 10)

UNDER A GRANT TO THE UNIVERSITY OF KANSAS, A STUDY WAS CONDUCTED ON AN INDIVIDUAL BEADED PANEL FROM THE HYPERSONIC WING TEST STRUCTURE. THE PANEL WAS TESTED AT ROOM TEMPERATURE UNDER A COMPRESSIVE LOAD TO FAILURE; THE FAILURE MODE AND LOAD WERE COMPARED WITH DESIGN PREDICTIONS AND TO A NASTRAN ANALYSIS. DURING TESTING, A MOIRÉ FRINGE TECHNIQUE WAS USED TO DEFINE OUT-OF-PLANE PANEL DEFORMATIONS.

BEADED PANEL COMPRESSION TEST

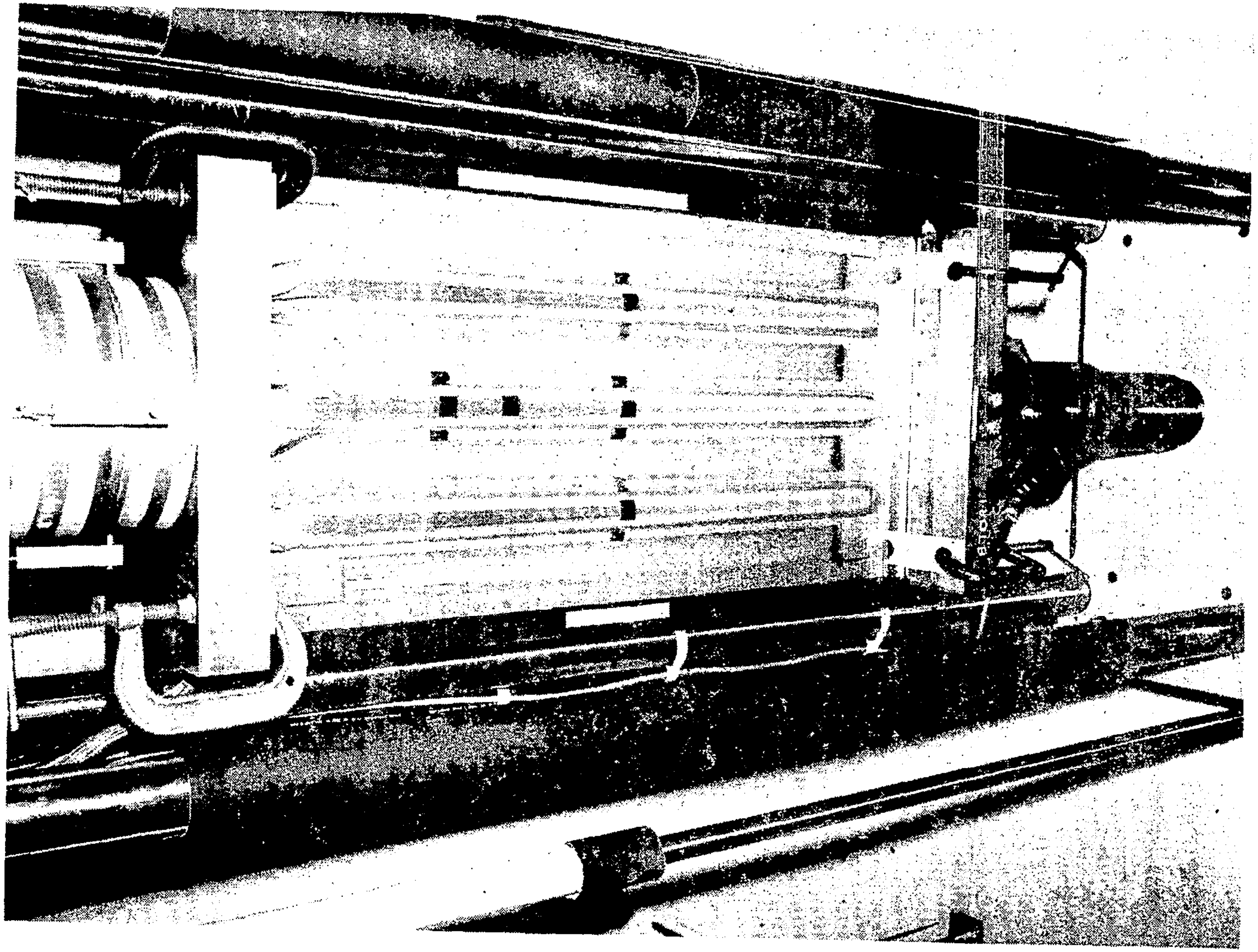

Figure 10

MOIRÉ FRINGE PHOTOGRAPH

(NO LOAD)

(FIGURE 11)

THE MOIRÉ FRINGE PATTERN THAT WAS ESTABLISHED ON THE PANEL AT A NO-LOAD CONDITION IS SHOWN. A GLASS WITH A GRID OF PARALLEL LINES IS SUPPORTED IMMEDIATELY IN FRONT OF THE PANEL AND A LIGHT SOURCE WAS POSITIONED ABOVE AND IN FRONT OF THE PANEL. INTERFERENCE FRINGES ARE PRODUCED ON THE PANEL SURFACE; PRODEEDING FROM ONE FRINGE TO AN ADJACENT FRINGE REPRESENTS A CHANGE OF OUT-OF-PLANE DISTANCE OF 1.22 MM (0.048 IN.). ALL POINTS ALONG A PARTICULAR FRINGE ON THE PANEL, SUCH AS THE PEAK OF A BEAD, ARE A CONSTANT DISTANCE FROM THE GRID GLASS.

MOIRÉ FRINGE PHOTOGRAPH
(NO LOAD)

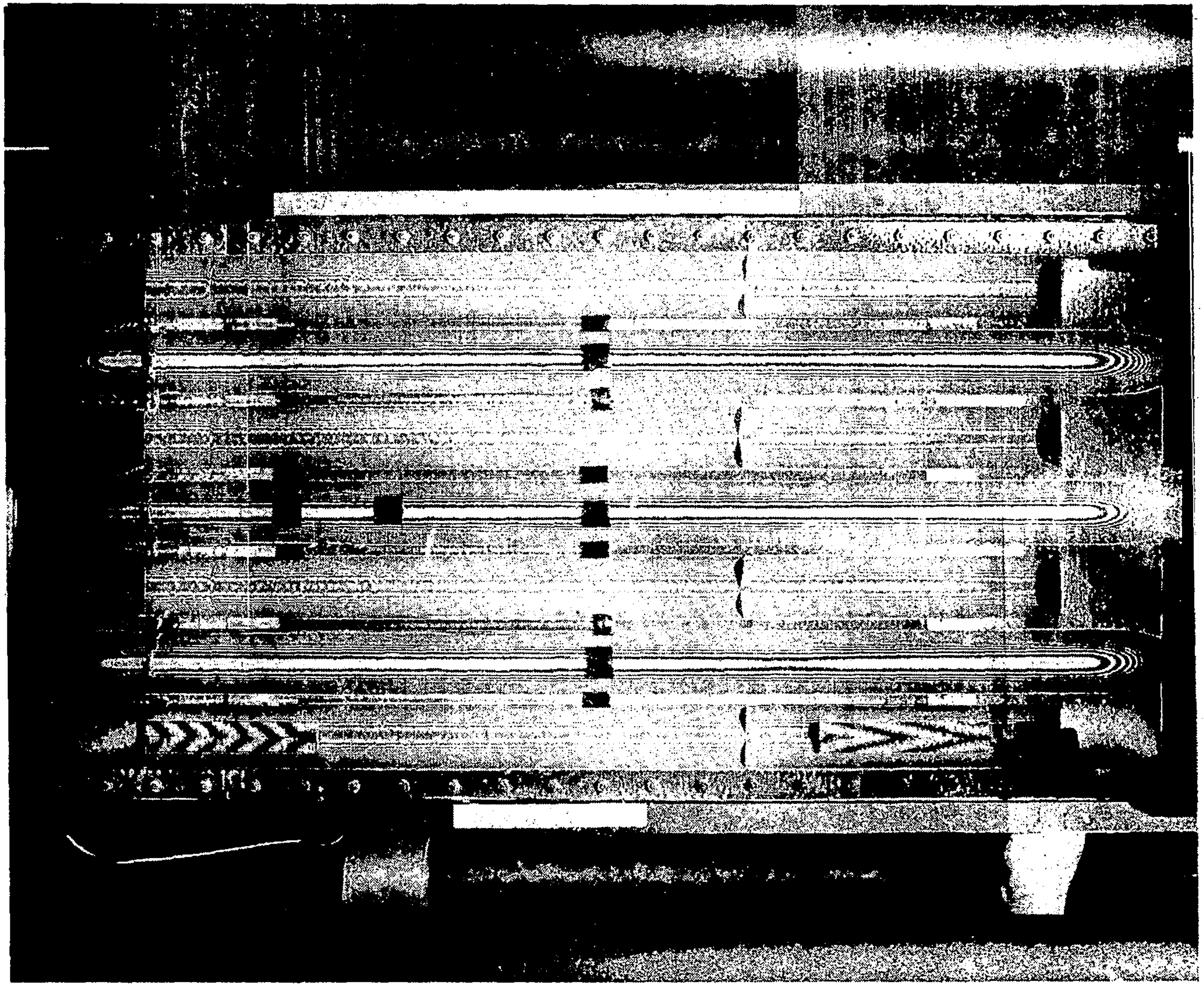

Figure 11

MOIRÉ FRINGE PHOTOGRAPH
(PRIOR TO ULTIMATE FAILURE)
(FIGURE 12)

THE PANEL IS SHOWN JUST PRIOR TO ULTIMATE FAILURE. SIGNIFICANT OUT-OF-PLANE DEFORMATION IS APPARENT ON THE CENTER BEAD, BASED ON THE NUMEROUS FRINGES ALONG THE BEAD PEAK. THE PHOTOGRAPH ALSO SHOWS LATERAL INPLANE DEFORMATION OF THE CENTER BEAD. POST-TEST STRAIN GAGE DATA SHOWED THAT THE CENTER PORTION OF THE PANEL HAD AN ELASTIC BUCKLING FAILURE PRIOR TO THIS PHOTOGRAPH. THE MEASURED OUT-OF-PLANE DEFORMATION AT THE CENTER OF THE PANEL WAS ABOUT 10 MM (0.4 IN.). POTENTIOMETRIC DISPLACEMENT TRANSDUCERS WERE INSTALLED ON THE BACKSIDE OF THE PANEL TO MEASURE OUT-OF-PLANE DISPLACEMENTS AT A FEW DISCRETE LOCATIONS. THE AGREEMENT BETWEEN THE TRANSDUCER DATA AND THE MOIRÉ GRID DATA WAS EXCELLENT.

MOIRÉ FRINGE PHOTOGRAPH
(PRIOR TO ULTIMATE FAILURE)

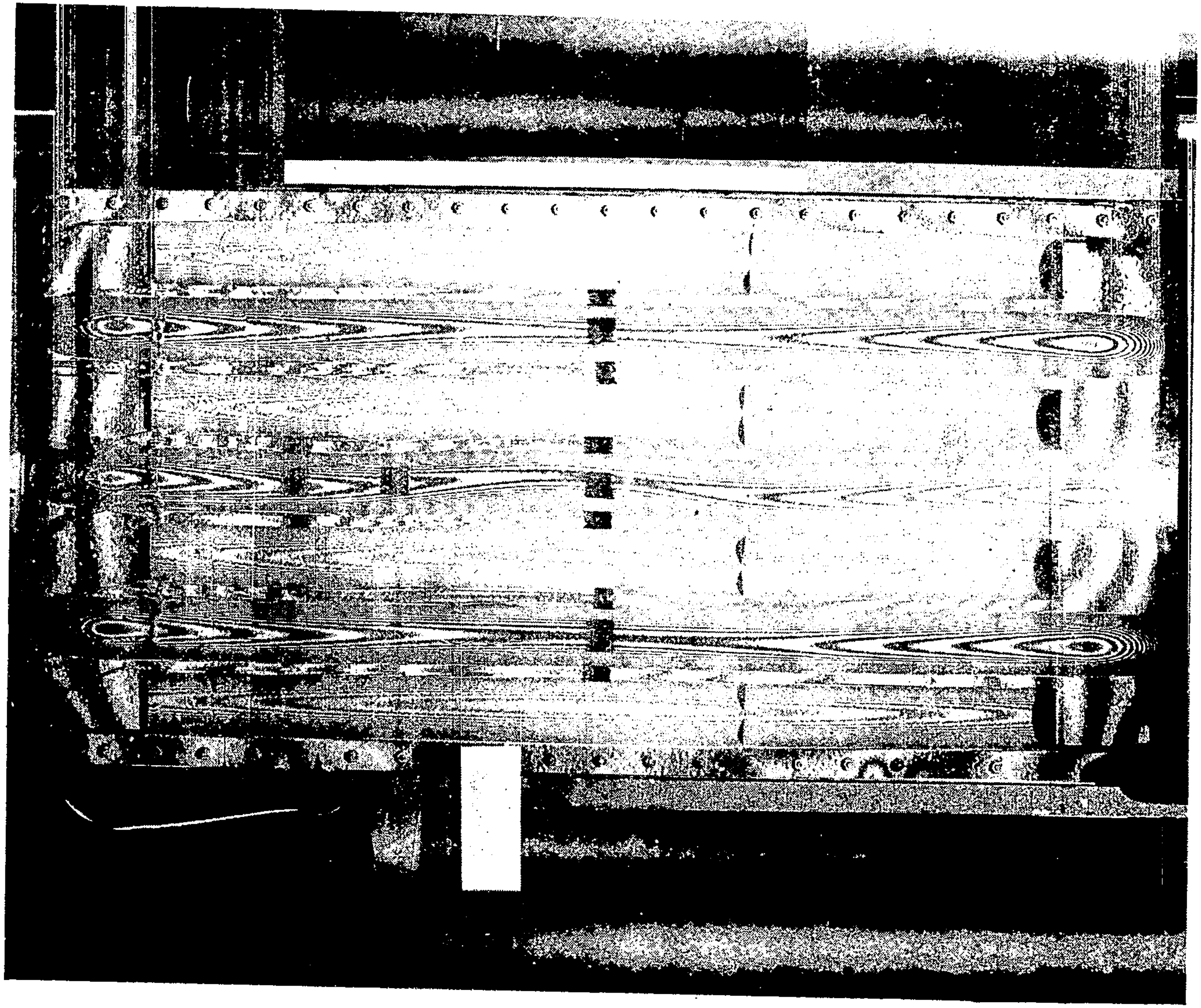

Figure 12

MOIRÉ FRINGE PHOTOGRAPH
(AFTER FAILURE)
(FIGURE 13)

THE FAILED PANEL WITH LOCAL BUCKLES AT THE CENTER CROSS-SECTION IS SHOWN.

MOIRÉ FRINGE PHOTOGRAPH
(AFTER FAILURE)

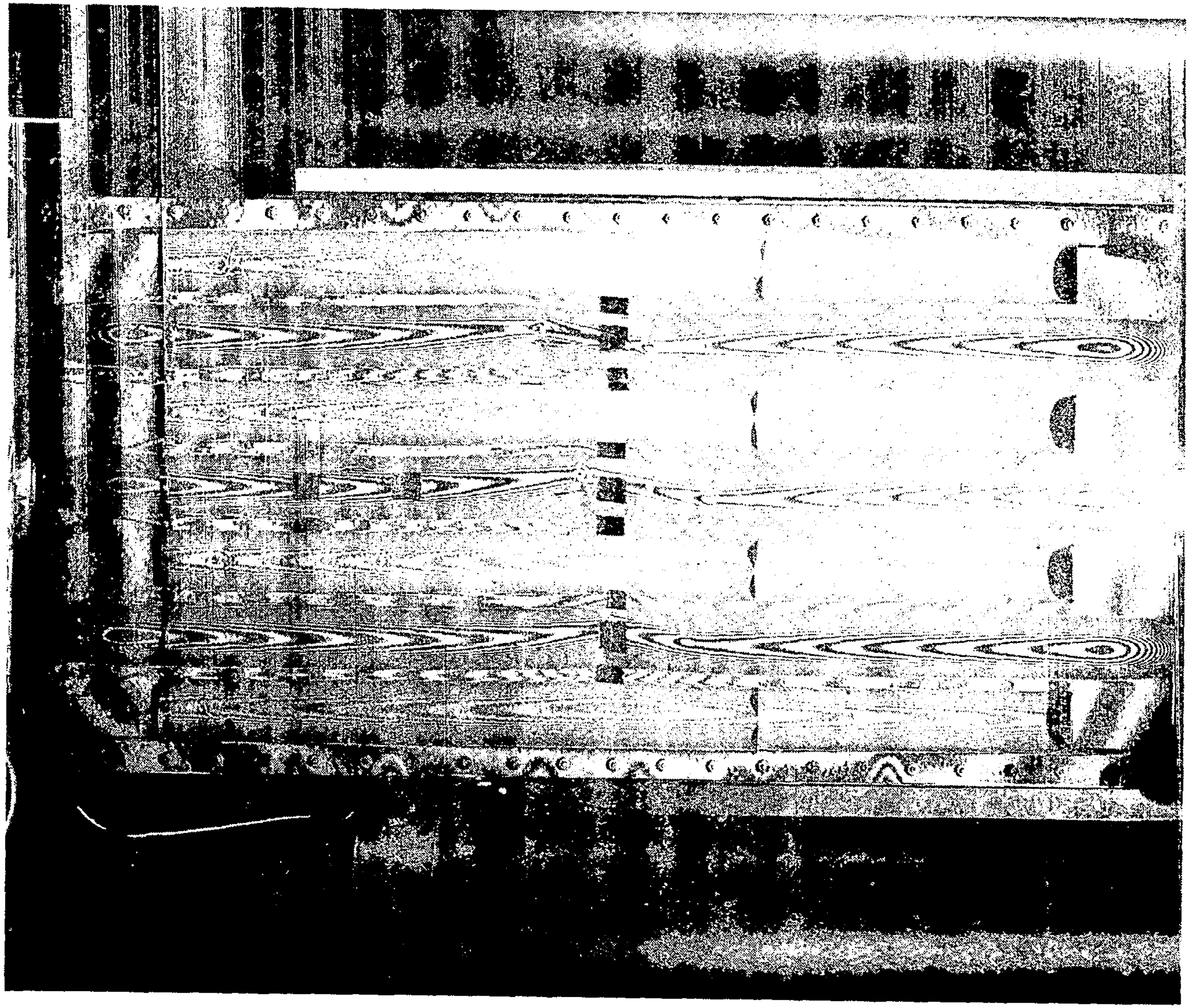

Figure 13

STRENGTH INTERACTION CURVES FOR THE HYPERSONIC BEADED SKIN PANEL
(FIGURE 14)

BEADED PANEL STRENGTH INTERACTION CURVES THAT WERE CALCULATED FOR ELEVATED TEMPERATURE WITH A NORMAL PRESSURE LOAD AND ROOM TEMPERATURE WITH NO PRESSURE ARE SHOWN. PANEL COMPRESSION IS PLOTTED AS A FUNCTION OF PANEL SHEAR. ALSO ON THIS FIGURE, IS THE POINT AT WHICH THE TEST DATA SHOWED THE PANEL TO FAIL. THE PANEL EXCEEDED THE EXPECTATIONS BASED ON THE DESIGN DATA FOR THIS PARTICULAR LOAD CONDITION BY 20 PERCENT.

STRENGTH INTERACTION CURVES FOR THE HYPERSONIC BEADED SKIN PANEL

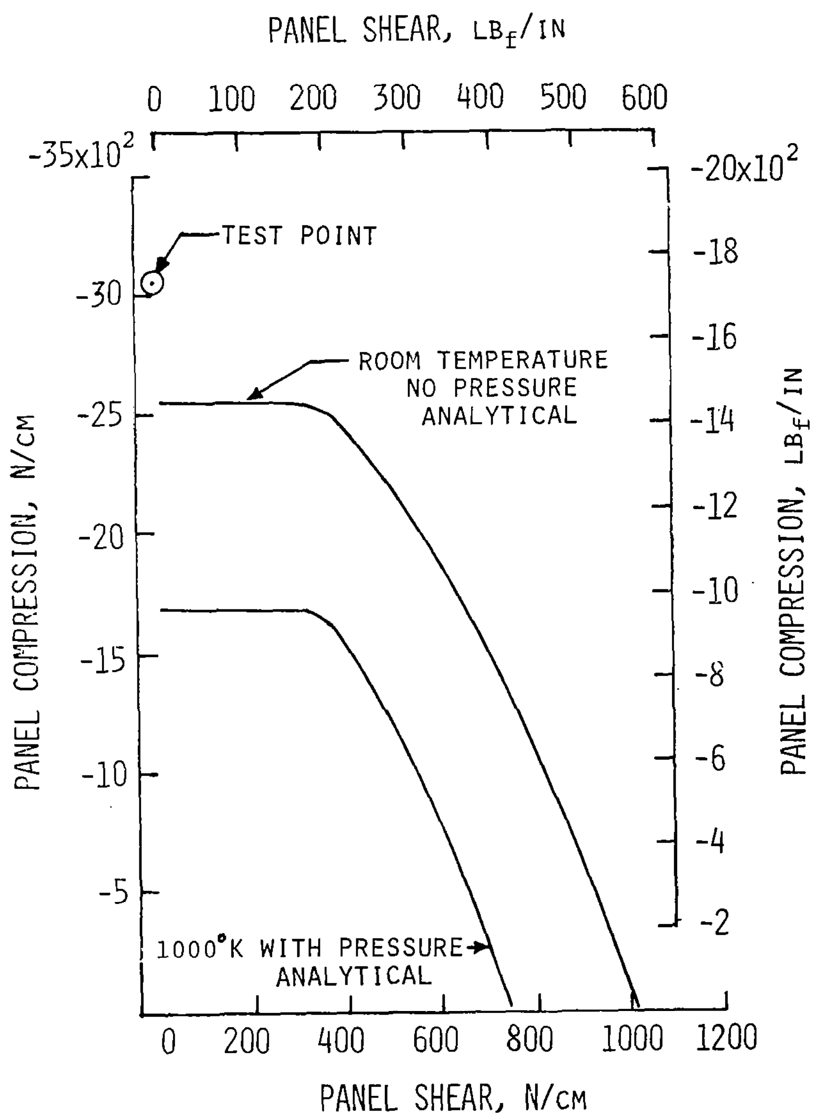

Figure 14

LOAD MEASUREMENT CALIBRATION POINTS AND REFERENCE AXES FOR HWTS
(FIGURE 15)

ONE OF THE IMPORTANT ASPECTS OF OUR PROGRAM WAS TO PERFORM FLIGHT LOADS MEASUREMENT RESEARCH ON A HYPERSONIC VEHICLE HOT STRUCTURAL WING CONCEPT. THE WING STRUCTURE WAS INSTRUMENTED WITH BOTH SHEAR AND BENDING STRAIN GAGE BRIDGES AT THE LOCATIONS SHOWN BY THE SQUARE SYMBOLS. THE SOLID CIRCULAR SYMBOLS ARE THE LOCATIONS WHERE VERTICAL LOADS WERE APPLIED, ONE AT A TIME, TO CALIBRATE THE STRAIN GAGE BRIDGES. DATA FROM THESE CALIBRATION LOADINGS WERE USED TO DERIVE LOAD EQUATIONS FOR THE MEASUREMENT OF WING SHEAR, BENDING MOMENT, AND TORQUE.

LOAD MEASUREMENT CALIBRATION POINTS AND REFERENCE AXES FOR HWTS

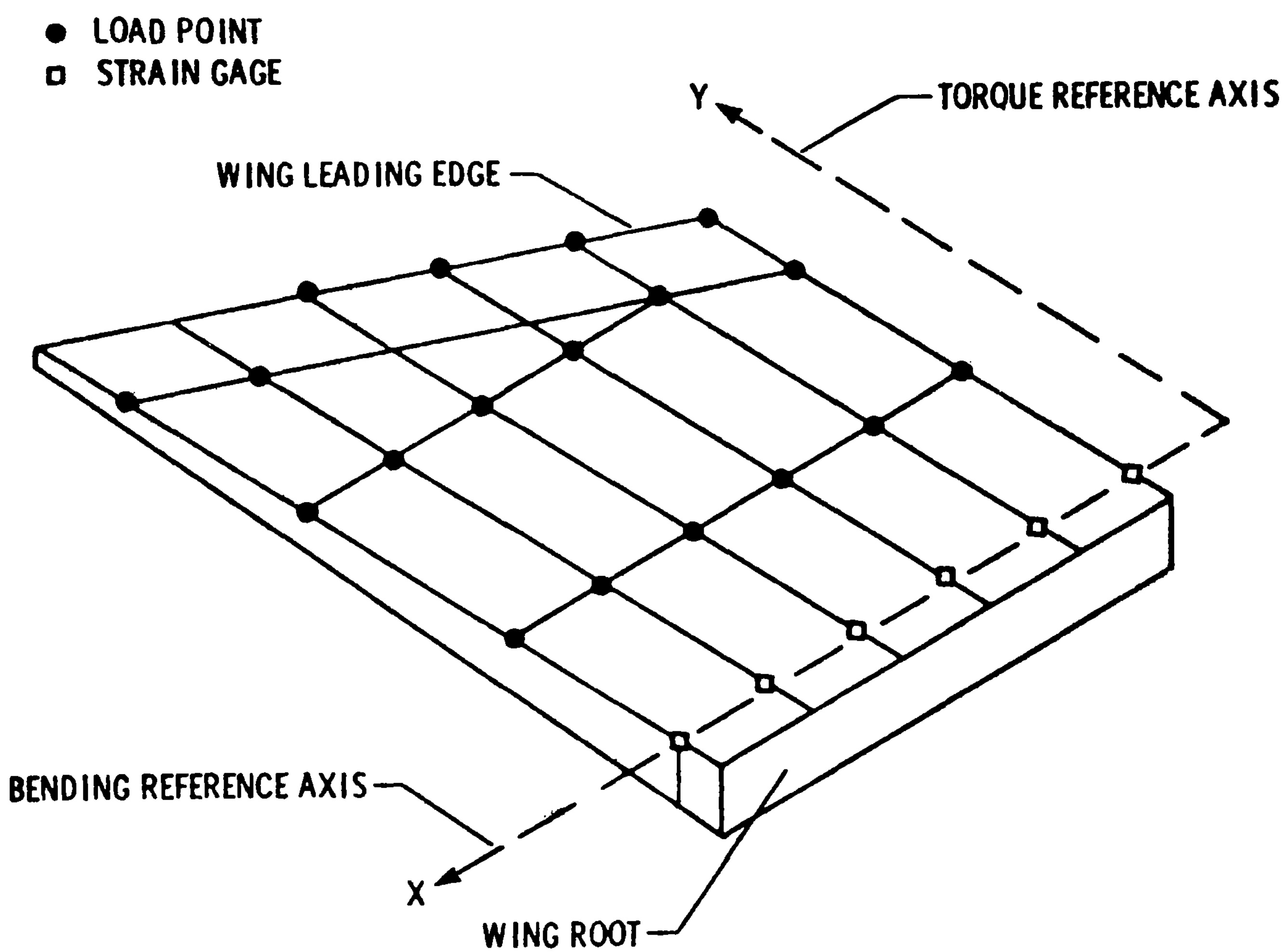

Figure 15

DISTRIBUTED LOADING USED TO COMPUTE PERFORMANCE OF LOAD EQUATIONS
(FIGURE 16)

THIS FIGURE SHOWS THREE DISTRIBUTED LOAD CONDITIONS THAT WERE APPLIED TO THE WING STRUCTURE TO PROVIDE A CHECK ON THE LOAD EQUATIONS THAT WERE DERIVED. THE DIRECTION AND LENGTH OF THE ARROWS REPRESENT THE DIRECTION AND MAGNITUDE OF THE LOADS THAT WERE APPLIED TO EACH LOCATION. ALL OF THE LOADS OF EACH CONDITION (A,B, AND C) WERE APPLIED SIMULTANEOUSLY.

DISTRIBUTED LOADING USED TO COMPUTE PERFORMANCE OF LOAD EQUATIONS

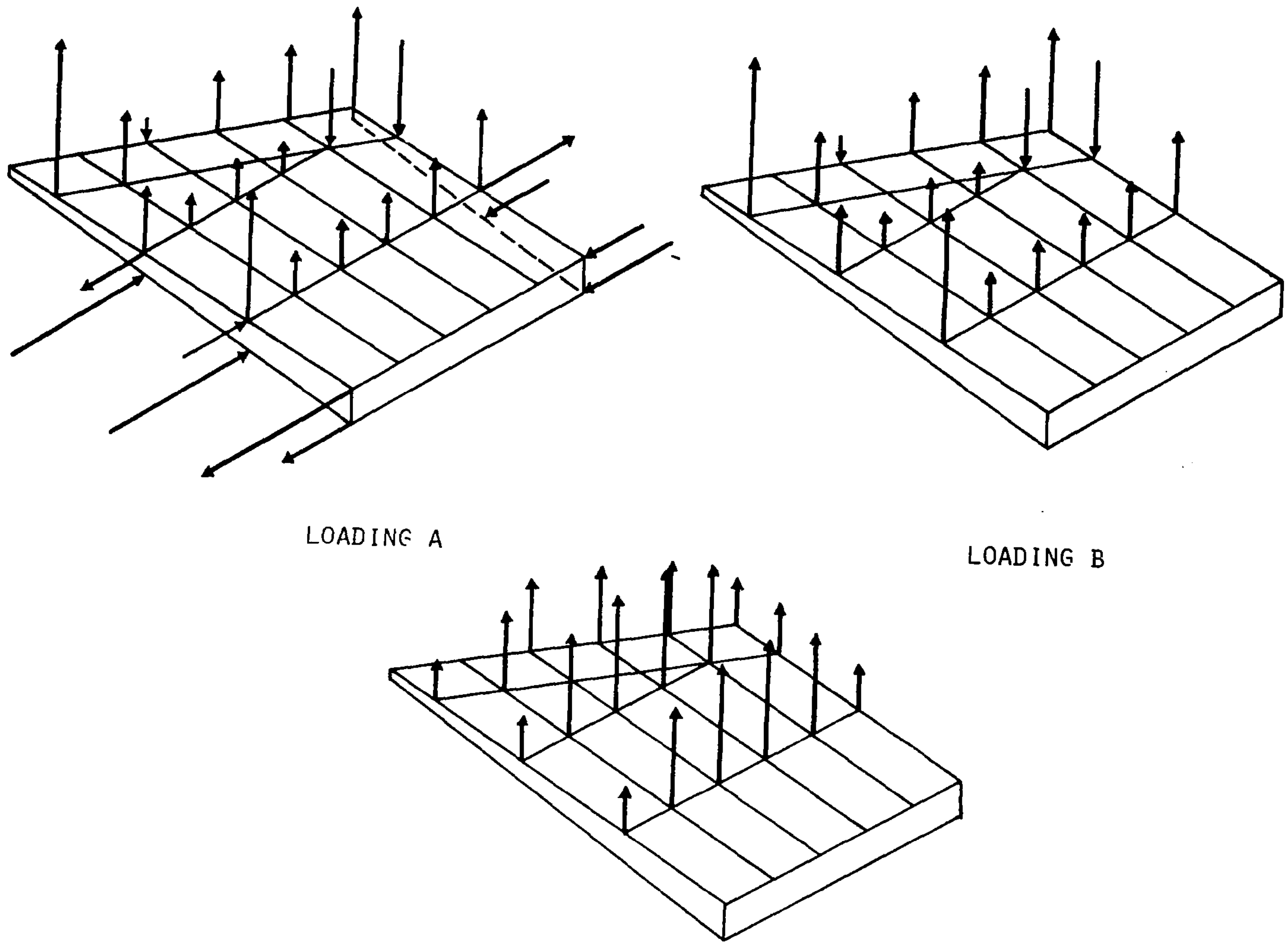

LOADING A

LOADING B

LOADING C

Figure 16

COMPARISON OF CALCULATED AND APPLIED LOADS
(FIGURE 17)

THE PERCENTAGE DIFFERENCE OR ERROR BETWEEN LOADS CALCULATED WITH STRAIN GAGE EQUATIONS AND THE ACTUAL APPLIED LOADS IS SHOWN. THE EQUATIONS, WITH ONE EXCEPTION, CALCULATED THE LOADS FROM THE THREE CONDITIONS TO WITHIN 5 PERCENT. LOAD CONDITION A, FOR WHICH THE BENDING MOMENT EQUATION DID NOT DO TOO WELL, WAS A PARTICULARLY DIFFICULT ONE, SINCE HORIZONTAL LOADS WERE INTRODUCED IN THAT CONDITION. THESE DATA ARE THE RESULT OF WORK AT ROOM TEMPERATURE ONLY; SIMILAR WORK IS IN PROGRESS FOR ELEVATED TEMPERATURE CONDITIONS. OTHER WORK THAT IS ONGOING IN THIS AREA INCLUDES THE USE OF NASTRAN AS A TOOL TO GENERATE STRAINS FOR DERIVING LOAD EQUATIONS ANALYTICALLY. IN GENERAL, HOWEVER, WE'VE FOUND THAT AN EXPERIMENTAL STRAIN GAGE CALIBRATION IS AN ESSENTIAL PART OF A FLIGHT LOADS MEASUREMENT PROGRAM.

COMPARISON OF CALCULATED AND APPLIED LOADS

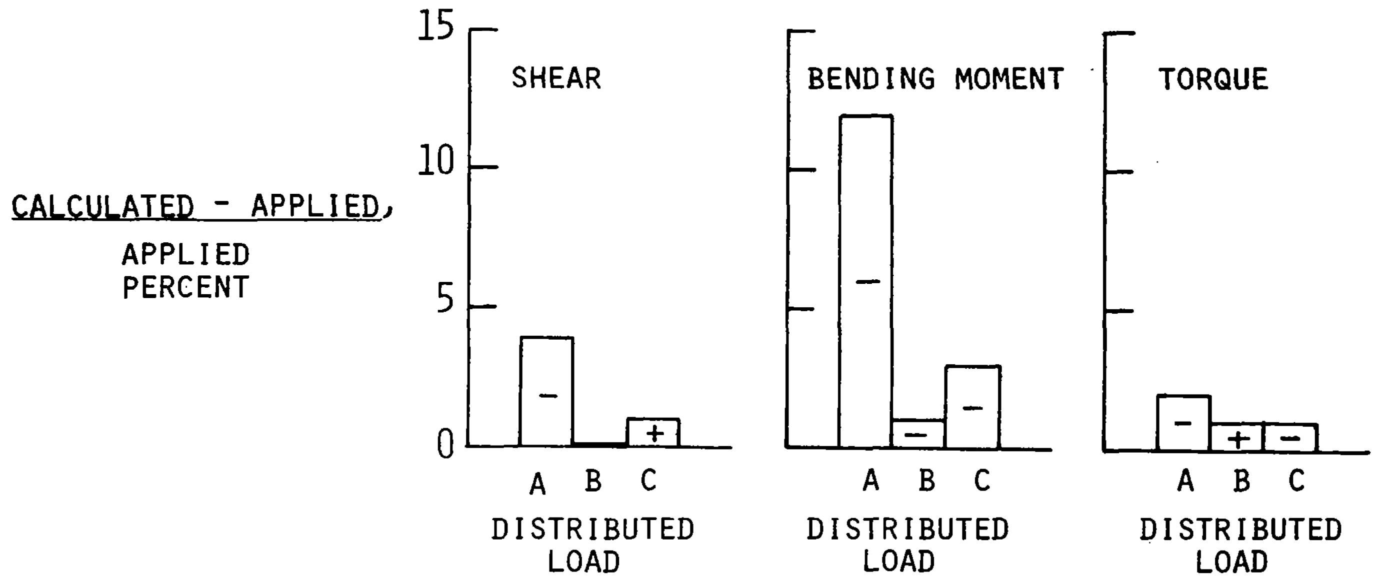

Figure 17

THERMAL STRESS EXPERIMENT

(FIGURE 18)

ANOTHER ONGOING PROGRAM AT DRYDEN, CONCERNING HYPERSONIC STRUCTURAL CONCEPTS, IS A THERMAL STRESS EXPERIMENT USING A HEAT-SINK OR LOCKALLOY TEST STRUCTURE. THE PRIMARY OBJECTIVE OF THIS PROGRAM IS TO ASSESS HOW WELL THERMAL STRESSES CAN BE PREDICTED USING NASTRAN. THIS INVOLVES NASTRAN MODELING OF THE TEST STRUCTURE AND THE DETERMINATION OF THERMAL STRESS TIME HISTORIES AND THERMAL STRESS DISTRIBUTION AT SPECIFIC TIME SLICES. THIS PROGRAM EVOLVED DURING RECENT STUDIES OF A HEAT-SINK STRUCTURAL CONCEPT FOR THE NATIONAL HYPERSONIC FLIGHT RESEARCH FACILITY.

THERMAL STRESS EXPERIMENT

(USING LOCKALLOY TEST STRUCTURE)

OBJECTIVE: ASSESS HOW WELL THERMAL STRESSES CAN BE PREDICTED USING NASTRAN

- NASTRAN MODELING
- THERMAL STRESS TIME HISTORIES
- THERMAL STRESS DISTRIBUTION

Figure 18

LOCATION OF LOCKALLOY TEST SPECIMEN ON VEHICLE
(FIGURE 19)

LABORATORY TEST SPECIMENS WERE FABRICATED TO REPRESENT A RECTANGULAR PORTION OF THE LOWER FUSELAGE AS SHOWN IN THIS FIGURE. THE COMPONENTS ARE BEING INSTRUMENTED WITH STRAIN GAGES AND THERMOCOUPLES TO PROVIDE DATA FOR COMPARISON WITH ANALYSIS. LABORATORY TESTS OF THE COMPONENTS CONSIST OF SUBJECTING THE SKINS TO SUPERSONIC AND HYPERSONIC HEATING PROFILES.

LOCATION OF LOCKALLOY TEST SPECIMEN ON VEHICLE

LAB TEST

- INSTRUMENTED COMPONENT WITH S/G AND T/C
- SUBJECTED THE SKINS TO SUPERSONIC AND HYPERSONIC HEATING

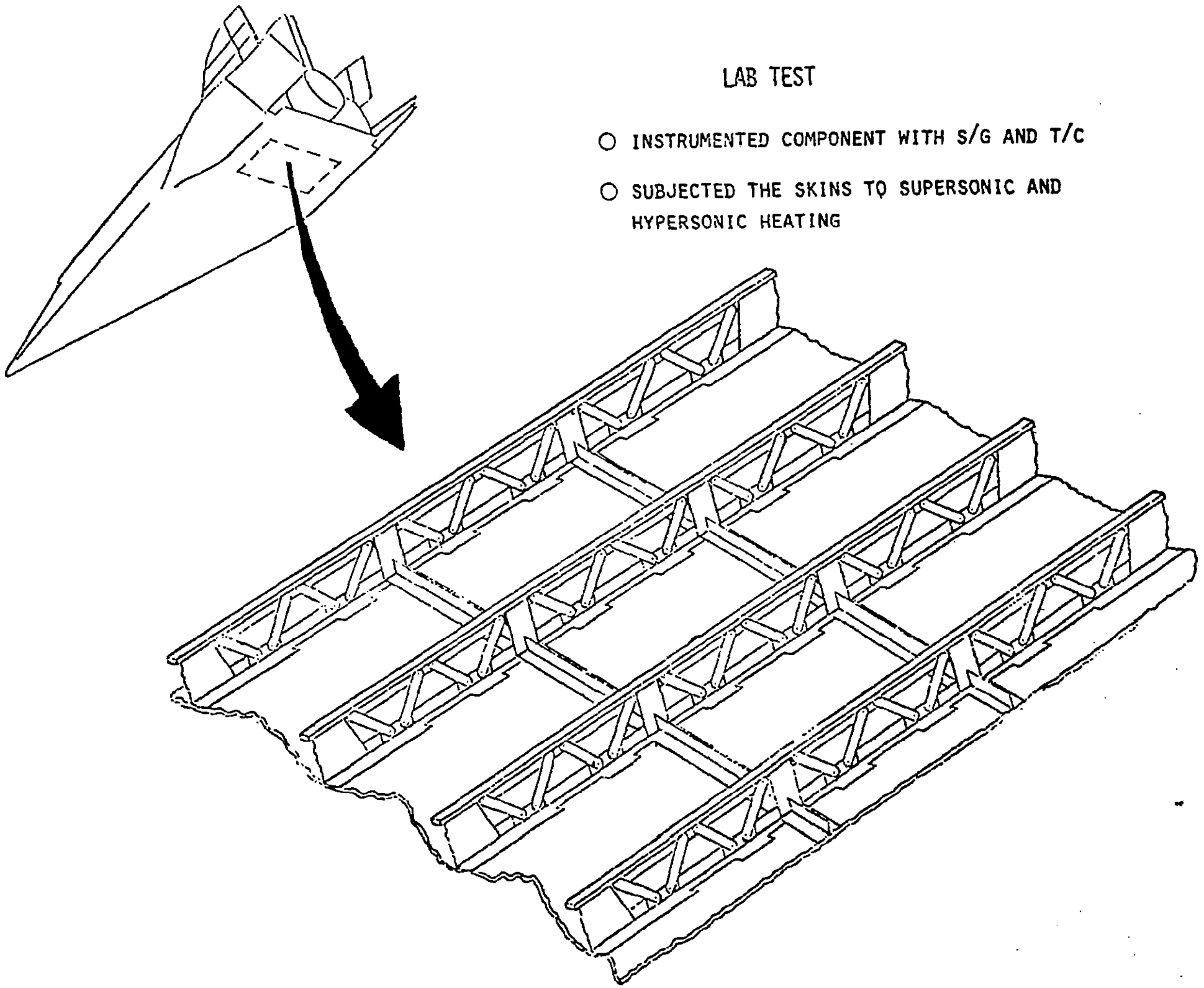

Figure 19

TEST SPECIMENS
(FIGURE 20)

THE THREE TEST SPECIMENS ARE SHOWN; ONLY THE ONE IN THE BACKGROUND IS SHOWN WITH THE LOCKALLOY SKINS ATTACHED. THREE DIFFERENT BACKUP STRUCTURES WERE CONSTRUCTED. A TRUSS STRUCTURE IS SHOWN IN THE FOREGROUND; THE AFT TWO TEST SPECIMENS BOTH HAVE BEAMS WITH SOLID WEBS; HOWEVER, ONE IS FABRICATED WITH TITANIUM AND THE OTHER WITH STAINLESS STEEL.

TEST SPECIMEN

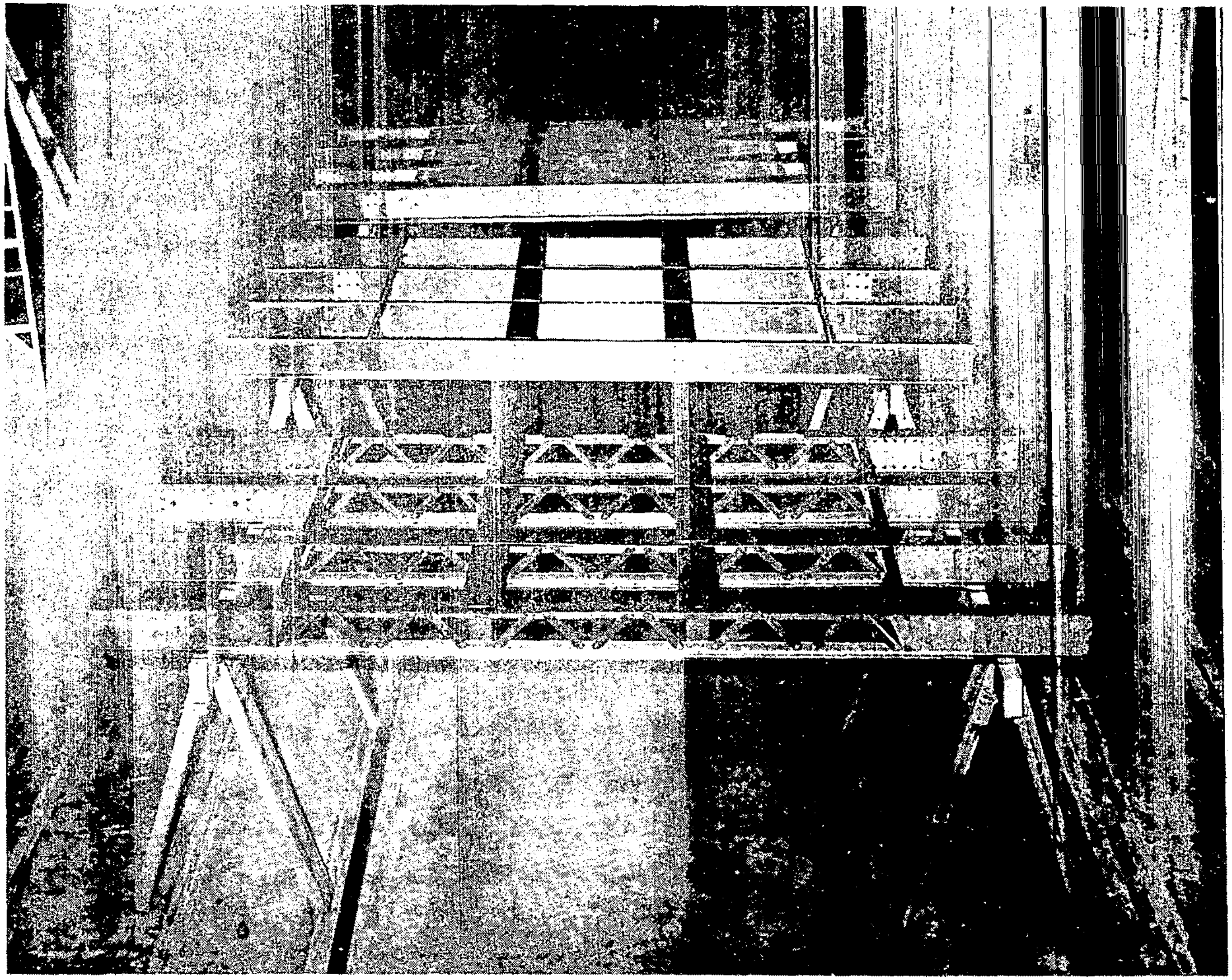

Figure 20

NASTRAN STRUCTURAL MODEL
(FIGURE 21)

THE NASTRAN STRUCTURAL MODEL CONSISTS OF ONE QUARTER OF THE TEST STRUCTURE, TAKING ADVANTAGE OF SYMMETRY CONDITIONS. THE MODEL CONTAINS 236 BAR, SHEAR PANEL, AND ROD ELEMENTS AND 100 GRID POINTS. TEMPERATURE INPUTS TO THE MODEL WERE THOSE MEASURED DURING TESTS.

NASTRAN STRUCTURAL MODEL

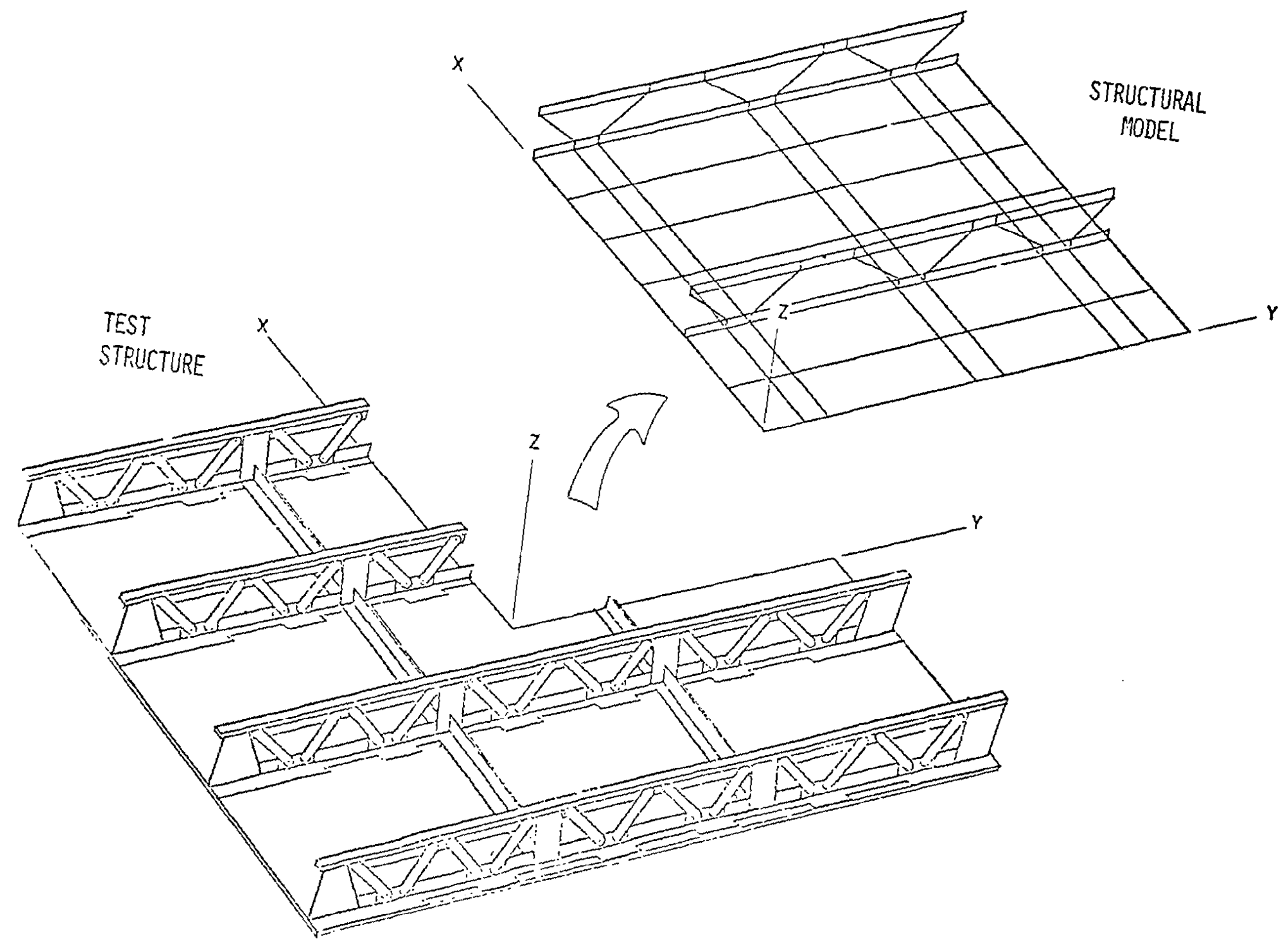

Figure 21

TRUSS STRUCTURE THERMAL STRESS PROFILES
(FIGURE 22)

MEASURED AND NASTRAN PREDICTED THERMAL STRESSES AS A FUNCTION OF PROFILE TIME AT FOUR LOCATIONS ARE SHOWN. THE HEATING PROFILE FOR THIS CASE WAS FOR A HYPERSONIC FLIGHT TO A MACH NUMBER OF 6.0 AT AN ALTITUDE OF ABOUT 25,000 M (85,000 FT). THE SKIN TEMPERATURES REACHED 560 K (550° F). MAXIMUM STRESSES OF 344 kN/m^2 (50,000 PSI) WERE OBTAINED ON THE LOWER CAPS NEAREST THE SKIN. THE DATA SHOWN ARE FOR THE TRUSS STRUCTURE. CORRELATION OF THE MEASURED AND PREDICTED DATA IS VERY GOOD.

TRUSS STRUCTURE THERMAL STRESS PROFILES

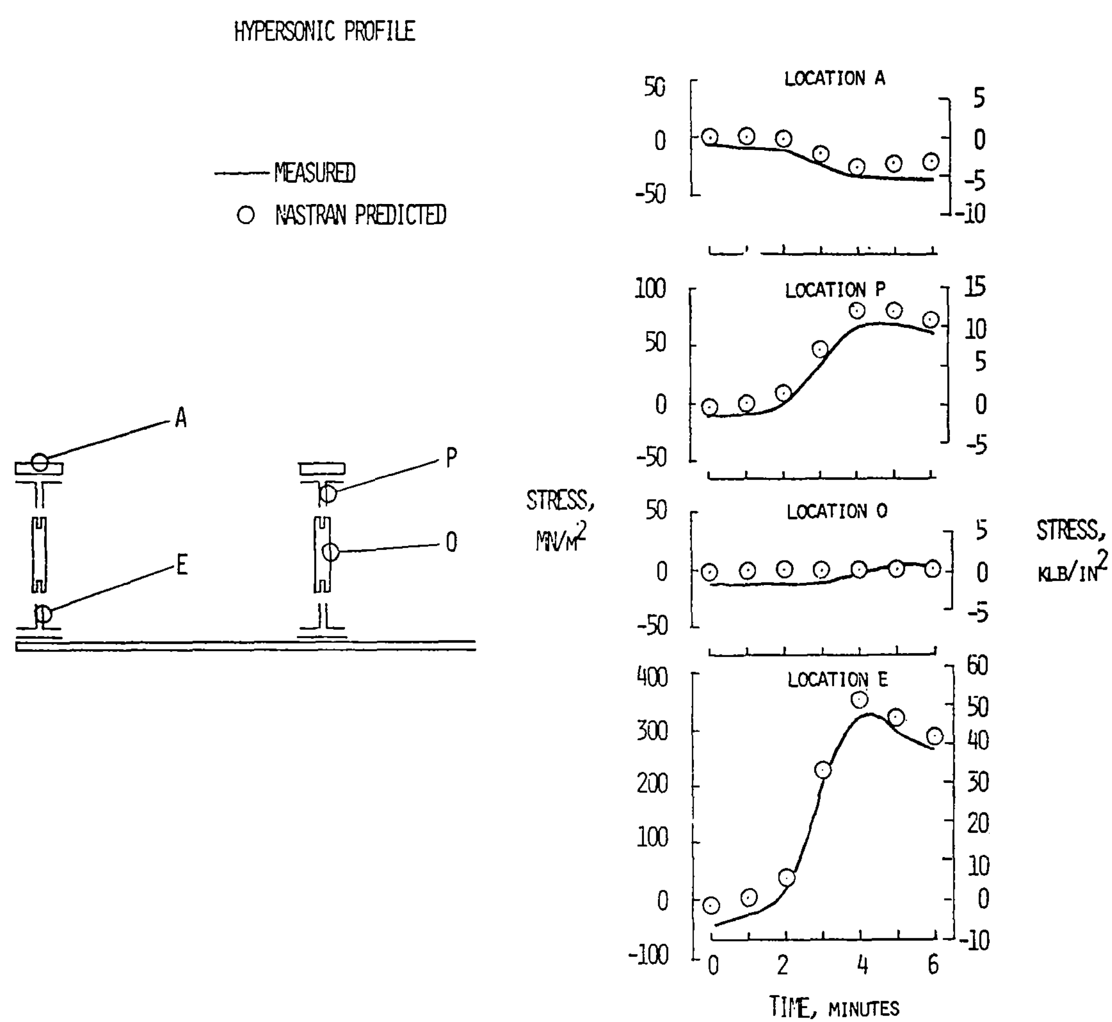

Figure 22

TRUSS STRUCTURE THERMAL STRESSES AT MAXIMUM TEMPERATURE
(FIGURE 23)

MEASURED AND PREDICTED STRESSES FOR THE BEAM CROSS-SECTIONS AND THE SKIN ARE SHOWN FOR A TIME SLICE AT THE MAXIMUM TEMPERATURE. THE MAXIMUM STRESS LEVELS ARE AT THE LOWER CAPS AND THE DATA CORRELATION IS QUITE GOOD. SIMILAR TESTS ARE CURRENTLY BEING CONDUCTED ON THE SOLID WEB STRUCTURAL CONFIGURATIONS.

TRUSS STRUCTURE THERMAL STRESSES AT MAXIMUM TEMPERATURE

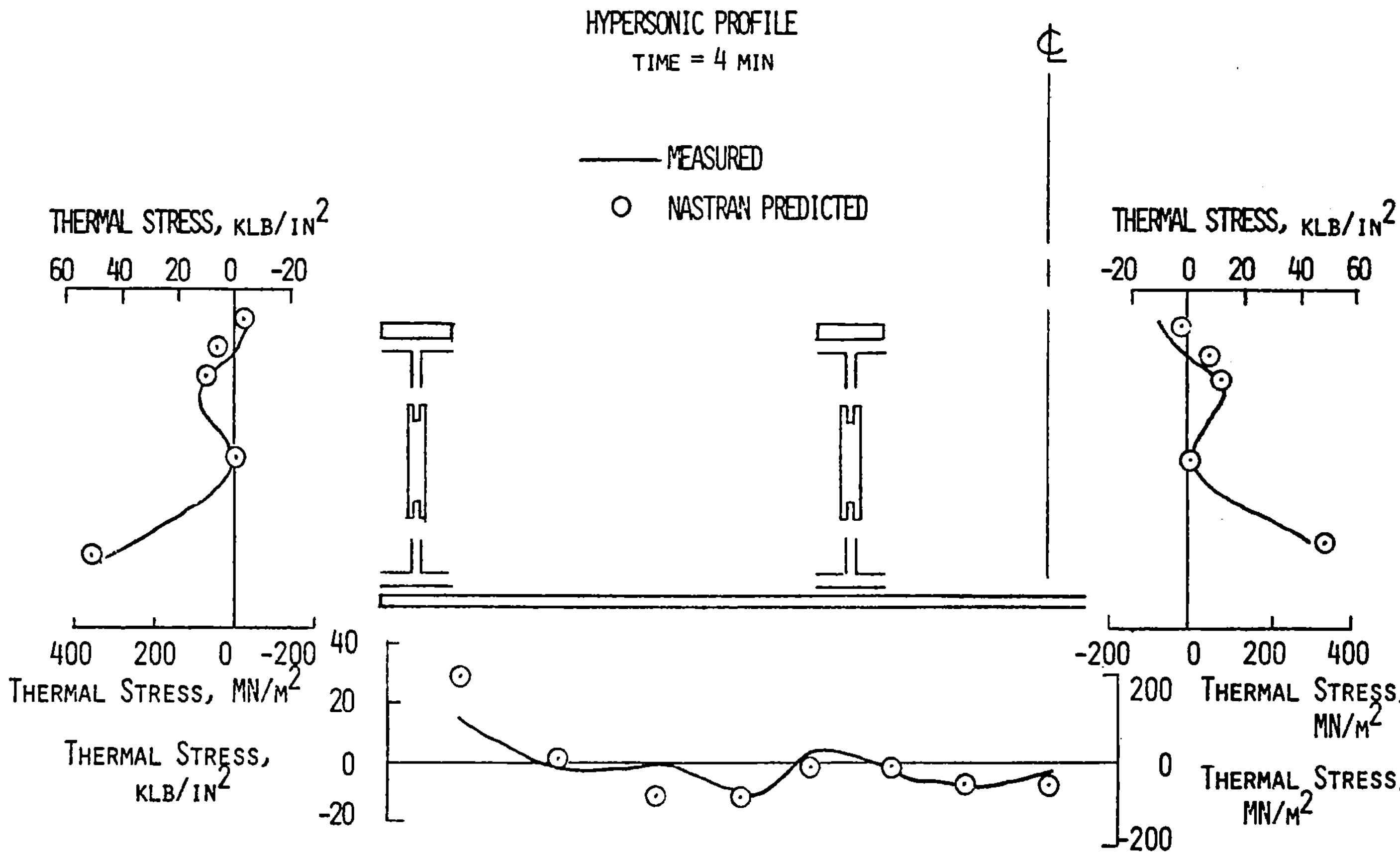

Figure 23

SHUTTLE ELEVON SEALS SYSTEM TESTS
(FIGURE 24)

A PROJECT THAT IS SCHEDULED TO BE TESTED IN OUR FACILITY, BEGINNING NEAR THE END OF THIS YEAR, IS THE SHUTTLE ELEVON SEALS SYSTEM TESTS. THE SPACE SHUTTLE ELEVONS CONTAIN A SEAL SYSTEM CONSISTING OF PRIMARY AND REDUNDANT SEALS WHICH PREVENT HOT GASES FROM ENTERING THE CAVITY BETWEEN THE WING AND ELEVON. DURING REENTRY, EXCESSIVE LEAKAGE OF THE ELEVON SEALS CAN RESULT IN OVERHEATING THE STRUCTURE OR SYSTEMS IN THAT AREA. IT IS THEREFORE NECESSARY TO TEST THE ELEVON SEALS SYSTEM UNDER THE COMBINED EFFECTS OF HEATING, LOADING, AND DIFFERENTIAL PRESSURE. THE TESTS WILL VERIFY THE FUNCTIONAL CAPABILITY OF THE SEALS SYSTEM AND DEMONSTRATE THE SYSTEM STRUCTURAL INTEGRITY AND COMPATIBILITY WITH THE WING ELEVON DESIGN. THE ELEVON SEALS WILL BE ASSEMBLED WITH AN OUTBOARD ELEVON AND WING BOX STRUCTURE TO FORM A REPRESENTATIVE TEST ARTICLE APPROXIMATELY 3.7 M BY 3.7 M (12 FT BY 12 FT).

SHUTTLE ELEVON SEALS SYSTEM TESTS

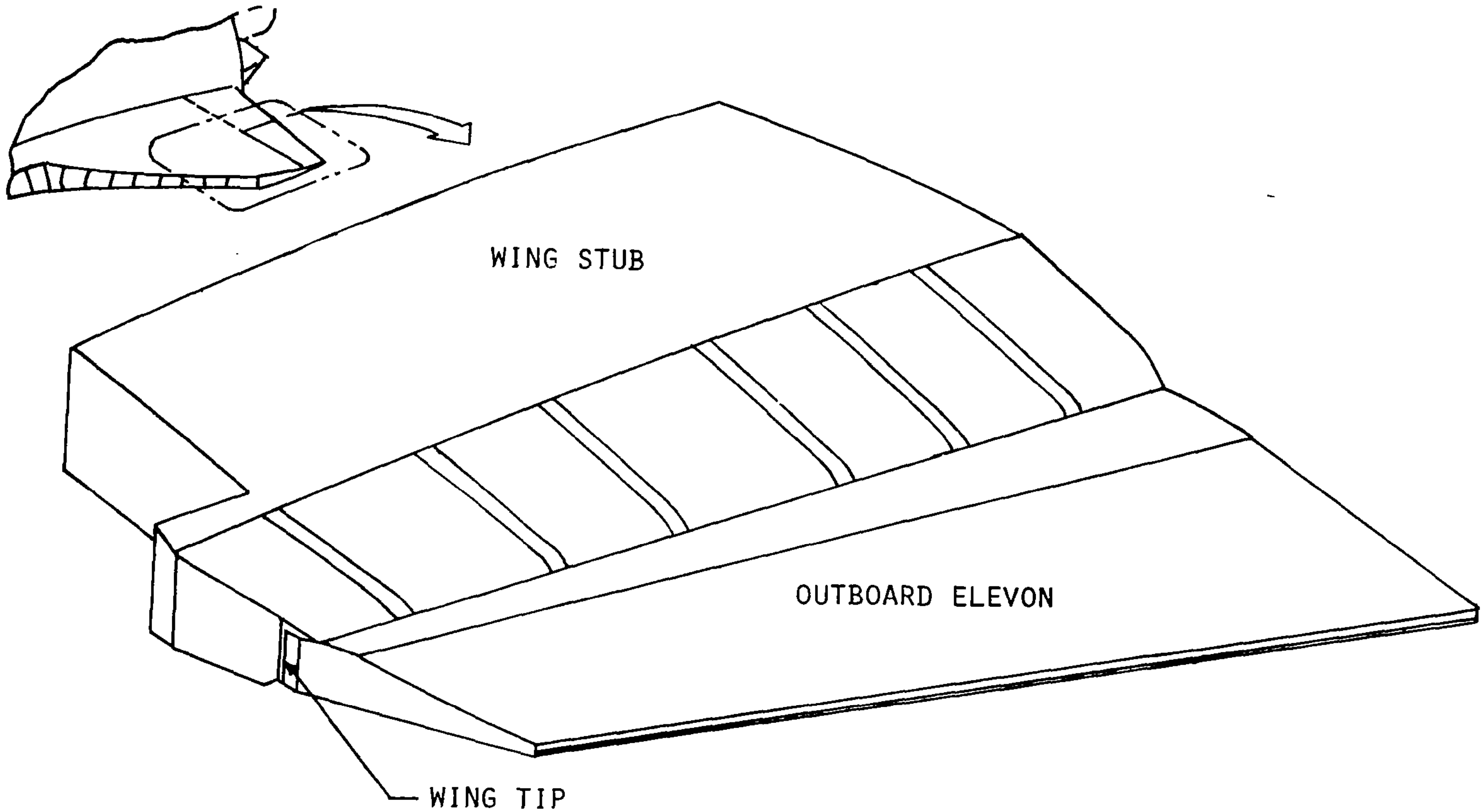

OBJECTIVES :

- O VERIFY FUNCTIONAL CAPABILITY OF THE ELEVON SEALS SYSTEM
- O DEMONSTRATE SYSTEM STRUCTURAL INTEGRITY
- O DEMONSTRATE SYSTEM COMPATIBILITY WITH WING/ELEVON DESIGN

Figure 24

CONCLUDING REMARKS

A CONSIDERABLE AMOUNT OF EXPERIMENTAL WORK ON HOT STRUCTURE CONCEPTS FOR HYPERSONIC VEHICLES HAS BEEN DONE AT DRYDEN. ALL OF OUR WORK IS NOT COMPLETE AT THIS POINT AND THERE ARE STILL PROBLEM AREAS TO BE RESOLVED. HOWEVER, THE RESULTS OF OUR PROGRAMS HAVE BEEN A POSITIVE STEP IN VALIDATING THE USE OF THE CONCEPTS WE HAVE LOOKED AT AND THE METHODS OF FLIGHT LOADS MEASUREMENTS ON THESE CONCEPTS.

SESSION V - TANKAGE AND INSULATION

LIQUID HYDROGEN TANKAGE DESIGN*

by George W. Davis
Lockheed-California Company, Burbank, Calif.

INTRODUCTION

Concern for the potential short supply of petroleum-base fuels has led to a series of studies sponsored by NASA which have explored the technological aspects and established the potential of using liquid hydrogen (LH_2) for fuel in advanced commercial transport aircraft. A recent study conducted by the Lockheed-California Company was directed at exploring the design problems presented by the fuel system of a representative LH_2-fueled transport.

This study was performed to define the characteristics of an efficient fuel system for a LH_2-fueled subsonic transport aircraft. Several engine concepts were examined to determine a preferred design which most effectively exploits the characteristics of hydrogen. The problems related to efficient containment of the liquid hydrogen fuel in aircraft tanks received major emphasis. Many candidate designs of tank structure and cryogenic insulation systems were evaluated. Designs of all major elements of the aircraft fuel system including pumps, lines, valves, regulators, and heat exchangers received attention. A final design LH_2-fueled transport aircraft was established which incorporates a preferred design of fuel system. That aircraft was then compared with a conventionally fueled counterpart designed to equivalent technology standards.

This paper will present a summary of the results of the structural evaluation associated with the design of the liquid hydrogen tank.

---

*This study was funded by NASA/LaRC under contract NAS1-14614 with Mr. Robert D. Witcofski as technical monitor.

BASELINE LH_2-FUELED SUBSONIC TRANSPORT (Figure 1)

This baseline LH_2-fueled aircraft was conceptually designed in a previous study (Reference 1) in which advanced technology features were incorporated representing an initial operational capability in the 1990s. The aircraft was sized to carry 400 passengers 10 200 km (5500 n.mi.) at a cruise speed of Mach 0.85. The takeoff gross weight (TOGW) is 177 700 kg (391 700 lbm) with 27 900 kg (61 600 lbm) of LH_2 fuel. In addition, some basic airplane dimensions are shown in this figure and include the wing span 53.0 m (174 ft), fuselage length 66.9 m (219.4 ft) and the overall height 18.6 m (61.1 ft).

The fuel tanks are located in the fuselage as indicated in this figure. In order to focus design and analysis attention as much as possible on constructive aspects, the aft tank of this aircraft was selected and used as the model for evaluation of candidate structure and insulation concepts.

BASELINE LH_2-FUELED SUBSONIC TRANSPORT

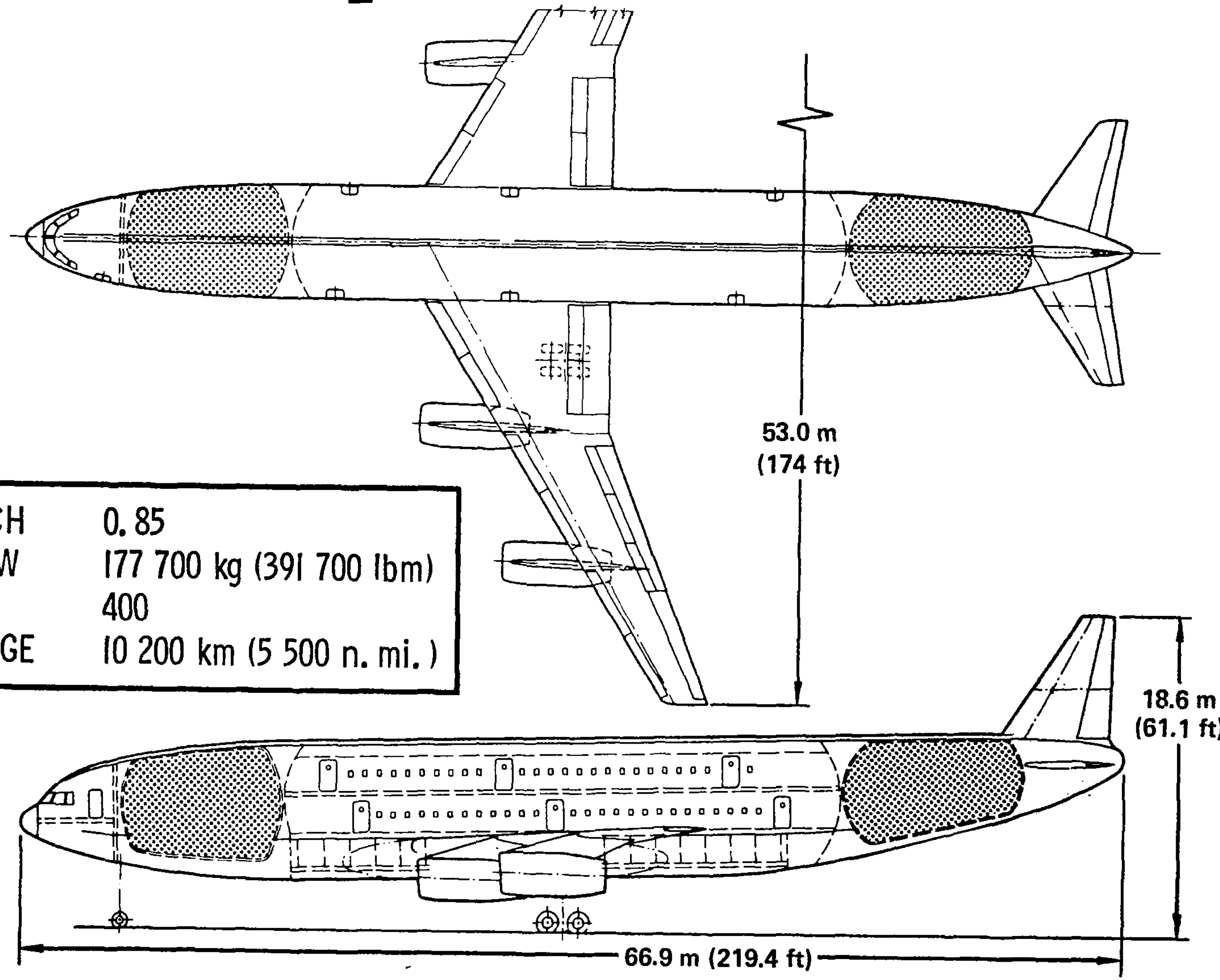

MACH	0.85
TOGW	177 700 kg (391 700 lbm)
PAX	400
RANGE	10 200 km (5 500 n. mi.)

Figure 1

TANK DESIGN STUDY
(Figure 2)

An investigation to determine a preferred concept for the fuel-tank design was conducted in parallel with that of the insulation study. This figure displays the study elements included in the structural investigation. Design criteria and loads were established, structural concepts for both integral and nonintegral type tanks were screened, and the most promising shapes selected. Parametric studies were conducted to determine:

- A preferred shape for the fuel-tank domes
- The viability of using pressure stabilized structure
- The effects of designing the tank for different pressure levels
- The effect on economics of specifying a reduced design life for the tank structure
- A suspension system for each basic tank type

As a result of the insulation-system and structural-concepts screening studies, four preferred fuel containment systems were selected and subjected to a further evaluation to determine which is best for application in a commercial transport aircraft.

The results of each of these study elements will be presented in the following figures with the exception of the last four items of the parametric studies, which due to time, cannot be discussed.

TANK DESIGN STUDY

- STRUCTURAL DESIGN CRITERIA
- CONCEPT SCREENING
- PARAMETRIC STUDIES
  - DOME SHAPE
  - PRESSURE STABILIZATION
  - PRESSURE LEVEL
  - DESIGN LIFE
  - TANK SUSPENSION
- FINAL-TANK DESIGN

Figure 2

STRUCTURAL DESIGN CRITERIA
(Figure 3)

The structural design criteria was defined to provide the basis for the structural evaluation of the candidate tank configurations and a level of safety equivalent to current transports for assessing structural mass trends resulting from application of these criteria.

In general, the criteria are based on the structural requirements of the Federal Aviation Administration FAR 25 with specific criteria being the same as that used for the L-1011 aircraft.

- Design Loads. - Loads were defined using the weight and dimensions of the previously shown baseline airplane. The forward cg limit was assumed to be at the 20 percent Mean Aerodynamic Chord (MAC) with a structural reserve fuel of 7 percent of total fuel. The design speed variation with altitude and the maneuver envelopes were defined. Five flight conditions were investigated for this study and are defined more fully in a later figure.

- Pressure Schedule. - LH_2 tanks for the baseline aircraft were designed to operate at a nominal pressure of 145 kPa (21 psia). Factors required for cabin pressure (FAR 25) are assumed applicable to the LH_2 tank design.

  The differential pressure (Δp) acting on the LH_2 tanks is the nominal pressure minus the pressure at the altitude under consideration. The operating pressure is defined by differential pressure multiplied by a factor of 1.1 to account for relief value tolerance and inertia effects.

  Limit, ultimate, proof, and burst pressures are defined by multiplying the operating pressure by 1.00, 1.50, 1.33 and 2.00, respectively. For example, the ultimate pressure at the cruise altitude 10.7 km (35 000 ft) is: $p = 1.1$ (144 kPA -23.8 kPa) x 1.5 = 199.3 kPa (28.9 psi).

- Factors of Safety and Combined Loads Criteria. - The factors of safety for the individual loading and the method of combining these loads were specified in the design criteria.

- Fatigue and Damage Tolerance Criteria. - These requirements were specified to ensure that flight safety is maintained in the event of structural damage. This criteria, because of its extreme importance, is discussed on the following chart.

STRUCTURAL DESIGN CRITERIA

- DESIGN LOAD CONDITIONS
- PRESSURE SCHEDULE
- FACTORS OF SAFETY AND COMBINED LOADS CRITERIA
- FATIGUE AND DAMAGE TOLERANCE CRITERIA

Figure 3

FATIGUE AND DAMAGE TOLERANCE CRITERIA
(Figure 4)

Fatigue design requirements are met by limiting the permissible design tension stress levels for the ultimate design and operating conditions. 50 000 hours of service with an average flight time of approximately 5 hr/flight are used for this LH_2-fueled transport. For the pressurized tanks, the skin hoop tension allowables are based on one internal pressure cycle per flight (5 hr/flight) and a life reduction factor of 4, i.e., N = 4 x (50 000/5) = 40 000 cycles.

The maximum circumferential stress is:

F_θ = 234 MPa (34 ksi) ultimate	2219 aluminum alloy R = 0.45
F_θ = 158.6 MPa (23 ksi) operating	K_t = 5.0 T = 20 K (-423°F)

For fuselage bending structure (unpressurized), the design allowables are based on a spectrum loading which includes both symmetrical flight and ground conditions. A life reduction factor of 2 is used in this calculation.

F_x = 310.3 MPa (45 ksi) ultimate	2024 Aluminum Alloy at RT

The damage tolerance (fail-safe) criteria is divided into accidental damage and damage accumulated during normal usage.

For the accidental damage condition, the tank structure must be capable of supporting the appropriate pressure and flight loads with a 30.5-cm (12.0 in.) through-the-thickness crack, including one attachment member. Cracks in both the longitudinal and circumferential direction are investigated in the design studies.

For the normal usage condition, the operating stress level and material shall be chosen to ensure through-the-thickness flaw remains subcritical for a sufficiently long period.

FATIGUE AND DAMAGE TOLERANCE CRITERIA

- FATIGUE DESIGN
  - SERVICE LIFE - 50 000 HR
  - AVERAGE FLIGHT TIME - 5 HR/FLIGHT
  - DESIGN ALLOWABLE
    - SPECTRUM LOADING (50 000 X 2)
    - CONSTANT AMPLITUDE (50 000 X 4)
- DAMAGE TOLERANCE (FAIL-SAFE)
  - ACCIDENTAL DAMAGE
  - NORMAL USAGE (LEAK-BEFORE-BREAK)

Figure 4

CONCEPT SCREENING
(Figure 5)

The objective of this task is to perform a structural evaluation of sufficient depth to screen, on the basis of weight and cost, the candidate tank and fuselage-wall concepts. To provide an overall picture of the depth of the screening effort, the contents are summarized in this figure and cover from the definition of the aft tank configuration and candidate concepts to the selection of the most promising concepts. The following figures display or summarize the results obtained in each step of this screening process.

CONCEPT SCREENING

- AFT TANK CONFIGURATION
- CANDIDATE CONCEPTS
- INTERNAL LOADS/STABILITY COMPUTER RUNS (BOSOR)
- LOAD/TEMPERATURE ENVIRONMENT
- SIZE CANDIDATE CONCEPTS AND DEFINE MINIMUM-WEIGHT PROPORTIONS
- SELECT MOST PROMISING CONCEPTS

Figure 5

GENERAL CONFIGURATION OF AFT TANK
(Figure 6)

The aft tank of the aircraft was used as a basis for both the structural and insulation screening phases. The general configuration of the tank and its geometric relationships, which were assumed for preliminary analysis purposes, are illustrated in this figure. Two basic types of tank design were considered; they are:

- Integral, where the tank serves both as the container of the fuel and also carries the fuselage loads.
- Nonintegral, in which the tank is simply a fuel container and doesn't actively participate in the support of the body loads which are carried by an external fuselage structure.

Solution to the relationship between internal volume, insulation thickness, and the basic tank dimensions is shown in the lower part of this figure. A constant volume tank of 219.3 m^3 (7746 ft^3) was postulated for a representative foam insulation system. Both baseline tanks contained 15.2 cm (6.0 in) of insulation and were approximately 12.2 m (40.0 ft) long with tank diameters of approximately 5.79 m (19.0 ft) and 3.65 m (12.0 ft) at the large and small ends, respectively.

GENERAL CONFIGURATION OF AFT TANK

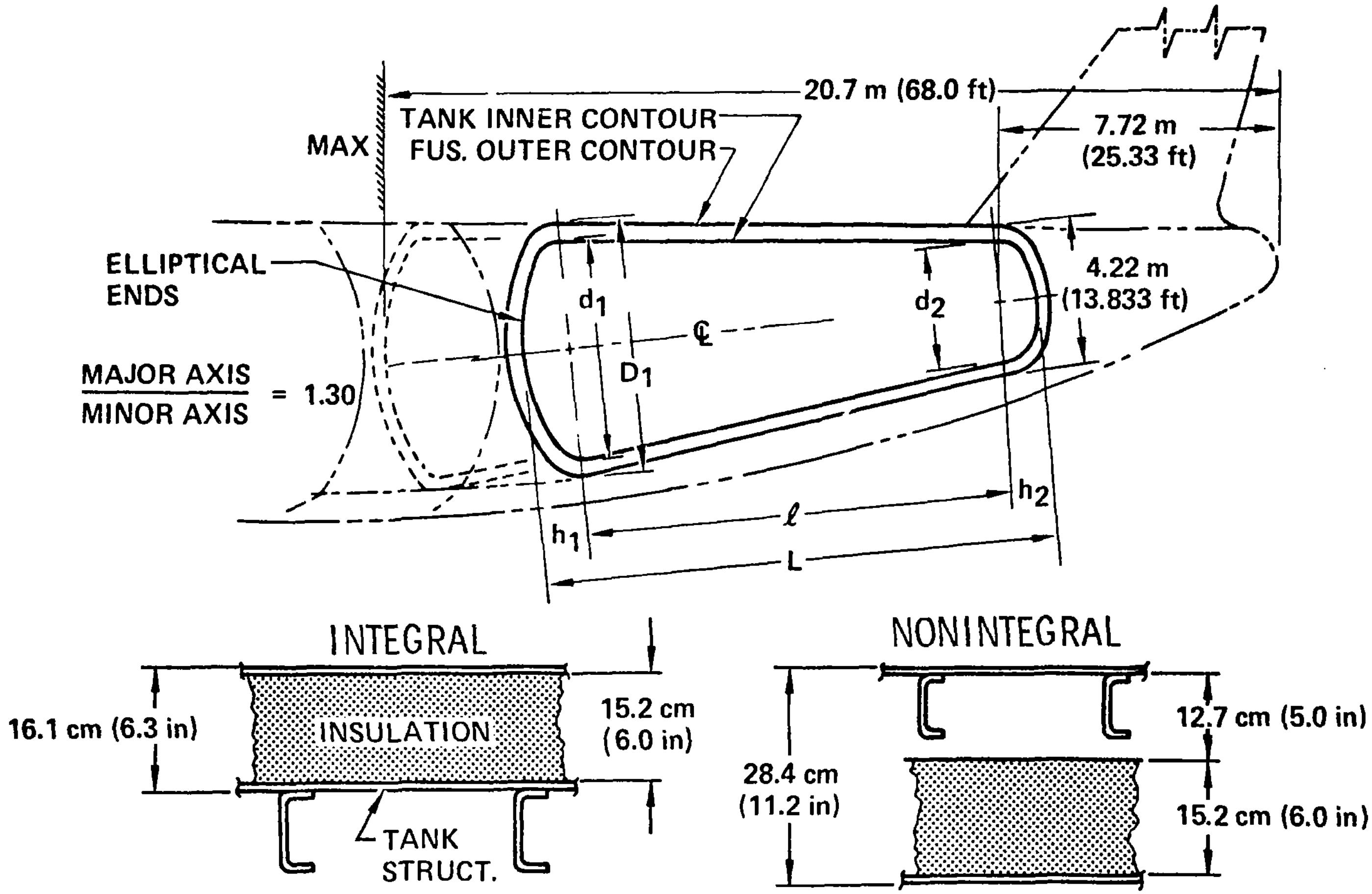

VOL	m^3 (ft^3)	219.3 (7746)	219.3 (7746)
d1	m (ft)	6.00 (19.70)	5.87 (19.25)
d2	m (ft)	3.90 (12.78)	3.65 (11.97)
L	m (ft)	12.20 (40.02)	13.0 (42.61)

Figure 6

TANK STRUCTURAL CANDIDATES
(Figure 7)

Promising structural design concepts were evaluated for each of the basic types of tank design (i.e., nonintegral and integral). This figure illustrates these structural candidates.

The wall concepts considered for the nonintegral tank design were the conventional construction zee- and hat-stiffened concepts for the fuselage shell and the blade-stiffened, zee-stiffened, and tee-stiffened designs for the tank. In addition, an unstiffened wall design was included in the candidate concepts for the tank design.

For the integral tank design, the same one-piece wall design as described for the nonintegral tank was used for this investigation. All tank wall concepts, both integral and nonintegral, were restricted to one-piece configurations to minimize potential sources of leaks.

Conventional aluminum alloys (2024 and 7075) were used for the materials for the fuselage shell of the nonintegral tank design; whereas, the aluminum alloy 2219 was selected for the tank material for both basic types of tanks. The 2219 aluminum alloy was selected because of its ductility at cryongenic temperatures, as well as its weldability, formability, stress corrosion resistance, and its high fracture toughness and resistance to flow growth.

TANK STRUCTURAL CANDIDATES

STRUCTURAL COMPONENT	TANK DESIGN		
	NONINTEGRAL		INTEGRAL
FUSELAGE	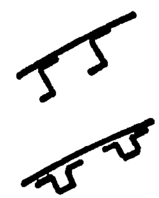	ZEE-STIFFENED HAT-STIFFENED	NOT APPLICABLE
TANK	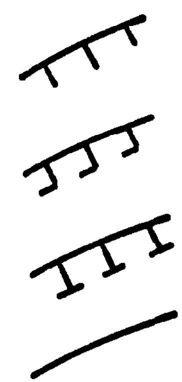	BLADE-STIFFENED ZEE-STIFFENED TEE-STIFFENED UNSTIFFENED	

Figure 7

SHELL ANALYSIS
(Figure 8)

The computerized shell analysis program BOSOR4 (Reference 2) was used to define the deflections and internal loads and to conduct the stability analyses. This computerized shell analysis program uses a finite-difference solution method based on an energy formulation.

Structural models were established from the baseline aft tank geometry established for the integral and nonintegral tank designs. The figure on the right illustrates the tank dimensions and some of the model data used for the nonintegral tank design. The tank was supported at the equators of the forward and aft tank closures. At the aft support, the tank and shell have compatible deflections (axial and radial) and rotational degrees of freedom; whereas, only compatible radial deflection was permitted at the forward support.

Representative structural/material arrangements were selected for both models. For the nonintegral tank model, a zee-stiffened panel concept was selected for the fuselage with a blade-stiffened wall concept used for the corresponding tank. The materials as described previously were used for these components.

The flight loads, tank internal pressure, and temperature distributions were coded using the 'BOSOR4' code for input into the structural models to define the overall internal loads. Results of the static solution defined the displacement components and the stress and moment resultants of the tank design.

SHELL ANALYSIS

- BOSOR4 COMPUTERIZED SHELL PROGRAM
- REPRESENTATIVE STRUCTURAL/MATERIAL CONCEPTS
- APPLIED LOADS - PRESSURE, TEMPERATURES AND BODY LOADS
- RESULTS - DISPLACEMENTS, INPLANE LOADS AND BENDING MOMENTS

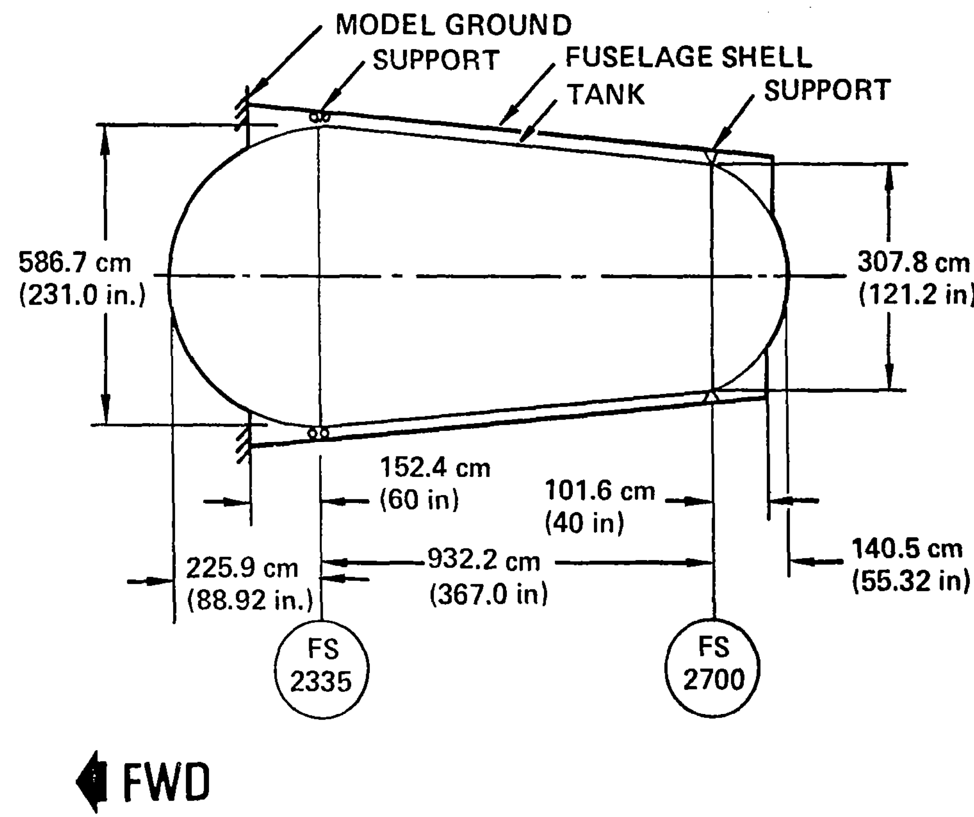

Figure 8

DESIGN LOAD CONDITIONS
(Figure 9)

Five flight conditions and an emergency landing condition were investigated for this study. The flight conditions included a positive low-angle-of-attack condition (PLA), an abrupt pitching-maneuver condition, a negative-maneuver condition, a cruise condition and a vertical-gust condition.

A description of these flight conditions is as follows:

- A PLA condition at 2.5g with a download on the tail of 445 kN (100 000 lb). Altitude is 6.64 km (21 800 ft).

- An abrupt pitching maneuver at 1.0g with a download on the horizontal tail of 578 kN (130 000 lb). Airplane is at sea level during this condition.

- The cruise condition was investigated in support of the fatigue evaluation. This condition is a 1.0 g at start of cruise with a down load on the horizontal tail of -222 kN (-50 000 lb).

- A vertical-gust condition was investigated at 3.05 km (10 000 ft), high-intensity nonstorm turbulence (U_{de} = 15.2 m/s (50 fps)). This condition was found to be noncritical.

- A negative-maneuver condition of -1.0g with an upload on the horizontal tail of 71.2 kN (16 000 lb). Altitude is 6.64 km (21 800 ft).

In addition, the emergency landing requirements specified in FAR 25 were considered in the design. The following load factors are specified: forward (n_x) = 9g, downward (n_z) = 4.5g, upward (n_z) = 2g and sideward (n_y) = 1.5g.

DESIGN LOAD CONDITIONS

- POSITIVE LOW ANGLE OF ATTACK (2.5g)
- ABRUPT PITCHING MANEUVER (1.0g)
- START OF CRUISE (1.0g)
- VERTICAL GUST
- NEGATIVE MANEUVER (-1.0g)
- EMERGENCY LANDING COND. (FAR 25)

Figure 9

POINT DESIGN LOAD ENVIRONMENT
(Figure 10)

Point design regions were selected for the structural-concept screening analysis. These regions correspond to the one-quarter and three-quarter lengths between the equators of the forward and aft tank closures. The load/temperature environments were defined at these locations using the results of the BOSOR4 internal load runs

This figure depicts a typical point design environment at the tank quarter-length region. These forces occur during the PLA flight condition and reflect only the membrane portion of the internal loads. The bending and torsional moments were included in the detail structural analysis but are not shown for clarity.

A typical bending distribution is indicated on the fuselage of the nonintegral tank design. The meridional force (N_1) has approximately 470 kN/m (2700 lb/in) on the extreme fibers of the shell and a corresponding 30 kN/m (170 lb/in) in the hoop direction. The tank for this design is predominately a biaxial stress field, 2:1 ratio of hoop-to-meridional stress, caused by the internal pressurization. Slight alterations of this ratio are noted due to the tank inertia loading.

For the integral tank design, a maximum tensile load of approximately 700 kN/m (4000 lb/in) is noted on the upper fibers with a compressive load of 200 kN/m (1100 lb/in) shown on the lower fiber. The hoop force is constant at approximately 420 kN/m (2400 lb/in).

POINT DESIGN LOAD ENVIRONMENT

STRUCTURAL COMPONENT	MEMBRANE FORCE kN/m (lbf/in)[1][2]					
	NONINTEGRAL TANK			INTEGRAL TANK		
	N_1	N_2	N_{12}	N_1	N_2	N_{12}
FUSELAGE						
UPPER	467 (2669)	30 (173)	0 (0)			
MID	0 (0)	0 (0)	74 (423)			
LOWER	-468 (-2670)	-30 (-174)	0 (0)			
TANK						
UPPER	207 (1184)	446 (2545)	0 (0)	698 (3983)	415 (2370)	0 (0)
MID	230 (1313)	467 (2667)	6 (33)	250 (1429)	416 (2378)	61 (347)
LOWER	252 (1442)	488 (2789)	0 (0)	-198 (-1129)	418 (2386)	0 (0)

1. PLA FLIGHT CONDITION, ULTIMATE LOADS
2. TANK QUARTER-LENGTH LOCATION FROM EQUATOR OF FORWARD HEAD

Figure 10

FATIGUE DESIGN
(Figure 11)

A description of the fatigue criteria was presented previously in the design criteria section. The intent of this figure is to describe the application of these criteria during the structural analysis of the candidate wall concepts.

The fatigue design requirements are met by restricting the permissible design tension stress levels used for design. Design allowables for both the operating and ultimate design conditions for 2219-T851 aluminum alloy were established and are shown in this figure. For the operating condition, the limit loads for the cruise condition were used and the circumferential skin stress of the fuel tank was restricted to a stress level of 172 MPa (25 ksi) which corresponds to a fatigue quality index of 5. The variation of this design allowable with K_t is shown by the lower curve in this figure.

The design allowables for the skin and substructure of the tank for the ultimate design conditions are shown by the two upper curves on this figure. The application is similar to the operating conditions, with the exception that the applied loads reflect the maximum ultimate design loads. The upper curve reflects the design stress level applicable to fuel-tank substructure other than skin, such as frames, which are uniaxially loaded. The second curve, and the lower curve, present the design allowable to be applied to the fuel tank circumferential stress and reflect a biaxial loading condition.

FATIGUE DESIGN

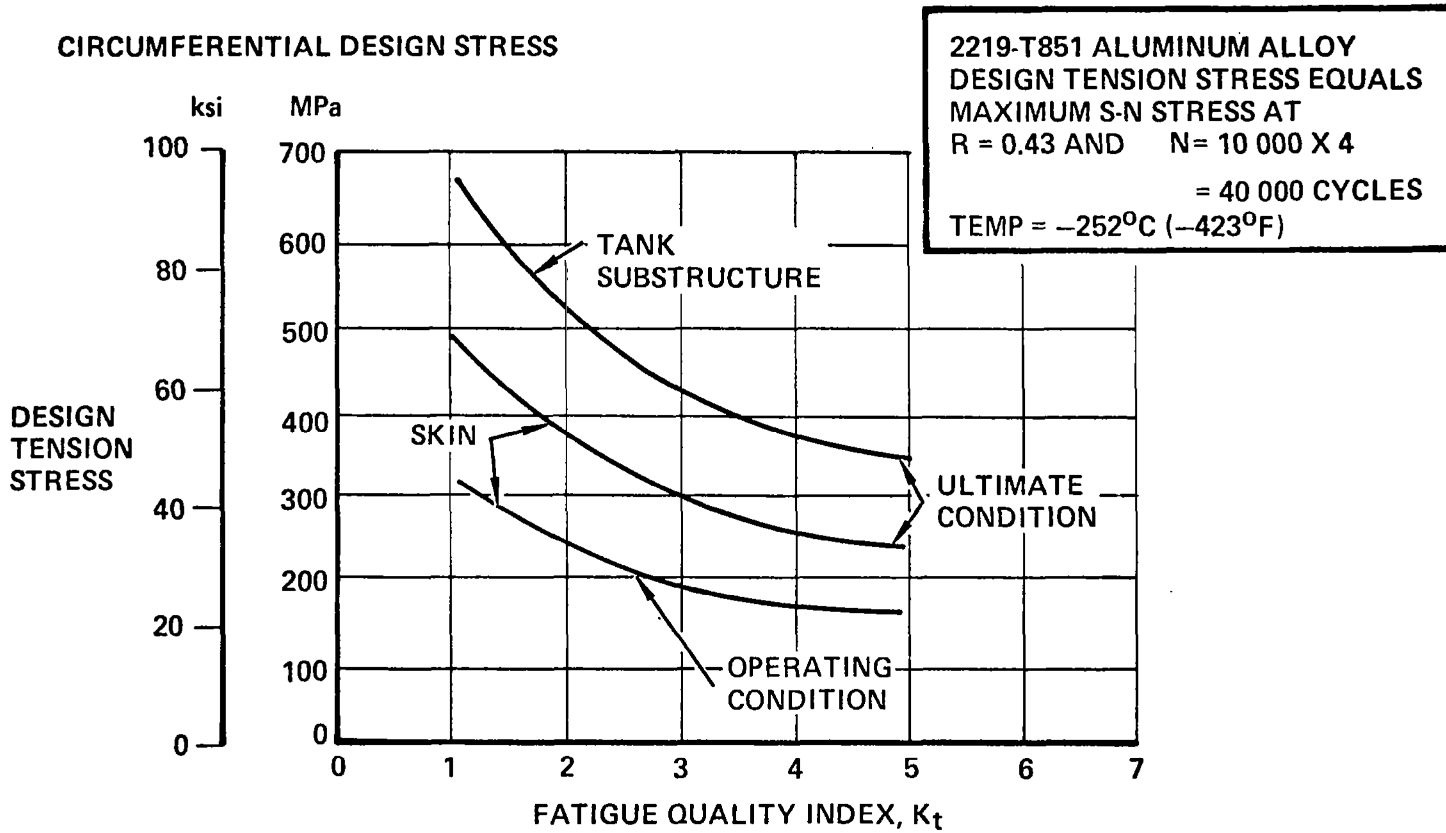

Figure 11

DAMAGE TOLERANCE
(Figure 12)

The objective of the fail-safe analysis is to ensure that the structure in the presence of an assumed damage condition is capable of supporting the design load of 100-percent limit load. Both normal and accidental damages were considered. The accidental damage condition is summarized in this figure.

Both circumferential and longitudinal damages were assumed for the accidental damage condition. A 30.5 cm (12 in.) crack was assumed for both damage cases. The residual strength or allowable stress of the damaged structure must be capable of supporting limit loads normal to the crack. The circumferential crack condition is pictured in the upper right-hand sketch, while the longitudinal damage condition is shown in the lower figures.

The circumferential crack case dictates the sufficiency of cross-sectional area and/or the requirements for longitudinal straps; whereas, the longitudinal crack case is used to assess both the frame and hoop strap requirements.

In general, for all tank wall concepts which have separately attached stiffeners (spot welded or riveted), the stiffeners reinforce the skin and provide crack-arresting capability; conversely, for one-piece wall designs, no crack-arresting capability is provided by the stiffener.

DAMAGE TOLERANCE

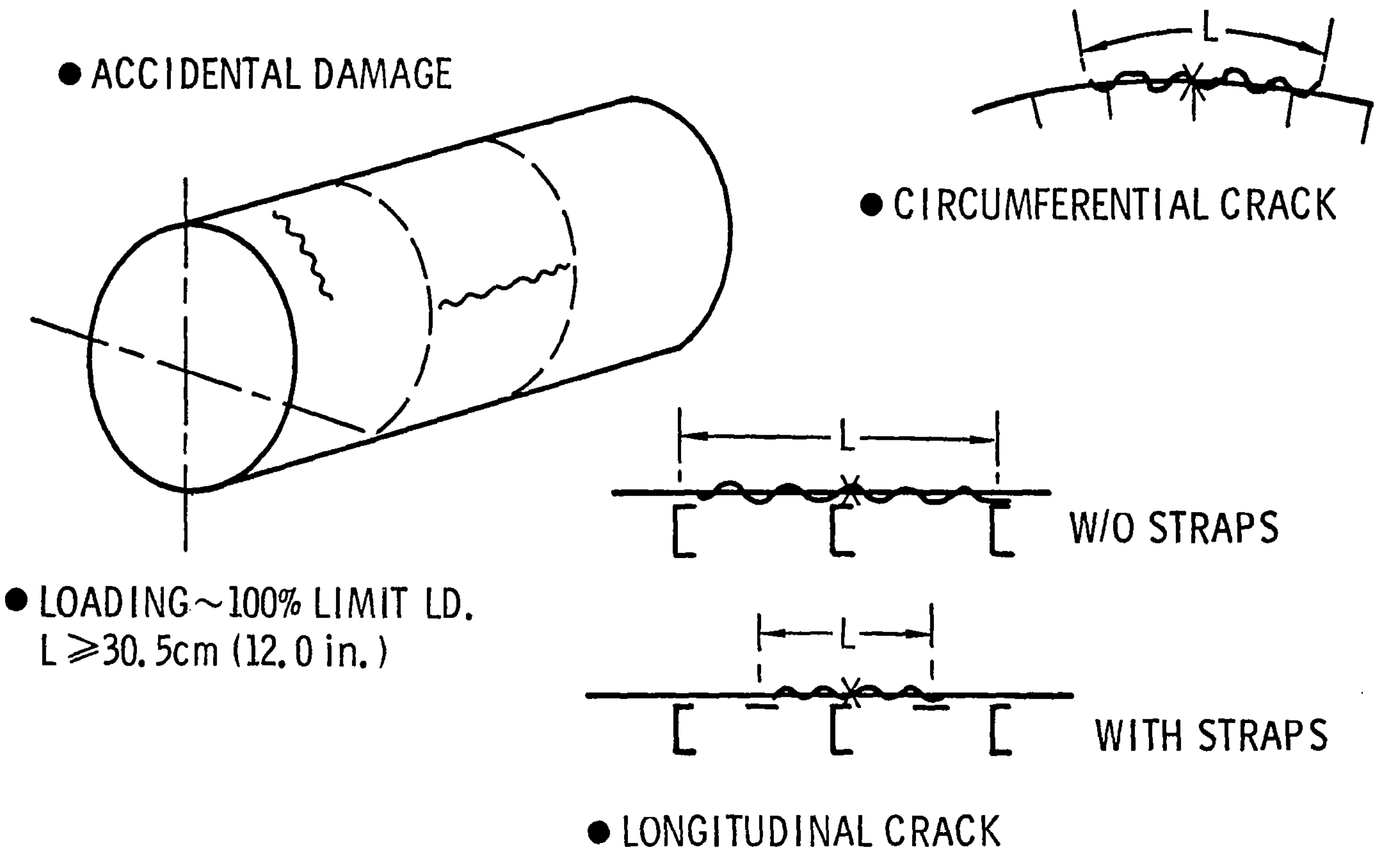

Figure 12

DAMAGE TOLERANCE
(Figure 13)

For the normal usage condition, the skin stress level for 2219 aluminum alloy was based on the leak-before-break criteria, i.e., a through-the-thickness flaw will remain subcritical for a sufficiently long period. Calculations were made to define the number of cycles from leak to final failure for the baseline aluminum alloy. The flaw shape is shown in this figure and corresponds to a crack geometry parameter (2c/a) equal to 3, and a ratio of minimum stress to maximum stress equal to 0.45. The figure to the left illustrates these results, the variation in skin stress with loading cycles for different skin thickness.

This data was replotted as a function of maximum stress versus thickness for the required 10 000 cycles. These results are illustrated by the right-hand figure. Allowable skin stresses (limit) of 255 MPa (37 ksi) and 234 MPa (34 ksi) are indicated for 0.203-cm (0.080 in.) and 0.254-cm (0.10 in.) wall thicknesses, respectively. This normal usage damage criteria was not a decisive aspect in the design of the tank and in most cases this criteria was merely used as a check on the final design.

DAMAGE TOLERANCE

- NORMAL USAGE
  - LEAK - BEFORE - BREAK
  - THROUGH-THE-THICKNESS FLAW
  - REMAIN SUBCRITICAL FOR A/P AIRPLANE LIFE

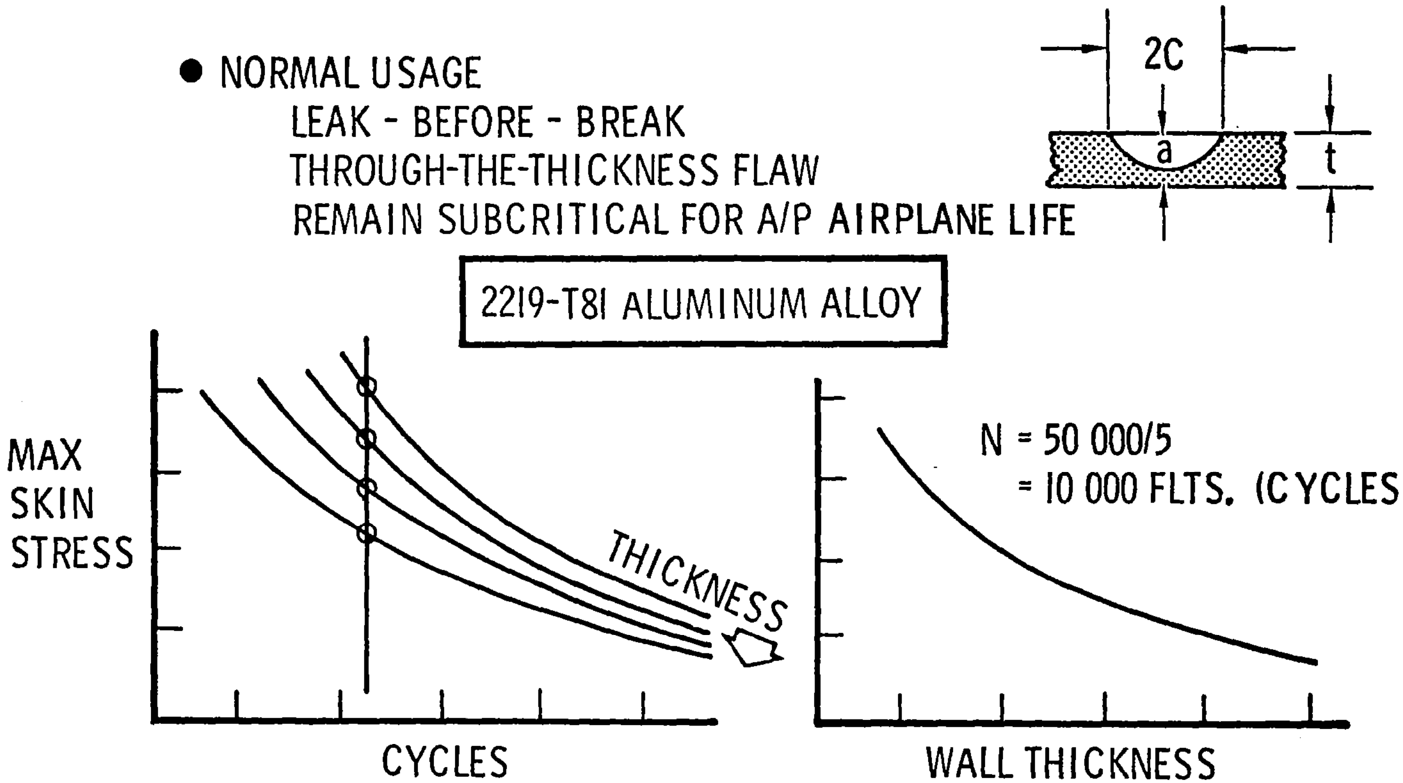

Figure 13

NONINTEGRAL TANK DESIGN-UNIT WEIGHT COMPARISON
(Figure 14)

The candidate wall concepts identified for the tank and fuselage were subjected to point design analyses to define the minimum-weight designs. This analysis was conducted at the tank one-quarter length and three-quarter length locations using the internal loads defined by BOSOR runs. At these locations a unit structure, incorporating each of the candidate concepts, was assumed and is illustrated in the left-hand sketch.

The structural investigation included basic strength, stability and damage tolerance analyses. The fuselage shell candidates (zee- and hat-stiffened concepts) were sized independently to define the minimum-weight concept which was then used with each of the candidate tank wall concepts to define a total unit weight.

The figure to the right illustrates the total unit weight (fuselage and tank) of the nonintegral design at the tank quarter-length region. Structural analyses were conducted at three circumferential locations and then averaged to define the unit weight for that point design region. The tank of the nonintegral design experiences only minor thermal loadings and flight inertia loads; therefore, the predominate loading was internal pressurization. Since the tank wall is tension designed and noncritical for buckling, the structural candidates were designed by applying the fatigue and damage tolerance criteria. Hence, the abscissa of the illustrated figure is presented in terms of the hoop fail-safe strap spacing.

The average circumferential unit weight and component unit weight at the upper, mid, and lower fibers indicate an insignificant difference in weight between any of the tank wall concepts. The average unit weight for all candidate concepts, which includes both the fuselage and tank, is approximately 22.4 kg/m^2 (4.60 lbm/sq ft).

NONINTEGRAL TANK DESIGN-UNIT WEIGHT COMPARISON

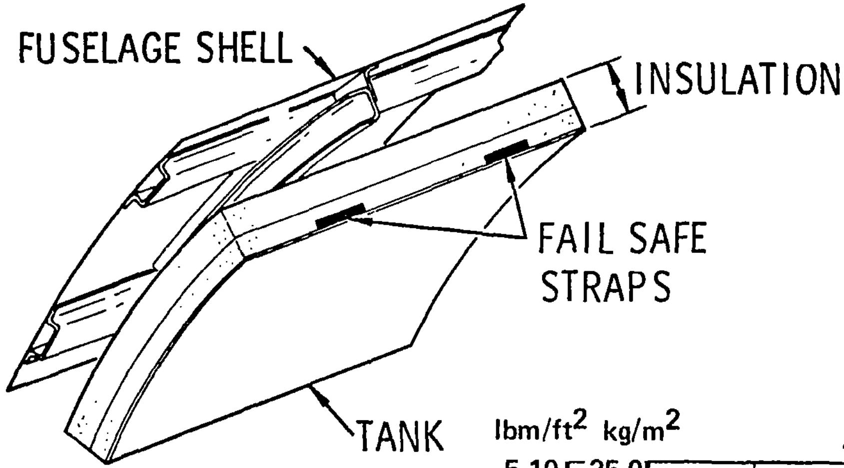

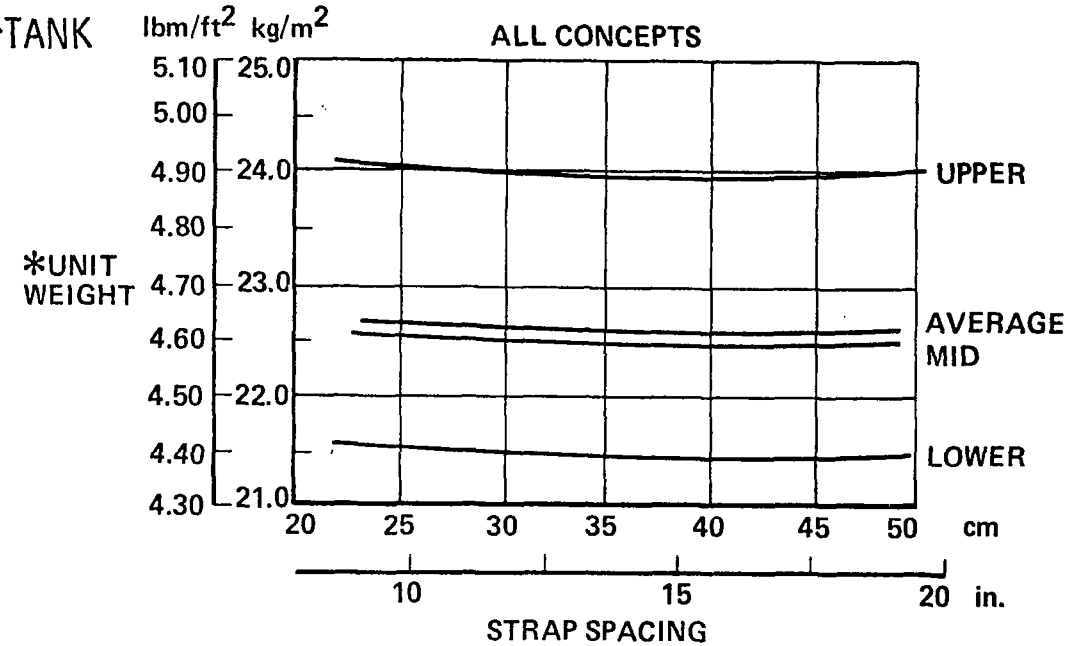

*INCLUDE MIN. WEIGHT FUSELAGE DESIGN AND TANK (SHELL, STRAPS AND NOF)

Figure 14

INTEGRAL TANK DESIGN-UNIT WEIGHT COMPARISON
(Figure 15)

Point design regions were selected on each tank for conducting the detail structural analysis. The two regions selected were the tank quarter and three-quarter length stations with three circumferential regions at each station. At these point design regions, the load/temperature environment was defined by the BOSOR4 runs and a unit structure was analyzed using each candidate wall configuration. For example, the integral tank unit structure consisted of the tank wall, frame, nonoptimum factor (NOF), fail-safe straps. This analysis included basic strength, stability, and damage tolerance analyses.

Unit weights were calculated at each circumferential location and averaged to define the unit weights at each station. An example of these results are shown in this figure for the integral tank design at the quarter-length station. Minimum-weight designs are noted at 1.27 m (50 in.) frame spacing for both the zee- and tee-stiffened designs and at approximately 1.02 m (40 in.) spacing for the blade-stiffened concept. Corresponding weights of 18.1 kg/m^2 (3.7 lbm/ft^2) and 19.0 kg/m^2 (3.9 lbm/ft^2) are noted for these respective designs.

INTEGRAL TANK DESIGN-UNIT WEIGHT COMPARISON

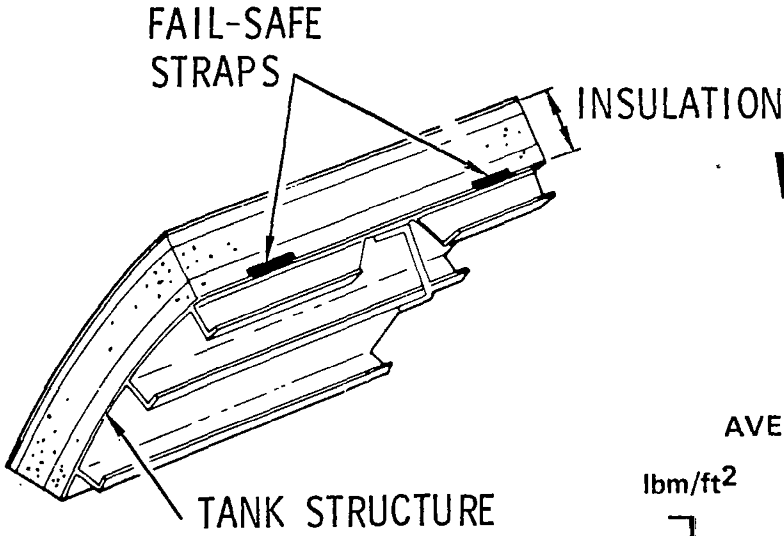

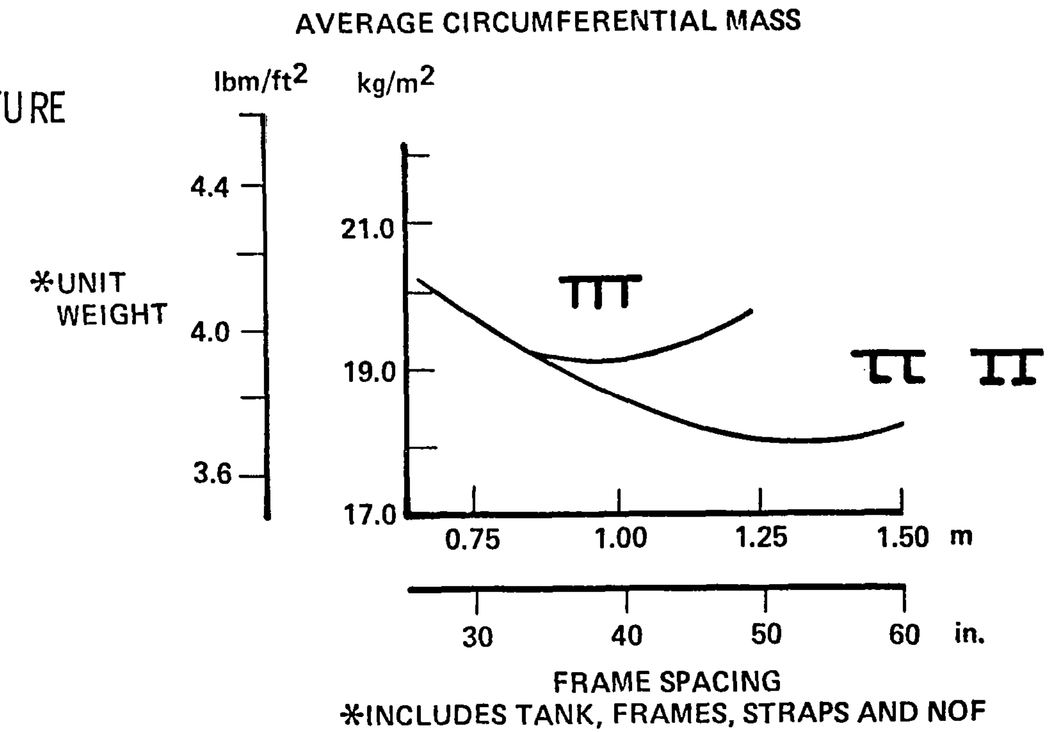

Figure 15

AFT TANK WEIGHT
(Figure 16)

The tank weight for each candidate concept for the integral and nonintegral tanks were extrapolated using the results of the point design analysis. This figure summarizes the tank weight for the basic types of tank and excludes any common structure and insulation, e.g., for the nonintegral tank design only the basic tank and fuselage are included.

For the nonintegral tank design, all tank wall concepts (blade, zee, tee and unstiffened) had approximately the same weight because they were predominately tension designed. The unstiffened wall concept was selected not only because of its low weight, but more importantly, its lower cost. The minimum-weight fuselage shell used for all the nonintegral designs was the hat-stiffened concept.

For the integral tank design the zee- and tee-stiffened concepts were lighter weight than the blade-stiffened wall concept, i.e., approximately 91 kg (200 lbm). This weight difference is mainly attributed to the higher compression efficiences of these designs at several of the point design regions. The zee-stiffened concept was selected over the tee-stiffened concept as the more promising concept mainly because it would be slightly less complicated to manufacture, i.e., less costly. All concepts used the unstiffened wall concept at the side panels.

AFT TANK WEIGHT

ITEM	WEIGHT kg (lbm)		
	NONINTEGRAL	INTEGRAL	
	ALL CONCEPTS	ZEE AND TEE	BLADE
TANK	2253 (4968)	2942 (6485)	3041 (6704)
CYLINDRICAL SECTION	1746 (3850)	2401 (5293)	2500 (5512)
DOMES	337 (743)	371 (817)	371 (817)
DIVIDER DOME	170 (375)	170 (375)	170 (375)
BODY SHELL	1516 (3342)	-	-
TOTAL	3769 (8310)	2942 (6485)	3041 (6704)

Figure 16

DOME SHAPE STUDY
(Figure 17)

Promising dome configurations were evaluated in compliance with the stated objective. The candidate configurations included in this study are a hemispherical dome and the general families of ellipsoidal and toroidal domes. The hemispherical dome configuration shown on the left is characterized by constant radii of curvature in both the meridional and hoop direction; whereas, the ellipsoidal dome has varying hoop and meridional radii of curvature. The toroidal dome is composed of a spherical cap and a torus. The torus is defined by the knuckle angle Ø and has a constant meridional radius of curvature and a varying hoop curvature.

The baseline tank diameter corresponded to the large diameter of the nonintegral tank design and only internal pressurization was considered for the analysis. The basic analysis was conducted in two stages; they are:

- A preliminary analysis which analyzed the complete range of ellipsoidal and toroidal heads and define their weight, internal volume, and surface area. Only membrane theory was applied with the von Mises failure criteria used for combining the applied stresses. From this data, total tank weights were calculated for a constant volume tank, 219.3 m^3 (7746 ft^3). This data was input into the ASSET Program to assess the effect on aircraft (L/D) for a constant payload range mission. The optimum dome proportions were defined for a minimun direct operating cost (DOC).
- The final analysis consisted of constructing structural models of the minimum DOC designs and conducting BOSOR static solutions to define the added weight increment involved if both membrane and bending stresses are considered. The von Mises failure was also used for this investigation. The best dome shape was selected from these results and used hereafter for all design studies.

DOME SHAPE STUDY

OBJECTIVE - CONDUCT TRADE STUDIES TO
DEFINE THE PROPER DOME SHAPE CONSIDERING
WEIGHT AND VOLUMETRIC EFFICIENCY

CANDIDATE CONFIGURATIONS

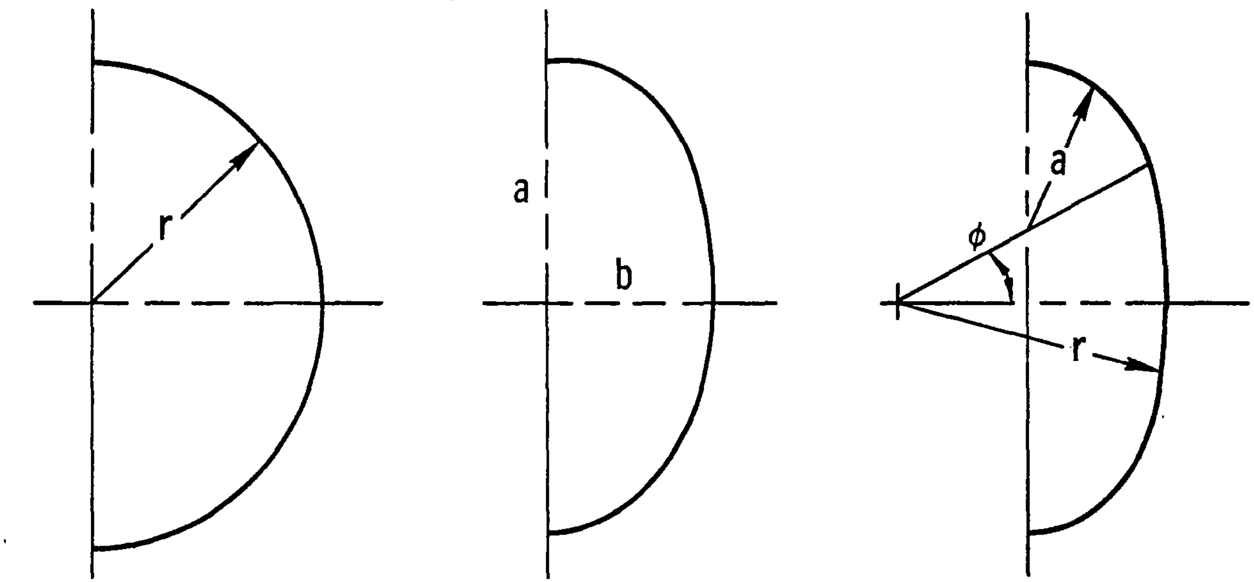

- HEMISPHERICAL
- ELLIPSOIDAL
- TOROIDAL

Figure 17

DOME SHAPE STUDY RESULTS
(Figure 18)

The first column in this figure reflects the results of the preliminary analysis and presents the optimum design weight and associated dome parameter when only the unit dome is considered. For this analysis, the ellipsoidal dome design has the lowest weight and indicates a weight savings of 3 percent over the minimum-weight toroidal design and approximately 20 percent over the hemispherical design.

When DOC is the object function and the tank weights using the two designs are compared, the toroidal design is the lightest design weighting 234 kg (516 lbm), which is approximately 4 percent lighter than the ellipsoidal dome. Both designs have a DOC of 0.985 ¢/seat-km (1.825 ¢/seat-n.mi.) when a total airplane weight is considered.

Based on these results, neither design afforded a decisive advantage when DOC is the object function; whereas, when head weight is the driver the ellipsoidal design reflects the best dome shape. The ellipsoidal dome was selected as the baseline configuration for any further studies.

DOME SHAPE STUDY RESULTS

CONCEPT	EVALUATION FUNCTION	
	MINIMUM WT.	MINIMUM DOC *
ELLIPSOIDAL DESIGN		
a/b	1.30	1.60
WEIGHT, kg(lbm)	215 (474)	240 (530)
TORISPHERICAL DESIGN		
ϕ, radians	0.95	0.36
WEIGHT, kg(lbm)	222 (489)	234 (516)

* 0.985 ¢/SEAT-km (1.825 ¢/SEAT-n. mi.)

Figure 18

NONINTEGRAL TANK EXTERNAL FOAM INSULATION
(Figure 19)

As a result of the insulation and structures investigations, four preferred fuel containment systems (FCS) were selected to determine which is best for application in a commercial transport aircraft. This evaluation was based on a comparison of performance and cost characteristics of aircraft designed specifically for each of the candidate systems.

Each of the candidate fuel containment systems was incorporated into an aircraft design which was then subjected to the sizing routine using the ASSET computer program. The result was a definition of four aircraft, one for each candidate FCS, each of which was optimized to perform the design mission at the lowest direct operating cost, while still meeting all design and operational constraints.

These next four figures are presented to illustrate the tank and insulation design of these preferred candidates. Some of the results of the final evaluation will be discussed.

The first candidate concept is shown on this chart and is for the nonintegral tank design. This concept has an exterior rigid closed-cell foam insulation system with a multilayer sandwich called MAAMF (Mylar-Alum.-Alum.-Mylar-Fabric). The total thickness of the vapor barrier (MAAMF) is 0.013 cm (0.005 in.) to 0.015 cm (0.006 in.) and weights 0.225 kg/m^2 (0.046 lbm/ft^2). The rigid foam is 10.0 cm (3.94 in.) deep.

The structural concepts represent the results of the concept screening analysis. The fuselage structure is a hat-stiffened shell with frames at 1.27 m (50 in.) spacing. A clearance of 1.91 cm (0.75 in.) is allowed between fuselage and insulation for clearance.

The aircraft using this candidate FCS weighed 175 900 kg (387 800 lbm) and cost $39.1 million based on a fleet size of 350 aircraft.

NONINTEGRAL TANK
EXTERNAL FOAM INSULATION

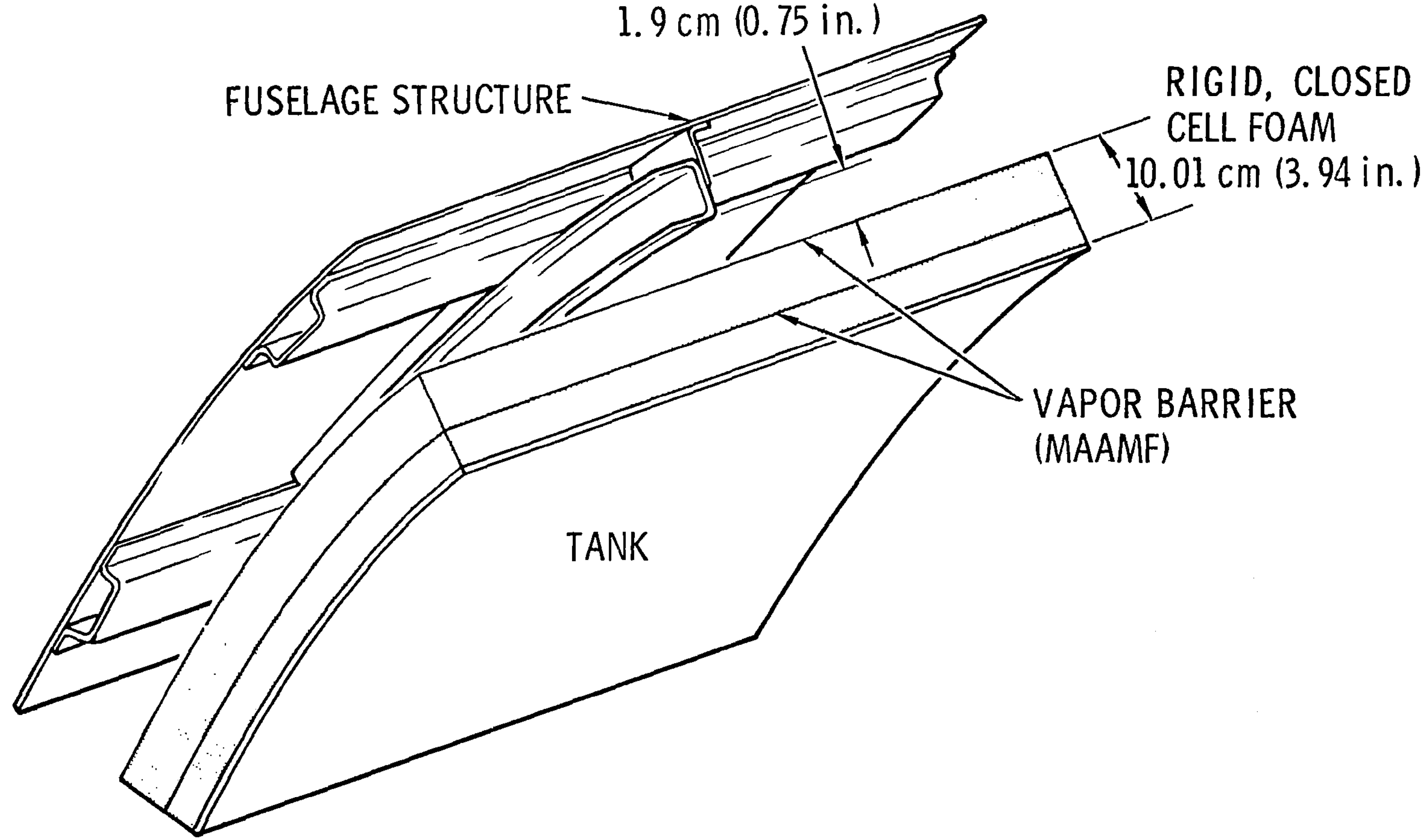

Figure 19

NONINTEGRAL TANK HARD SHELL VACUUM
(Figure 20)

The second candidate was the nonintegral fuel tank with a hard shell vacuum jacket. Rigid closed-cell foam 1.27 cm (0.50 in.) thick was located at the tank wall to prevent air liquification in event of external leakage into the vacuum space. Aluminized Mylar is bonded to the interior surface of the jacket and exterior surface of the foam to reduce radiation heat transfer.

The fuselage structure is a 7.62-cm (3 in.) deep aluminum-honeycomb sandwich structure capable of withstanding the body loads and vacuum pressure. A clearance of 6.35 cm (2.50 in.) is allowed between the honeycomb structure and foam for evacuated air space. The tank is the unstiffened wall configuration resulting from the concepts screening analysis.

The aircraft design using this candidate FCS weighed 179 400 kg (395 600 lbm) and cost approximately $40 million per aircraft.

NONINTEGRAL TANK
HARD SHELL VACUUM

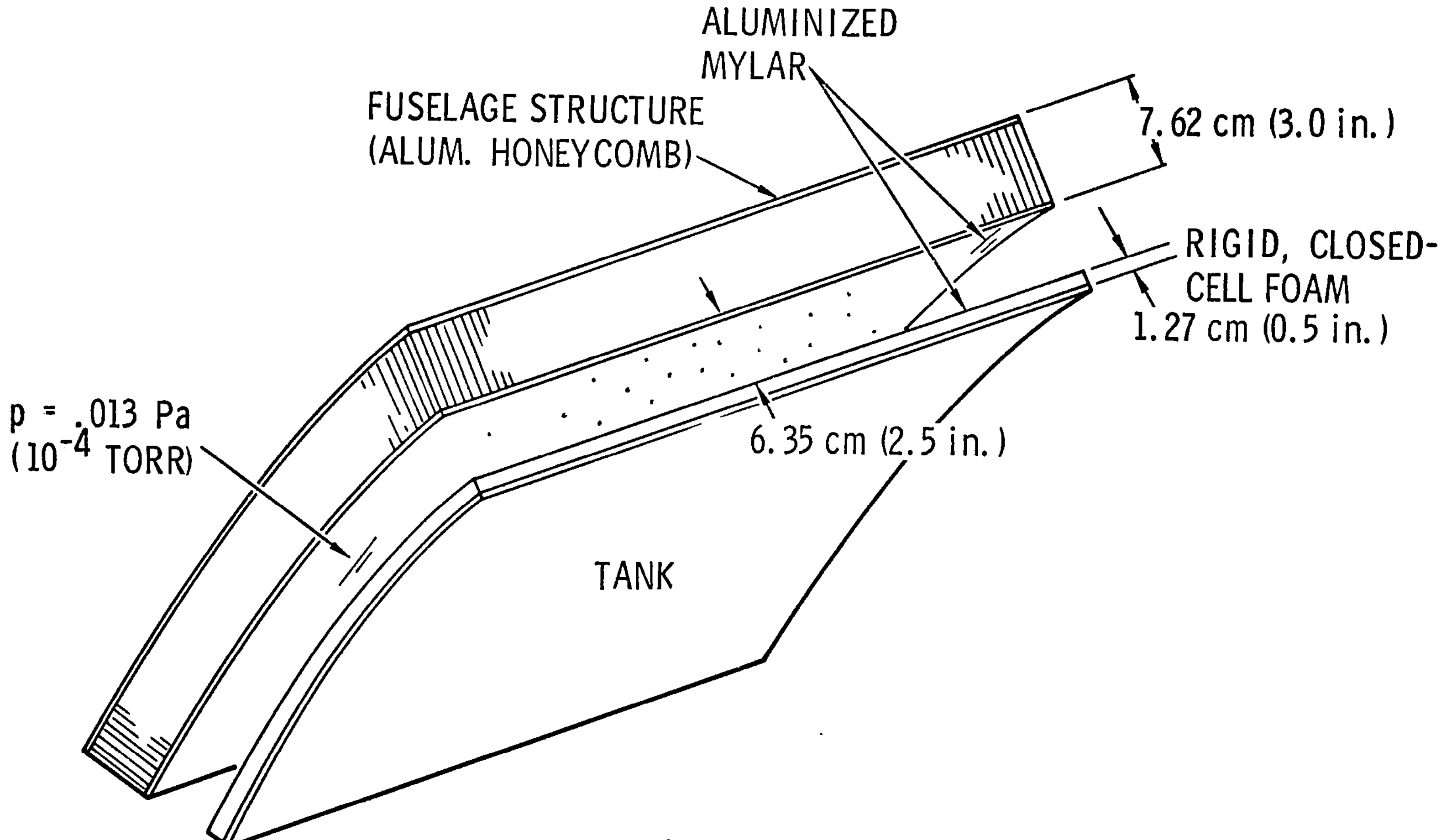

Figure 20

INTEGRAL TANK EXTERNAL FOAM INSULATION
(Figure 21)

This candidate FCS is an integral tank design which incorporates a zee-stiffened wall configuration with internal frames. A rigid closed-cell foam 6.83 cm (2.69 in.) deep is used for primary insulation. An open-cell flexible foam, exterior to the primary insulation, is used to accommodate dimensional changes and to support the exterior fairing. MAAMF vapor barriers are provided as shown. In addition, a composite fairing is provided for aerodynamic smoothness and protection.

The aircraft incorporating this FCS was one of the lighter weight designs. A gross weight of 172 100 kg (379 500 lbm) and a cost of approximately $38.3 million were indicated for this design.

INTEGRAL TANK
EXTERNAL FOAM INSULATION

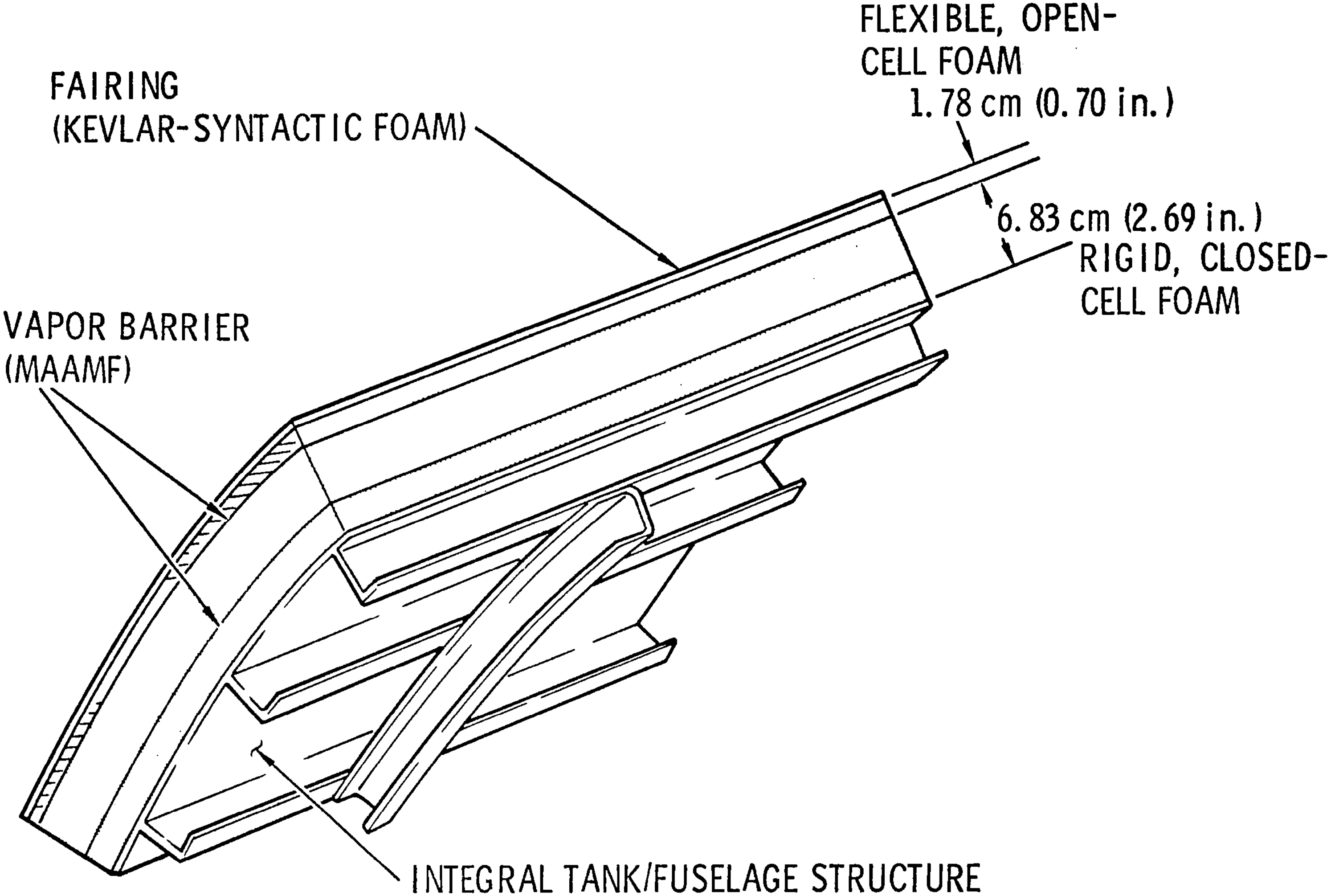

Figure 21

INTEGRAL TANK MICROSPHERE INSULATION
(Figure 22)

The cross section of the last preferred fuel containment systems is shown on this chart. This system is for an integral fuel-tank design and incorporates the zee-stiffened tank wall concept. An external evacuated microsphere insulation with a flexible metal vacuum jacket is provided as the primary insulation. A thickness of 3.89 cm (1.53 in.) is noted for this insulation. A flexible open-cell foam and an aerodynamic fairing, similar to the previous FCS, are provided.

The aircraft sized using this FCS was the lightest weight and least costly of all the candidates. A gross weight of 171 400 kg (377 800 lbm) and a cost $38.1 million was calculated for this candidate.

INTEGRAL TANK MICROSPHERE INSULATION

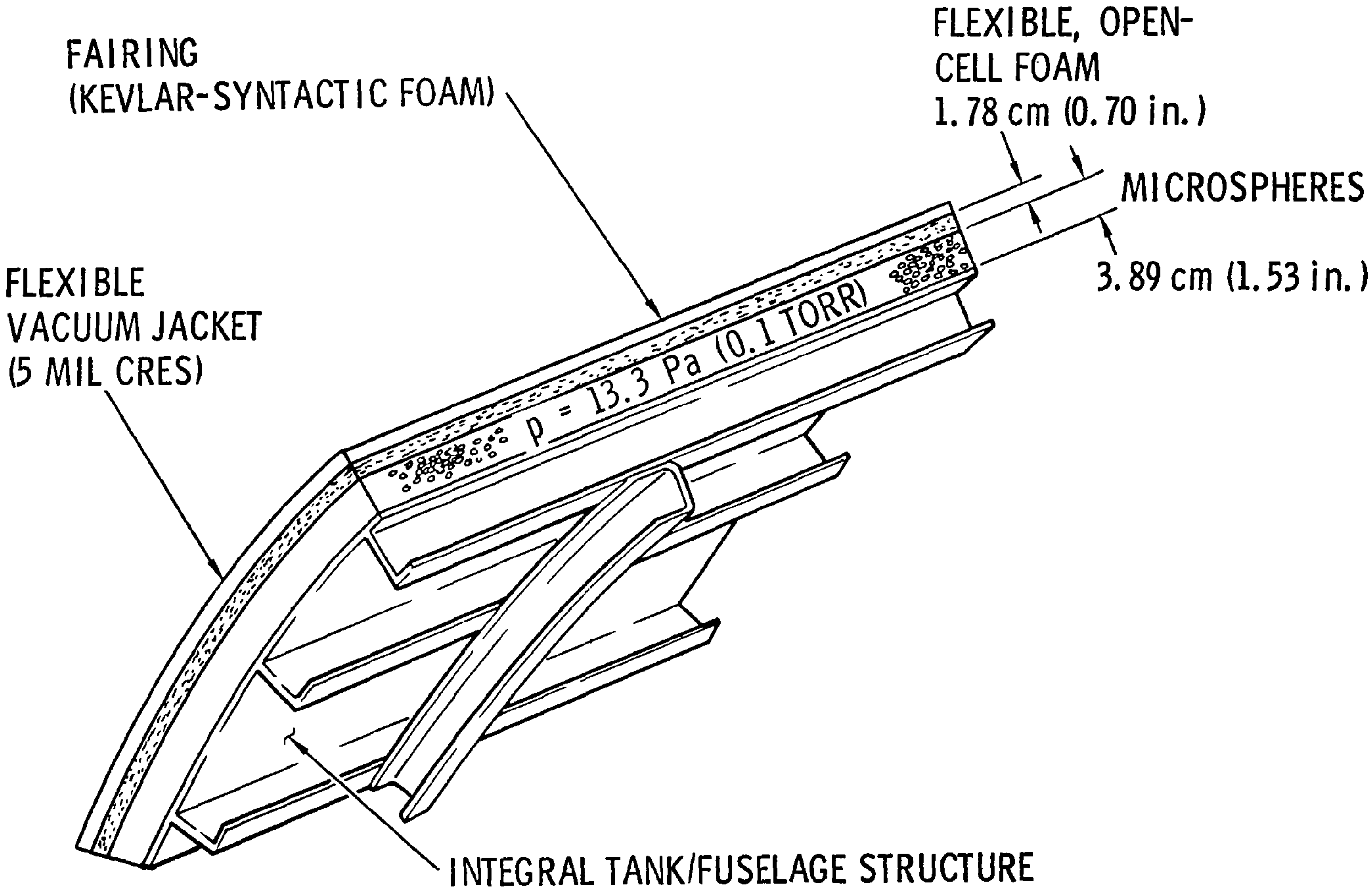

Figure 22

CONCLUSIONS
(Figure 23)

The application of a realistic fatigue and damage tolerance criteria must be accounted for in the design of liquid hydrogen tankage. These criteria should include, among other things, a definition of the loading spectrum, type and size of possible damage and valid analytical methods to ensure that flight safety is maintained over the life expectancy of the airframe. For this study, the tankage experienced only minor thermal loadings and flight loads, hence, the predominate loading was the tank pressurization. Since the tanks were basically tension designed, the fatigue and damage tolerance criteria played the most important part in the overall design of the tank.

Special investigations are required to define the most efficient overall tank design. For example, parametric studies involving considerations of such items as: dome shape, pressure stabilization, pressure level, design life and tank suspension methods were conducted on this program to appraise various design aspects related to the design of the entire LH_2-fuel containment tanks.

Sensitivity factors were generated for the reference LH_2-fueled airplane to provide a basis for evaluation of the effects of changes from the baseline design. For example, the various candidate insulation systems and tank structural concepts offer trade-offs of the tankage offset distance (distance between exterior surface to tank) and weight. As the offset varies, the aircraft fuselage length must change to provide the required fuel volume within the fixed fuselage cross-section and hence the sensitivity on the aircraft DOC could be assessed. Using this technique, the results of the various designs and parametric investigations could be defined in terms of airplane weight and DOC, hence, these factors were used in the evaluation procedure to assist in screening attractive candidates.

CONCLUSIONS

- IMPORTANCE OF FATIGUE AND DAMAGE TOLERANCE CRITERIA IN TANK DESIGN
- REQUIREMENT FOR SPECIAL INVESTIGATIONS TO SELECT MAJOR TANK COMPONENTS
- IMPORTANCE OF 'DOC' MERIT FUNCTION IN THE DESIGN PROCESS

Figure 23

REFERENCES

1. Brewer, G. D.; Morris, R. E.; Lange, R. H.; and Moore, J. W.: Volume II - Final Report: Study of the Application of Hydrogen Fuel to Long-Range Subsonic Transport Aircraft. NASA CR-132559, 1975.
2. Bushnell, David: Stress, Stability, and Vibration of Complex Branched Shells of Revolution: Users Manual for BOSOR4, Lockheed Missiles and Space Co., LMSC-D457038, May 1975.

EXTERNAL INSULATION FOR LIQUID HYDROGEN TANKS

Ellsworth L. Sharpe
NASA Langley Research Center

INTRODUCTION

Before hydrogen can be considered as the fuel for future hypersonic aircraft, several problems associated with the storage of liquid hydrogen must be solved. These problems include:

- Cryopumping of air because of the low temperature of hydrogen (21 K(-423°F)). This continual condensation at the tank wall results in the release of large quantities of heat which must be absorbed by evaporation of the fuel;

- Excessive fuel boil off as a result of the large temperature difference between the environment and the fuel tank. During cruise conditions this temperature difference can be as high as 1120 K (2000°F) since the outer surface temperature of the vehicle can be 1144 K (1600°F).

In addition to solving these problems, the thermal protection system (TPS) must also be lightweight, retain its structural integrity under all environmental conditions, require minimum preflight preparation, and offer dependable reusability.

This report presents the results of an analytical and experimental investigation of a purged multilayer insulation system for liquid hydrogen tanks which was conducted at Bell Aerospace Textron, Buffalo, New York, under NASA contract. This system, which would use either nitrogen or carbon dioxide as a purge gas, would use the layer of insulation next to the tank wall to restrict or prevent the cryodeposition of purge gas. The analytical support of the investigation included a study of the environmental conditions to which the tankage is exposed, purge gas cryopumping analysis, and heat transfer analysis. The experimental investigation consisted of screening candidate inner layer insulation materials for permeability, temperature capability, thermal conductivity, density, and strength; modifying candidate materials to improve their properties; and testing insulation specimens to verify their multicycle capability. Insulation specimens were scaled in size in order to duplicate the stress conditions which will be imposed on the insulation applied to a large tank.

Certain commercial materials are identified in this paper in order to specify adequately which materials were investigated in the research effort. In no case does such identification imply recommendation or endorsement of the product by NASA, nor does it imply that the materials are necessarily the only ones or the best ones available for the purpose. In many cases equivalent materials are available and would probably produce equivalent results.

A LIQUID HYDROGEN TANK THERMAL PROBLEM

CRYOGENIC PUMPING

(Figure 1)

The use of liquid hydrogen fuel at a temperature of 20 K (-423°F) presents several problems in fuel tankage area design. The high temperatures associated with hypersonic speeds in the atmosphere will cause the surface of the vehicle to reach a temperature above 1144 K (1600°) while the liquid hydrogen tanks will be at 20 K (-423°F), a temperature difference of over 1100 K (2000°F). Another problem is that the extremely low temperatures associated with liquid hydrogen cause air to condense on the tank surface, thereby reducing the pressure (cryopumping) and producing an inflow of additional air. If unimpeded, the liquid air will flow down the tank wall (leaving a cold bare surface for further liquification) and drip from the tank onto the hot exterior surface. There the air is revaporized, only to condense again when it comes in contact with the cold tank. Thus a continuous flow is established which, because of the large quantities of heat associated with the phase change (condensation and vaporization) of the air, causes rapid fuel boil off. In addition, cryodeposited air increases the mass of the aircraft and selective liquification of oxygen (the gas with the higher boiling temperature) introduces a potential safety hazard.

A LIQUID HYDROGEN TANK THERMAL PROBLEM

CRYOGENIC PUMPING

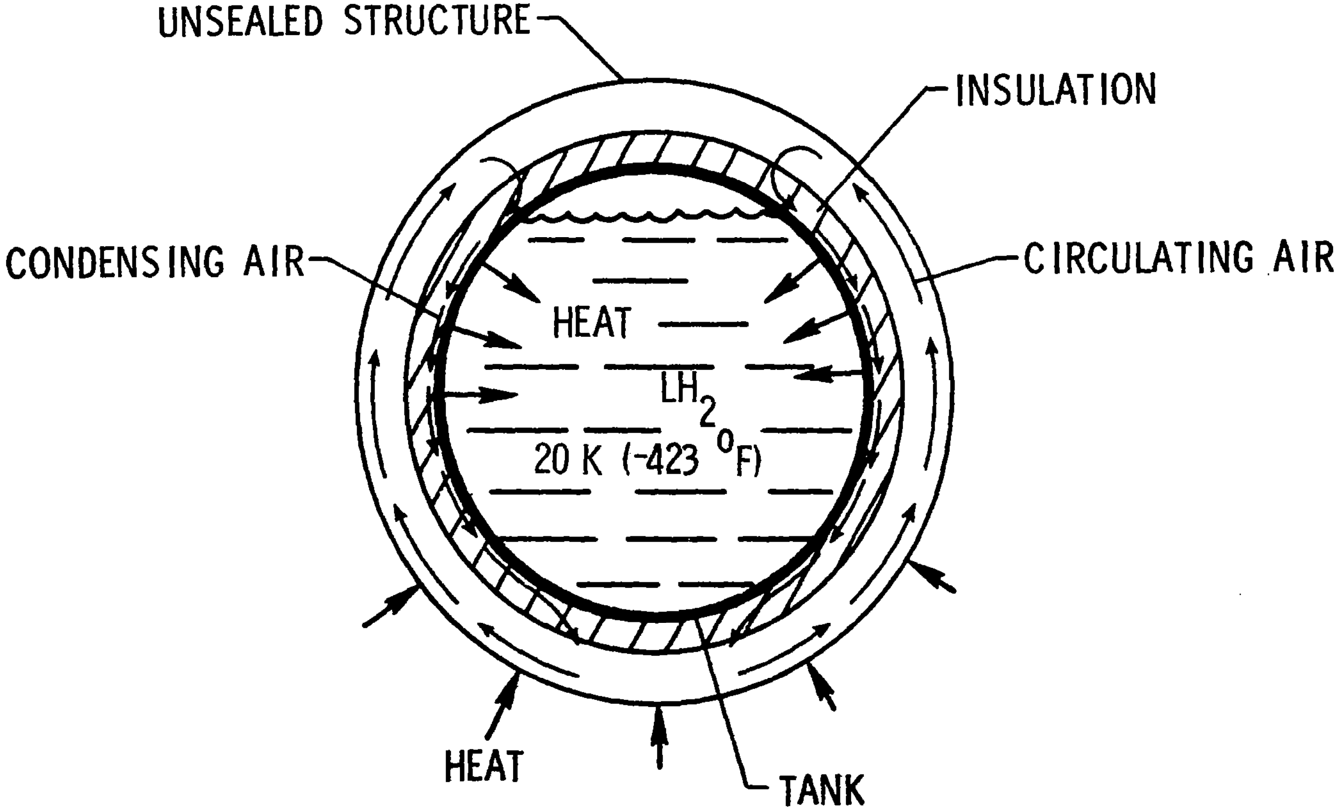

Figure 1

POTENTIAL SOLUTIONS

(Figure 2)

In an attempt to find solutions to these problems, a variety of thermal protection systems including internal, sealed, and purged systems have previously been investigated.

Internal insulation systems become inefficient because hydrogen gas permeates the insulation, resulting in high thermal conductivity (refs. 1, 2, and 3). Lightweight sealed systems have proven to be unreliable because they are susceptible to leaks (refs. 4 and 5). Helium purge gas systems (helium is the only gas which does not condense at liquid hydrogen temperatures) have been found to be relatively inefficient and expensive due to the high thermal conductivity and cost of this rare gas (ref. 6). A CO_2 frost insulation system which relies on the sublimation of the frost to supply the purge gas (refs. 7, 8, 9, and 10) offers weight advantages over the helium purge system but requires significant preflight servicing. In addition, expensive helium gas is used during frost deposition to control the frost density.

This report will discuss a purged, condensation restricting, multilayer insulation system for liquid hydrogen tanks which uses the layer of insulation next to the tank wall to restrict or prevent the cryodeposition of purge gas.

POTENTIAL SOLUTIONS

- INTERNAL INSULATION
- SEALED VACUUM JACKET
- NON-CONDENSABLE PURGE GAS (He)
- CO_2 FROST
- CONDENSATION RESTRICTING INSULATION

Figure 2

TPS FOR LH_2 TANKS OF HYPERSONIC AIRCRAFT

(Figure 3)

This figure shows a sketch of a hypersonic aircraft and a cutaway view of an upper section of the tankage area. The outer surface of the aircraft could be either the heat shields of an integral tank configuration or the structure within which a nonintegral tank is suspended.

A purge space, where a nonflammable gas is supplied, at a pressure slightly elevated above ambient, is located between the outer aircraft surface and the insulated tank.

The thermal protection system considered in this study uses multilayered insulation. The outer layer is composed of an efficient high temperature insulation (a fibrous quartz insulation such as Dynaflex or Thermoflex). Because the performance of the outer high temperature insulation is already known, the study concentrated on the insulation layer next to the tank wall where cryopumping of the purge gas is a problem. This layer of insulation has to have low permeability in order to restrict or eliminate cryodeposition. Two general material types were identified: one with zero permeability and low density, but relatively low service temperature (closed organic foam materials); the other with low but finite permeability, much higher density, and a high service temperature (inorganic materials). If the latter materials were used, cryodeposition would occur but the low permeability would limit and contain the deposition.

TPS FOR LH_2 TANKS OF HYPERSONIC AIRCRAFT

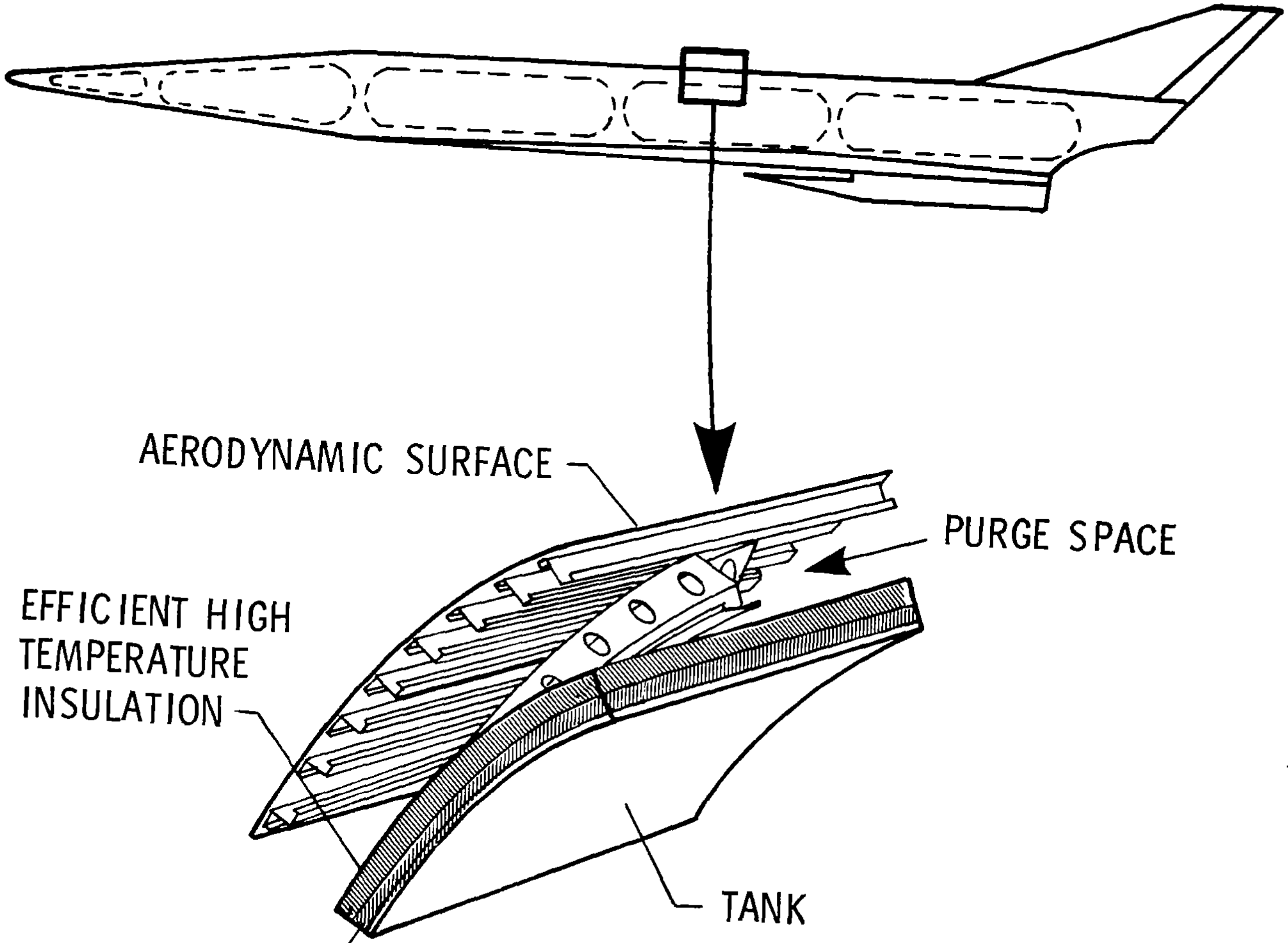

Figure 3

INITIAL GROUND RULES

(Figure 4)

The initial ground rules for this study were to:

- Provide a minimum mass system. Optimize the systems being considered by minimizing the sum of the insulation mass and the mass of the fuel boiled off during flight.
- Use either nitrogen or carbon dioxide purge gas. Minimum system mass will be the selection criteria.
- Minimize preflight preparation.
- Avoid sealed systems. The foam systems are not considered sealed since a localized breach of the foam would not affect the performance of the entire insulation as in the case of a vacuum jacket.
- Permit tank temperatures to 811 K (1000°F). Mass savings may be realized by allowing empty tank temperatures to rise to this maximum allowable temperature.

INITIAL GROUND RULES

- PROVIDE RELIABLE MINIMUM MASS SYSTEM (INSULATION PLUS FUEL BOIL OFF)
- PURGE WITH N_2 OR CO_2
- MINIMIZE PREFLIGHT PREPARATION
- AVOID SEALED SYSTEMS
- PERMIT TANK TEMPERATURES TO 811 K (1000^0 F)

Figure 4

ANALYTICAL RESULTS

(Figure 5)

With optimum insulation thickness, tank temperatures were always below 311 K (100°F), even when a tank was emptied at the start of a flight. This temperature indicates aluminum tanks may be used with these thermal protection systems.

Nitrogen purged systems were always lighter than carbon dioxide purged systems. Although the diffusion coefficient of carbon dioxide is lower and the heats of vaporization and condensation are higher, the higher condensation temperature makes purge systems using carbon dioxide heavier than those using nitrogen regardless of flight trajectory, ground hold time, or location on the aircraft.

Closed cell foam systems were lighter. Densities of high temperature insulations with permeability coefficients low enough to control deposition in the inner layer were high and systems using these insulations were heavier than those using closed cell foams even though the latter required additional high temperature fibrous insulation in the outer layer.

ANALYTICAL RESULTS

- WITH OPTIMIZED INSULATION THICKNESS, TANK TEMPERATURES WERE ALWAYS BELOW 311 K (100^0 F)

- N_2 PURGED SYSTEMS WERE ALWAYS LIGHTER THAN CO_2 PURGED SYSTEMS

- CLOSED CELL FOAM SYSTEMS WERE LIGHTEST

Figure 5

EFFECT OF MAXIMUM FOAM TEMPERATURE ON TPS MASS

(Figure 6)

The effects of maximum allowable foam temperature on TPS mass were investigated analytically. The analysis was based on properties of an efficient foam insulation (polymethacrylimide) and included the variation of these properties with temperature. The analysis identified the minimum mass (insulation plus fuel boil off mass) configuration for each maximum temperature. As shown in the figure, the results indicate that if the maximum allowable foam temperature was increased from 316 K (110°F) to 450 K (350°F), a mass saving of 25 percent could be realized.

EFFECT OF MAXIMUM FOAM TEMPERATURE ON TPS MASS

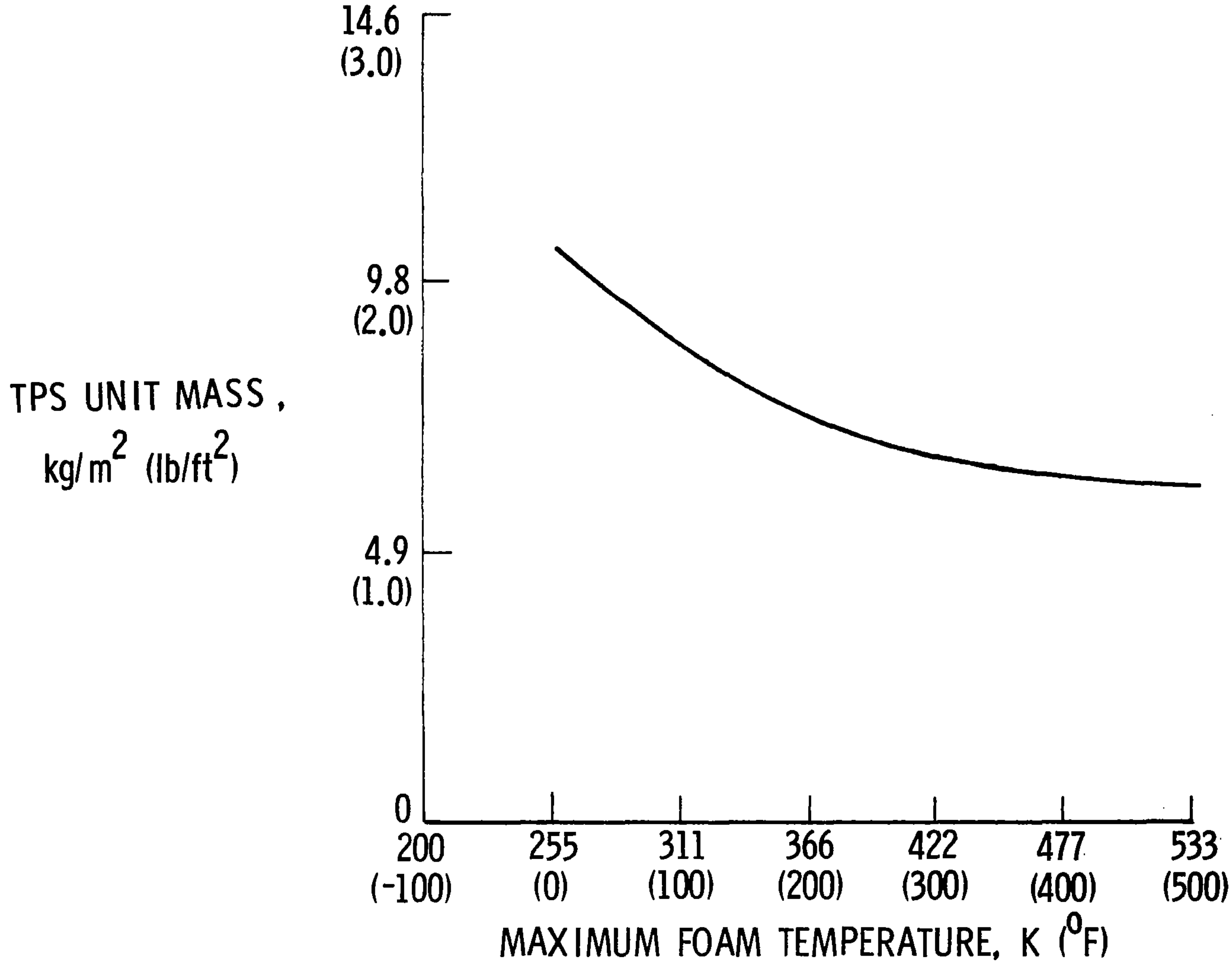

Figure 6

CRYOGENIC INSULATION FOAMS

(Figure 7)

In order to determine the effect of maximum temperature on several foam insulations, the insulations were heated in an oven. The photograph shows five of these insulations in the as received condition, after two hours at 450 K (350°F), and after two hours at 477 K (400°F). Note that there is no significance in the sample sizes because all insulation samples shown were not originally the same size. The only materials which did not change color (indicative of chemical change) and show obvious evidence of distortion were the polybenzimidazole (PBI) and the polymethacrylimide materials. The PBI was found to be an open cell material and not suitable for this application. The polymethacrylimide (made by Rohacell) was picked as the prime insulation for this application.

CRYOGENIC INSULATION FOAMS

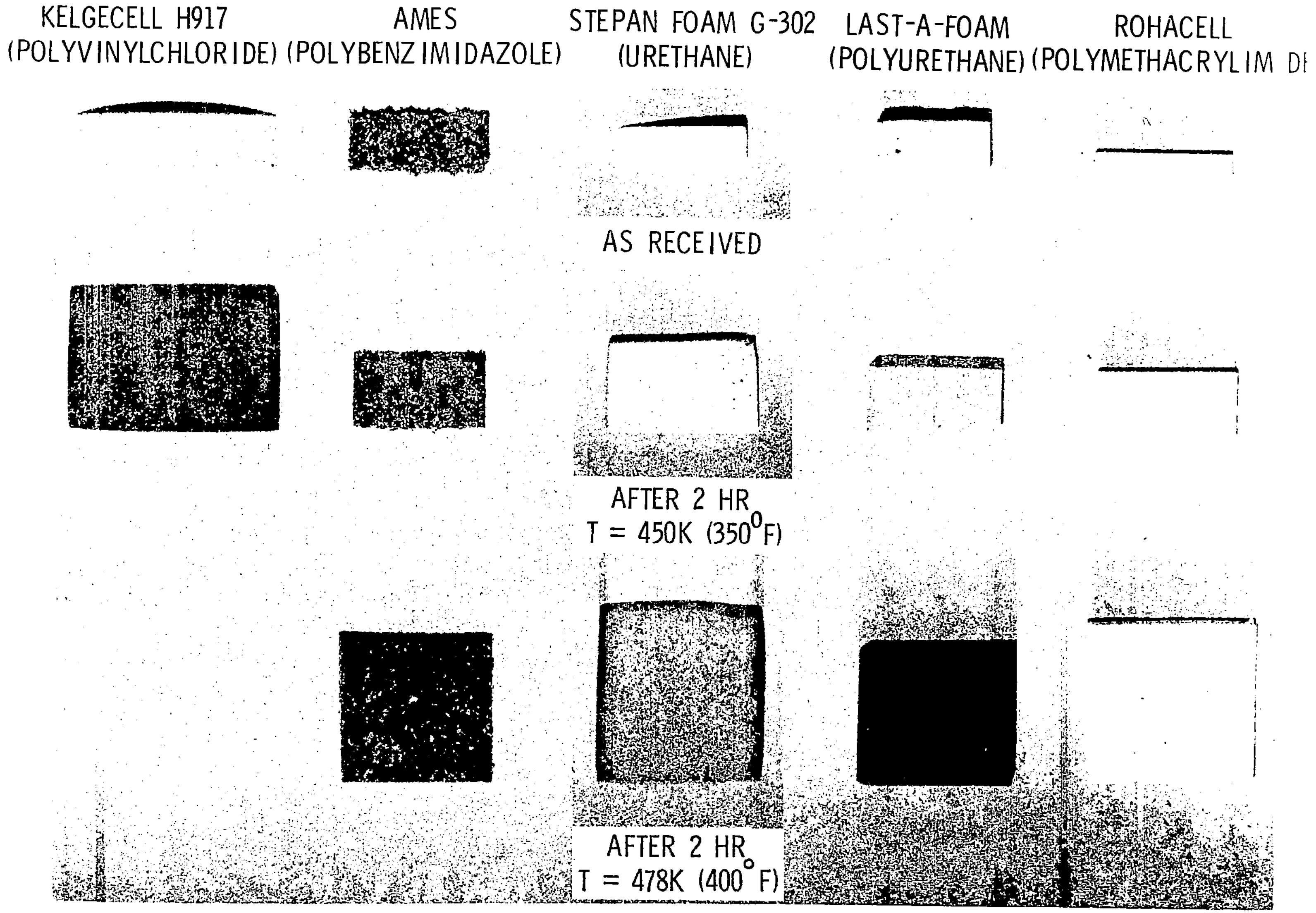

Figure 7

PERFORMANCE TESTS OF CRYOGENIC INSULATION

Hypersonic Transport

(Figure 8)

The apparatus for the cryogenic insulation performance test consists of a liquid hydrogen vessel, a 76 cm (30 in.) diameter insulation sample (shown here lying free under the liquid hydrogen vessel to which it will be bonded), and a purge gas vessel which contains a heater. The purge gas vessel and heater allow both the sample exterior temperature and the pressure in the purge space to be varied to simulate typical flight cycles. The pressure in the purge space was maintained slightly above the projected pressure at altitude. (In an actual application, purge gas pressure would be maintained slightly above ambient to prevent air leakage into the purge space.)

A polymethacrylimide insulation sample (Rohacell 31) successfully survived eight simulated hypersonic flight cycles (insulation external temperatures from 78 K (-320°F) to 450 K (350°F) when a malfunction of the heater resulted in external foam temperatures above 506 K (450°F). This high temperature caused foam damage and the tests were terminated (ref. 11).

PERFORMANCE TESTS OF CRYOGENIC INSULATION
(HYPERSONIC TRANSPORT)

APPARATUS

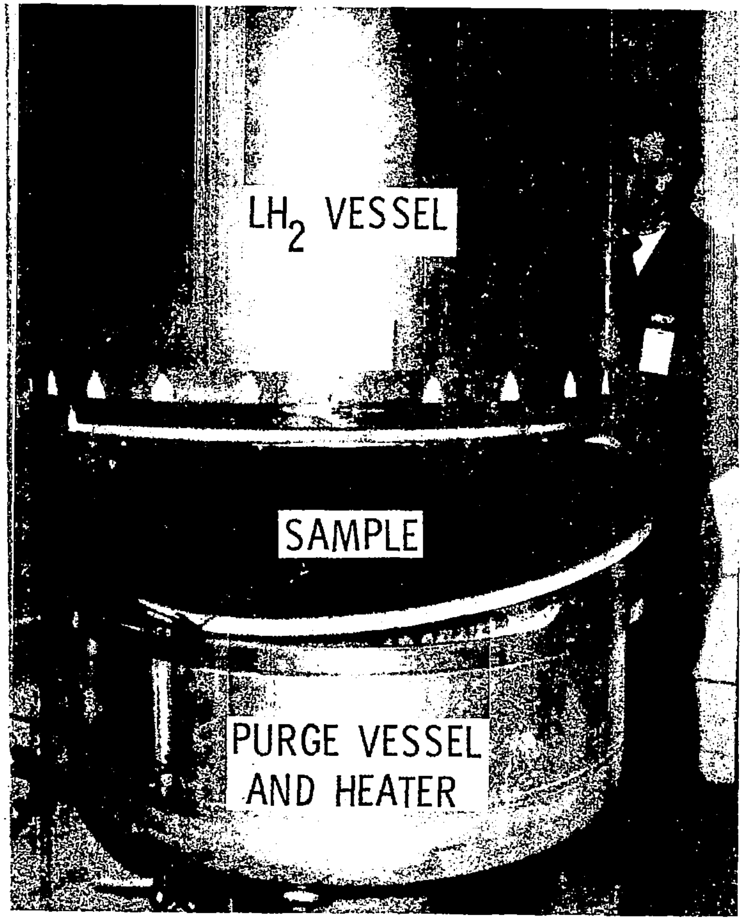

RESULTS

SPECIMEN SURVIVED
8 SIMULATED HYPERSONIC
FLIGHT CYCLES
78 K (-320^0 F) TO 450 K (350^0 F)

Figure 8

TEST SPECIMEN ASSEMBLY

(Figure 9)

Recent interest in hydrogen as an alternate fuel for subsonic aircraft (ref. 12) has led to more extensive cyclic testing of foam materials. Although the maximum temperature of the cycles was only 317 K (110°F), the tests were relevant to hypersonic aircraft. Figure 6 indicates that, although a system with a 450 K (350°F) foam temperature limit would be 25 percent lighter, the total mass (insulation plus boil off) of a 317 K (110°F) system would be less than 8.5 kg/m^2 (1.75 lb/ft^2).

The apparatus used for the subsonic study (ref. 13) was designed for thermally cycling six specimens at the same time. The specimens, which were 0.3 m (1 ft) by 0.6 m (2 ft) by 5.1 cm (2 in.) thick, were bonded to a compartmented tank as shown in the figure. The 5.1 cm (2 in.) thickness was selected to produce thermal stresses representative of 15.2 cm (6 in.) of insulation (the optimum thickness for a subsonic transport) on a large tank; otherwise, edge effects would have significantly reduced stresses in the smaller samples. The tank, which was 1.8 m (6 ft) by 0.6 m (2 ft) by 3.8 cm (1.53 in.) thick was fabricated from an extruded aluminum, web core sandwich.

The tank was compartmentalized so that the boil off rate of the fuel in the tank behind each specimen could be measured by monitoring liquid level thermocouples located at the bottom, top, and center of each specimen compartment. The tank also had guard compartments located between specimen compartments to reduce the flow of heat from one specimen compartment to the other.

TEST SPECIMEN ASSEMBLY

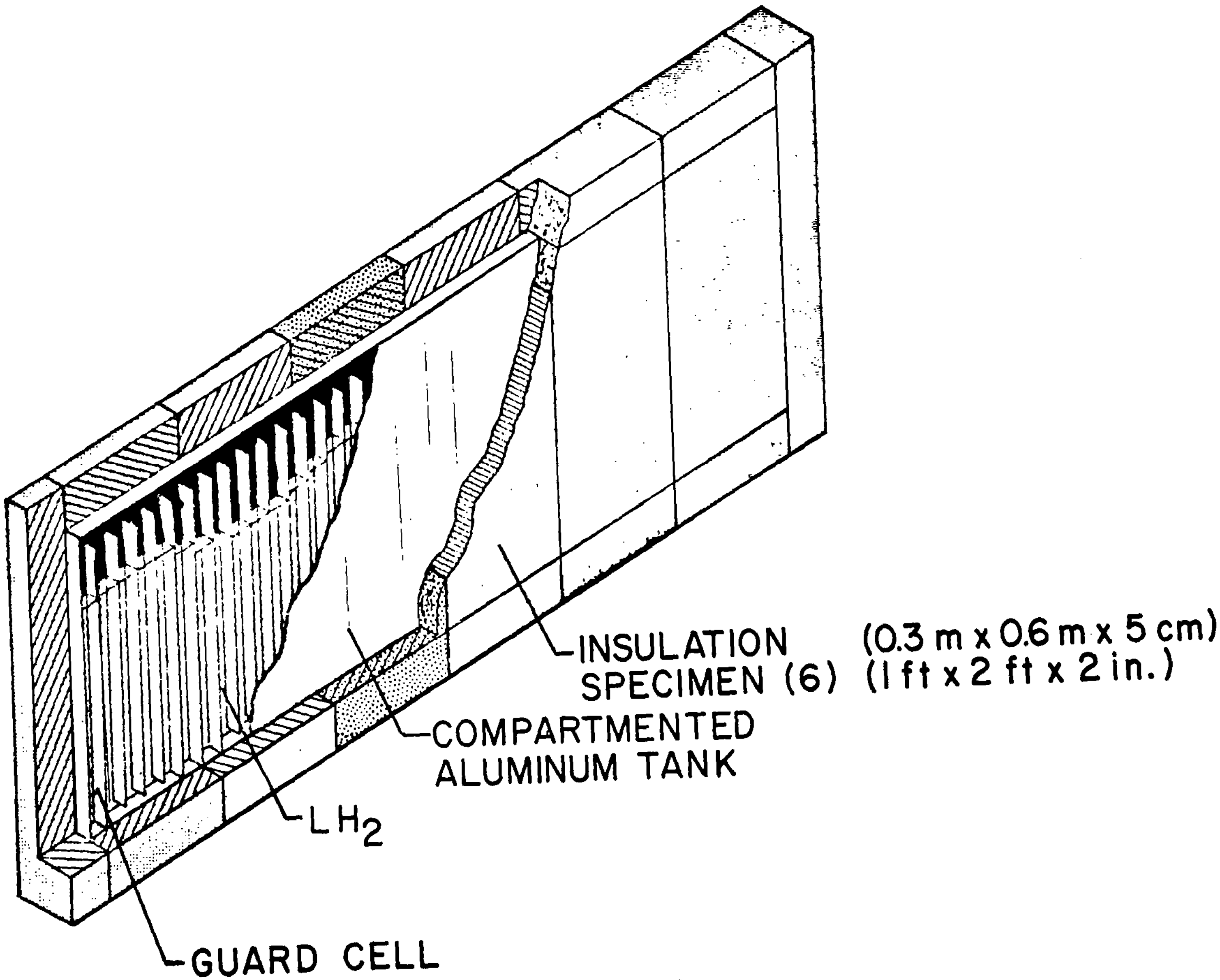

Figure 9

a

COMPARTMENTED ALUMINUM TANK

Edge View

(Figure 10)

This figure is an edge view of a central portion of the web core sandwich tank. Specimens of the same type of insulation are bonded to each side of the tank. Wedge shaped insulation sections (triangular prisms) are used between specimens to provide good bond contact at specimen joints. A two part polyurethane adhesive (Crest 7410) was used to bond specimens to the tank and to each other.

The four central cells in the center of the test specimens are connected together at the bottom of the tank, thus forming the test compartment. The guard compartments, each composed of three cells between test compartments, serve to reduce the interaction between specimens. However, because of drastic differences in boil off rates in adjacent compartments for some insulations, analytical corrections for heat flow between compartments were required.

COMPARTMENTED ALUMINUM TANK

EDGE VIEW

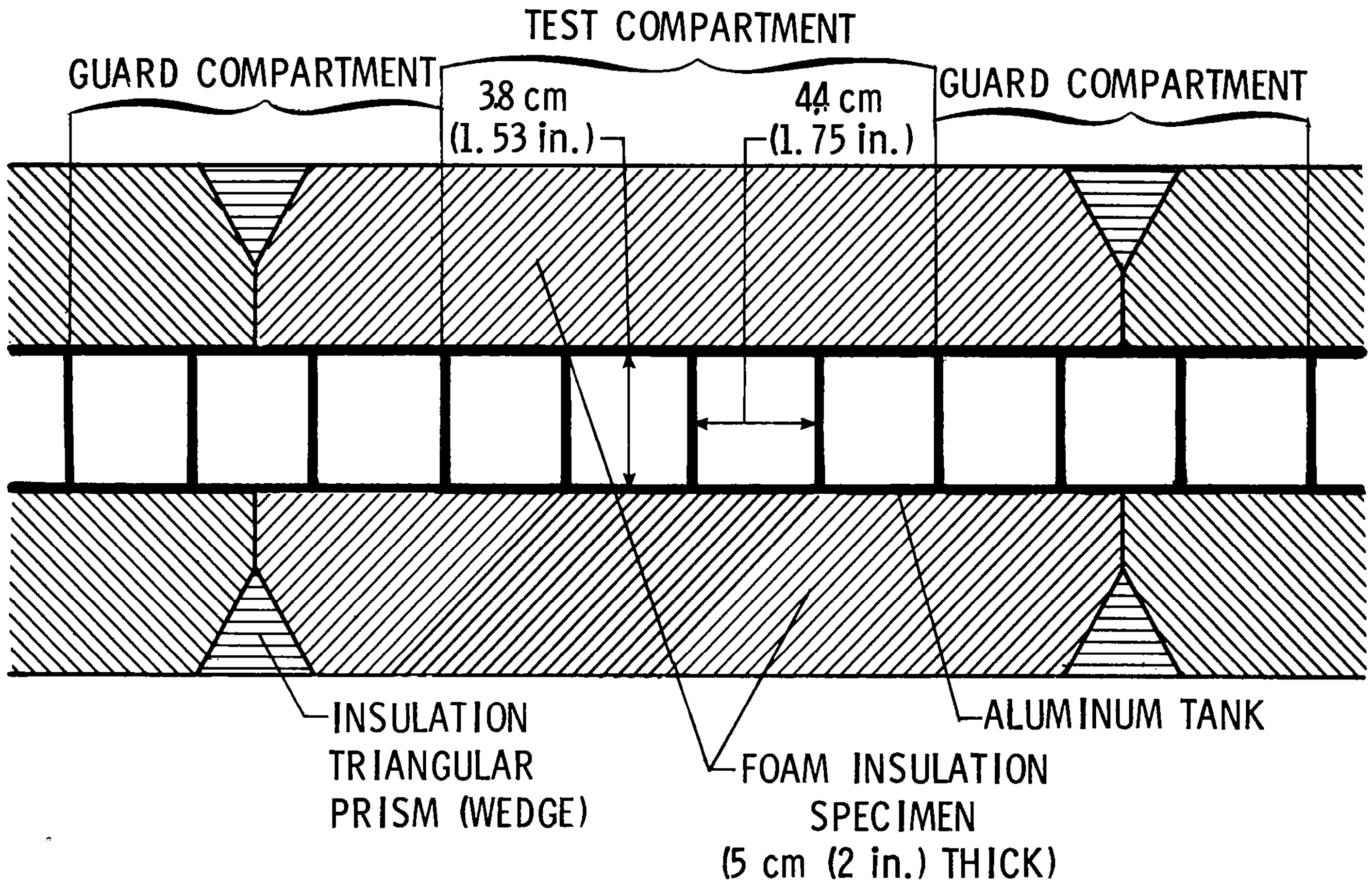

Figure 10

TEST TEMPERATURE HISTORIES

(Figure 11)

Earlier studies (ref. 11) had indicated that the LH_2 tank should be maintained at cryogenic temperatures at all times (except during overhaul periods) in order to minimize the probability of fatigue failures of both the cryogenic fuel tank and the thermal protection system. Therefore, if the aircraft is refueled immediately after each flight and the tank is maintained at cryogenic temperatures, the primary effect of the typical flight cycle is to impose a temperature perturbation on the external surface of the insulation. This perturbation can be simulated by a relatively short (10 minutes or less) thermal cycle such as the typical test temperature history presented in the figure since the maximum stresses on the insulation are encountered shortly after the maximum external temperature of the insulation is reached. (The figure shows the temperature histories of both the insulation outer surface and the temperature of the air blowing over this surface.) A less frequent but more severe thermal stress variation will be encountered when the aircraft is removed from service for periodic maintenance or overhaul and then returned to service. During this time the tanks and insulation will be cycled from cryogenic temperatures, to ambient temperature, back to cryogenic temperatures. The overhaul cycle was simulated in the present test by simply suspending cryogenic testing, allowing the tank to reach ambient temperature, and then resuming cryogenic testing.

During a test period the tank was filled with liquid hydrogen and the temperature history of the exterior of the insulation was cycled repeatedly as the hydrogen was allowed to boil off. Five thermocouples strategically distributed over the insulation surfaces indicated the temperatures of the outer surface, and the exact cycle time was controlled by the thermocouple which last reached the desired temperature. The tank was refilled when the lowest liquid level thermocouples indicated that all tank compartments emptied to 2.54 cm (1 in.) or less. Thus, in contrast to an aircraft application for which the tank would be filled and emptied once per flight, the external temperature and hydrogen level cycled independently during the tests.

Tests were conducted on a three shift basis so that once a test series began, it ran for twenty-four hours a day, five days per week or until deteriorating performance indicated that the tests should stop and specimens should be examined. The shutdown periods represented the time an aircraft would be overhauled and the tank would be allowed to warm up. While the tank was warm, decisions were made pertaining to sample replacement or continuation of cyclic thermal loading on the individual test specimens. The criteria for sample replacement were poor thermal performance and/or extensive structural damage to the insulation.

TEST TEMPERATURE HISTORIES

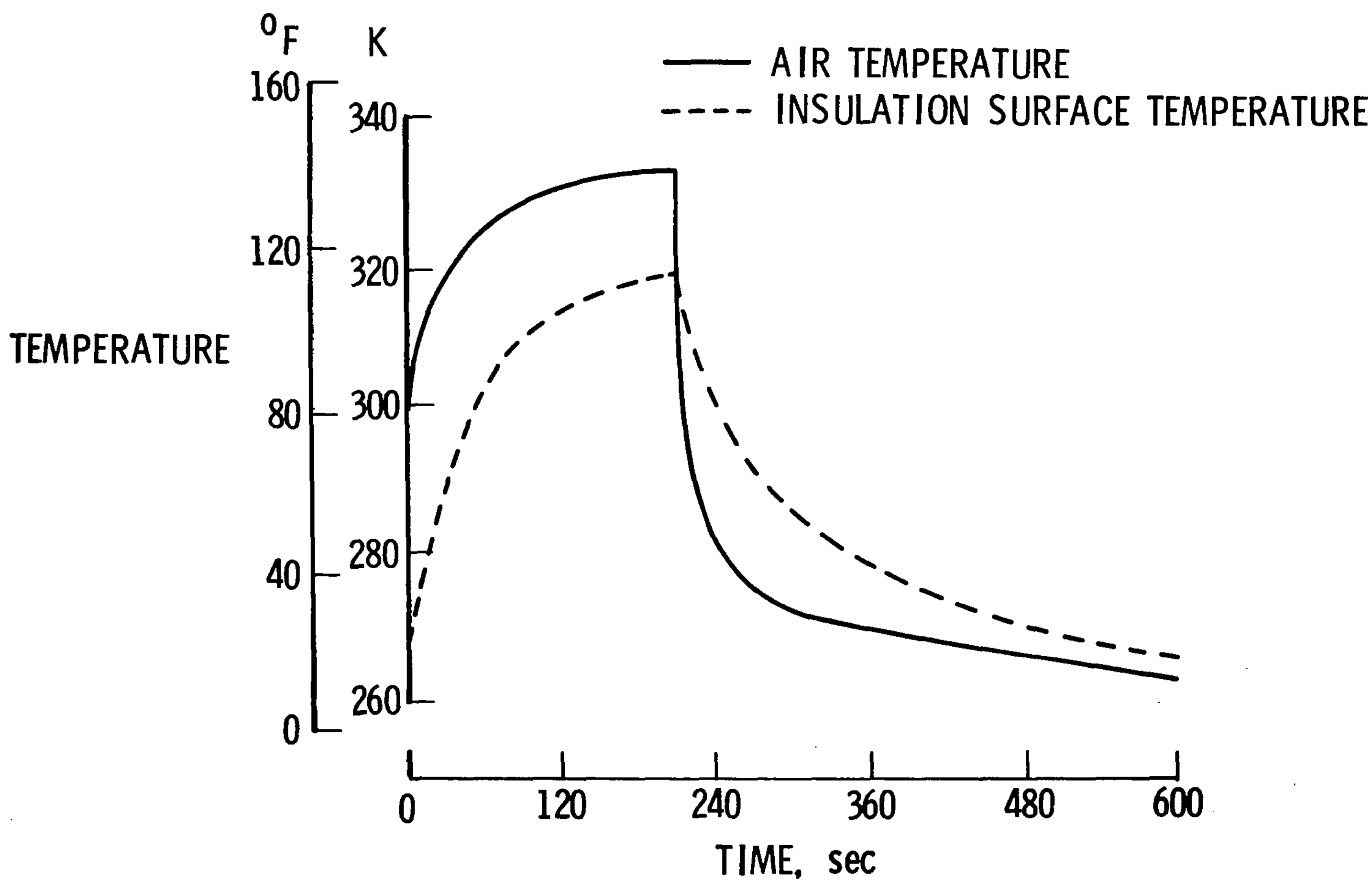

Figure 11

TEST APPARATUS

(Figure 12)

The test apparatus illustrated in the schematic drawing is composed of a large centrifugal blower, a diverter valve, hot and cold heat exchangers, a test chamber, and appropriate ducting to provide a closed circuit for flowing heated (or cooled) air over the test specimens. Air flowing from the blower is directed by the diverter valve through the hot or cold heat exchanger, depending upon which portion of the flight cycle is being simulated. The air is then manifolded into the test chamber. The manifold consists of a tee section in the duct which allows flow to go to two sides of the test chamber. Both sides of the test chamber have three ports which are connected to the incoming air supply ducts (all ducts and ports are 20.3 cm (8 in.) in diameter). Upon entering the test chamber, air strikes a perforated aluminum plate which diffuses the flow over the insulation. After passing over the insulation specimens, the air leaves the test chamber through three ports in the bottom of the test chamber. Ducts from the three ports merge into one duct that returns air to the blower. The ducts, test chamber, and heat exchangers in the test apparatus were insulated; the humidity was not controlled.

TEST APPARATUS

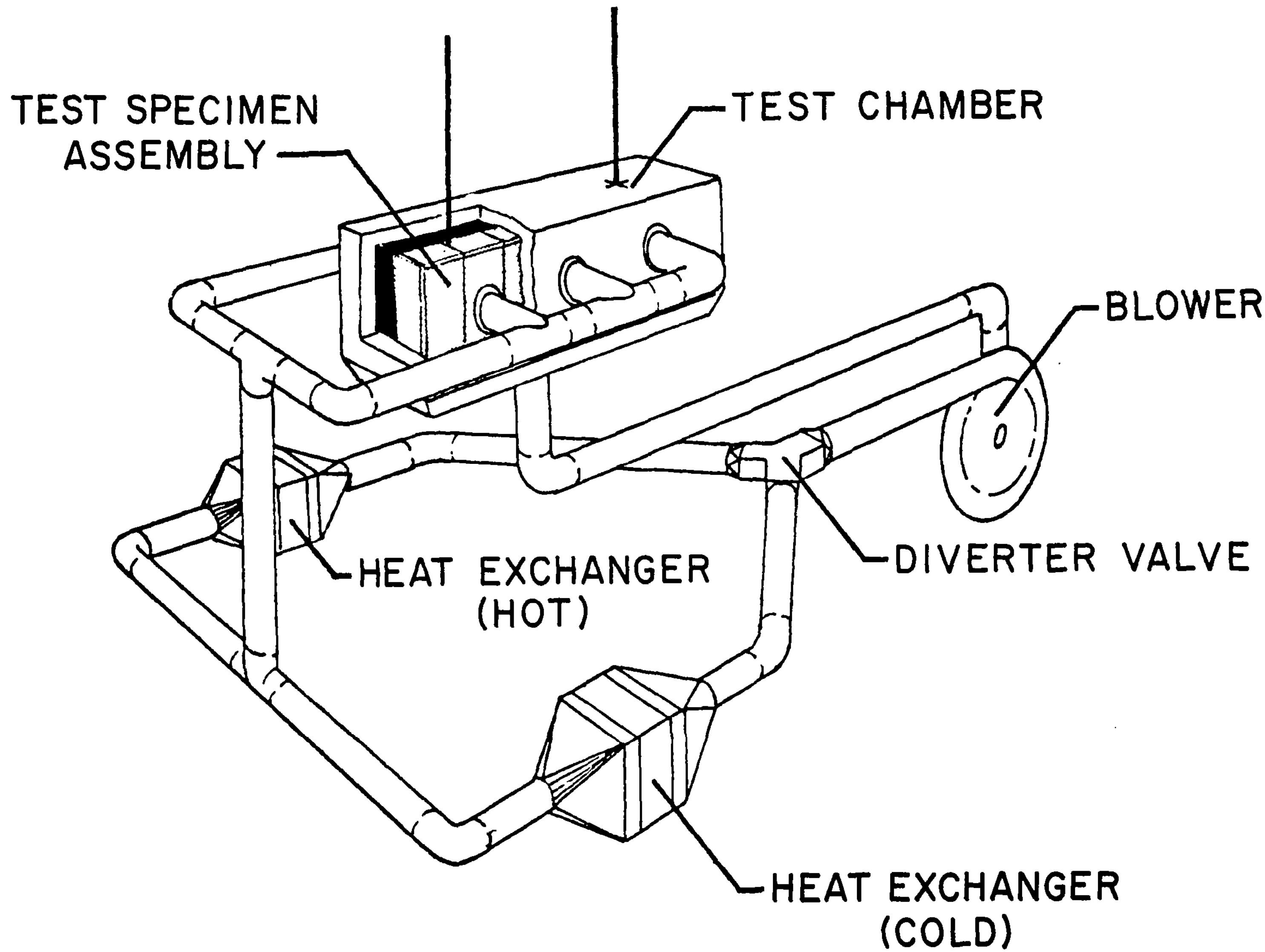

Figure 12

INSULATION SPECIMENS

(Figure 13)

A photograph of the first six insulation specimens, installed on the tank, can be seen at the top of the figure. The chart lists the thirteen insulation specimens tested which included: different generic foam materials, materials from different manufactureres, and two foam systems. Both foam systems had fiberglass reinforcements and two vapor barriers--one on the outer surface and the other located within the insulation, two-thirds of the distance from the outer surface to the tank wall. The fiberglass reinforcement was added to the foam during foam formulation.

INSULATION SPECIMENS

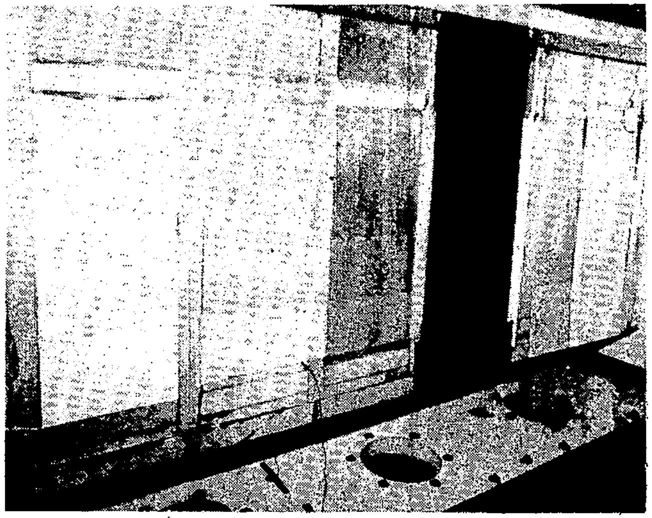

SPECIMEN	MATERIAL
GENERAL ELECTRIC FOAM STEPAN FOAM LAST-A-FOAM	POLYURETHANE
ROHACELL 41S ROHACELL 31 ROHACELL 51	POLYMETHACRYLIMIDE
ADL SYSTEM (UPJOHN)	POLYMETRIC ISOCYANATE + CHOPPED FIBERS & VAPOR BARRIERS
ADL SYSTEM (STAFOAM)	TOLUENEDI ISOCYANATE + CHOPPED FIBERS & VAPOR BARRIERS
COMPOSITE	SIDE 1: POLYMETRIC ISOCYANATE SIDE 2: POLYMETRIC ISOCYANATE + CHOPPED FIBERS
PBI	POLYBENZIMIDAZOLE
CPR 488 TEXTHANE 333	POLYISOCYANURATE
MARVACELL	MODIFIED POLYISOCYANATE

Figure 13

INSULATION PERFORMANCE

Polyurethane

(Figure 14)

The time required to boil off the fuel in a test compartment is directly proportional to the thermal performance of the insulation covering that compartment. This figure and the ones that follow are plots of the boil off time as a function of the number of simulated flight cycles. The boil off times have been normalized by dividing by the initial time value of the best performing insulation.

The triangular symbols on the graph indicate inspection or warm up cycles (discussed earlier) while the circular symbols signify reasons for termination of tests for each sample. The data of the insulation exhibiting the best thermal performance are included in all data plots as a reference.

Two polyurethane foams (Stepan BX 250A, and General Electric Polyurethane) exhibited the best overall performance. The thermal performance of these insulations was initially excellent and degraded very slowly. (See fig. 14.) Both of these insulations survived the entire test series (over 4200 thermal cycles or the equivalent of approximately 15 years of airline service), with no evidence of structural failure. The Stephan foam was used on the Saturn booster while the G.E. material is a candidate for LNG tanker insulation.

The third polyurethane specimen, Last-A-Foam, exhibited good thermal performance for approximately 800 cycles (approximately 3 years of airline service) before experiencing a large degradation in thermal performance. The failure of the Last-A-Foam was first detected by a significant increase in the hydrogen boil off rate. Visual examination of the warm insulation at that time revealed only a few very fine tributary type cracks. When the insulation was examined immediately after the next test period while the insulation was still cold, there was significant frost buildup around these cracks, as well as a stream of white vapor flowing from these cracks. This suggested that the cracks propagated all the way to the tank surface and that air was cryopumping to the tank surface. This was confirmed during sample removal at which time the sample separated along these cracks. Similar failure modes occurred for polyurethane materials in reference 11.

INSULATION PERFORMANCE

POLYURETHANE

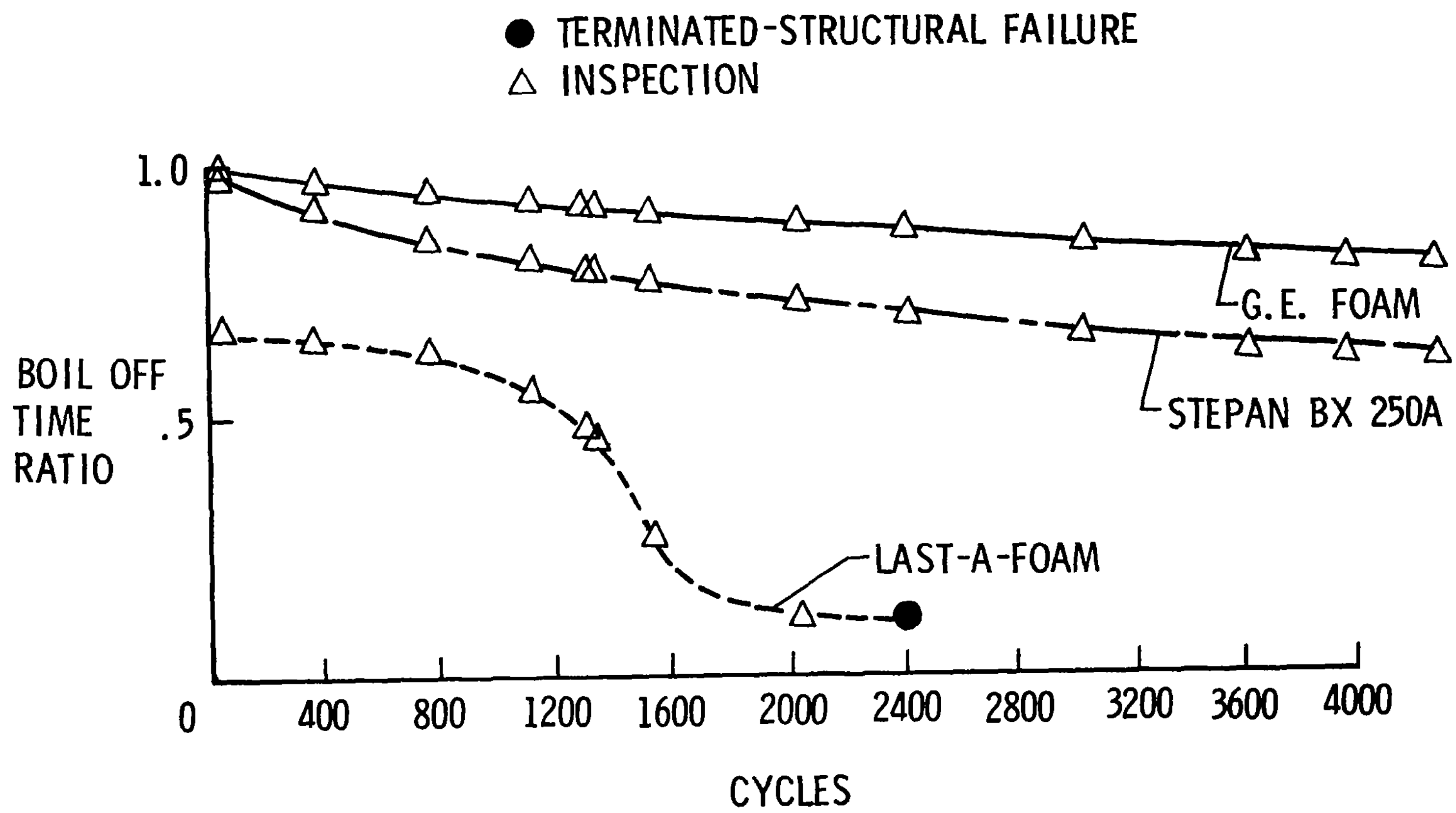

Figure 14

INSULATION PERFORMANCE

Polymethacrylimide

(Figure 15)

Based on previous experience with cryogenic foams for hypersonic application (mentioned earlier) and calculations which indicated the highest margin of any of the foams between the ultimate stress of the foam and the anticipated thermal stress, the polymethacrylimide foam insulations (Rohacell 31, 51, and 41S) were leading candidates for the subsonic transport application at the onset of the test program. However, the thermal cycle performance as shown in the figure was poorer than that shown for the best polyurethane foams.

Rohacell 31, a 30 kg/m^2 (1.87 lbm/ft^3) density foam, displayed the best combined thermal and physical performances of polymethacrylimide materials. After the first few warm-up periods, short hairline surface cracks were observed. However, the Rohacell 31 specimen sustained over 1600 thermal cycles with little degradation of the thermal performance.

The Rohacell 51 specimen cracked on one side after (or during) the first 371 cycles. However, because the thermal properties had not degraded significantly, the specimen was retained until 1296 cycles at which time the cracked side was removed and another Rohacell 51 specimen installed.(The other side was still unblemished and was retained.) The next warm-up cycle revealed that the new insulation specimen had also cracked, apparently because of voids in the bond under the foam, but was not removed until it had undergone a total of 1104 cycles. A third piece was bonded to the troublesome side and the cycling resumed. After 1200 cycles on the new piece and a total of 3968 cycles on the side with the original insulation, the insulation was cracked badly on both sides and its useful life was over. Although the Rohacell 51 failed structurally, the thermal performance of the insulation degraded slowly.

Rohacell 41S, which contains a flame retardant additive, was badly damaged after 371 thermal cycles and therefore the specimen was removed. The initial thermal performance appeared to be excellent, but the structural failures were extensive.

The Rohacell foam insulations all failed in a similar manner. The first indication was a curved hairline surface crack which had a very shallow inclination angle with respect to the surface of the insulation. As the insulation was exposed to more thermal cycles the crack grew in length and depth and began to lift on the concave side of the crack. After repeated cyclic exposure, both ends of the crack met and a circular crack was formed. The lack of an initial through crack to the tank surface is consistent with the gradual deterioration of the thermal properties of the polymethacrylimide foams.

INSULATION PERFORMANCE

POLYMETHACRYLIMIDE

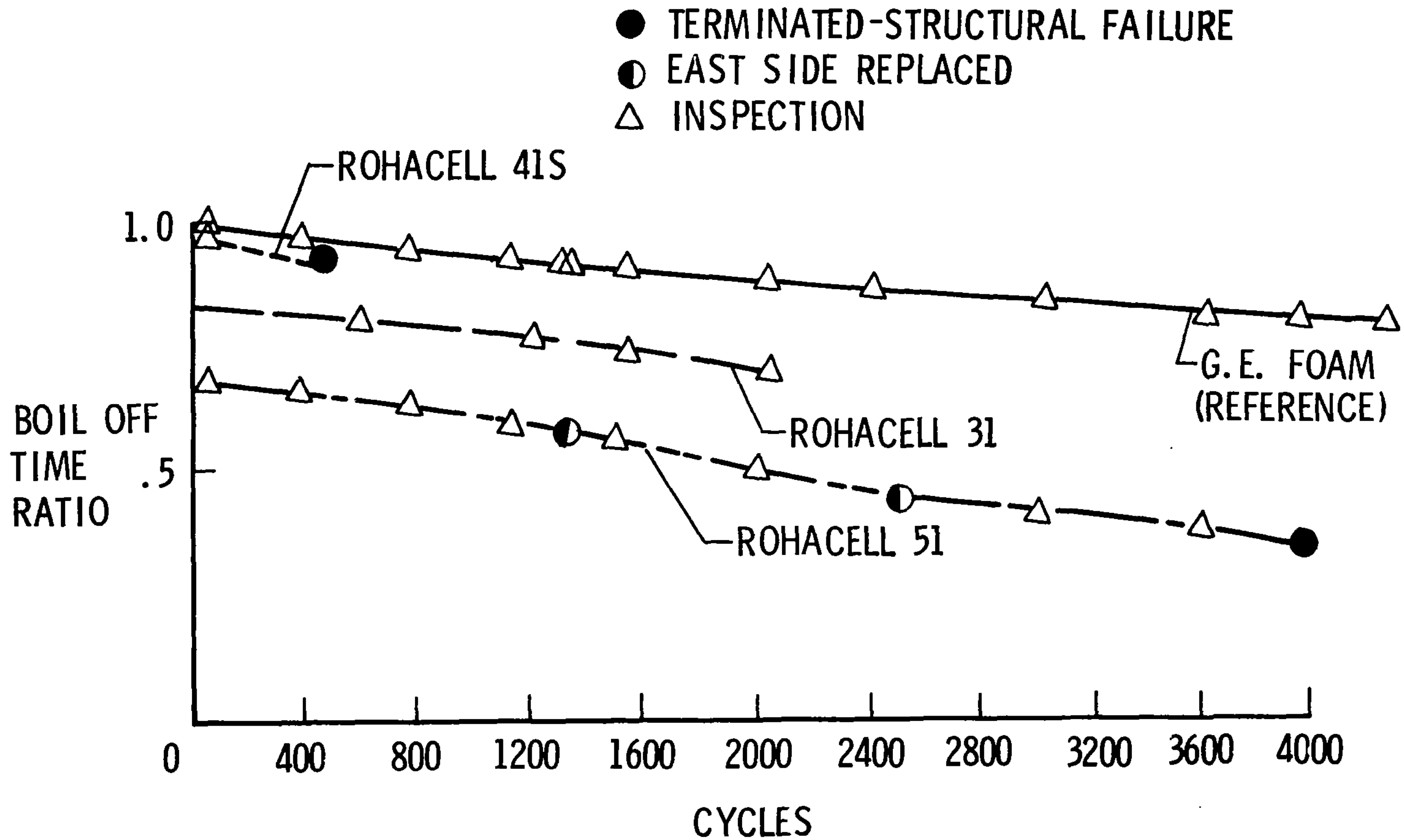

Figure 15

INSULATION PERFORMANCE

Polyisocyanurate

(Figure 16)

The two polyisocyanurate materials examined in this study are currently the prime and back-up insulations for the single-use, throw-away LH_2 fuel tank for the boost stage of the space shuttle. These two insulations, Texthane 333 and CPR 488, exhibit good thermal performance. Both foam insulations deteriorated structurally and had to be removed after a relatively short time by aircraft standards. However, both materials survived over 900 thermal cycles while maintaining fairly good thermal performance.

These foams were either poured or sprayed in layers. Their failure was characterized by relatively wide and ragged cracks along the 0.6 m (2 ft) edges of the specimen and other smaller cracks that propagated under the surface of the specimen into the interior. As the specimens were exposed to repeated cycling, the width and depth of the cracks increased, but no piece of insulation separated from the main panel. Upon removal of the specimens from the apparatus, a slight handling load caused the insulations to delaminate at the interfaces between the poured layers. In addition, the insulation that was nearest the tank wall was relatively spongy with a very low abrasive resistance, suggesting a complete disintegration of the foam cells or possibly a chemical change.

INSULATION PERFORMANCE

POLYISOCYANURATES

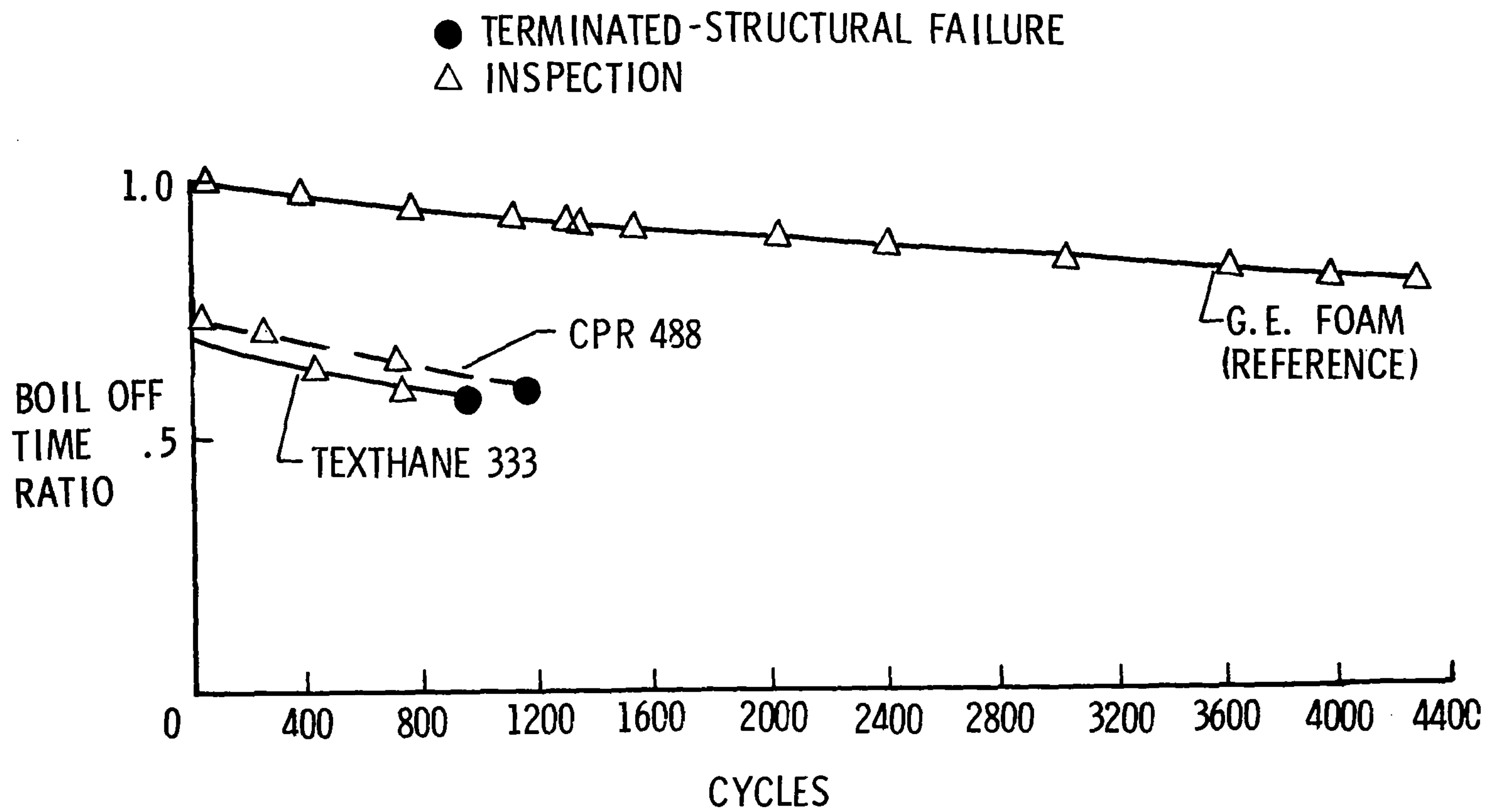

Figure 16

INSULATION PERFORMANCE

Polyisocyanate

(Figure 17)

The results of the tests of an A. D. Little insulation system (ADL) using polyisocyanate foam (Upjohn 452) and tests of the same basic foam (composite) are indicated on the figure. As mentioned earlier, the system had two vapor barriers and chopped fiberglass reinforcement (added during foam formulation). This system had fair thermal performance initially but the performance deteriorated rapidly with thermal cycles. (The other foam system (not shown) had similar performance.)

Visual examination of the insulation system after a week of cyclic testing showed that the specimen was covered with frost within 7.6 cm (3 in.) of the edges of the sample (indicative of high thermal conductivity). Initially, the exterior vapor barrier of the ADL Upjohn system appeared relatively smooth. After the first set of cyclic tests, the vapor barrier was drawn tight against the outer surface of the foam insulation and had a cratered appearance. This behavior suggests that the insulation was permeable and some cryopumping was occurring. After the specimen was removed from the test apparatus, no cracks were detected; however, the insulation was found to be permeable.

In an effort to determine the effect of chopped fiberglass reinforcement and vapor barriers on foam thermal performance and strength, two specimens of Upjohn 452 were bonded to a single test compartment (one on each side). One of the specimens had fiberglass reinforcement, but neither had a vapor barrier. Even though the foam in this specimen, the composite specimen, cracked, the thermal performance was better than the ADL Upjohn system. The fiberglass reinforced side cracked much more than the unreinforced side. Furthermore, the reinforced side had a great deal of frost on it and it was concluded that the fiberglass reinforcement degraded both the thermal and structural performance of the foam. In contrast, vapor barriers, while not improving the thermal performance, apparently improved the structural integrity since the insulation specimens without a barrier cracked while the insulation systems which had barriers did not crack.

INSULATION PERFORMANCE

POLYISOCYANATE

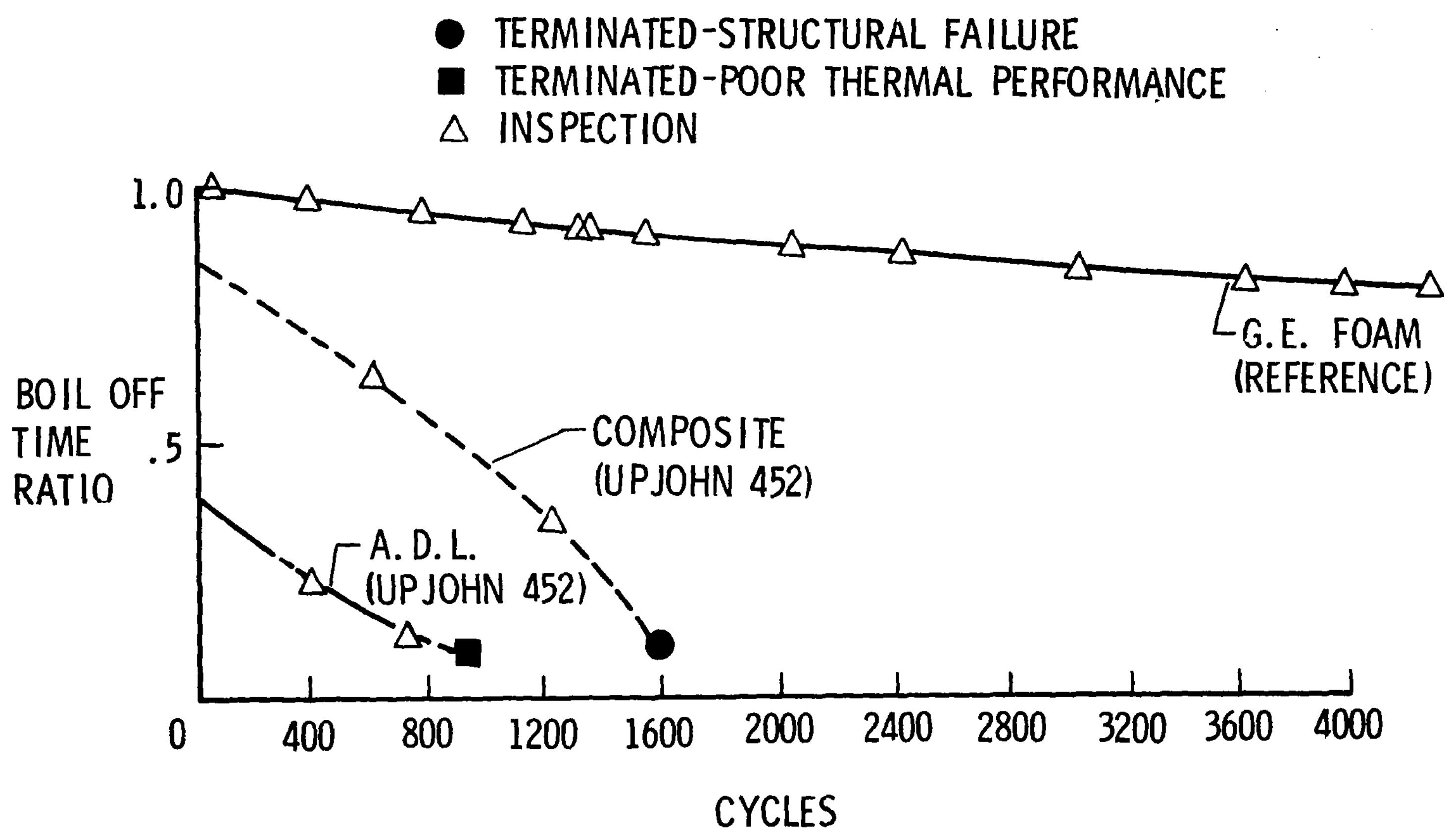

Figure 17

FOAM TEST RESULTS (316 K (110°F) MAXIMUM TEMPERATURE)

(Figure 18)

Significant findings of cyclic testing of foams for a subsonic transport application are summarized in the figure.

FOAM TEST RESULTS (316K (110°F) MAXIMUM TEMPERATURE)

TWO POLYURETHANE FOAM INSULATIONS SURVIVED OVER 4000 THERMAL CYCLES (15 YEARS OF AIRLINE SURVICE) WITH EXCELLENT THERMAL PERFORMANCE

CHOPPED FIBER REINFORCEMENT DEGRADED BOTH THERMAL AND STRUCTURAL PERFORMANCE

VAPOR BARRIERS HAD LITTLE INFLUENCE ON THERMAL PERFORMANCE BUT DID ENHANCE STRUCTURAL PERFORMANCE

BOUNDARIES BETWEEN LAYERS FORMED WHEN FOAMS ARE EITHER POURED OR SPRAYED IN LAYERS SERVE AS NUCLEATION SITES FOR CRACK PROPAGATION

Figure 18

CONCLUSIONS

(Figure 19)

- With optimized insulation thickness, tank temperatures were always below 311 K (100°F) - this conclusion indicates that an aluminum tank could be used with an optimized insulation system if desired.
- N_2 purged systems were always lighter than CO_2 purged systems. - The lower condensation temperature was the controlling factor.
- Closed cell foam systems were lightest - Closed cell foams, in spite of their need for protective outer insulation, produced insulation systems which were lighter than systems which allowed cryodeposition.
- Foam system durability established for T_{max} = 316 K (110°F) - Tests for a subsonic application established this durability; higher temperature limit foam durability is unknown at this time.
- An increase in foam T_{max} from 316 K (110°F) to 450 K (350°F) potentially decreases TPS mass by 25 percent.

CONCLUSIONS

- WITH OPTIMIZED INSULATION THICKNESS, TANK TEMPERATURES WERE ALWAYS BELOW 311 K (100^{0} F)
- N_2 PURGED SYSTEMS WERE ALWAYS LIGHTER THAN CO_2 PURGED SYSTEMS
- CLOSED CELL FOAM SYSTEMS WERE LIGHTEST
- FOAM SYSTEM DURABILITY ESTABLISHED FOR T_{MAX} = 316K (110 ^{0}F)
- AN INCREASE IN FOAM T_{MAX} FROM 316 K (110^{0} F) to 450 K (350 ^{0}F) POTENTIALLY DECREASES TPS MASS BY 25 %

Figure 19

REFERENCES

1. Hammond, M. B., Jr.: An Analytical Model for Determining the Thermal Conditivity of Closed Cell Foam Insulations; Advances in Cryogenic Engineering, Vol. 15, Plenum Press, 1970, pp 332-342.

2. Norton, Francis J.: Thermal Conductivity and Life of Polymer Foams; Journal of Cellular Plastics. Vol. 3, No. 1, January 1967, pp 23-37.

3. Bennett, R. B.: A Structural Plastic Foam Thermal Insulation for Cryogenic Service. Advances in Cryogenic Engineering, Vol. 18, Plenum Press, 1973, pp 393-399.

4. Heathman, John H., and Kelley, Larry G.: Hydrogen Tankage for Hypersonic Cruise Vehicles. AIAA/ASME Seventh Structures and Materials Conference, April 1966, pp 430-438.

5. Jackson, L. Robert, Davis, John G., Jr., and Wichorek, Gregory, R.: Structural Concepts for Hydrogen-Fueled Hypersonic Airplanes. NASA TN D-3162, 1966.

6. Norton, Allan M.: Advanced Structural Concepts, Experimental Program - Project ASCEP. Volume II, AFFDL-TR-67-146, June 1968.

7. Jackson, L. R., and Anderson, M. S.: A Carbon Dioxide Purge and Thermal Protection System for Liquid Hydrogen Tanks of Hypersonic Airplanes. Advances in Cryogenic Engineering Volume 12, Plenum Press, Inc., 1967, pp 146-156.

8. Sharpe, Ellsworth L.: The Control of Carbon Dioxide Cryodeposits. NASA TN D-7334, 1973.

9. Clay, John P.: Carbon Dioxide Frost as Insulation for Hypersonic Spacecraft. Insulation-Materials and Processes for Aerospace and Hydrospace Applications. Soc. Aerospace Materials Process Engineering. May 1965.

10. Sharpe, Ellsworth L., and Jackson, L. Robert: Performance of a Hypersonic Hot Fuselage Structure with a CO_2 Frost Purged Cryogenic Tank. NASA TN D-7799, March 1975.

11. Helenbrook, R. G., and Colt, J. Z.: Development and Validation of Purged Thermal Protection Systems for the LH_2 Fuel Tanks of Hypersonic Vehicles. NASA CR-2829, June 1977.

12. Brewer, G. D., and Moore, J. W.: Study of the Application of Hydrogen Fuel to Long-Range Subsonic Transport Aircraft. NASA CR-132559, January 1975.

13. Sharpe, Ellsworth L.; and Helenbrook, Robert G.: Durability of Foam Insulation for LH_2 Fuel Tanks for Future Subsonic Transports. International Cryogenic Materials Conference; Munich, West Germany, July 10-11, 1978. (To be published in Nonmetallic Materials and Composites at Low Temperatures in Jan. 1979.)

SESSION VI - ANALYSIS METHODS

23

RECENT ADVANCES IN THERMOSTRUCTURAL FINITE ELEMENT ANALYSIS

Earl A. Thornton
Old Dominion University

and

Allan R. Wieting
NASA Langley Research Center

RECENT ADVANCES IN THERMOSTRUCTURAL FINITE ELEMENT ANALYSIS

Earl A. Thornton
Old Dominion University
and
Allan R. Wieting
NASA Langley Research Center

INTRODUCTION

(Figure 1)

An inherent design characteristic for hypersonic vehicles is the strong interaction between thermal and structural analyses. The paper presented at this conference on the thermostructural analysis of the scramjet fuel-injection strut (ref. 1) has illustrated this interaction. Thus an integrated thermal/structural analysis is desirable. Often combined thermal/structural analyses join a lumped parameter thermal analysis and a finite element structural analysis. However, because the analysis methods differ an efficient interface between the two analyses is difficult to achieve. The finite element method is attractive because it provides capability for both thermal and structural analyses. Finite element structural analysis capability has reached a state of mature development, and the finite element method has been almost universally accepted as a routine method of structural analysis. The finite element thermal analysis methodology is not as well developed, and the majority of complex thermal analyses are currently performed by the lumped parameter method.

The purpose of this paper is to describe recent finite element methodology development for thermal analysis of convectively cooled structures. First, a comparison study of the NASTRAN thermal analyzer and MITAS, a lumped parameter finite difference program, will be described. Next, some finite elements developed for convectively cooled structures will be described. Then, some comparative analyses made to evaluate the convective finite elements will be presented. Finally, some methodology areas which need development will be identified.

RECENT ADVANCES IN THERMOSTRUCTURAL FINITE ELEMENT ANALYSIS

<u>MOTIVATION</u>

- STRONGLY INTERACTING THERMAL/STRUCTURAL DESIGN FOR HYPERSONIC VEHICLES
- INTEGRATED THERMAL/STRUCTURAL ANALYSES DESIRABLE
- FINITE ELEMENT METHOD OFFERS THERMAL/STRUCTURAL CAPABILITIES
  - STRUCTURAL WELL ESTABLISHED
  - THERMAL REQUIRES FURTHER DEVELOPMENT

<u>PURPOSE OF PRESENTATION</u>

- TO DESCRIBE FINITE ELEMENT METHODOLOGY DEVELOPMENT FOR CONVECTIVELY COOLED STRUCTURES

<u>SCOPE</u>

- COMPARISON STUDY OF NASTRAN AND MITAS
- NEW CONVECTIVE FINITE ELEMENTS
- APPLICATIONS AND COMPARATIVE ANALYSES
- METHODOLOGY AREAS FOR FUTURE DEVELOPMENT

Figure 1

COMPARISON STUDY OF NASTRAN AND MITAS

(Figure 2)

A comparison study of NASTRAN and MITAS (ref. 2) was carried out to evaluate the capabilities of NASTRAN to thermally analyze convectively cooled structures. At the time of the study, there was relatively little user experience with NASTRAN for convectively cooled structures; however, MITAS was a well established, finite difference, lumped parameter thermal analyzer. The scramjet fuel-injection strut was selected for the comparison study because of its complex thermal/structural behavior. In the study, a nonlinear steady-state thermal analysis was made to determine detailed structural and coolant temperature distributions. The nonlinearity arose from temperature dependent thermal parameters. Subsequent to the thermal analysis, the NASTRAN finite element model was used to perform a detailed stress analysis (ref. 3).

COMPARISON STUDY OF NASTRAN AND MITAS

- EVALUATION OF NASTRAN THERMAL ANALYZER
- STRUT SELECTED BECAUSE OF COMPLEX THERMAL/ STRUCTURAL BEHAVIOR
- NONLINEAR STEADY-STATE CONDUCTION/CONVECTION THERMAL ANALYSIS

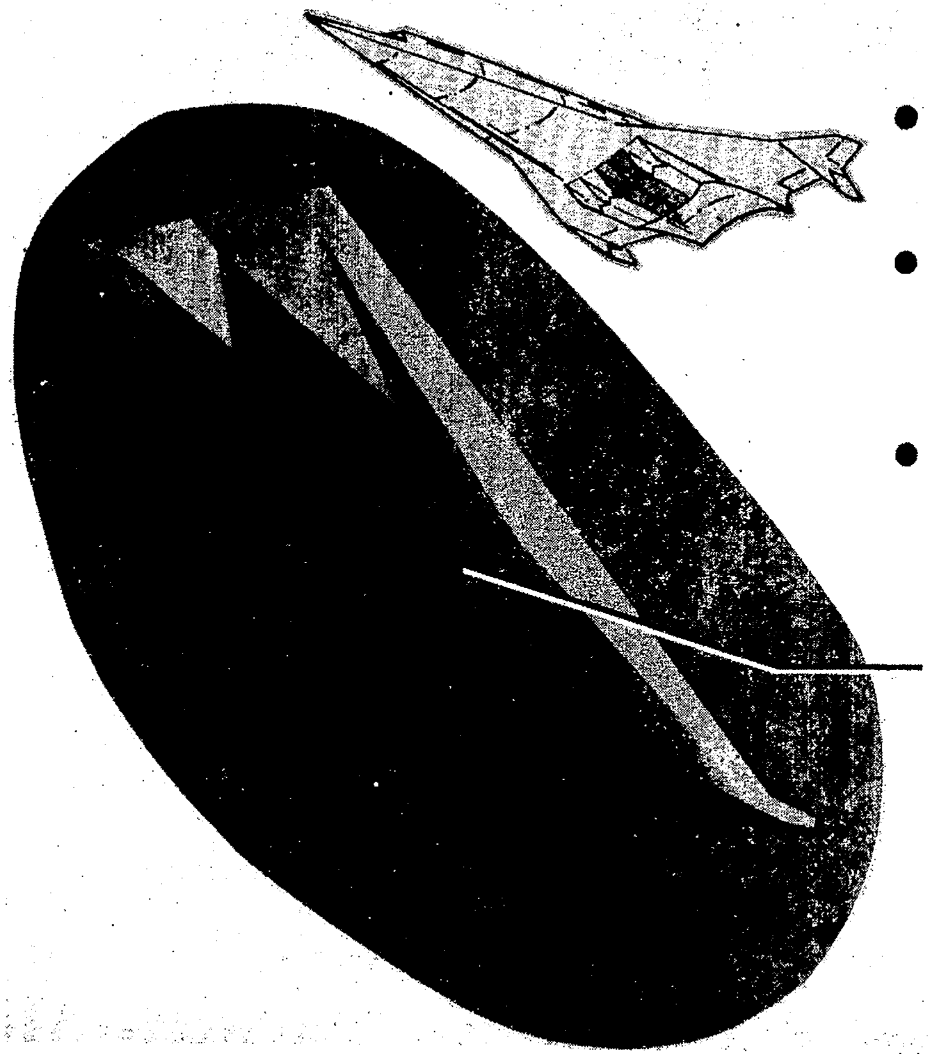

Figure 2

AERODYNAMIC HEATING DISTRIBUTIONS

(Figure 3)

A cross section of a fuel-injection strut is shown along with the aerodynamic heating distributions. Severe thermal gradients arise in the strut because of nonuniform aerodynamic heating and internal convective heating from hydrogen in the coolant manifolds. As shown, the aerodynamic heating ($\dot{q}$) varied considerably along each side because of flow stagnation at the leading edge, shock interaction and combustion. Internally, the coolant at 55 K (100^{o}R) in the forward manifold is injected through a slot, impinges on the leading edge and splits unequally to flow through an offset-fin plate-fin heat exchanger which is brazed to the primary structure. Flow proceeds along each wall to the trailing edge where it is collected in the aft manifold at about 890 K (1600^{o}R).

AERODYNAMIC HEATING DISTRIBUTIONS

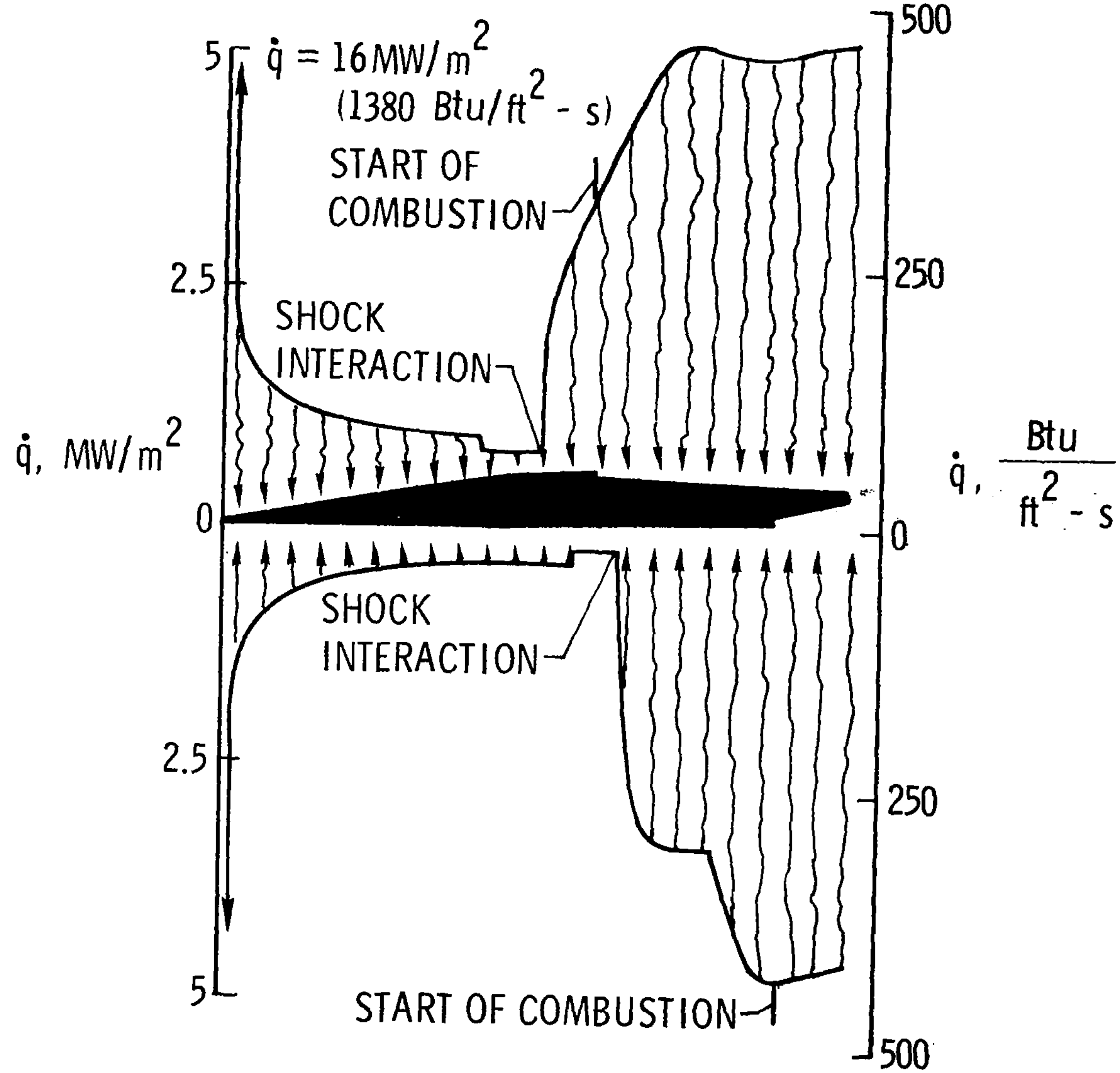

Figure 3

NASTRAN FINITE ELEMENT MODEL

(Figure 4)

The NASTRAN finite element model of the strut cross section is shown. A common finite element model was used for both thermal and structural analyses. The finite element model of a typical wall section shown represents the primary structure, a hydrogen coolant passage, and the aerodynamic skin. The model was determined primarily by structural requirements. For example, four elements were needed through the primary structure to represent the bending stresses in the wall. In the thermal analysis the temperature of each of 3000 nodes was unknown, and in the stress analysis two displacements at each node were unknown.

A basic difficulty in the NASTRAN thermal analysis arose in modeling the convective heat transfer due to the fluid flow. NASTRAN had no means of modeling heat transfer due to mass transport convection. Thus, coolant temperatures could not be computed using NASTRAN. Instead, coolant temperatures were computed in MITAS and input to NASTRAN as a boundary condition.

NASTRAN FINITE ELEMENT MODEL

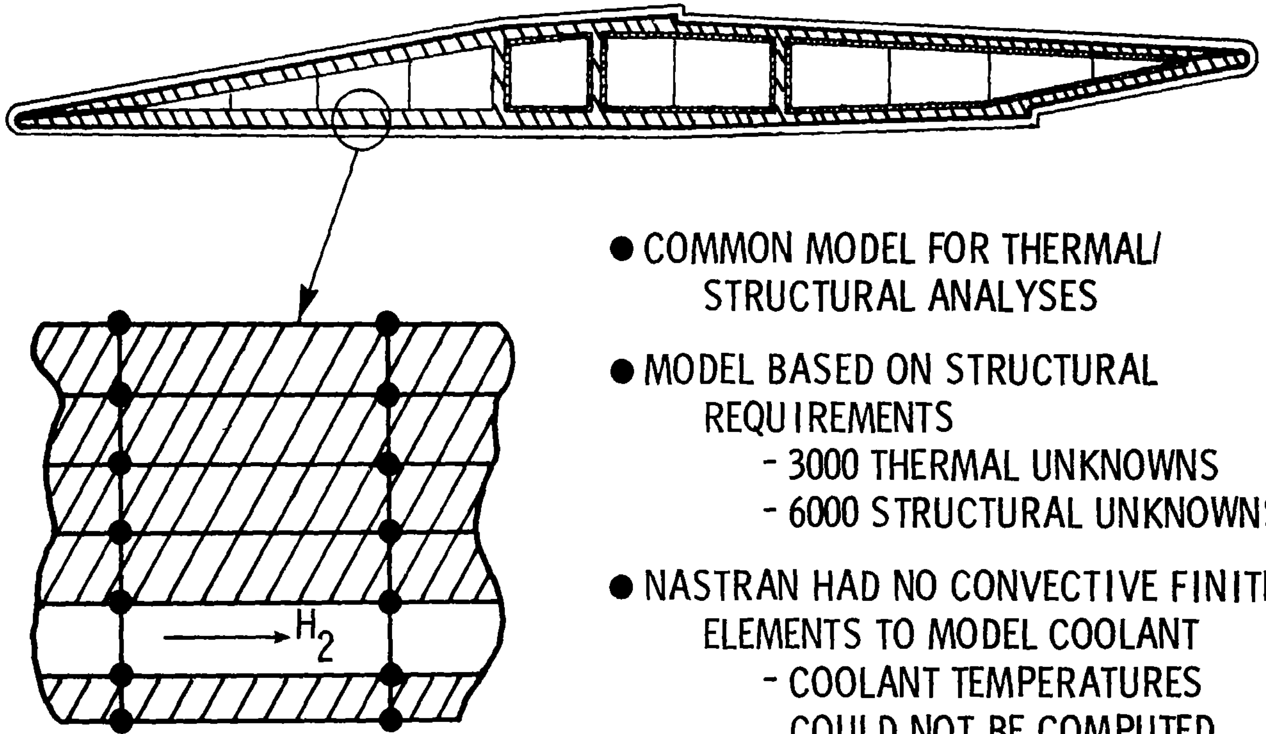

- COMMON MODEL FOR THERMAL/ STRUCTURAL ANALYSES
- MODEL BASED ON STRUCTURAL REQUIREMENTS
  - 3000 THERMAL UNKNOWNS
  - 6000 STRUCTURAL UNKNOWNS
- NASTRAN HAD NO CONVECTIVE FINITE ELEMENTS TO MODEL COOLANT
  - COOLANT TEMPERATURES COULD NOT BE COMPUTED
  - INPUT FROM MITAS

Figure 4

TEMPERATURES ALONG STARBOARD AERODYNAMIC SKIN

(Figure 5)

NASTRAN and MITAS calculated temperature distributions along the starboard coolant passage and starboard aerodynamic skin are shown. The lower curve is the hydrogen-coolant temperature distribution. These coolant temperatures were computed with MITAS and input to the NASTRAN model as boundary conditions. The increase in coolant temperature at $x/L = 0.6$ reflects an increase in aerodynamic heating and combustion. The upper two curves are the predicted aerodynamic skin temperatures. The open symbols represent NASTRAN computed temperatures and the solid symbols the MITAS computed values. The aerodynamic skin temperatures reflect the nonuniform aerodynamic heating from stagnation to the increased heating due to combustion. Agreement between the predicted temperatures was excellent with the largest difference less than 6 percent.

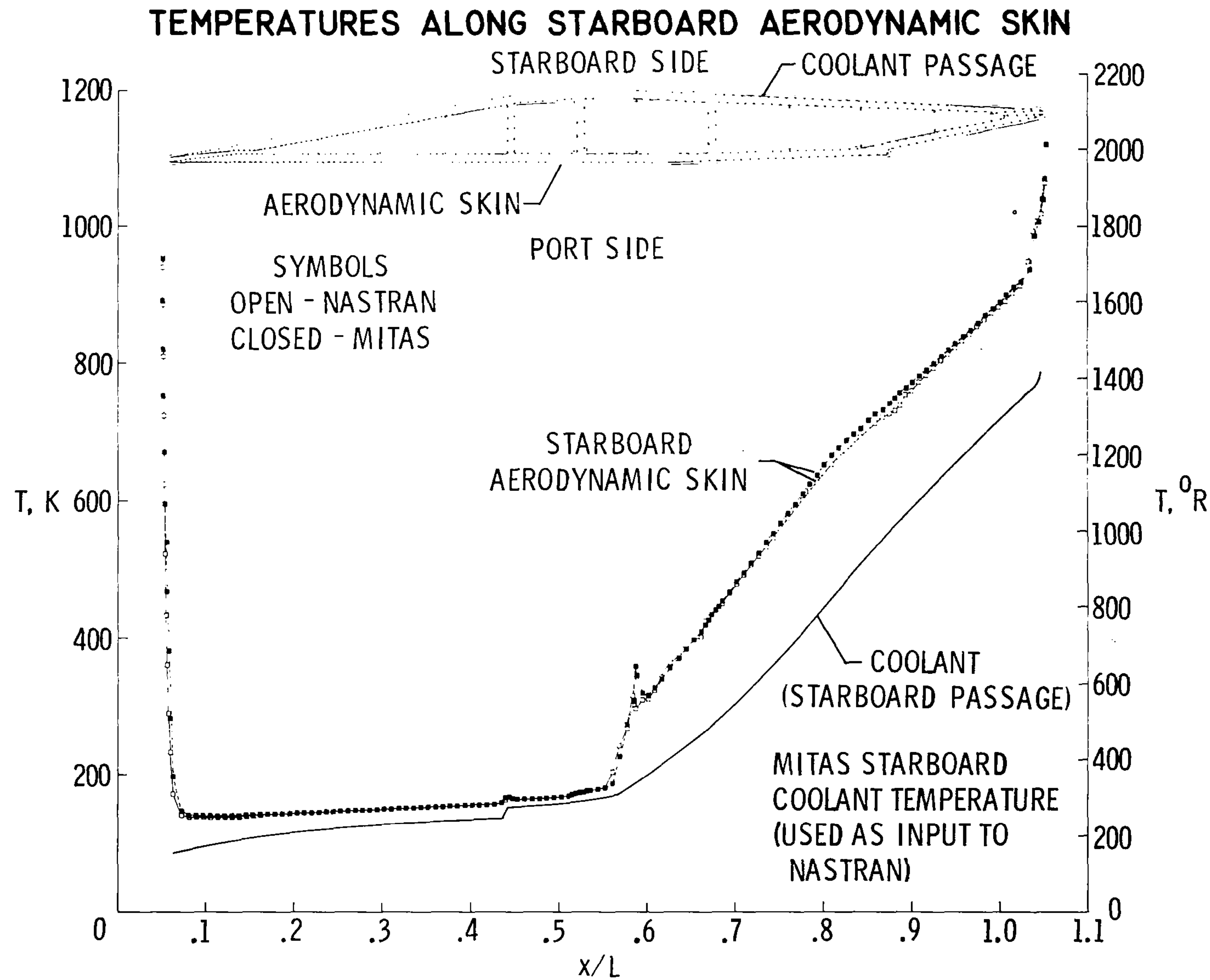
TEMPERATURES ALONG STARBOARD AERODYNAMIC SKIN
STARBOARD SIDE
COOLANT PASSAGE
AERODYNAMIC SKIN
PORT SIDE
SYMBOLS
OPEN - NASTRAN
CLOSED - MITAS
STARBOARD
AERODYNAMIC SKIN
COOLANT
(STARBOARD PASSAGE)
MITAS STARBOARD
COOLANT TEMPERATURE
(USED AS INPUT TO
NASTRAN)
T, K
0
200
400
600
800
1000
1200
T, °R
0
200
400
600
800
1000
1200
1400
1600
1800
2000
2200
x/L
0
.1
.2
.3
.4
.5
.6
.7
.8
.9
1.0
1.1

Figure 5

RESULTS OF NASTRAN-MITAS COMPARISON STUDY

(Figure 6)

The NASTRAN-MITAS comparison showed that NASTRAN did not have the capability to model heat transfer due to mass transport. A subsequent literature search revealed a lack of the basic finite element methodology for such analyses. One proprietary computer program could model heat transfer due to fluid flow in a pipe, but otherwise the methodology needed to analyze the strut was not available.

The comparative study demonstrated the finite element capability for performing a complex nonlinear conduction/convection thermal analysis. Computer costs for the NASTRAN and MITAS analyses were comparable based on the LRC cost algorithm which includes computer storage and run times.

One significant asset of the finite element method is that finite element graphics are advantageous for model verification. For example, several months after these results were presented in reference 1 an error in the MITAS model was found accidently. The error would have easily been detected by a computer plot of the model.

One justification often given for thermal/structural analysis by finite elements is that the same model can be used by both analyses. In this case, a common model was used but it was not cost-effective since an excessively detailed and expensive thermal analysis was done because the finite element mesh was dictated by the structural model requirements.

RESULTS OF NASTRAN–MITAS COMPARISON STUDY

- LACK OF METHODOLOGY TO PERFORM FINITE ELEMENT THERMAL ANALYSIS OF CONVECTIVELY COOLED STRUCTURES
- DEMONSTRATION OF FINITE ELEMENT ANALYSIS CAPABILITY FOR NONLINEAR STEADY-STATE CONDUCTION/CONVECTION
  - COMPARABLE COMPUTER COSTS
- FINITE ELEMENT GRAPHICS ADVANTAGEOUS FOR MODEL VERIFICATION
- COMMON FINITE ELEMENT MODEL OF SCRAMJET STRUT DID NOT YIELD EFFICIENT THERMAL ANALYSES

Figure 6

TYPICAL CONVECTIVELY COOLED STRUCTURES

(Figure 7)

As a result of the NASTRAN-MITAS comparison study a program was undertaken to develop finite element methodology for convectively cooled structures. An objective in the finite element methodology development was to have the capability for modeling heat transfer in general convectively cooled structures for hypersonic aircraft such as those shown in the figure. The left figure shows a discrete tube configuration in which coolant flows through tubes bonded to a panel, and the right figure shows a plate-fin configuration in which the coolant flows through a heat exchanger bonded to a structure.

Four new convective elements were developed to analyze such configurations. The new elements will be described in the next four figures. Details of the element derivations are given in reference 4.

TYPICAL CONVECTIVELY COOLED STRUCTURES

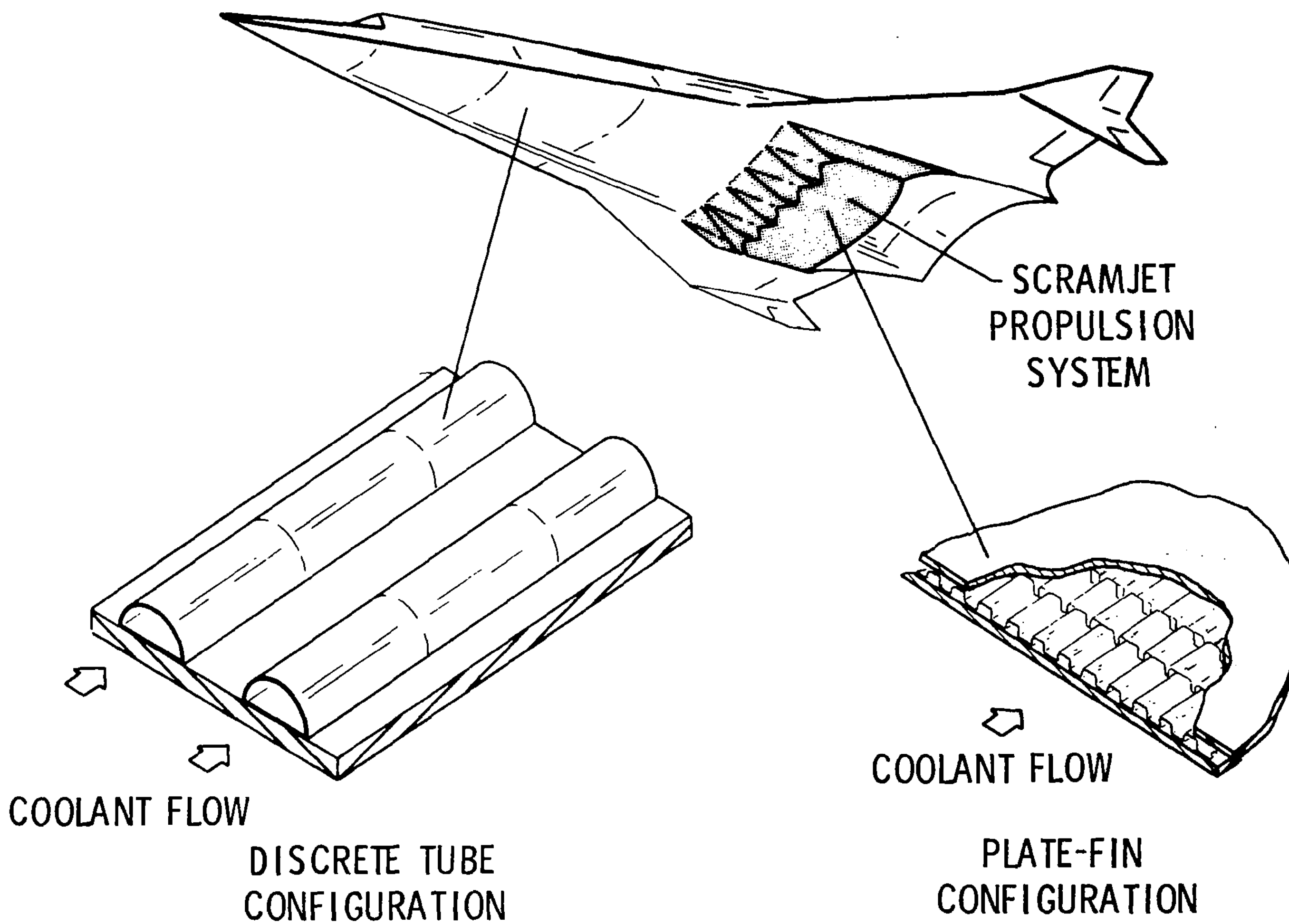

Figure 7

MASS TRANSPORT ELEMENT

(Figure 8)

The mass transport element accounts for heat transfer due to energy transported in the direction of the fluid flow. The element is based on a uniform velocity profile over the cross section of the element, and bulk temperatures are used to represent the fluid temperature field. The element has two fluid nodes with unknown fluid bulk temperatures. A linear variation of temperature between the nodes is assumed.

MASS TRANSPORT ELEMENT

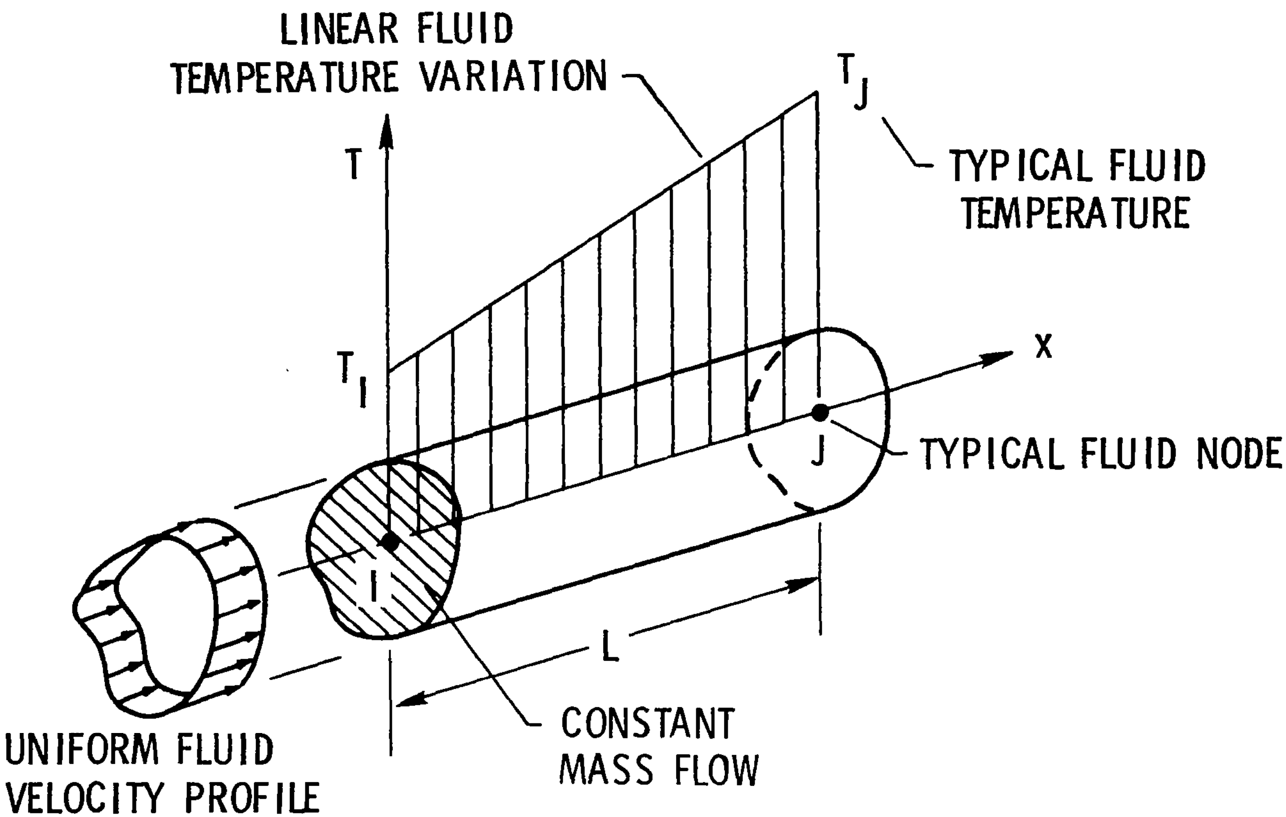

Figure 8

SURFACE CONVECTION ELEMENTS

(Figure 9)

Surface convection elements are used to represent heat transfer between a coolant passage surface and coolant. Both quadrilateral and triangular elements are used. Heat is transferred between nodes on the convection surface, such as L and K, and fluid nodes I and J. The conductance is expressed in terms of the area of the convection surface and the convection coefficient h.

In previous finite element heat transfer analyses (such as NASTRAN) convection heat transfer between a surface and a fluid customarily has been represented as a boundary condition since the fluid temperatures were assumed to be known. The quadrilateral and triangular surface convection elements shown have unknown temperatures at both fluid and wall surface nodes.

The basic finite elements were combined with conduction elements to give two integrated elements which represent heat transfer in the typical cooling passages shown in Figure 7.

SURFACE CONVECTION ELEMENTS

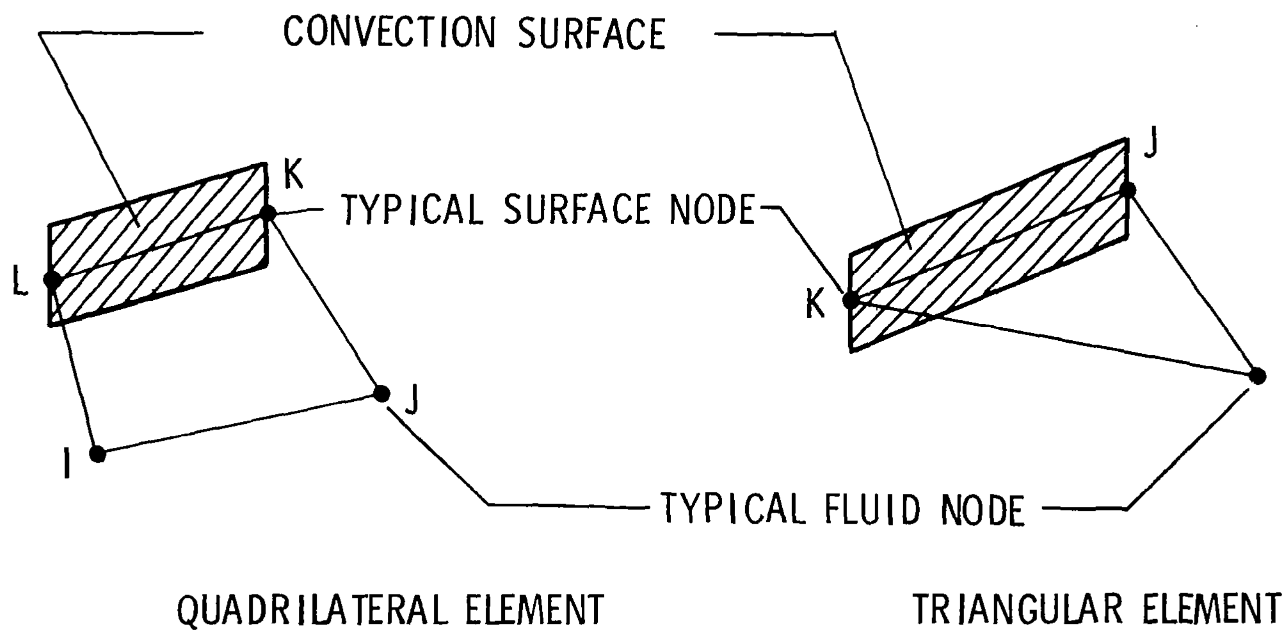

Figure 9

TUBE/FLUID ELEMENT

(Figure 10)

The tube/fluid element consists of fluid within a thin tube of arbitrary cross section. The tube wall temperature is constant around the perimeter but may vary in the axial direction. The element has two fluid nodes I and J and two tube nodes L and K.

The following heat transfer modes are represented: (1) Axial conduction in the tube (L to K); (2) Convection between tube inner surface nodes (L and K) and fluid nodes (I and J); (3) Mass transport convection (downstream I to J); and (4) convection between tube outer surface (nodes L and K) and a surrounding medium.

TUBE/FLUID ELEMENT

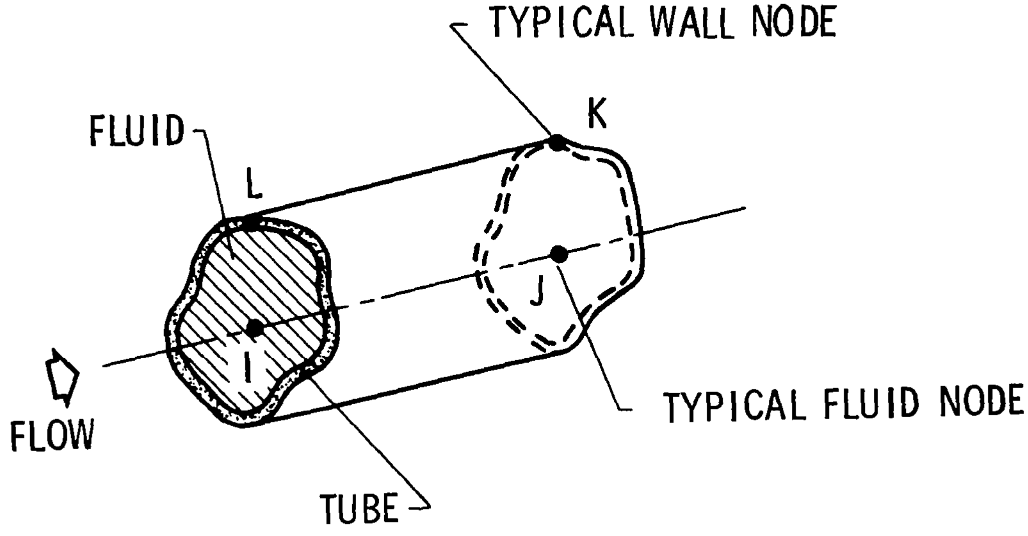

Figure 10

PLATE-FIN/FLUID ELEMENT

(Figure 11)

Plate-fin/fluid elements are used to model heat transfer in plate-fin heat exchangers. The plate-fin/fluid element consists of top and bottom walls (plates) connected by an internal fin. A single plain fin is shown in this schematic but other fin configurations as well as several fins can be represented within a single element. The flow cross section may vary along the element. The element has 6 nodes: two fluid nodes (N and K) and four plate-fin nodes (I,J,L,M). The fluid node locations are arbitrary at a given flow section.

The following heat transfer modes are represented in the element: (1) two dimensional conduction in the fin, (2) convection between the top and bottom wall surfaces and the fluid, (3) convection between the fin surfaces and the fluid, (4) mass transport convection (downstream N to K).

PLATE-FIN/FLUID ELEMENT

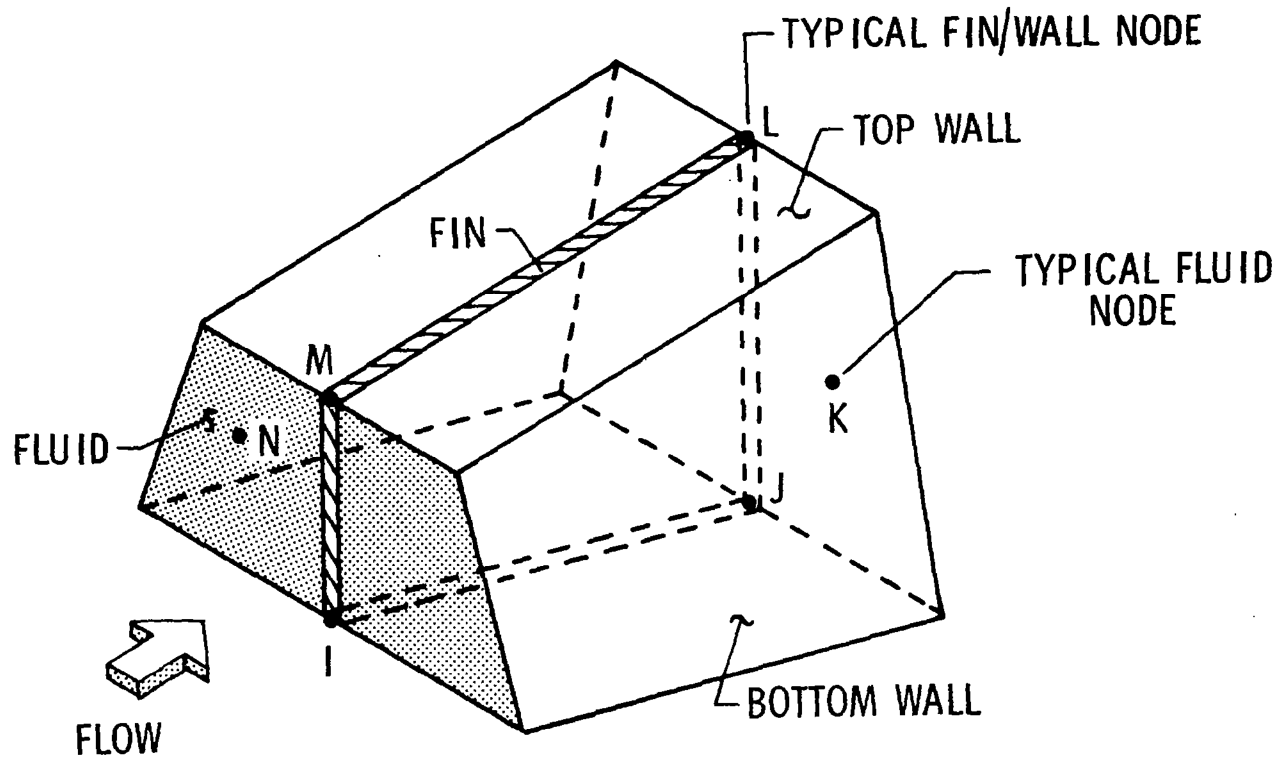

Figure 11

CONVECTIVE FINITE ELEMENT METHODOLOGY APPLICATION

(Figure 12)

In the next six figures applications of the new convective finite elements will be presented. The first applications will be to nonlinear steady-state analysis. The elements were developed using an exploratory finite element program TAP1 (ref. 5) which is available from COSMIC. The elements are also available in a recent release of SPAR. SPAR is a production program for efficient thermal/structural analysis of complex structures, and it is described in further detail in reference 6. Two steady-state applications of the elements will be presented here. Other examples have been presented previously in reference 4.

The steady-state convection methodology is currently being extended to nonlinear transient problems. An exploratory code TAP2 is being utilized in this methodology development. Some recent transient applications will be presented. A comparison with an analytical solution will be presented first, and then a preliminary transient analysis of the scramjet fuel-injection strut will be described.

CONVECTIVE FINITE ELEMENT METHODOLOGY APPLICATIONS

- NONLINEAR STEADY-STATE

  TAP1 EXPLORATORY PROGRAM (COSMIC)

  ELEMENTS BEING INSTALLED IN SPAR

  COMPARISONS OF LUMPED PARAMETER AND FINITE ELEMENT

- NONLINEAR TRANSIENT

  TAP2 EXPLORATORY PROGRAM

  COMPARISONS WITH ANALYTICAL

  SCRAMJET RESPONSE

Figure 12

APPLICATION OF TUBE/FLUID ELEMENT TO A CONVECTIVELY HEATED, COOLED PIPE

(Figure 13)

In the first application, tube/fluid elements are used to analyze a convectively heated, cooled pipe. Shown here is the cross section of the tube with the finite element mesh superimposed. A typical tube/fluid element is shown crosshatched. The pipe is subjected to external convective heating and is cooled by internal flow at a specified flow rate. The entrance temperature (283 K) of the coolant is specified; downstream coolant temperatures and the pipe wall temperatures are to be determined. Temperature dependent thermal parameters (k, h, c_p) were used, and the nonlinear equations were solved using the Newton-Raphson iteration method.

Finite element calculated temperatures are compared with temperatures from an equivalent lumped parameter (MITAS) analysis. The lumped parameter results are shown in parenthesis with the finite element results below. Excellent agreement can be seen.

APPLICATION OF TUBE/FLUID ELEMENT TO A CONVECTIVELY HEATED, COOLED PIPE

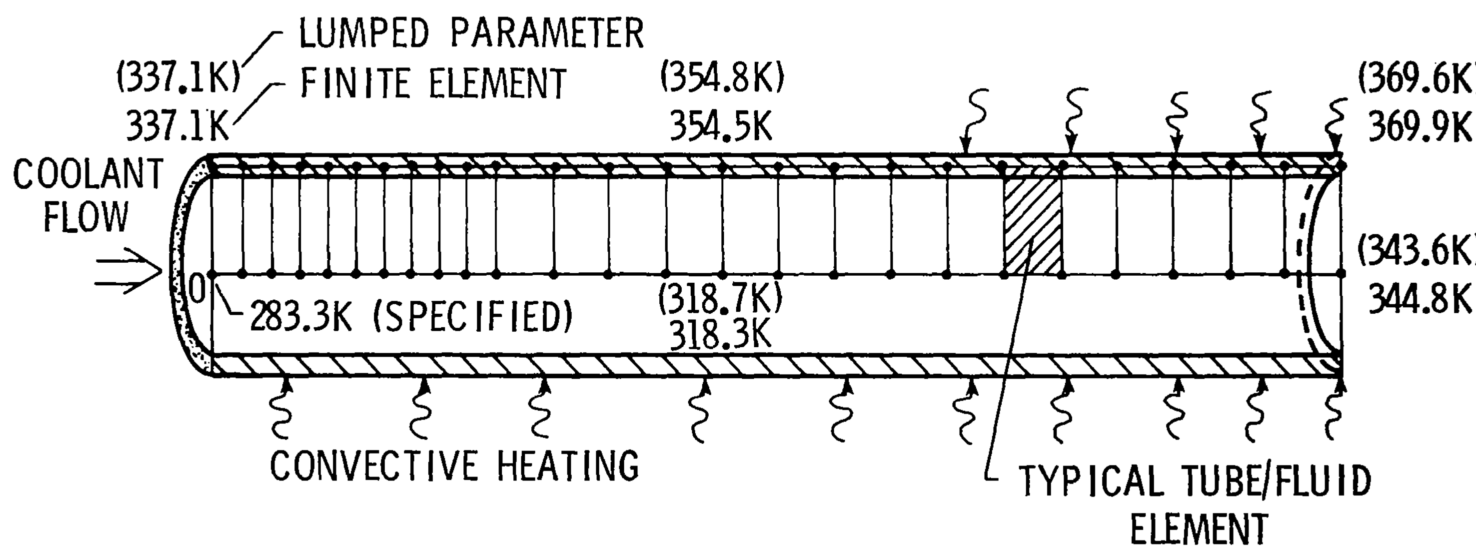

Figure 13

SCRAMJET FUEL-INJECTION STRUT CROSS SECTION

(Figure 14)

Another application of the convective finite elements was to the scramjet strut (previously had been analyzed with NASTRAN and MITAS, ref. 2). For convenience a simplified model was used. The model had 122 thermal unknowns in contrast to the 3000 unknowns in the previous study. Some details of the finite element model of the forward portion of the strut are shown in the next figure.

SCRAMJET FUEL-INJECTION STRUT CROSS SECTION

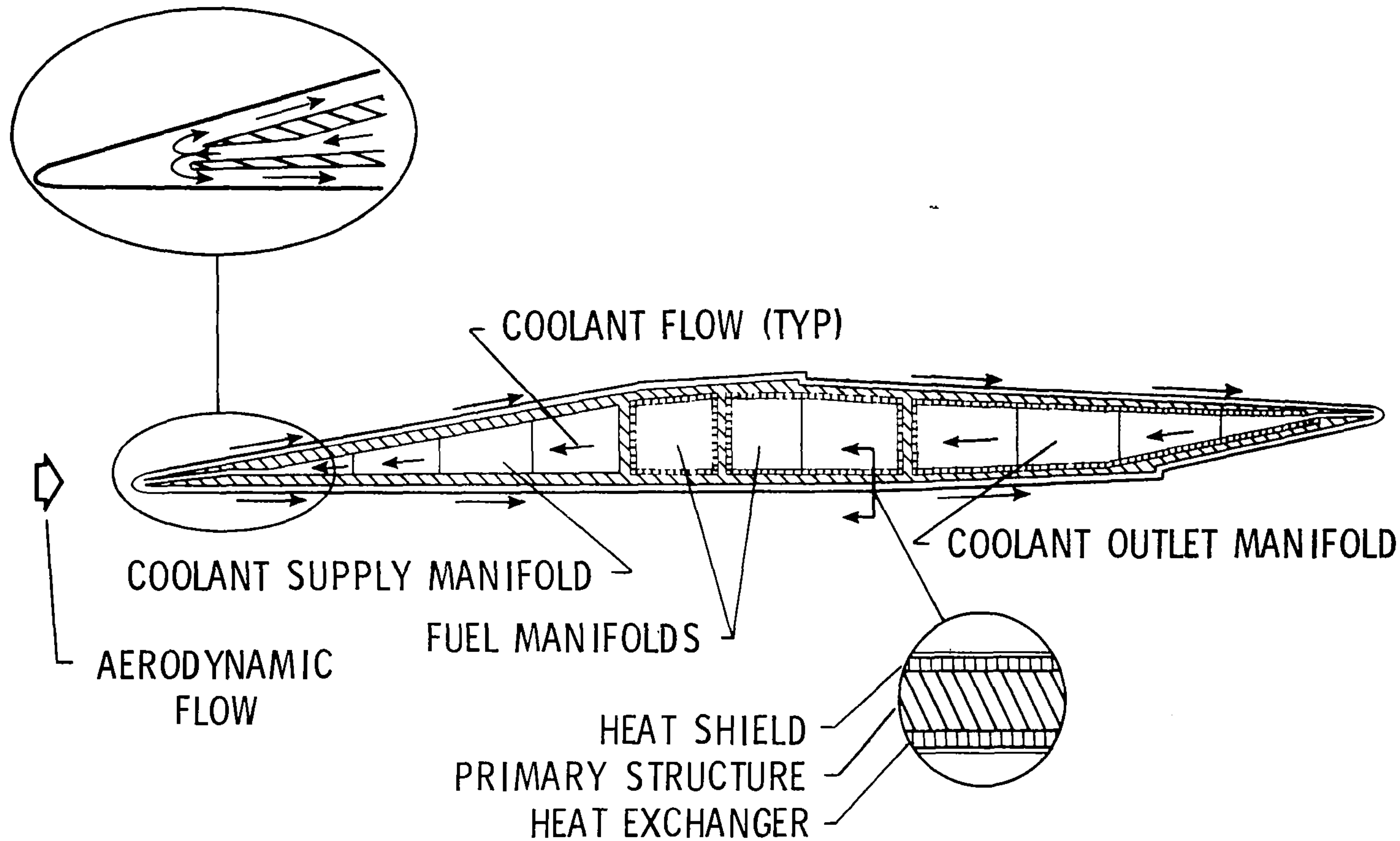

Figure 14

FINITE ELEMENT THERMAL METHODOLOGY

(Figure 15)

The finite element model of the forward portion of the strut is shown. The lower half of the figure shows the physical model, and the top half shows the mathematical model.

Mass transport elements are used to represent the flow into the coolant inlet manifold, the flow to the leading edge and the split flow to the plate-fin coolant passages. Convective heat transfer between the coolant and internal surfaces is represented by triangular surface convection elements. Triangular elements are shown at the leading edge and in the manifold. The coolant passages are represented by plate-fin/fluid elements. Conduction heat transfer is represented by quadrilateral elements in the primary structure and by rod elements in the aerodynamic skin and interior bulkheads.

FINITE ELEMENT THERMAL METHODOLOGY

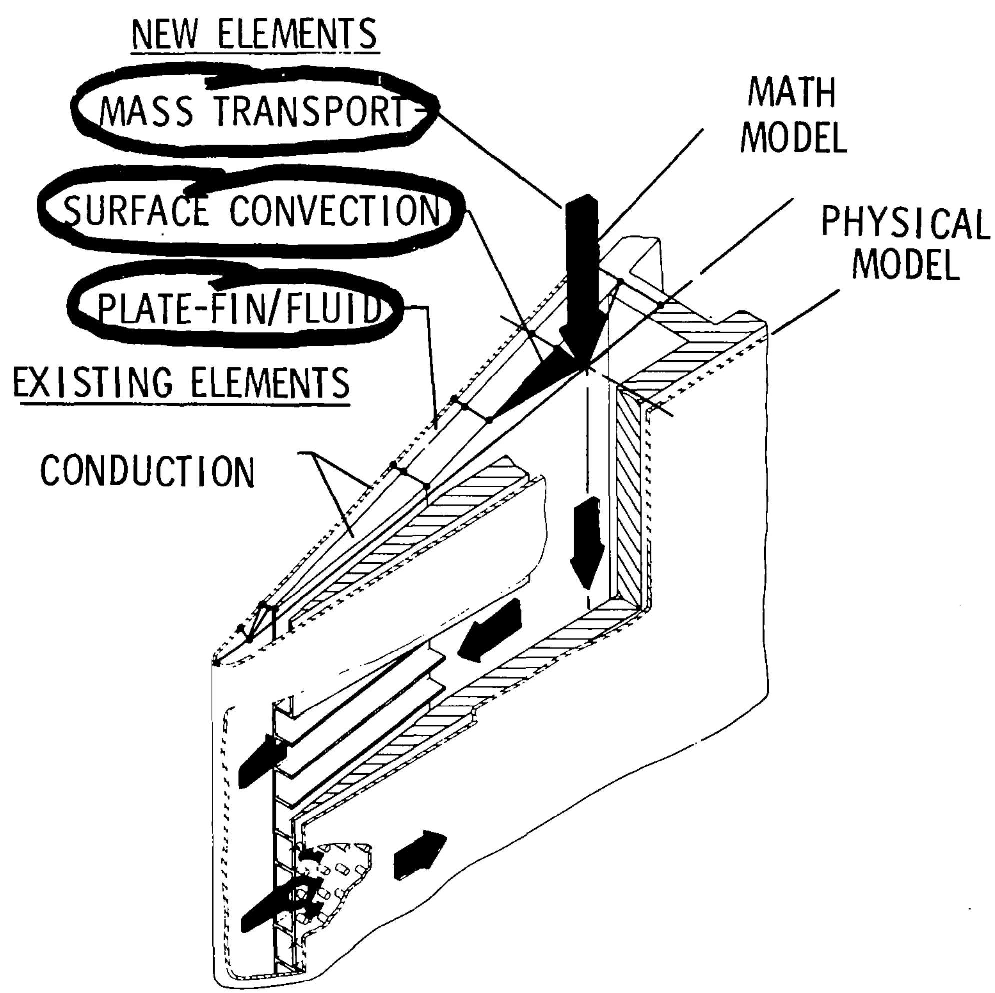

Figure 15

FINITE ELEMENT AND LUMPED PARAMETER COOLANT TEMPERATURES

(Figure 16)

Finite element and lumped parameter calculated coolant temperatures for the starboard coolant passage are compared. The coolant temperature variation along the starboard coolant passage is shown. The lumped parameter (MITAS) coolant temperature distribution was shown previously in Figure 5 in the discussion of the NASTRAN-MITAS comparison. The agreement between the finite element and lumped parameter temperatures is good although there is some tendency for the finite element temperature curve to oscillate about the MITAS result. Structural temperatures (not shown) were also computed and showed good agreement (see ref. 4).

FINITE ELEMENT AND LUMPED PARAMETER COOLANT TEMPERATURE

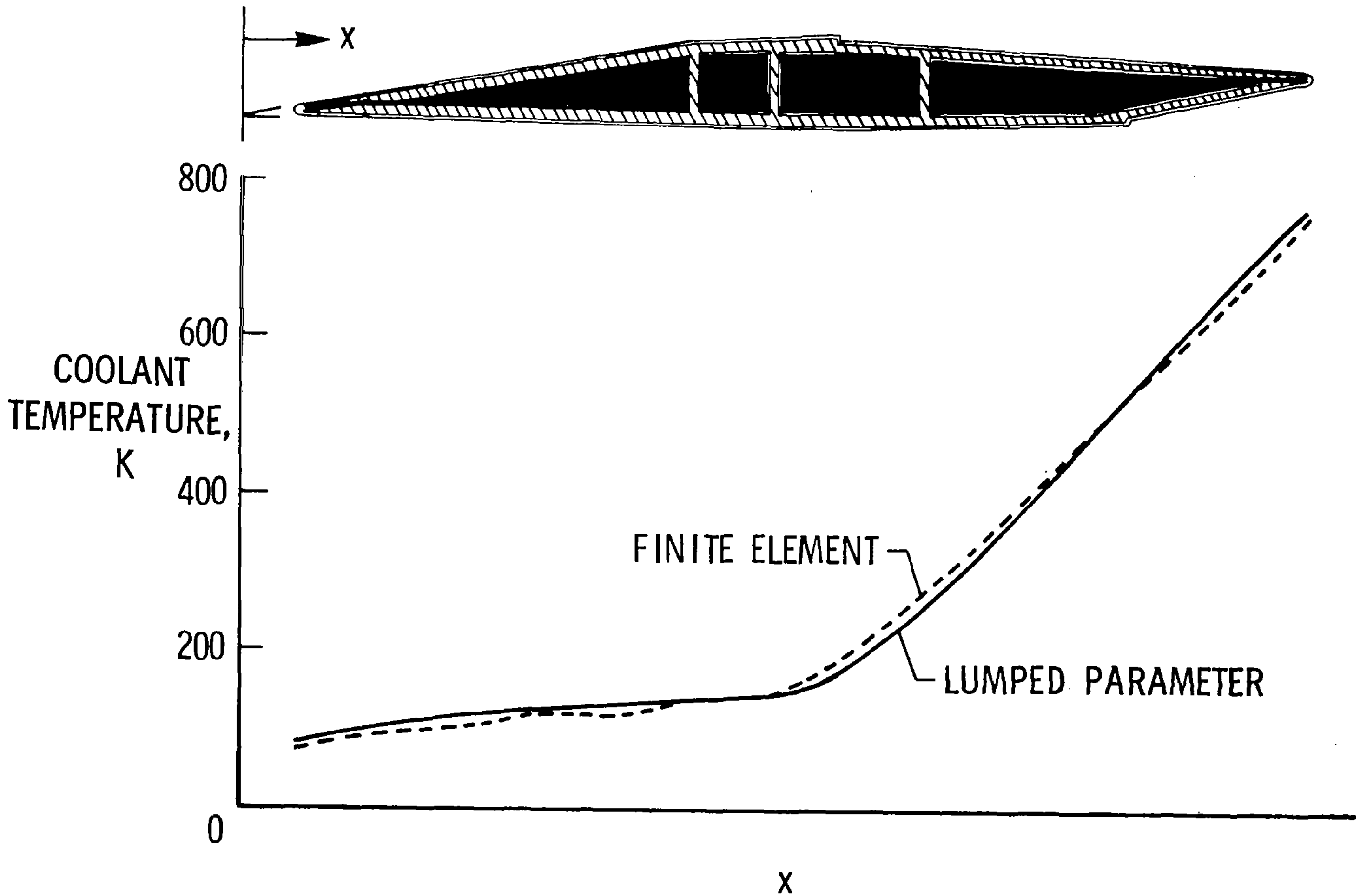

Figure 16

NONLINEAR CONDUCTION/CONVECTION TRANSIENT FLUID TEMPERATURES

(Figure 17)

This figure presents a nonlinear transient analysis of fluid flowing in a passage. At time zero a portion of the coolant passage has the specified temperature distribution shown in the upper figure, and the subsequent time variation of the coolant temperatures is to be determined. The exact formulation of the problem is described by a nonlinear partial differential equation (P.D.E.) containing terms which represent fluid conduction, convection, and capacitance. The convective term - $T \frac{\partial T}{\partial x}$ represents the nonlinearity. For the specified initial conditions, the equation has an exact closed-form solution (ref. 7). In the finite element analysis, nodal temperatures were computed as a function of time using an iterative solution at each time step.

The graph shows the time history of temperature at one node ($x = 0.3$). The exact solution is the solid line and the open circles denote the finite element predictions. The agreement is excellent.

NONLINEAR CONDUCTION / CONVECTION TRANSIENT FLUID TEMPERATURES

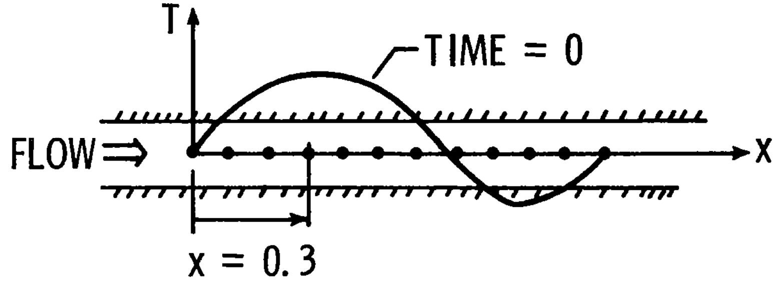

NONLINEAR P.D.E. - EXACT SOLUTION

$$\frac{\partial^2 T}{\partial x^2} - T\,\frac{\partial T}{\partial x} = \frac{\partial T}{\partial t}$$

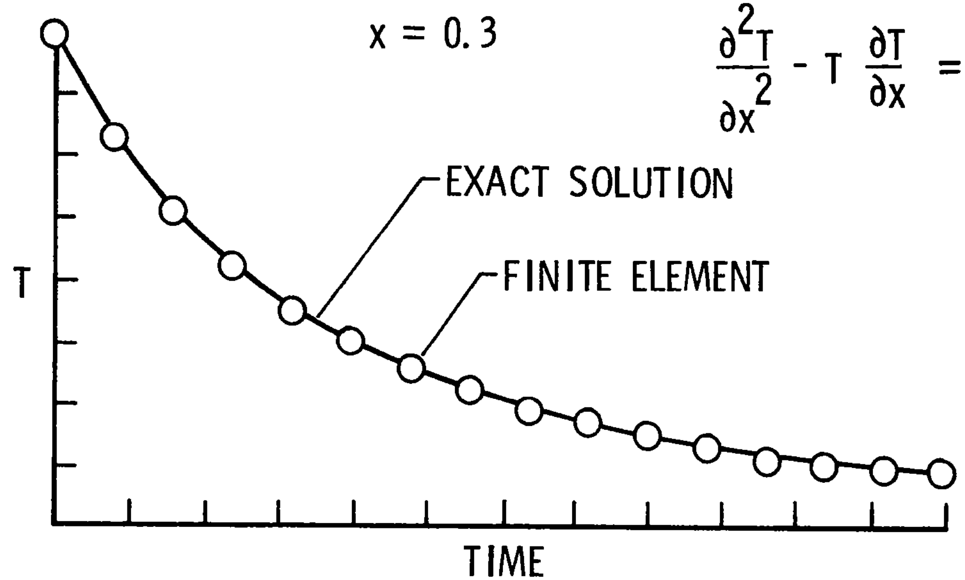

Figure 17

STRUT TRANSIENT COOLANT TEMPERATURE VARIATION

(Figure 18)

This figure shows some recent preliminary predictions for transient coolant temperatures in the fuel-injection strut. The problem consisted of the strut operating at a steady-state condition such as presented in Figure 16. At time zero there is a loss of combustion on the starboard side resulting in the heating distribution shown in the figure. The graph presents the initial starboard coolant temperature and computed temperatures (solid and dashed lines) at time equal to 5 seconds.

The predicted temperatures indicated by the solid line at 5 seconds shows physically unrealistic oscillations. At the time of the oral presentation of this paper the source of the oscillations was unknown. Since the conference, the oscillation problem has been traced to the mathematical formulation of the mass transport element used to model coolant flow between the manifolds and coolant passages, see reference 4. A new formulation of the mass transport element, based upon the upwind finite element concept (ref. 7), has been utilized in the computer program to remove the spurious coolant temperature oscillations. Coolant temperatures predicted utilizing the upwind element are shown by the dashed line.

STRUT TRANSIENT COOLANT TEMPERATURE VARIATION

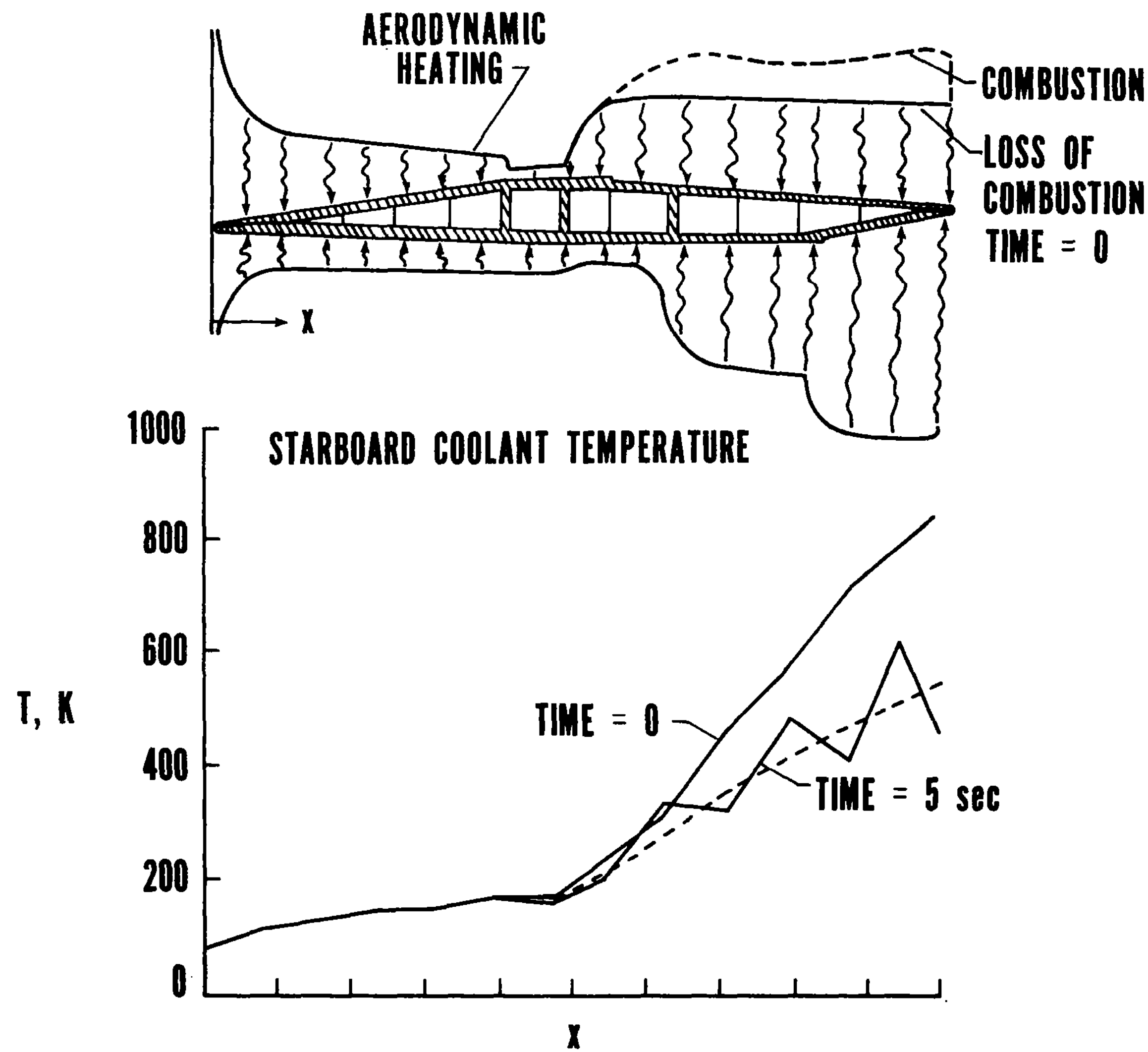

Figure 18

THERMAL/STRUCTURAL FINITE ELEMENT MODEL COMPATABILITY

(Figure 19)

Some observations of thermal/structural finite element model compatibility will now be presented. In the NASTRAN study of the scramjet fuel-injection strut (see figure 4), common thermal and structural finite element models were utilized. To obtain adequate stress detail, the common model required an excessively detailed thermal analysis.

This figure shows simplified finite element models of the thermal/structural behavior. Considering a typical wall section, the thermal model uses a single quadrilateral element to model the primary structure with convective finite elements for the coolant passages. Temperatures are then computed at the nodes shown. From the computed nodal temperatures the thermal loads, e.g. the average wall temperature $\bar{T}$ and the wall gradient ΔT, can be found.

An adequate structural model on the other hand utilizes beam or plate elements to model the primary structure. Typical nodal unknowns are displacement and rotation. The nodes are at different locations from the thermal model, namely at the midplane of the primary structure.

Each finite element model is efficient for the respective analysis. However, there is a lack of compatability between the models because: (1) the thermal analysis does not directly produce the thermal loads required for the structural analysis, and (2) the structural model utilizes different node locations and elements than the thermal model. Thus, this example illustrates that there exists a need within finite element methodology to improve the compatability between thermal and structural models.

THERMAL/STRUCTURAL FINITE ELEMENT MODEL COMPATABILITY

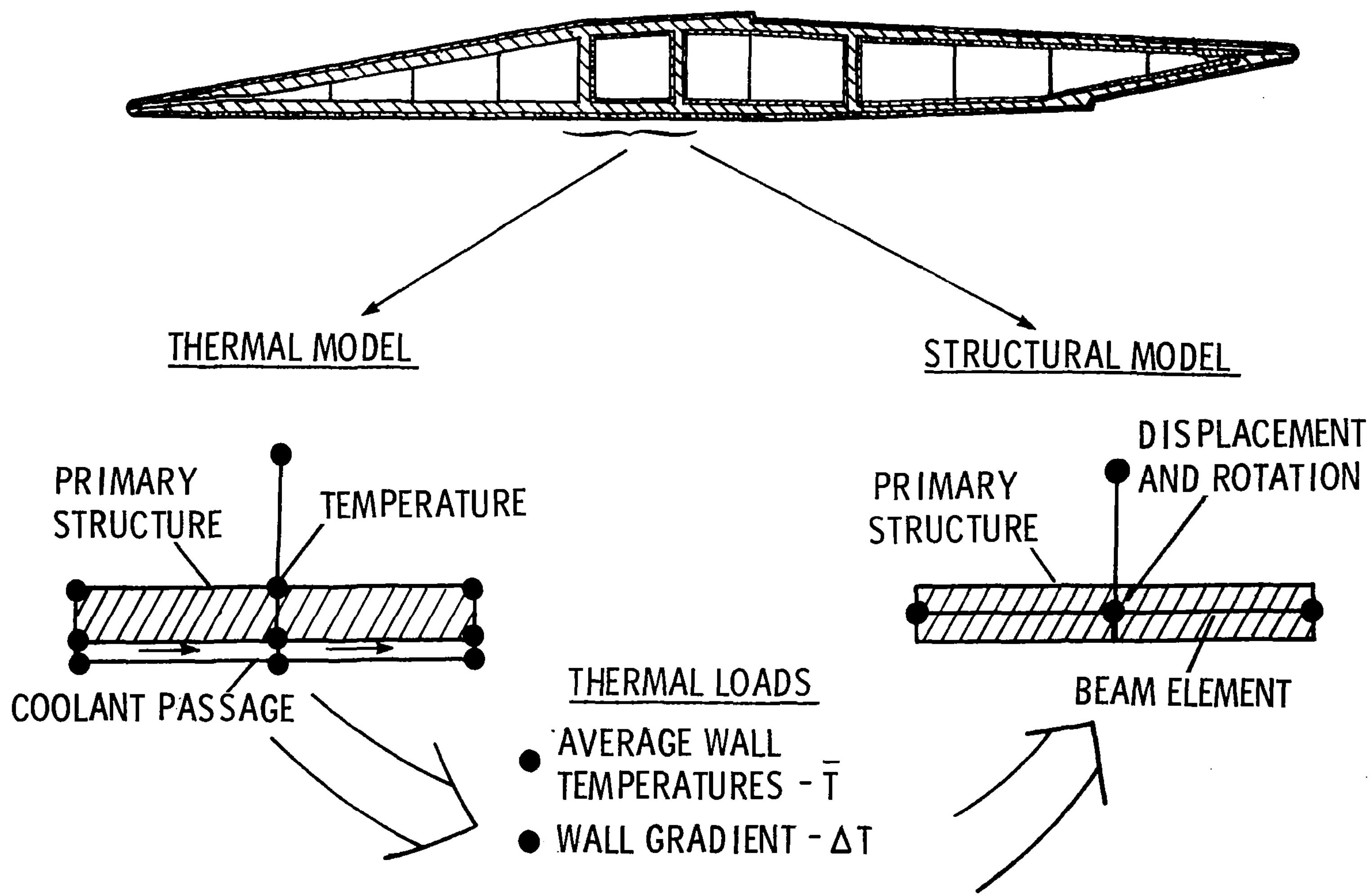

Figure 19

FINITE ELEMENT METHODOLOGY NEEDS

(Figure 20)

The previous figure illustrated the need for improved compatability between thermal/structural models. One concept which could be used to improve model compatability is element interpolation schemes. These schemes would allow the thermal analyst to specify the output required for the structural analysis, e.g. wall temperature gradients, average wall temperatures and node locations for the structural model. A second concept is new structurally compatible thermal finite elements. For example a layered thermal element could be used to do a three dimensional thermal analysis of an insulated panel and then could be used to output nodal quantities required for analyzing the structure utilizing plate bending elements.

FINITE ELEMENT METHODOLOGY NEEDS

- THERMAL/STRUCTURAL MODEL COMPATABILITY

  - INTERPOLATION SCHEMES

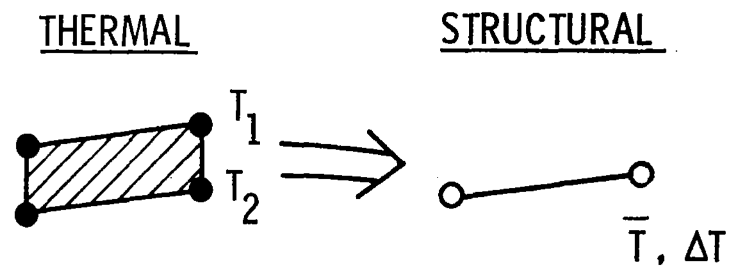

  - NEW COMPATABLE ELEMENTS

LAYERED THERMAL ELEMENT:

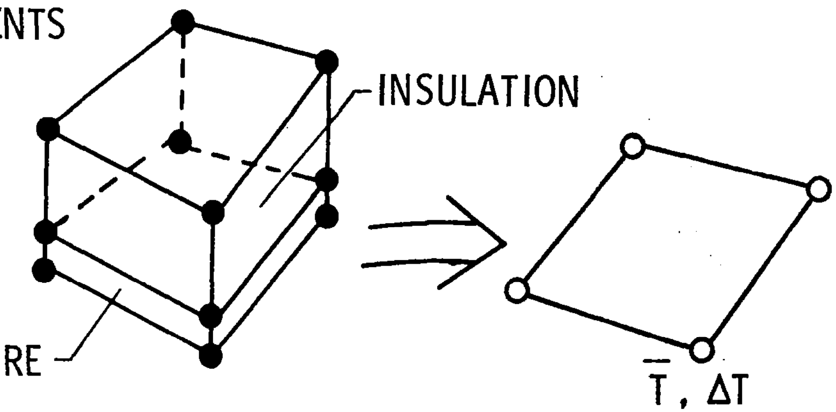

Figure 20

FINITE ELEMENT METHODOLOGY NEEDS

(Figure 21)

Another area of finite element methodology needs concerns efficient nonlinear transient algorithms. There is some indication that existing finite element production programs cannot compete with the lumped parameter programs for large problems due to high computer costs. There is a need for critical evaluation of existing finite element algorithms by comparison studies because further practical experience is needed to identify problem areas. Some recent experience at Langley Research Center has suggested that new algorithms may offer potential to reduce high computer costs and make the finite element method more competitive with lumped parameter methods for complex, nonlinear analyses.

FINITE ELEMENT METHODOLOGY NEEDS

- EFFICIENT NONLINEAR TRANSIENT ANALYSIS

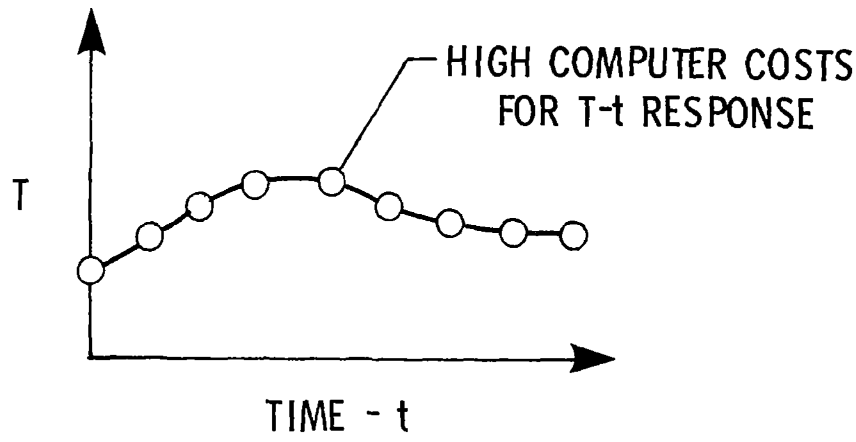

- EVALUATION OF EXISTING ALGORITHMS BY COMPARISONS
- DEVELOPMENT OF NEW ALGORITHMS

Figure 21

CONCLUDING REMARKS

(Figure 22)

A comparison study has been described which has indicated that the finite element and lumped parameter methods are comparable for steady-state conduction/convection analyses. The finite element model is advantageous because of the ease of model verification with computer graphics. Some problems encountered in constructing compatible thermal and structural models have indicated the need for further methodology developments to automate the transition between thermal and structural analyses. The need for more efficient finite element nonlinear transient algorithms has been cited. With further development in the thermal analysis area, the finite element method offers high potential for an integrated thermal/structural analysis capability.

CONCLUDING REMARKS

- FINITE ELEMENT - LUMPED PARAMETER COMPARABLE FOR STEADY-STATE CONDUCTION/CONVECTION
- FINITE ELEMENT GEOMETRIC MODEL ADVANTAGEOUS FOR MODEL VERIFICATION WITH COMPUTER GRAPHICS
- FINITE ELEMENT THERMAL/STRUCTURAL MODEL COMPATABILITY REQUIRES FURTHER DEVELOPMENT
- NEED FOR IMPROVED FINITE ELEMENT NONLINEAR TRANSIENT ALGORITHMS
- FINITE ELEMENT METHOD DEMONSTRATES HIGH POTENTIAL FOR AN INTEGRATED THERMAL/STRUCTURAL ANALYSIS CAPABILITY

Figure 22

REFERENCES

1. Wieting, Allan R.; and Thornton, Earl A.: Thermostructural Analysis of a Scramjet Fuel-Injection Strut. Recent Advances in Structures for Hypersonic Flight. NASA CP-2065, 1978. (Paper no. 6 of this compilation.)

2. Thornton, Earl A.; and Wieting, Allan R.: Comparison of NASTRAN and MITAS Nonlinear Thermal Analyses of a Convectively Cooled Structure. NASTRAN: User's Experiences. NASA TM X-3278, 1975.

3. Thornton, Earl A.: Thermal-Structural Analyses of a Scramjet Fuel Injection Strut. NASA CR-146839, 1976.

4. Thornton, Earl A.; and Wieting, Allan R.: Finite Element Methodology for Thermal Analysis of Convectively Cooled Structures. Heat Transfer and Thermal Control Systems. Leroy S. Fletcher, ed. AIAA, c.1978.

5. Thornton, Earl A.: TAP1: A Finite Element Program for Steady-State Thermal Analysis of Convectively Cooled Structures. NASA CR-145069, 1976.

6. Adelman, Howard M.; and Robinson, James C.: Recent Advances in Thermal-Structural Analysis and Design. NASA CP-2065, 1978. (Paper no. 24 of this compilation.)

7. Chung, T. J.: Finite Element Analysis in Fluid Dynamics, McGraw-Hill, 1978, pp. 217-218.

RECENT ADVANCES IN THERMAL-STRUCTURAL ANALYSIS AND DESIGN

Howard M. Adelman and James C. Robinson
NASA Langley Research Center

INTRODUCTION

This paper describes the results of some recent activity aimed at improved analytical design capability for structures subjected to a thermal environment. The paper is divided into two parts - analysis and design.

The analysis portion concentrates on recent improvements in the SPAR computer program - particularly improvements in the finite element library and the SPAR thermal analyzer. A recent application to calculations for the National Transonic Facility is discussed.

The design portion of the paper presents a digest of recently developed methods for sizing structures in which thermal stresses and/or temperatures are major considerations in the design process. Included is a modification of fully stressed design which accounts for thermal effects more efficiently than ordinary fully stressed design. Also an optimality criterion method for temperature constraints and a method for optimally sizing insulated structural panels under transient heating are described. A design-oriented approximate transient thermal analysis technique is illustrated and initial attempts at extending design capability to large complex structures are discussed.

CONFIGURATION OF SPAR

(Figure 1)

SPAR is a general-purpose finite element computer program developed for structural analysis and recently extended to thermal analysis (ref. 1). SPAR was developed and is currently maintained under contract and supported jointly by NASA's Langley Research Center and Marshall Space Flight Center. The program consists of a number of technical modules or processors which perform the basic tasks of finite element analysis. Each processor is programed in a highly efficient manner both from the standpoint of speed and core usage. Furthermore the processors communicate with each other through the data base. As a result of the above configurational considerations, SPAR is an extremely flexible and efficient computer program and has had extensive usage. Of particular usefulness, in terms of thermal-structural analysis capability, is the fact that once the temperatures are computed by one of the thermal analysis processors, these temperatures are available to the structural analysis processors through the data base. Such an availability saves the effort of having to manually transfer the temperatures from a thermal analyzer to a separate structural analyzer.

CONFIGURATION OF SPAR

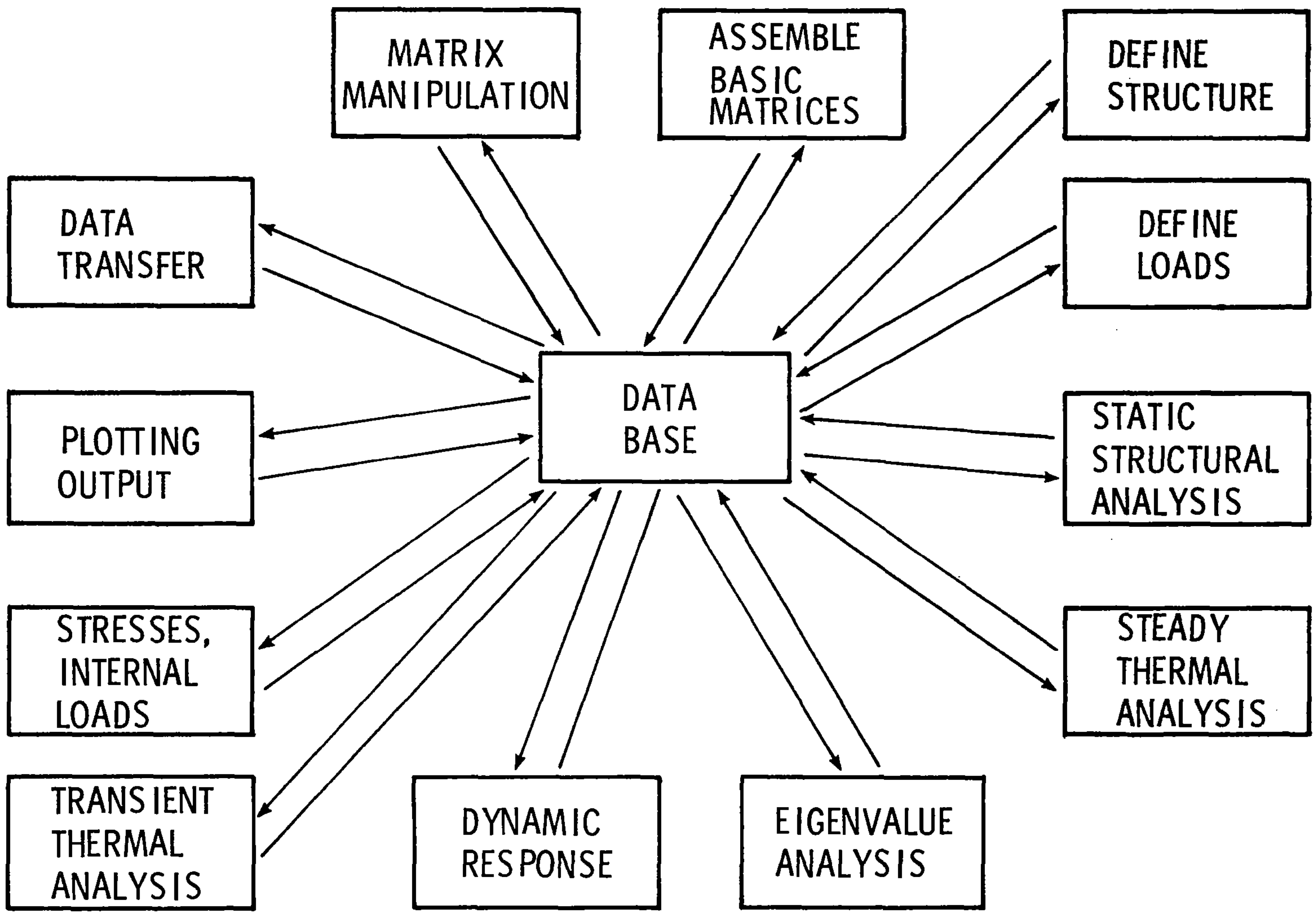

Figure 1

KEY FEATURES OF SPAR

(Figure 2)

As a result of the configuration and efficient programing of each processor of SPAR, there are a number of key features of the program. Fast execution and low minimum field length requirements are particular attributes. Also, provision for free-field input eases the task of preparing input to the program. The user has the flexibility to call the various processors in any order appropriate to his solution needs. The data base is designed to allow the user to interface between SPAR and other computer programs. Also a high degree of flexibility is available for output. For example, a large amount of output may be stored in the data base following execution, but only selected results need be printed or plotted initially. Later if necessary, other selected results may be printed. SPAR is presently operational on the CDC and UNIVAC computer systems and also on the PRIME and DEC minicomputers.

KEY FEATURES OF SPAR

- o FAST EXECUTION
- o LOW MINIMUM CORE REQUIREMENT ($\approx 60\,000_8$)
- o FREE-FIELD INPUT
- o USER-DEFINED EXECUTION STREAM
- o EXCELLENT DATA MANAGEMENT
- o OPERATIONAL ON CDC, UNIVAC, MINI

Figure 2

BASIC SPAR STRUCTURAL CAPABILITY

(Figure 3)

SPAR has a rather broad capability for structural analysis. Linear static and eigenvalue calculations (vibration modes and bifurcation buckling) are available as is dynamic response analysis. Efficiency of eigenvalue analysis is enhanced by substructuring capability. The finite element library is sufficient for most practical structural components. Newly developed elements may be evaluated and tested in a large-problem environment by use of the element test capability.

BASIC SPAR STRUCTURAL CAPABILITY

- LINEAR STATIC AND EIGENVALUE ANALYSIS
- DYNAMIC RESPONSE
- DYNAMIC SUBSTRUCTURING
- MATRIX MANIPULATION
- EXTENSIVE FINITE ELEMENT LIBRARY
- ELEMENT TEST CAPABILITY
- CONTAINED-FLUID ELEMENT

Figure 3

SPAR THERMAL ANALYZER

(Figure 4)

A thermal analyzer has been added to SPAR which provides the preliminary capability for integrated thermal-structural analysis. The thermal analyzer provides for rather general structural heat transfer analysis. Conduction, convection, and radiation to space are included and both transient and steady-state problems may be solved. Also included is an element test capability which provides a mechanism for evaluating new thermal finite elements in SPAR.

There are three improvements in progress: the addition of a set of finite elements for modelling mass transport effects (see ref. 2); provision for material properties which vary jointly with temperature and time; the capability to model radiant heat transfer between surfaces is being added to the thermal analyzer. The need for the time and temperature-dependent capability resulted from the fact that certain insulation materials have voids and the pressure of the gas in the voids varies with time during a vehicle trajectory. Consequently the thermal properties of the insulation vary with flight time as well as insulation temperature.

SPAR THERMAL ANALYZER

- THERMAL AND STRUCTURAL ANALYSIS IN SAME PROGRAM
- CONDUCTION, CONVECTION, AND RADIATION (TO SPACE)
- ONE-, TWO-, THREE-DIMENSIONAL ELEMENTS
- STEADY-STATE AND TRANSIENT ANALYSES
- ELEMENT TEST CAPABILITY
- ONGOING ADDITIONS
  - MASS TRANSPORT ELEMENT
  - TIME AND TEMPERATURE - DEPENDENT MATERIAL PROPERTIES
  - RADIATION BETWEEN SURFACES

Figure 4

NATIONAL TRANSONIC FACILITY

(Figure 5)

The National Transonic Facility (NTF) is based on the concept of using a cryogenic fluid as the test medium in order to achieve appropriate Reynolds numbers by the reduced viscosity of the fluid. Nitrogen operating at temperatures as low as $-184^{\circ}C$ is used as the test medium. Because of the low temperatures in the containing and supporting structure, thermal stresses become important design considerations. SPAR was used to perform thermal and structural analyses of the NTF structural components. In particular, the design of the downstream nacelle was greatly influenced by results from the SPAR analysis.

NASA
L-78-503

NATIONAL TRANSONIC FACILITY

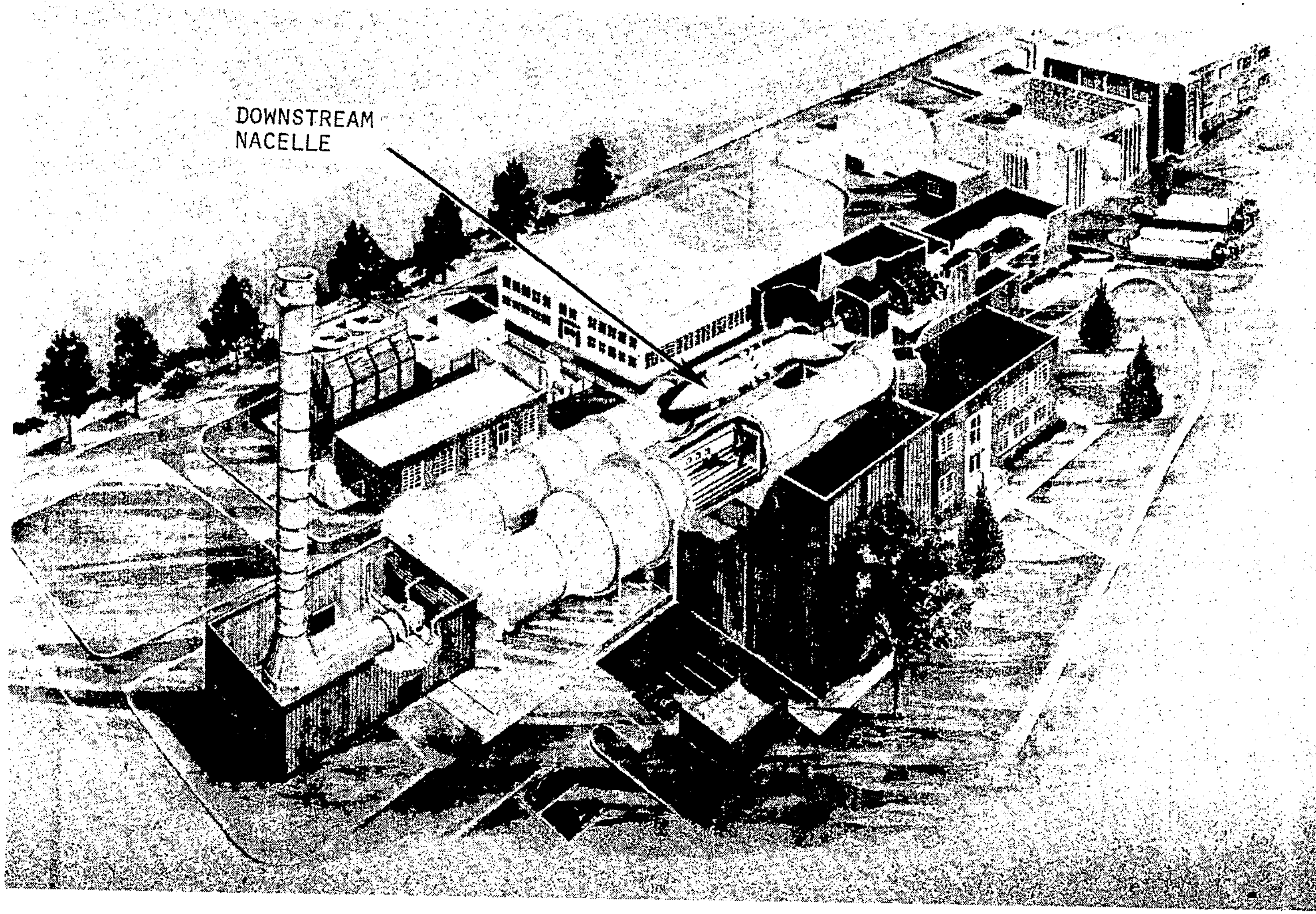

Figure 5

APPLICATION OF SPAR TO DOWNSTREAM NACELLE OF NTF

(Figure 6)

The finite element model of the structure had 2300 grid points and the same grid-point layout was used for the thermal and structural analysis. The thermal model had 6100 elements including convective boundary elements. The structural model had 13000 degrees of freedom (dof) after boundary conditions were applied) and a total of 2200 finite elements. Transient analyses were carried out to assure acceptable thermal and structural behavior for three load cases--the most critical being a sudden drop of -30°C in the temperature of the test medium.

APPLICATION OF SPAR TO DOWNSTREAM NACELLE OF NTF

- FINITE ELEMENT MODEL
  - THERMAL-2300 dof, 6100 ELEMENTS
  - CONDUCTION AND CONVECTION
  - STRUCTURAL-13000 dof, 2200 ELEMENTS
  - 3 LOAD CASES

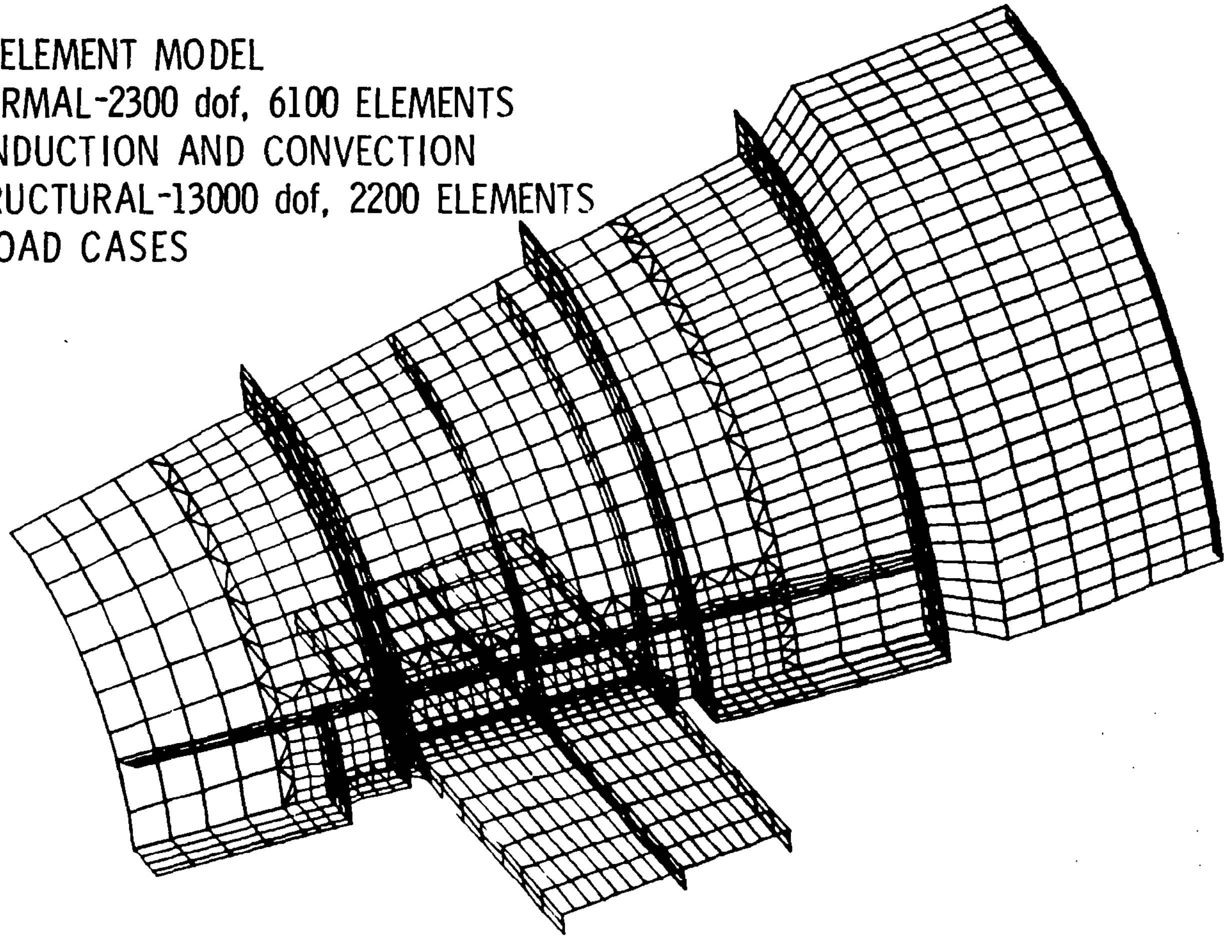

- DESIGN FOR ACCEPTABLE STRUCTURAL AND THERMAL PERFORMANCE DURING TRANSIENT RESPONSE TO STEP DECREASE IN TEMPERATURE

Figure 6

SUMMARY OF SPAR NTF NACELLE ANALYSIS

(Figure 7)

Several important benefits resulted from the SPAR analysis. Before discussing these, some background information is necessary. When the need for a thermal analysis of the nacelle was identified, the SPAR thermal analyzer was not available. A decision was made to use a lumped parameter program denoted MITAS (ref. 3). Because of the laborious effort of constructing a lumped parameter model of the entire nacelle, only a portion of the structure was modelled. Temperatures were computed and extrapolated from the modeled portion of the structure. Model generation using the SPAR thermal analyzer was less tedious and a finite element model of the complete nacelle was generated. The resulting temperatures from SPAR were found to be different from the extrapolated temperatures from the MITAS model. A more complete lumped parameter model was used in lieu of extrapolation and MITAS then produced the same temperatures as SPAR. Further, the computed temperatures were found to lead to excessive thermal stresses in the strut of the nacelle and the shell of the nacelle was vented to produce more uniform temperatures and lower stresses in the strut.

The thermal stress analysis revealed that some of the support rings were overstressed and these rings were resized. It was estimated that as a result of performing the thermal and structural analysis in the same program, about 10-15 man days of engineering effort were saved--principally from not having to manually transfer temperatures from a separate thermal analyzer to the structural analysis.

SUMMARY OF SPAR NTF NACELLE ANALYSIS

- BACKGROUND
  - INITIAL ANALYSIS USED LUMPED PARAMETER PROGRAM (MITAS)
  - USED PARTIAL MODEL - TEMPS EXTRAPOLATED
  - SPAR PERMITTED MORE REFINED AND COMPLETE MODEL
- BENEFITS
  - INACCURACIES REVEALED IN TEMPERATURES OF LUMPED PARAMETER MODEL
  - IMPROPERLY SIZED RINGS REDESIGNED
  - SAVED 10-15 MAN DAYS ENGINEERING EFFORT

Figure 7

THERMAL MODEL OF SHUTTLE ORBITER

(Figure 8)

One of the most challenging thermal structural analysis problem faced by aerospace engineers is the space shuttle orbiter. The modelling and analysis is being undertaken by Johnson Space Center and the shuttle contractor Rockwell International. Langley Research Center personnel are following this work in order to assess analytical needs and capabilities for shuttle and for future vehicles.

The thermal model of the shuttle orbiter consists of 118 three-dimensional lumped parameter models, each having about 200 nodes. Temperatures are computed in each of the models and interpolated between the modeled regions to obtain temperatures in the unmodeled regions. To determine the times of occurrence of the critical combinations of thermal and mechanical internal loads, it is necessary to inspect output temperature time histories from the thermal analyses. It is observed that the above procedures, while somewhat standard for analysis of such complicated structures, constitute a tedious, laborious, and expensive task.

THERMAL MODEL OF SHUTTLE ORBITER

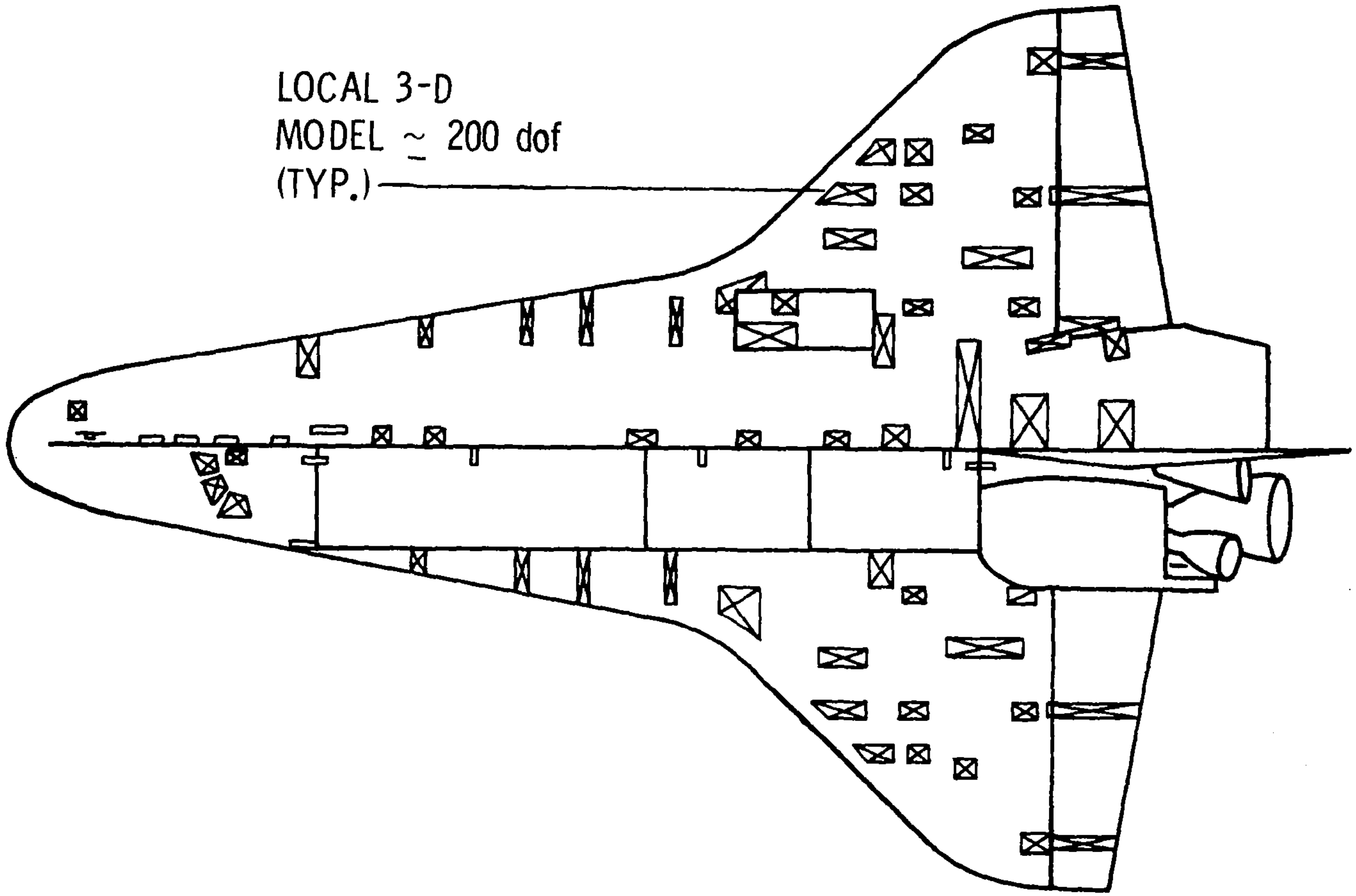

Figure 8

IMPRESSION OF REQUIREMENTS FOR EXTENSION OF ANALYTICAL CAPABILITY AS REFLECTED BY SHUTTLE EXPERIENCE

(Figure 9)

As a result of observations made regarding thermal modelling of the shuttle orbiter, the following requirements are identified:

(1) Methods to automate the more tedious aspects of generating lumped parameter and finite element thermal models. This need would appear to be especially pressing for the lumped parameter method wherein there is a considerable amount of hand calculation necessary and, as far as can be discerned, there has been little effort directed at automated model generation.

(2) Faster solution techniques for large-order matrix equations governing nonlinear, transient heat transfer.

(3) Methods to transfer temperatures from a thermal finite element model to a structural finite element model.

(4) A means of automating the determination of the times at which the critical combinations of thermal and mechanical internal loads occur.

IMPRESSION OF REQUIREMENTS FOR EXTENSION OF ANALYTICAL CAPABILITY AS REFLECTED BY SHUTTLE EXPERIENCE

- o AUTOMATED MODEL GENERATION
- o FASTER SOLUTION TECHNIQUES FOR NONLINEAR TRANSIENT HEAT TRANSFER
- o AUTOMATED DATA TRANSFER BETWEEN THERMAL AND STRUCTURAL MODELS
- o CRITICAL TIMES DETERMINATION

Figure 9

AUTOMATED MODEL GENERATION

(Figure 10)

A program has recently been developed by Sperry and provided to the Langley Research Center under contract to automate the more tedious aspects of generating lumped parameter thermal models (ref. 4). In using the program, the user first defines the geometry of the lumped parameter system by executing SPAR. The program uses the geometric information from the SPAR model to compute the necessary lumped parameters such as conduction path lengths, conductances, and capacitance terms and formulates the governing equations. The option for plotting the geometry of the lumped parameter model is available. Such an option is useful for detecting and correcting input data errors and has generally not been available in lumped parameter thermal analyzers.

AUTOMATED MODEL GENERATION

- PROGRAM GENERATES LUMPED PARAMETER THERMAL MODEL

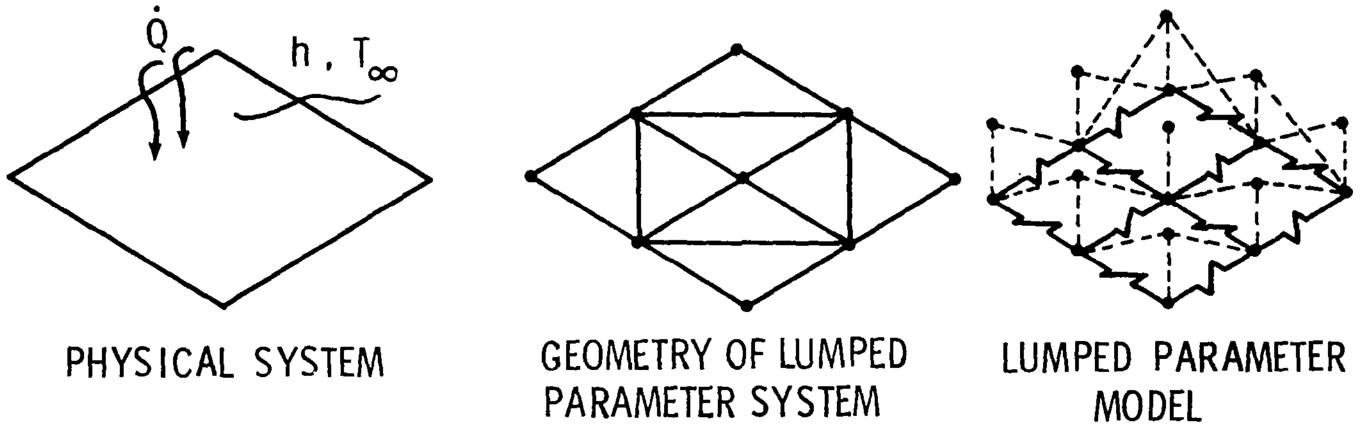

- REDUCES MODEL GENERATION EFFORT
- ALLOWS PLOTTING OF LUMPED PARAMETER MODEL

Figure 10

THERMAL STRUCTURES - DESIGN CONSIDERATIONS AND CONCEPTS

(Figure 11)

Turning to the topic of automated sizing of flight structures, attention is focused on three classes of design situations as shown in the figure. Work is in progress to develop and validate sizing methods appropriate to each situation. In the first case temperatures are at or below acceptable levels, but thermal stresses must be accommodated. This case is typified by a supersonic cruise aircraft or a "hot" structure. A second case is one in which structural temperatures would be excessively high if not controlled and heating takes place over a long cruise time. This situation is typified by the use of active cooling for a hypersonic cruise aircraft. Finally there is the case of a vehicle subjected to a short, intense heating environment and insulation is used to maintain structural temperatures at acceptable levels. This last situation is typified by the space shuttle orbiter vehicle but also applies to insulated components on hypersonic cruise vehicles.

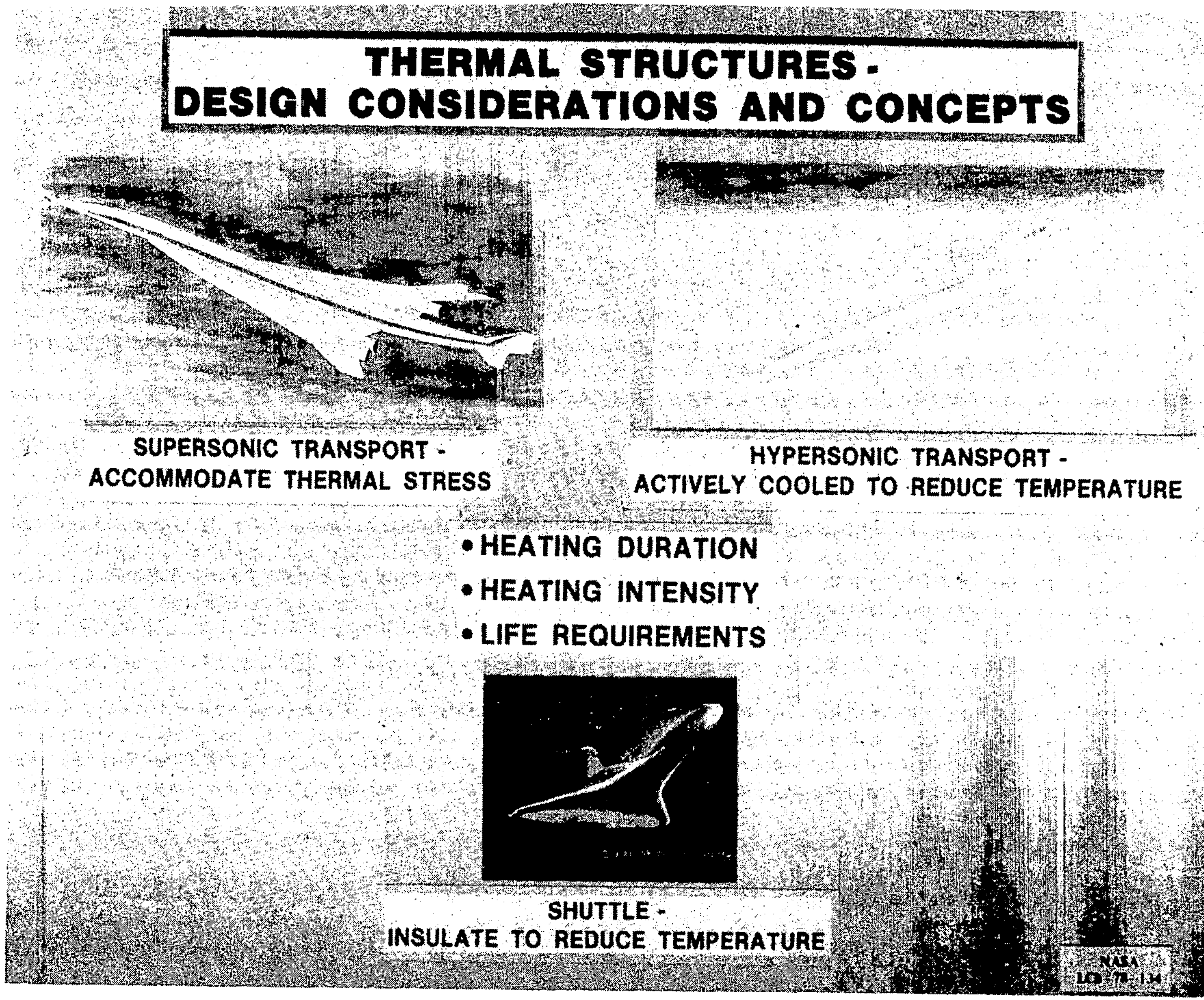
THERMAL STRUCTURES -
DESIGN CONSIDERATIONS AND CONCEPTS
SUPERSONIC TRANSPORT -
ACCOMMODATE THERMAL STRESS
HYPERSONIC TRANSPORT -
ACTIVELY COOLED TO REDUCE TEMPERATURE
• HEATING DURATION
• HEATING INTENSITY
• LIFE REQUIREMENTS
SHUTTLE -
INSULATE TO REDUCE TEMPERATURE
NASA

Figure 11

ACCOMMODATE THERMAL STRESS

(Figure 12)

Because of computational efficiency and convenience, fully stressed design (FSD) is widely used to size structures for strength constraints. When applied to structures under mechanical loads plus prescribed temperatures typified by the wing model, FSD may demonstrate slow convergence when thermal stresses are comparable in magnitude to mechanical stresses. The slow convergence of FSD for structures with large thermal stresses is associated with the relative insensitivity of thermal stresses to structural sizing. An extreme example of the insensitivity is illustrated by the fixed, heated bar in the figure, which develops a stress completely independent of size. In an attempt to circumvent the slow convergence of FSD while retaining its computational convenience, a modified procedure was implemented and given the name thermal fully stressed design (TFSD). The development of the algorithm is described in references 5 and 6.

The TFSD resizing algorithm for uniaxial stress members from reference 5 is

$$A_{i+1} = \frac{\sigma_{Mi}}{(\sigma_{aM} - \sigma_{Ti})} A_i \qquad (1)$$

In equation (1), σ_M is the stress due to mechanical loads acting alone, σ_T is the stress due to thermal loads acting alone, and σ_a is either the tensile or compressive allowable stress, depending on the sign of σ_M. By separating the mechanical and thermal stresses, TFSD tends to avoid the slow convergence exhibited by FSD for thermal problems.

The sizing formula for isotropic membranes is obtained by generalizing equation (1). The formula derived in reference (6) is

$$t_{i+1} = \left[\frac{b_i}{2\left(\sigma_a^2 - V_{Ti}^2\right)} + \sqrt{\frac{b_i^2}{4\left(\sigma_a^2 - V_{Ti}^2\right)^2} + \frac{V_{Mi}^2}{\sigma_a^2 - V_{Ti}^2}} \right] t_i \qquad (2)$$

where V_M and V_T are the Von Mises stress for mechanical and thermal loads, respectively, and b is a coupling term containing products of mechanical and thermal stresses.

ACCOMMODATE THERMAL STRESS

- KEY FEATURE - THERMAL STRESS INSENSITIVE TO MEMBER SIZE

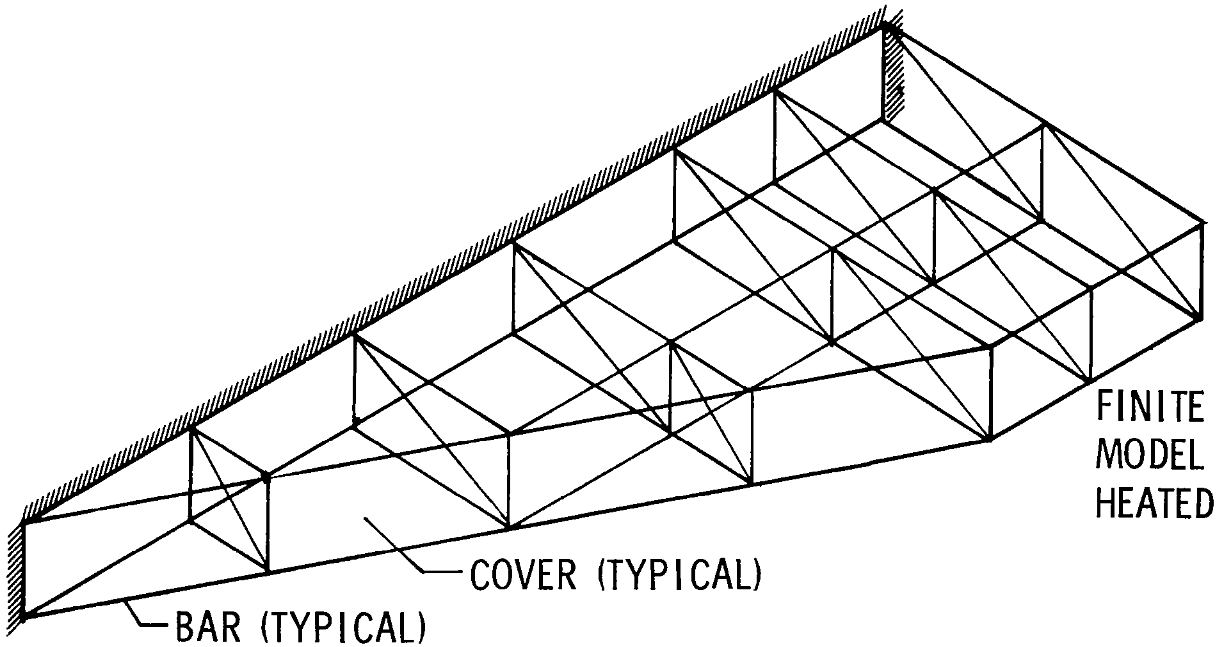

FINITE ELEMENT
MODEL OF
HEATED STRUCTURE

- EXTREME EXAMPLE

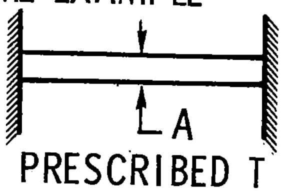

$\sigma_T = -E\alpha T$

Figure 12

CONVERGENCE OF THERMAL FULLY STRESSED DESIGN

(Figure 13)

An illustration of TFSD is the simplified low-aspect-ratio wing shown in the previous figure. Complete details of the finite element model are contained in reference 7. The finite element model has 85 bars, 10 membranes and 36 grid points. A study of the effect of thermal load level on relative convergence rates of FSD and TFSD for the wing is shown in the figure. The number of iterations required for TFSD and FSD to converge to within 5 percent of the final mass is plotted for increasing levels of thermal loading. The number of cycles for FSD to converge increases sharply with thermal stress level, while TFSD converges in only a few cycles. At the highest thermal stress level TFSD required three cycles to converge while FSD required 29 cycles. It is concluded from this and other examples (reference 5, 6) that the TFSD algorithm is worthy of consideration for use by designers concerned with sizing structures with significant thermal stresses.

CONVERGENCE OF THERMAL FULLY STRESSED DESIGN

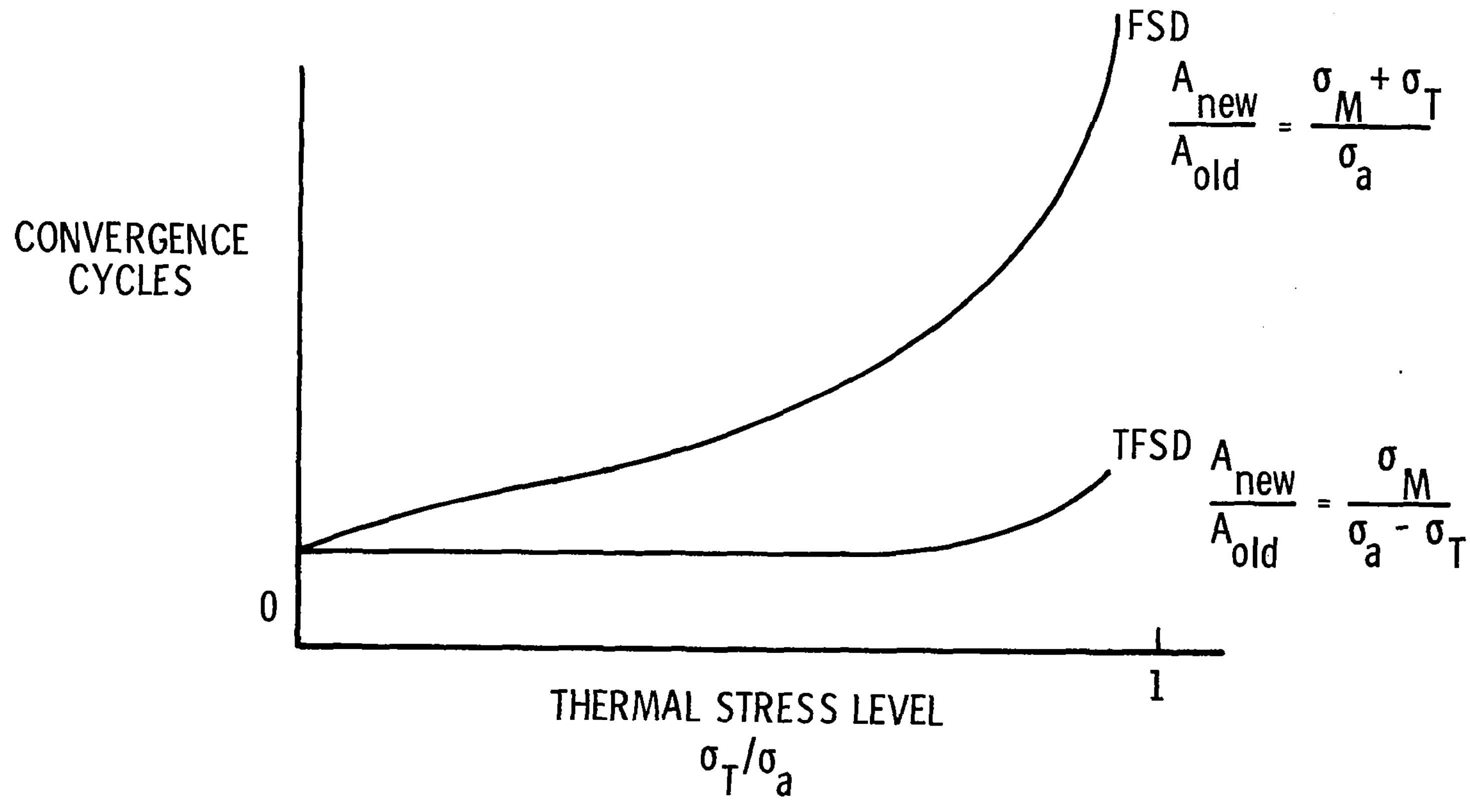

Figure 13

CONTROLLING TEMPERATURE BY CONDUCTION

(Figure 14)

When the structural temperatures need to be controlled for acceptable performance, such as actively cooling a structural panel, the design problem is one of obtaining a minimum mass design subject to constraints on both strength and temperature. Two sizing procedures have been implemented for such a situation. The first procedure consists of TFSD or FSD sizing formula together with a sizing formula based on an optimality criterion for temperature constraints (discussed further on the next figure). The second procedure is based on nonlinear mathematical programming with constraints on temperatures at points in the structure and on stresses in the structural elements. The mathematical programming method is facilitated by the general-purpose optimizer computer program AESOP (ref. 8).

CONTROLLING TEMPERATURE BY CONDUCTION

- KEY FEATURE - CONDUCT HEAT TO HEAT SINK
- SIZING METHODS
  - OPTIMALITY CRITERION
  - MATH PROGRAMING

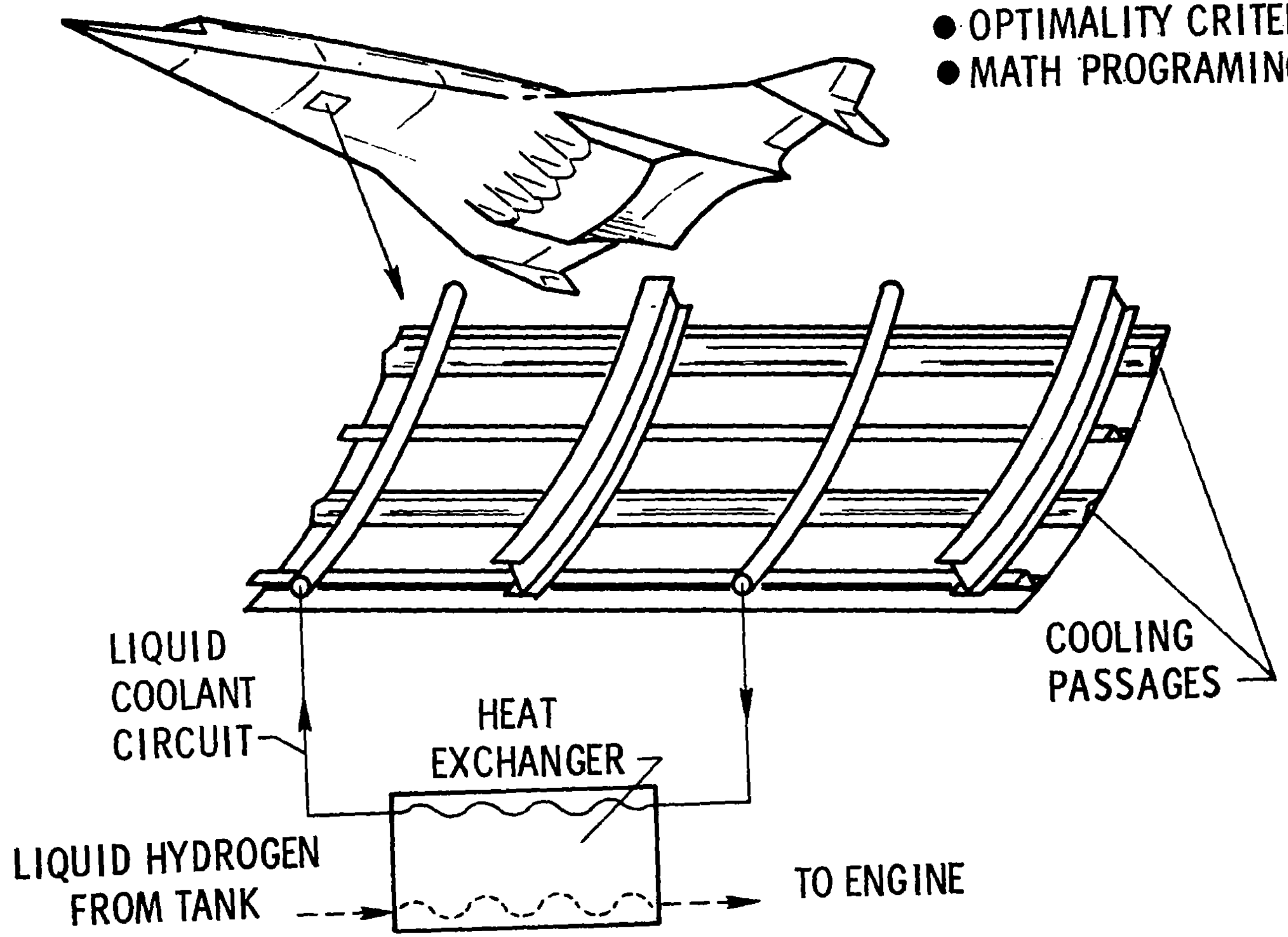

Figure 14

APPLICATION AND EVALUATION OF THERMAL OPTIMALITY CRITERION

(Figure 15)

The need for a method to size structures based solely on temperature constraints led to consideration of optimality criteria. Such methods share the convenience with FSD and TFSD of having explicit resizing formulas and are useful when a single type of constraint is involved.

Using Lagrange multipliers the problem is formally posed as follows: minimize

$$W^* = W + \sum_{k=1}^{N} \lambda_k \, (T_k - T_{a,k}) \qquad (3)$$

where W is the mass of the structure, T_k is the k-th controlled temperature, $T_{a,k}$ is the allowable temperature at the k-th point, and λ is a Lagrange multiplier. The necessary condition for an optimum design is obtained by equating to zero the first partial derivatives of W^* with respect to the design variables, $\{A\}$. This process leads to resizing formulas for individual finite elements used to model the structure of the following form

$$A_{i+1} = \left(\frac{E_e}{M_e}\right)^{\gamma} A_i \quad \text{and} \quad \lambda_{k,i+1} = \left(\frac{T_k}{T_{a,k}}\right)^{\gamma} \lambda_{k,i}$$

where M_e and E_e are derivatives of the first and second terms on the right side of equation (3), respectively, and γ is chosen as 0.5 for fast convergence. The method has been used to size square and triangular plates and the final designs are verified by designs from a math programing technique. The figure contains a summary of these results and indicates that the method is within 1.5 percent of the optimum mass. Additionally, neither convective heat transfer effects nor multiple temperature constraints affect the accuracy of the final designs, but both have a tendency to slow convergence.

APPLICATION AND EVALUATION OF THERMAL OPTIMALITY CRITERION

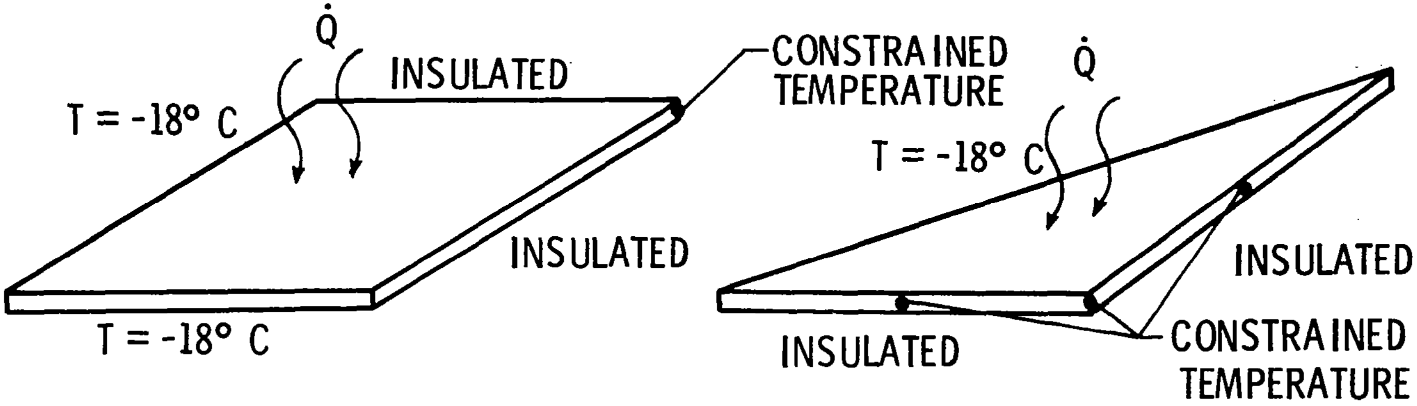

PROBLEM	DIMENSIONLESS OPTIMIZED VOLUME: OPTIMALITY CRITERION	DIMENSIONLESS OPTIMIZED VOLUME: MATH PROGRAMING	NUMBER ITERATIONS FOR OPTIMALITY CRITERION
SQUARE PLATE CONDUCTION ONLY	0.0474	0.0479	22
SQUARE PLATE CONDUCTION AND CONVECTION	0.0343	0.0342	50
TRIANGULAR PLATE	0.0316	0.0312	45

Figure 15

SIZING A PANEL FOR STRENGTH AND TEMPERATURE

(Figure 16)

The two coupled thermal-structural sizing procedures are applied to a highly idealized model of a cooled panel. The configuration shown in the figure consists of a titanium panel with aluminum bars. This configuration is representative of a class of structures where one material satisfies strength requirements and the other acts as an efficient conductor to transfer incident heat to a heat sink. The finite element model includes 24 membrane elements, 12 bar elements, and 61 grid points resulting in 36 design variables.

The optimality criterion with FSD yielded an optimum total mass of 4.80 kg while the mathematical programing approach yielded essentially the same design and had a total mass of 4.79 kg. The design is governed by both temperature and strength requirements and is shown in the right side of the figure. Convergence to within five percent of final mass was obtained in 16 iterations and required only 22 seconds of execution time on a CDC CYBER 175 computer. The mathematical programing procedure required about an order of magnitude more computing effort.

SIZING A PANEL FOR STRENGTH AND TEMPERATURE

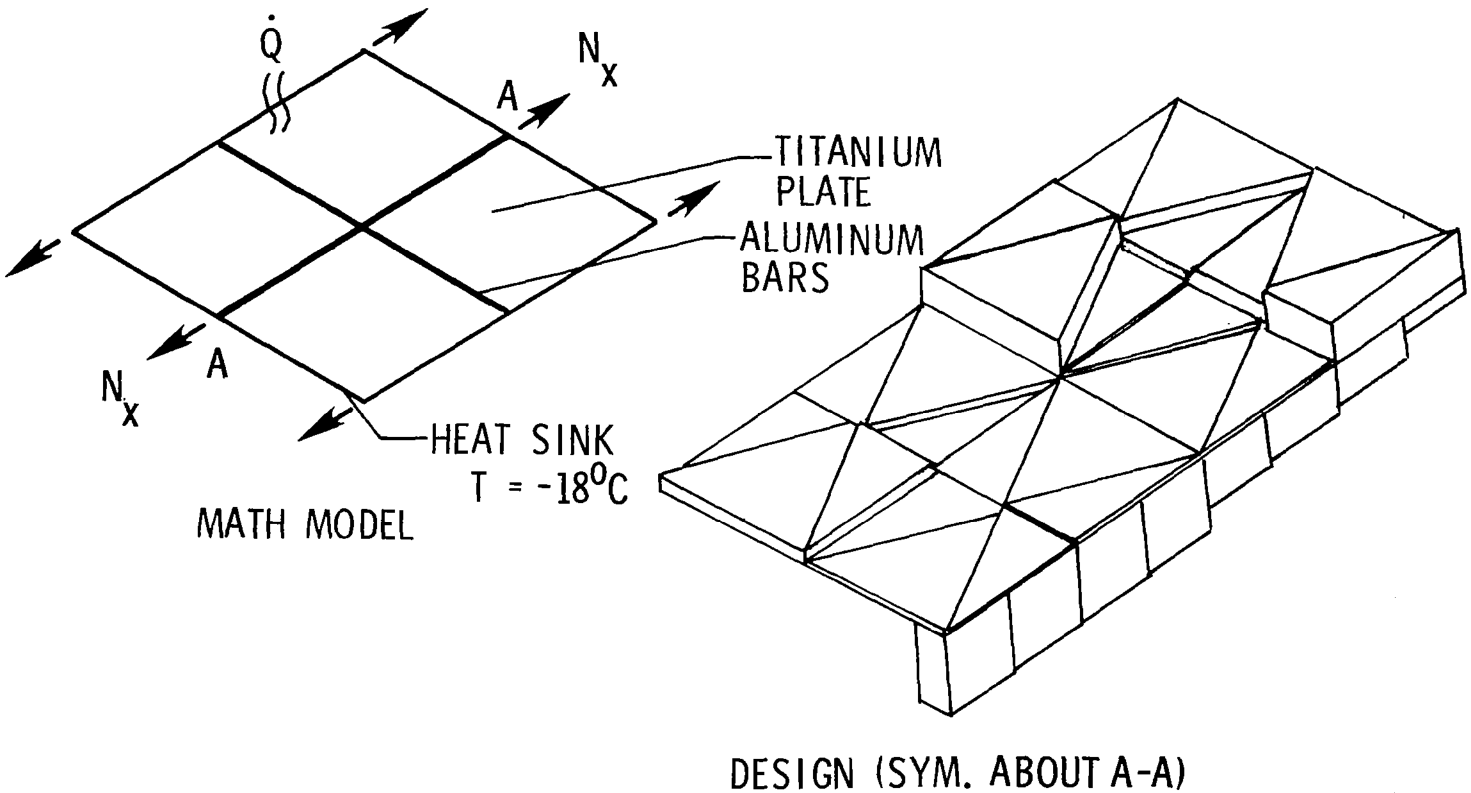

- MASS: 4.73 kg (OPTIMALITY CRITERION)
  4.72 kg (MATH PROGRAMING)
- OPTIMALITY CRITERION IS ORDER OF MAGNITUDE FASTER

Figure 16

TEMPERATURE CONTROLLED BY INSULATION

(Figure 17)

In design for transient loading, it is necessary to size a structure subject to constraints that must be satisfied over a period of time. Moreover, the analysis of each trial design entails the calculation of time histories of the appropriate response quantities such as stresses and temperatures. Clearly, optimization of complex structures for transient loading poses a challenge to existing structural optimization techniques.

Attention is directed to the problem of determining the minimum-mass design of the insulated panel shown in the figure. The panel is taken to represent a small section of a large structural component for which a finite element analysis is typically used to determine gross loads N_x, N_y, and N_{xy}. The problem is to determine the minimum insulation and structural layer thickness necessary to withstand the loads and heating. A transient temperature T_{eq} typical of a reentry heating trajectory is applied to the outer surface of the insulation layer. One-dimensional heat transfer is assumed and the back wall of the panel is adiabatic. The structure is either metallic or a balanced symmetric composite laminate with 0^o, $\pm 45^o$ and 90^o plies subjected to a general set of in-plane forces. The quantity to be minimized is the total mass per unit surface area. Constraints are imposed on the structure to prevent excessive temperatures and structural failure over an appropriate period of time. The accommodation of time-varying constraint equations presents analytical difficulties. An approach being tried in the present work is to satisfy the constraints at a number of specified times. The optimization problem is solved by the AESOP program (ref. 8). The transient temperature history is obtained by an analytical solution given in reference 9.

TEMPERATURE CONTROLLED BY INSULATION

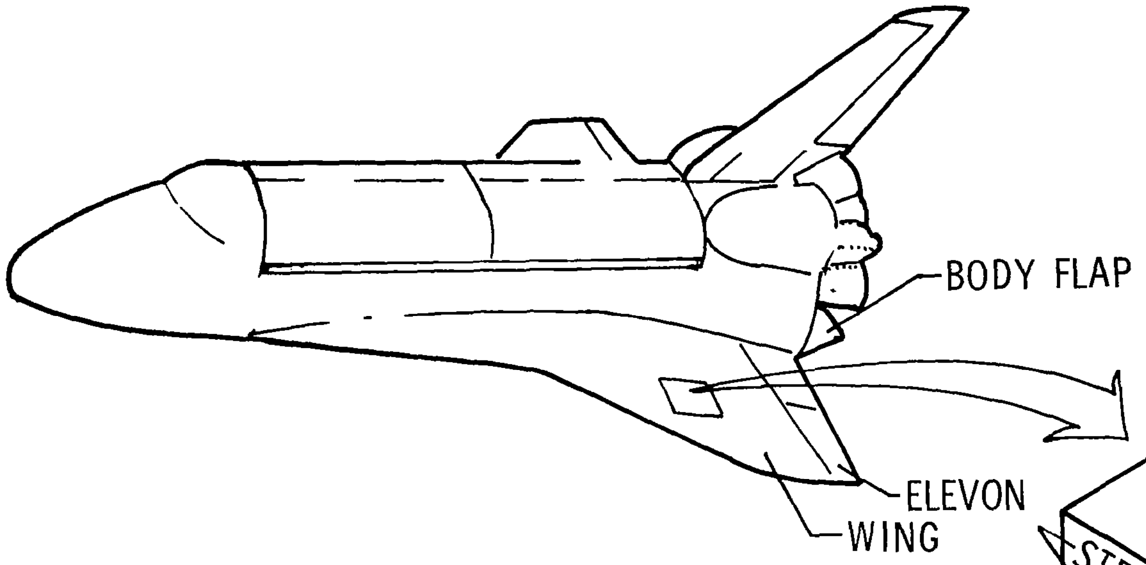

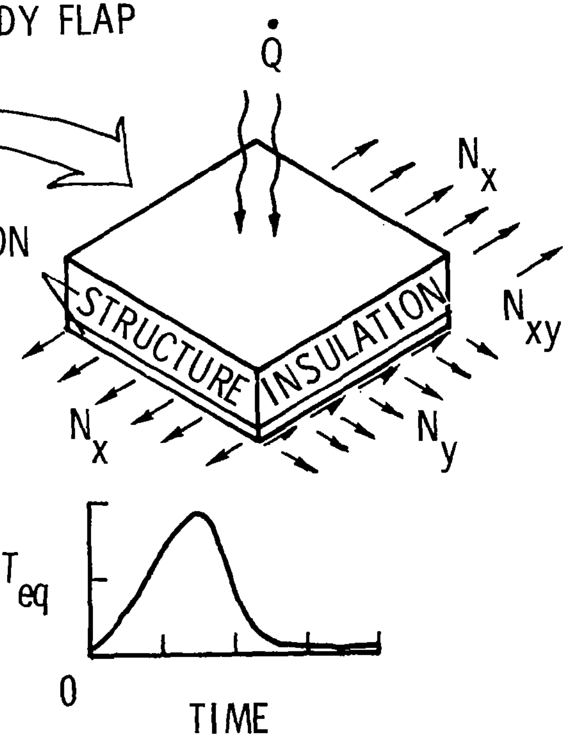

- TRANSIENT PROBLEM
- TIME-DEPENDENT CONSTRAINTS
- MATH PROGRAMING USED

Figure 17

MASS OF VARIOUS INSULATED PANELS

(Figure 18)

The foregoing procedure is demonstrated by sizing the insulation and panel thickness for three structural materials: aluminum, graphite polyimide (G/PI) and René 41 (uninsulated). These materials are of interest in connection with high temperature structural applications. The outer surface of the insulation (or in the case of René the upper structural surface) is heated by a pulse having a peak value of 816°C. The load N_x varies up to 2.6 MN/M with $N_y = N_x$ and $N_{xy} = -2/3\ N_x$. The symbols along the horizontal axis correspond to approximate load levels for key locations on a vehicle such as the space shuttle orbiter.

As shown in the figure, the curve for René is linear due to the absence of insulation and the fact that all Rene designs are strength-critical so that mass is proportional to load. For the aluminum designs, the upper portion of the curve corresponds to strength-critical designs and is nearly linear. The break in the aluminum curve corresponds to a transition point below which designs are both strength and temperature-critical. At the lower end of the curve, the designs are temperature-critical only, and at the highest load the designs are strength critical only. The G/PI designs are both temperature and strength critical except at the highest and lowest load values. Thus the mass versus load line is curved over the entire load range.

The figure indicates that for highly loaded structures, G/PI appears to be the most efficient, and at low loads, such as control surfaces, René 41 is the most efficient. The accuracy of the actual values in figure 18 of course must be tempered by the simplicity of the mathematical model used.

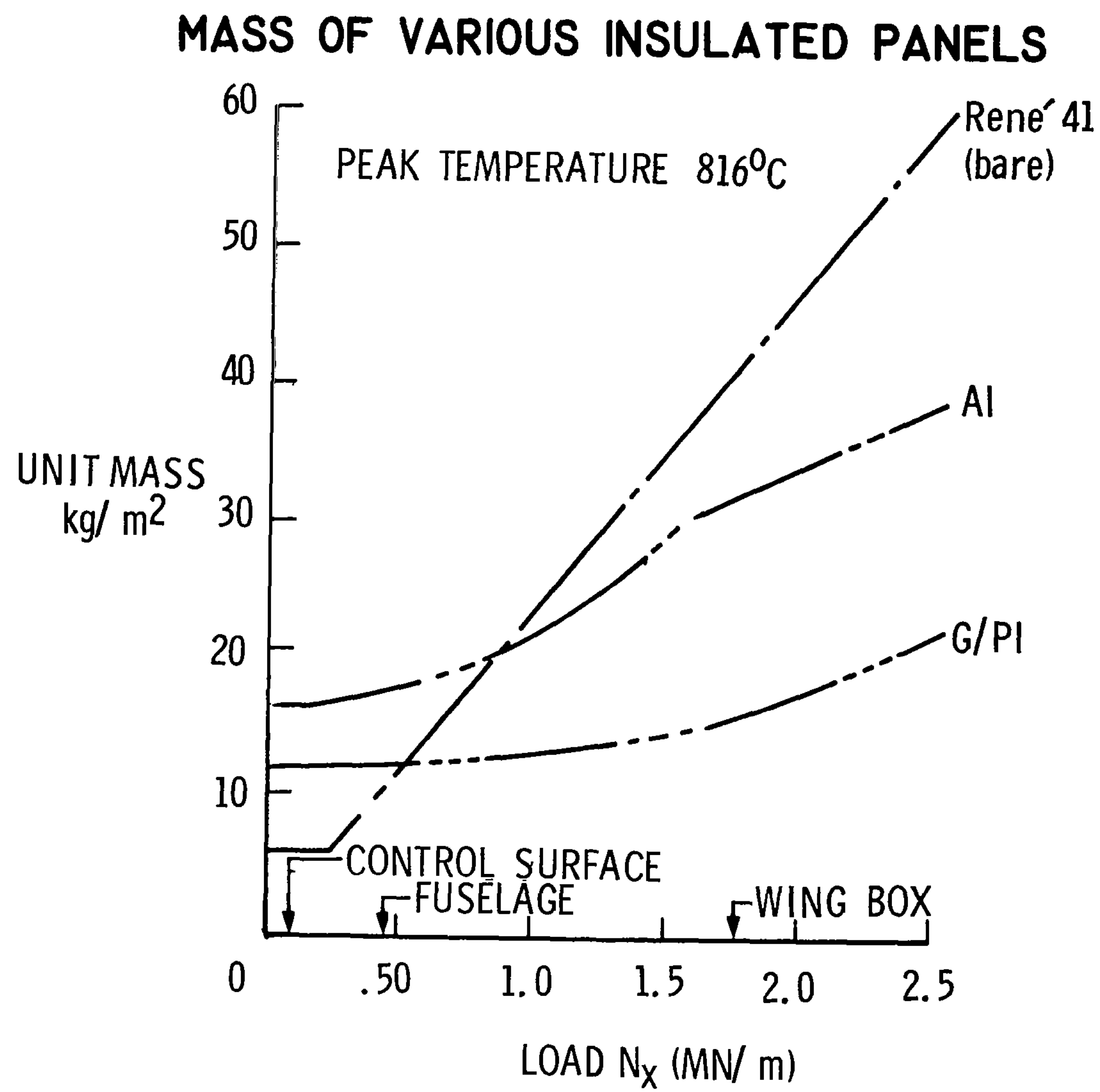
MASS OF VARIOUS INSULATED PANELS
PEAK TEMPERATURE 816°C
UNIT MASS kg/ m2
60
50
40
30
20
10
0
.50
1.0
1.5
2.0
2.5
LOAD Nx (MN/ m)
Rene´ 41 (bare)
Al
G/PI
CONTROL SURFACE
FUSELAGE
WING BOX

Figure 18

APPROXIMATE TRANSIENT THERMAL ANALYSIS FOR DESIGN CALCULATIONS

(Figure 19)

In looking toward sizing complex thermal structures, it is apparent that the analysis phase of the sizing process will become expensive computationally, especially for transient heat transfer calculations. One technique to partially alleviate the expense of analysis is the use of approximate reanalysis. One such approximation technique is Taylor series expansion as shown in the figure. This method, which has been successfully employed for design oriented structural reanalysis (ref. 10), consists of updating the temperature each time the structure is changed by a correction term containing the derivative of the temperature with respect to the design variables. The derivatives are relatively simple and computationally easy to obtain.

To demonstrate the potential benefit of approximate transient thermal reanalysis in design calculations, the insulated panel sizing program was modified by replacing the exact analysis by the approximation. The result was a 75 percent reduction in computer time to obtain a design with a negligible error in the final (optimum) mass.

APPROXIMATE TRANSIENT THERMAL ANALYSIS FOR DESIGN CALCULATIONS

$$T^* = T + \frac{\partial T}{\partial a} \Delta a$$

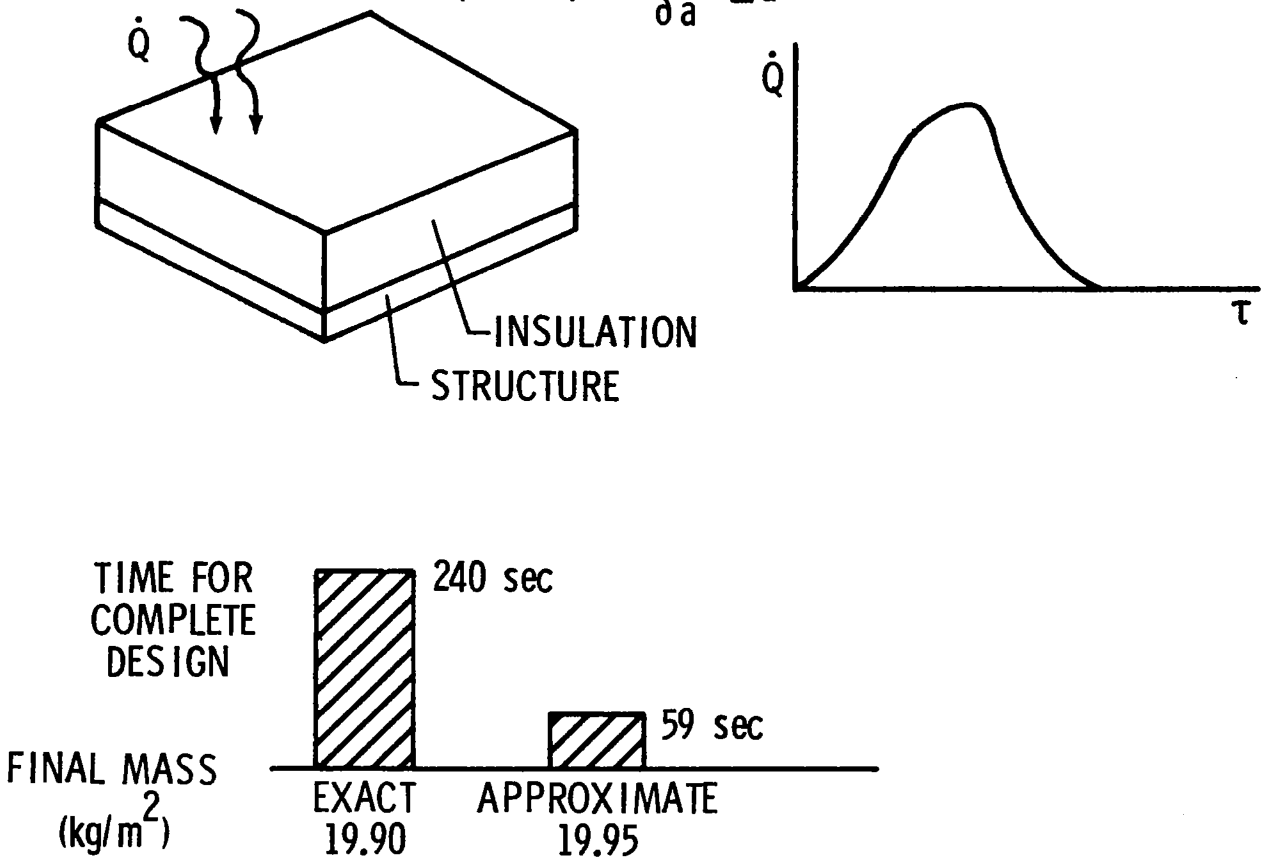

Figure 19

PARS (PROGRAM FOR ANALYSIS AND RESIZING OF STRUCTURES)

(Figure 20)

PARS is a user-oriented system of programs for the minimum mass design of complex structures modeled by finite elements. The system utilizes SPAR and consists of a series of processors that communicate through the use of the SPAR data base. A description of PARS together with sample results are presented in reference 11. An efficient optimizer based on the Sequence of Unconstrained Minimization Technique (SUMT) with an extended interior penalty function and Newton's method is used. Additional optimization procedures may be easily installed in the optimizer module. The design variable interface processor allows the user the flexibility of assigning a single design variable (e.g. a structural element thickness) to control a large number of finite elements. The sensitivity processors generate certain derivatives useful for determining how response variables such as displacements and stresses are affected by changes in structural sizes. At present PARS is in the early development stage but its configuration which features modularity and flexibility plus the efficiency of the SPAR analyzer holds promise for achieving the goal of efficient design techniques for complex structures.

PARS (PROGRAM FOR ANALYSIS AND RESIZING OF STRUCTURES)

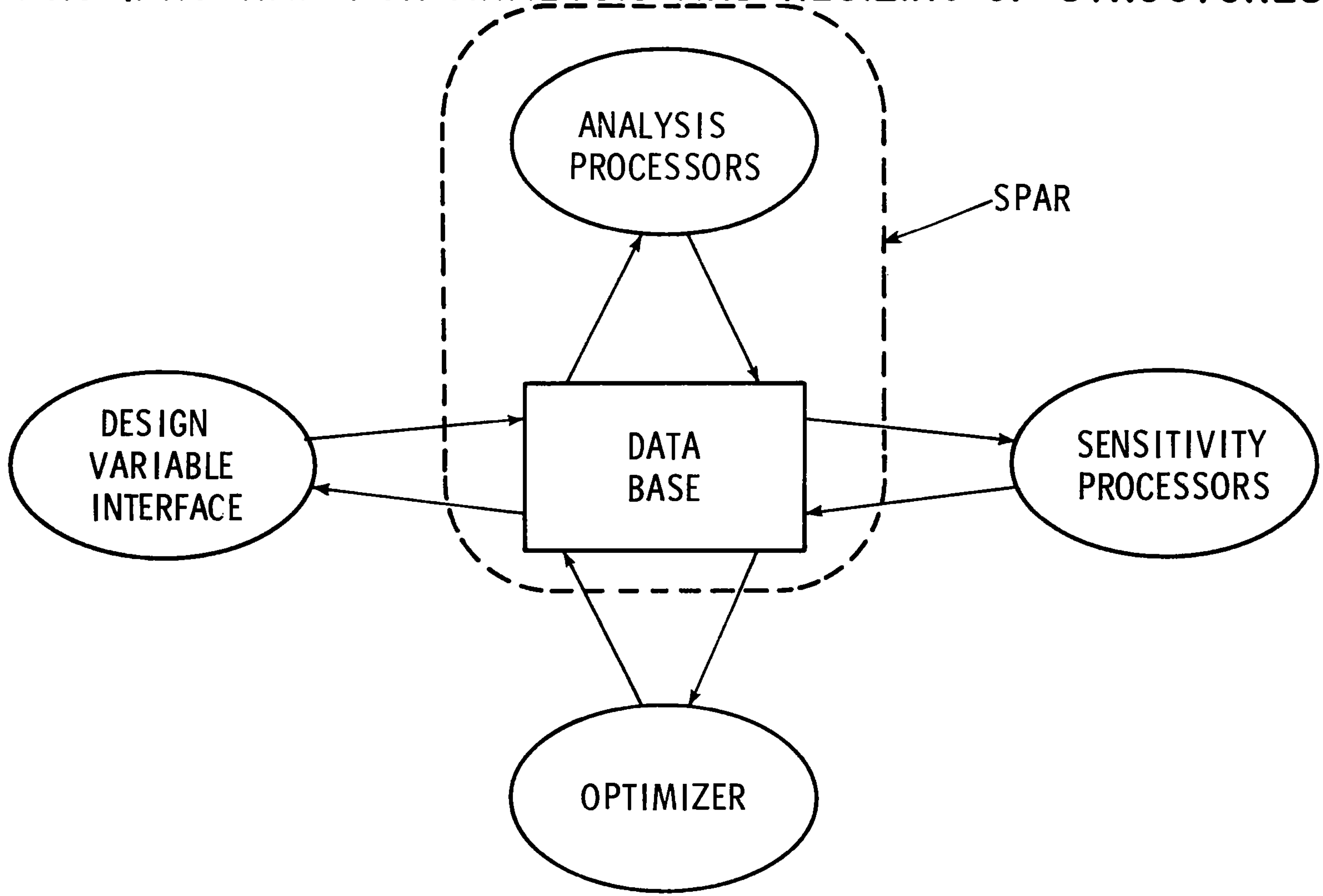

- MODULAR AND FLEXIBLE
- GOAL-EFFICIENT GENERATION OF DESIGNS FOR COMPLEX STRUCTURES

Figure 20

SUMMARY

(Figure 21)

This paper reviews a continuing effort to develop a comprehensive capability for thermal-structural analysis and automated design (sizing). A principal role in the activity is played by the finite element program SPAR which contains both an efficient structural and thermal analysis capability. The benefit of having thermal and structural analyses in the same finite element program is illustrated by the application of SPAR to design calculations for the National Transonic Facility - a cryogenic wind tunnel under construction at Langley.

Some experience with large-scale thermal structural analysis problems - particularly the space shuttle orbiter - has led to the identification of some analysis needs. Those needs include automated model generation and data output for lumped parameter thermal analysis, faster solution methods for nonlinear transient heat transfer, automated interpolation of temperature data from a thermal finite element model to a dissimilar structural finite element model, and automated techniques to identify the times at which the critical conbinations of transient heating and loads occur on a structure.

Techniques for automated design of thermal structures are discussed for three classes of structures: first where temperatures are accepted but thermal stresses must be accommodated; second where both temperatures and stresses are controlled and temperatures are controlled by conduction to a heat sink, and third where temperatures are controlled by insulating the structure from transient heating. Additionally a technique for design-oriented transient thermal analysis is discussed and development of design capability for large problem built around the SPAR analysis program is outlined.

SUMMARY

- o DEVELOPING INTEGRATED THERMAL-STRUCTURAL ANALYSIS CAPABILITY
- o SIGNIFICANT PROGRESS MADE TO DATE IN SPAR DEVELOPMENT
  - o EFFICIENT STRUCTURAL ANALYSIS
  - o THERMAL ANALYZER
  - o STRUCTURAL AND THERMAL ANALYSIS IN SAME PROGRAM
- o NTF ANALYSIS DEMONSTRATED INTEGRATION BENEFITS
- o EXPERIENCE WITH LARGE PROBLEMS IDENTIFIED NEEDS
  - o AUTOMATED MODEL GENERATION
  - o SOLUTION TECHNIQUES
  - o AUTOMATED DATA TRANSFER BETWEEN MODELS
  - o CRITICAL TIMES DETERMINATION
- o DEVELOPING ANALYTICAL DESIGN CAPABILITY
  - o VARIETY OF RESIZING TECHNIQUES DEVELOPED AND APPLIED
  - o LARGE PROBLEM DESIGN CAPABILITY BEING DEVELOPED IN PARS

Figure 21

SYMBOLS

A	area of a bar
a	design variable
E	Young's modulus
h	film coefficient
N	number
N_x	force per unit length
$\dot{Q}$	applied heat flux
T	temperature
T_∞	film temperature
T^*	temperature due to change in design variable
t	membrane thickness
W^*	augmented mass function
α	coefficient of thermal expansion
τ	time

Subscript:

i	iteration number

1. Whetstone, W. D.: SPAR Structural System Reference Manual, NASA CR-145098, 1977.

2. Thornton, Earl A.; and Wieting, Allan R.: Recent Advances in Thermostructural Finite Element Analysis. Recent Advances in Structures for Hypersonic Flight, NASA CP-2065, 1978. (Paper no. 23 of this compilation.)

3. Anon.: Martin Interactive Thermal Analysis System, Version 1.0, Martin Marietta Corp. MDS-SPLPD-71-FD238 (Rev. 3) 1972.

4. Anon.: Creation of Lumped Parameter Thermal Model By Use of Finite Elements, NASA CR-158944, 1978.

5. Adelman, H. M.; Walsh, J. C.; and Narayanaswami, R.: A Improved Method for Optimum Design of Mechanically and Thermally Loaded Structures, NASA TND-7965, 1975.

6. Adelman, H. M.; and Narayanaswami, R.: Resizing Procedure for Structures Under Combined Mechanical and Thermal Loading. AIAA J. Vol. 14, No. 10, Oct. 1976, pp. 1484-1486.

7. Adelman, H. M.; and Narayanaswami, R.: Resizing Procedure for Optimum Design of Structures Under Combined Mechanical and Thermal Loading. NASA TMX-72816, 1976.

8. Jones, R. T.; and Hague, D. S.: Application of Multivariable Search Techniques to Structural Design Optimization. NASA CR-2038, 1972.

9. Harris, Robert S.; Davidson, John R.: An Analysis of Exact and Approximate Equations for the Temperature Distribution in an Insulated Thick Skin Subjected to Aerodynamic Heating. NASA TN D-519, 1961.

10. Storaasli, Olaf O.; and Sobieszczanski, Jaroslaw: On the Accuracy of the Taylor Approximation for Structural Resizing. AIAA J., Vol. 12, No. 2, Feb. 1974, pp. 231-233.

11. Haftka, R. T., and Prasad, B.: Programs for Analysis and Resizing of Complex Structures. Paper presented at Symposium on Future Trends in Computerized Structural Analysis and Synthesis. Washington, D.C. Oct. 30 - Nov. 1, 1978.

SYMPOSIUM ATTENDEES

National Aeronautics & Space Administration
Washington, DC

D. A. Gilstad
Arthur Henderson

National Aeronautics & Space Administration
Dryden Flight Research Center
Edwards, CA

R. A. Fields

National Aeronautics & Space Administration
Langley Research Center
Hampton, VA

H. M. Adelman
D. E. Avery
H. L. Bohon
R. W. Boswinkle
R. D. Brown
C. J. Camarda
M. F. Card
L. M. Couch
S. C. Dixon
J. M. Eggers
C. H. Eldred
R. W. Faison
R. Garcia
G. L. Giles
L. D. Guy
T. W. E. Hankinson
H. F. Hardrath
R. V. Harris
J. E. Hasel
D. P. Hearth
R. R. Heldenfels
B. Z. Henry
J. L. Hunt
L. R. Hunt
L. R. Jackson
P. J. Johnston
R. A. Jones
H. N. Kelly
F. S. Kirkham
P. J. Klich
J. A. Koegler
I. O. Macconochie
E. A. Mackley
D. C. Marcum
J. A. Martin
H. G. McComb
O. W. Nicks
R. J. Nowak
R. A. Rainey
J. C. Robinson
J. W. Sawyer
E. L. Sharpe
J. L. Shideler
C. P. Shore
W. J. Small
J. Sobieski
S. J. Stack
D. P. Swofford
M. G. Torrence
R. L. Trimpi
G. D. Walberg
W. C. Walton
J. D. Watts
G. L. Webb
I. Weinstein
A. R. Wieting
A. W. Wilhite
J. W. Wilkey
R. D. Witcofski
K. E. Wurster

AEROSPACE COMPANIES

Aerospace Corporation
Los Angeles, CA

E. G. Kendall

AiResearch Manufacturing Company
Torrance, CA

O. Buchmann

Applied Physics Laboratory
The Johns Hopkins University
Laurel, MD

W. C. Caywood

Bell Aerospace
Buffalo, NY

F. Anthony

Boeing Aerospace Company
Seattle, WA

V. Duriugin
A. Hepler

Grumman Aerospace Corporation
Bethpage, NY

P. Bell

Lockheed-California Company
Burbank, CA

G. W. Davis

McDonnell Aircraft Company
St. Louis, MO

L. Koch
V. Pagel

McDonnell Douglas Corporation
St. Louis, MO

B. Haeffele
M. H. Heinz
H. A. Holman

ORI, Incorporated
Silver Spring, MD

E. Harris
J. Schneider

Rockwell International Corporation
Los Angeles Division
Los Angeles, CA

P. A. Boukidis
H. J. Hoge

Rockwell International Corporation
Rocketdyne Division
Canoga Park, CA

R. Ackerman
R. P. Jewett

Rockwell International Corporation
Space Division
Downey, CA

C. S. Beuyukian
L. M. Smith
S. Y. Yoshino

Rohr Industries
Chula Vista, CA

W. Blair

Vought Corporation
Hampton Tech. Center
Hampton, VA

C. Breiner
R. W. LeMessurier
A. L. Taylor

SELF-EMPLOYED

J. V. Becker, Newport News, VA

UNIVERSITIES

Illinois Institute of Technology
Chicago, IL

R. Haftka

Old Dominion University
Norfolk, VA

E. A. Thornton

New York University
New York, NY

A. M. Agnone

USAF

Wright-Patterson AFB, OH

S. E. Kaminski
P. Lane
R. N. Mueller
A. D. Straw

USN

Naval Surface Weapons Center
Dahlgren, VA

F. Moore

☆U.S. GOVERNMENT PRINTING OFFICE: 1979-635-004/31

1. Report No. NASA CP-2065, Part II	2. Government Accession No.	3. Recipient's Catalog No.
4. Title and Subtitle RECENT ADVANCES IN STRUCTURES FOR HYPERSONIC FLIGHT		5. Report Date December 1978
		6. Performing Organization Code
7. Author(s)		8. Performing Organization Report No. L-12653
9. Performing Organization Name and Address NASA Langley Research Center Hampton, VA 23665		10. Work Unit No. 505-02-53-01-00
		11. Contract or Grant No.
12. Sponsoring Agency Name and Address National Aeronautics and Space Administration Washington, DC 20546		13. Type of Report and Period Covered Conference Publicatio
		14. Sponsoring Agency Code

15. Supplementary Notes

16. Abstract

The proceedings of the NASA Symposium - Recent Advances in Structures for Hypersonic Flight held at Langley Research Center on September 6-8, 1978, are reported in this NASA Conference Proceedings. The papers at this Symposium were presented by 24 speakers representing airframe, missile, and engine manufacturers, the U.S. Air Force, and two NASA Research Centers. The papers cover a variety of topics including engine structures, cooled airframe structures, hot structures, thermal protection systems, cryogenic tankage structures, cryogenic insulations, and analysis methods for thermal/structures.

17. Key Words (Suggested by Author(s)) Hypersonic aircraft Actively cooled structure Thermal/Structures analysis methods Thermal protection Cryogenic tankage Cryogenic insulation	18. Distribution Statement Unclassified - Unlimited Subject Category 39

19. Security Classif. (of this report)	20. Security Classif. (of this page)	21. No. of Pages	22. Price*
Unclassified	Unclassified	415	$13.25

* For sale by the National Technical Information Service, Springfield, Virginia 22161